Optimisation of Piston Bowl Geometry and Double Injection Strategy in Diesel Engines Using a Bespoke Hybrid Regression-Based Technique.

Submitted to the University of Hertfordshire in partial fulfilment of the requirements for the degree of
Doctor of Philosophy

Area of Study: Sustainable Energy Technology

School of Physics, Engineering and Computer Science, University of Hertfordshire

November 2021

Abstract

This research work is driven by the requirement for more efficient and cleaner internal combustion engines that meet fuel saving demands, stringent emissions regulations, and compatibility with hybrid powertrain technology. Despite the improvements made in current engines as useful industrial power units, the environmental and health effects of their emissions as well as relatively low fuel efficiency are still a cause for further research and development.

In this work, a 3D Computational Fluid Dynamics (CFD) engine model is validated against experimental data obtained from a single cylinder Ricardo Hydra diesel engine. The validated engine model is used to simulate the in-cylinder combustion processes and emissions characteristics of the engine using AVL Fire software. The engine model is used to investigate the effects of piston bowl geometry, and double injection strategy on diesel combustion and emissions at low and high engine loads operating with double fuel injection strategy. During the investigation, the synergies between piston bowl geometry, injection timing and injection ratio were analysed. This analysis yielded interesting findings on the influence of these parameters on engine performance and emissions at low and high loads. The results showed that exhaust emissions are more sensitive to piston bowl geometry while injection timing and split injection ratio can significantly influence both performance and emissions. In addition, the re-entrance curvature of the piston bowl geometry showed to influence air-fuel mixing by modifying the surface area of the mixing front closer to the surface of bowl side and base walls. In this investigation, larger radius piston bowls denoted by ORB1 and ORB2 resulted in a larger mixing front area.

The investigation was extended further towards the multi-objective optimisation of piston bowl geometry and double injection strategy which was performed using a two-stage optimisation approach. The first stage involved a non-pareto constraining optimisation of piston bowl geometry that considered the results from the initial investigation at low and high loads. The goal was to obtain a piston bowl geometry that was suitable for the second stage of the optimisation process which focused on the double injection strategy. The results from the first stage showed that ORB2 was most suitable at low and high loads due to enhanced combustion phasing stability.

The second stage involved the optimisation of double fuel injection strategy at low and high engine loads. A unique optimisation methodology called the Hybrid Regression-based Technique (HRT) was proposed and implemented for this stage to achieve optimal solutions at significantly reduced computational time and cost. The initial aspect of the HRT involved the implementation of a unique hybrid dataset of designs generated using a coupled DoE-Optimiser algorithm approach which proved efficient in enabling an early indication of the pareto region of the multi-objective domain. The HRT also involved an ensemble approach for regression modelling over the hybrid dataset in a bespoke manner. The bespoke predictive learner/model was a hybrid of multiple models obtained from the consideration of a library of regression methods via a comparative analysis. This hybrid model was coupled with the MOGA-II to obtain optimal solutions for the double injection strategies with respect to each performance and emissions parameter considered.

Validation of the results showed that the HRT provided acceptable optimal solutions for double injection strategy. At low load, optimal double injection strategies were characterised by relatively early first injection events occurring at about 15°bTDC which contained 80% to 85% of the total injected fuel and about a 10CA dwell angle. At high load, optimal double injection strategies were also characterised by relatively early first injection events occurring at about 11°bTDC which contained 90% to 95% of the total injected fuel and a dwell angle between 8CA and 12CA. More also, the Hybrid Regression-based Technique was able to achieve these improvements with a significantly reduced computational time of over 80% compared to the conventional optimisation approaches in similar studies.

The objectives of this research work were to develop a numerical model capable of predicting diesel combustion and emission under different operating conditions, study the effects that arise from the interactions between piston bowl geometry and injection strategy and to identify an optimisation methodology that tackles the complexity involved in engine CFD multi-objective optimisation. The investigations carried out in this work thereby contribute to the knowledge in this field by offering a new perspective for engine modelling and optimisation involving advanced injection strategy and piston bowl geometry which may be useful in providing insight to other researchers in the quest for further engine development and optimisation.

Acknowledgements

Firstly, the author of this written work expresses that an editor has not been used in the drafting of this thesis. This research work has been completed with the guidance and support provided by a special group of people. First, I want to thank the Almighty God for giving me the strength and perseverance to realise and complete this research. I also want to express my immense gratitude to my parents, Prof. and Mrs Asimiea for their love, support, and sponsorship.

To my Principal Supervisor, Associate Prof. Mohammad Reza Herfatmanesh; I am immensely grateful for his priceless support and guidance which led to the completion of this work. His knowledge challenged my efforts in the work significantly. To my second supervisor, Prof. Yong-Kang Chen; my sincerest thanks for his support in the transition of my supervisory team, and the completion of my programme.

To my third supervisor, Prof. Zhijun Peng; I am forever grateful for the opportunity he gave me from the beginning of my study and for always being available to answer my questions. To my fourth supervisor, Dr. Alexis Ihracska; I am thankful for his immerse assistance, and sincerity as well as his attention to detail and the ability to ask important questions which helped me prepare the earlier stages of this work.

I owe special thanks to the members of staff at the University of Hertfordshire who aided me at various stages of my study. I would like to also thank AVL GmbH List for its technical support, Mayur Jani for his enormous help with the laboratory, Lambros Kaiktsis, Panagiotis Kontoulis, Hadi Taghavifar and Daniele Piazzullo for their invaluable support with CFD Diesel engine simulations and optimisation. They encouraged me to explore the capabilities of the CFD software beyond the current progressions made with it.

Finally, I would like to acknowledge my friends, and colleagues who have supported me through this journey and especially my wife Tanya, for her immeasurable support and encouragement at all times.

Contents

List of Figures

List of Tables

Nomenclature

Symbols

a	Acceleration
x, y, z	3 dimensional coordinates
μ *and* λ	Dynamic viscosity and shear stress
∇	Derivative
℃	Degree Celsius
K	Degree Kelvin
N	Engine speed
C_aH_b	General chemical formula of a hydrocarbon
kW	Kilowatt
mg	Milligram
P or p	Pressure
Q	Rate of heat transfer to the system
t	Time
T	Torque
u, v, w	Velocities in x, y, z directions respectively
$V, \vec{V}$	Velocity, Vector velocity,

Abbreviations

1D	One Dimensional
2D	Two Dimensional
3D	Three Dimensional
ABDC	After Bottom Dead Centre
ASTM	American Society for Testing and Materials
ATDC	After Top Dead Centre
ARMOGA	Adaptive Range Multi-Objective Genetic Algorithm
BBDC	Before Bottom Dead Centre
BTDC	Before Top Dead Centre
BMEP	Brake Mean Effective Pressure
BP	Brake Power
BSFC	Brake Specific Fuel Consumption
BTE	Brake Thermal Efficiency
CA	Crank Angle
CARB	California Air Resource Board
CFD	Computational Fluid Dynamics
CI	Compression Ignition
CI-ICEs	Compression Ignition-Internal Combustion Engines
CIDI	Compression Ignition Direct Injection
CN	Cetane Number
CO	Carbon Monoxide
CO_2	Carbon Dioxide
CR	Compression Ratio
CRS	Common Rail System
DI	Direct injection
DOC	Diesel Oxidation Catalysts
DoE	Design of Experiment
DPF	Diesel Particulate Filter
ECFM-3Z	Extended Coherent Flame Model 3 Zones

EER	Emissions Efficiency Ratio
ECU	Electronic Control Unit
EGR	Exhaust Gas Recirculation
EPA	Environmental Protection Agency
ESE	Engine Simulation Environment
Eq-R	Equivalence Ratio
EVC	Exhaust Valve Closing
EVO	Exhaust Valve Opening
Exp.	Experimental
FAAE	Fatty Acid Alkyl Ester
FAEE	Fatty Acid Ethyl Ester
FAME	Fatty Acid Methyl Ester
FFA	Free Fatty Acids
FFT	Fast Fourier Transform
FQIP1	Fuel Quantity Injected in Pulse 1
FQIP2	Fuel Quantity Injected in Pulse 2
GA	Genetic Algorithm
H_2O	Water
HCCI	Homogenous Charge Compression Ignition
HRR	Heat Release Rate
HRT	Hybrid Regression-Based Technique
HSDI	High-Speed Direct Injection
HTHDC	High Temperature Highly Diluted Combustion
IC	Internal Combustion
ICE	Internal Combustion Engine
ID	Ignition Delay
IMEP	Indicated Mean Effective Pressure
ISFC	Indicated Specific Fuel Consumption
IP	Indicated Power
IVC	Intake Valve Close
IVO	Intake Valve Open
LEV	Low Emission Vehicle
LHV	Lower Heating Value
LTC	Low Temperature Combustion
LES	Large Eddy Simulation
LPG	Liquified Petroleum Gas
LNG	Liquified Natural Gas
MEP	Mean Effective Pressure
Micro-GA	Micro Genetic Algorithm
MOGA	Multi-Objective Genetic Algorithm
NLEV	National Low Emission Vehicle
NLPQL	Non-Linear Programming by Quadratic Lagrangian
NOx	Nitric oxide(s)
NO_2	Nitrogen Dioxide
NO	Nitric Oxide
NSGA	Non-dominated Sorting Genetic Algorithm
O_2	Oxygen
PCCI	Premixed Charge Compression Ignition
PPCI	Partially Premixed Compression Ignition
PM	Particulate Matter

PDF	Probability Density Function
ppm	Parts Per Million
RANS	Reynolds Averaged Navier-Stokes
RCCI	Reactivity Charge Compression Ignition
RNG	Renormalisation Group
RSM	Reynolds Stress Model
rpm	Revolutions Per Minute
SA	Spray Angle
SCA	Spray Cone Angle
SCR	Selective Catalytic Reduction
SIMPLE	Semi-Implicit Method for Pressure Linked Equations
SoC	Start of Combustion
SoI	Start of Injection
TDC	Top Dead Centre
uHC	Unburned Hydrocarbons
VCO	Varied Covered Orifice
WCO	Waste Cooking Oil

1 Introduction

1.1 Background

The compression ignition engine also commonly referred to as the diesel engine is an attractive power unit used in the transportation and power generation sectors due to its advantages which include higher durability and reliability, improved torque characteristics at low loads, lower fuel consumption and lower Carbon Monoxide (CO) emissions compared to conventional spark ignition (i.e., gasoline) engines. Nevertheless, diesel engines have been reported to emit higher levels of Particulate Matter (PM), unburned Hydrocarbons (uHC) and Nitrogen Oxides (NOx) emissions in comparison to gasoline engines [1].

Diesel combustion characteristics and emissions formation are highly influenced by air-fuel mixing as well as the physical and chemical processes that result in the combustion within the combustion chamber. Of all the emissions produced by CI engines, Soot, a predominant constituent of PM formed in rich mixing regions, and NOx, formed in regions of high temperature and oxygen concentration, have been subjected to greater scrutiny due to their adverse environmental and health effects. These concerns led to the introduction of emissions legislation such as the Environmental Protection Agency (EPA), the California Air Resource Board (CARB) Low-Emission Vehicle (LEV) regulation standards LEV I, II and III, the Clean Air Act regulation standards Tier 1, 2 and 3 in the United States of America since the 1960's and the Euro 1, 2, 3, 4, 5, 6 and 7 in the European Union since 1992 [2].

Furthermore, the growing effects of emissions have driven the increased attention towards alternative "clean" energy applications with a recent call for the ban on the production and sale of new gasoline and diesel-powered vehicles by 2030 in the UK [3]. This drive has been reinforced by a gradual depletion of fossil fuel reserves as both global energy demand and Carbon Dioxide (CO_2) production are reported to increase by 28% and 15%, respectively, between 2015 and 2040 [4], [5]. While on one hand, this shift has been perceived as the immediate phase out of conventional engines, on the other hand, it has accelerated research and development of cleaner and more efficient Internal Combustion (IC) engines especially for hybrid powertrain

applications given the current global limitations of electric vehicles especially in regions such as India and Africa.

In this regard, research into the advancement of various engine technologies continue to gain attention. Some of these technologies include aftertreatment systems, Exhaust Gas Recirculation (EGR), Low Temperature Combustion (LTC) modes and alternative fuels as well as multiple fuel injection strategies and piston bowl geometry [6]–[9]. However, multiple injection strategies and as well as piston bowl and injector spray geometrical optimisation continue to be given even more attention due to their direct interaction and influence on air-fuel mixing and combustion as well as the consequential effects on engine performance and emissions.

The challenges of homogenous mixture preparation and combustion phasing control result in high engine emissions and combustion noise regardless of performance [10]. These challenges have been linked to an inadequate control over the spatial and temporal distribution of the injected fuel with respect to residence pressure and temperature in the combustion chamber.

Multiple injection strategies address these challenges by allowing pre-defined smaller quantities to be injected and in current developments, up to nine times per cycle at stipulated injection times. This provides a greater control over the air-fuel mixing formations that produce homogeneity as well as desired combustion phasing that results in both improved performance and reduced emissions. Multiple injection strategies are classed as controllable engine parameters which can be adjusted during engine run time along with other parameters such as EGR rate and free valve miller cycles.

The double injection strategy is considered as the simplest form of multiple injection strategy because it involves two injection events over which a high degree of control can be imposed and the fuel injection characteristics such as timing and duration can be correlated to the consequential in-cylinder air-fuel mixing and emission formations. The optimisation of double injection strategy therefore provides insight in the interaction of the injection control implemented and the resulting in-cylinder air-fuel mixing behaviour in a simple manner that informs on the implementation of more injection events per engine cycle [11].

Piston bowl geometry optimisation involves the improvement of the combustion chamber shape and in many investigations, the shape of the piston bowl to improve in-cylinder flow direction and turbulence which enhances air-fuel mixing. As fixed engine parameters (i.e., parameters which cannot be changed easily duration engine operation), various investigations have been performed on this avenue with the goal of achieving bowl-in-piston geometries that are suitable for a wide range of engine operating conditions [12]. Current studies on the optimisation of piston bowl geometries often lead to a single geometry configuration which is sensitive to the selected optimal fuel injection strategy. However, variable optimal engine operation could be better realised from the identification of geometry which is suitable and optimal over a wide range of optimal injection strategies. The interactions between the injection strategy and piston bowl geometry and the effects of such interactions on performance and emissions is an avenue that is vital to this notion but scarcely investigated.

Developments in double injection strategy and piston bowl geometry can be assessed through engine experiments and/or Computational Fluid Dynamics (CFD) engine model simulations. Experimental investigations are commonly conducted to determine performance and emissions characteristics; however, they are rather costly to set up, run and maintain. In addition, the implementation of new designs and strategies require engine modifications which often increase the cost and complexity of engine experimental investigations.

CFD engine model investigations can be used to predict engine performance and emissions from the exploration of new designs in a manner that both saves time and cost. Currently, CFD engine model simulations can be performed using various software including the ANSYS Fluent packages, IC Engine and Forte, KIVA, OpenFOAM, Converge, GT Power, AVL Suite Boost and Fire packages, etc. Furthermore, CFD engine models can be coupled with optimisation methods for the optimisation of various engine model parameters to achieve predictions on improved performance and emissions [13], [14]. In this research work, AVL Fire is the CFD engine modelling software package used for 3D engine modelling and simulation. As discussed in a later section of this work, it is widely used due to its sub models which are heavily supported by detailed experimental investigations carried out by its

developer AVL GmbH List as well as developmental work carried out by researchers. The CFD engine model is this research work features various CFD sub models that have been used extensively in the research with reported accurate predictions of in-cylinder turbulence, air-fuel mixing, combustion, and emission behaviours.

Computational optimisation is used to further explore the newly generated designs and solutions for engine parameters with the goal of seeking the areas and directions for further improvement. It utilises the relationship and correlation between engine parameters which serve as predictors and the output performance and emission parameters which serves as response to drive the search for optimal engine design solutions which result in improvements. Various investigations on use of computational optimisation for improving engine performance and/or emissions have been performed over the years [14],[15],[16],[17]. Despite the benefits of computational optimisation in realising improvements in engine performance and emissions, the process currently suffers the drawback of extensive computational cost and time as well as a lack of abundant approaches towards the combined consideration of fixed and controllable parameters such as piston bowl geometry and double injection strategy respectively.

Despite the benefits of multiple injection strategies reported in various investigations, obtaining optimal injection strategies for a broad range of engine loads is still an issue. Although various studies have been performed on the optimisation of multiple injection strategies, as well as the optimisation of piston bowl geometry, insights on the interaction between multiple injection strategies such as the double injection strategy and piston bowl geometry especially under different engine loads are yet to be fully explored and require further investigation.

This research work focuses on this area as the benefits of such insights are vital to improving engine performance and emissions. For this work, a CFD engine model is created to include sub models that predict in-cylinder phenomena such as turbulence, fuel spray and breakup, combustion as well as emission formation. The CFD engine model is also validated against an actual diesel engine to provide certainty that it can accurate depict the in-cylinder phenomena which result in combustion and emission formation. The engine CFD model is used to investigate the interactions between piston bowl geometry and double injection strategy to later inform on the approach

used for the optimisation of both engine parameters. The optimisation of both engine parameters is computational and is performed based on CFD engine model simulations in AVL Fire coupled with modeFRONTIER and MATLAB. More importantly, a bespoke computational optimisation technique referred to as the Hybrid Regression-based Technique (HRT) is designed and implemented using these tools to seek improvements on the CFD engine model formulated in a manner which incurs minimal computational costs and time while maintaining accurate predictions compared to the techniques used in current studies.

1.2 Aim and Objectives

The aim of this research is to provide further insight on diesel engine in-cylinder mixture formation, combustion characteristics and emissions formation through thorough assessment and optimisation of double injection strategy and piston bowl geometry using a unique optimisation technique.

The objectives of this research are to:

- Validate a 3D CFD engine model based on experimental data.
- Investigate the interaction between piston bowl geometry and double injection strategies at low and high loads and thus, the effects on in-cylinder performance and emissions.
- Select optimal piston bowl geometry based on the interactions at low and high load conditions.
- Optimise double injection strategies at low and high loads using the preselected optimal piston bowl geometry.

1.3 Contribution to Knowledge

- Insights on the synergies between multiple injections and piston bowl geometry at different engine loads that drives the methodology for their optimisation.
- The proposal of a unique approach to optimisation that simultaneously considers multiple injection strategy and piston bowl geometry at different engine loads.

- The multi-objective optimisation of double injection strategy that involves the use of a novel hybrid regression-based optimisation technique, based on a hybrid design of experiments data for training and validation, that consists of sampling and optimised designs generated through CFD engine simulations.

1.4 Thesis Outline

The research work presented in this thesis is organised into seven chapters as follows:

Chapter 1 provides the direction of the research work and states its aim, objectives, and contribution to knowledge.

Chapter 2 provides a review on conventional diesel engine combustion, emissions and regulations, advancements in various methods of emission reduction, engine CFD modelling, diesel engine optimisation and the computational algorithms used.

Chapter 3 presents the details of the experimental setup used to produce the baseline experimental data to validate the 3D engine CFD model.

Chapter 4 presents the setup of the engine 3D CFD simulation model and its validation in AVL Fire.

Chapter 5 presents the investigation on the interaction between double injection strategy and piston bowl geometry at low and high engine loads.

Chapter 6 presents the multi-objective optimisation of the piston bowl geometry and double injection strategy at low and high engine loads.

Chapter 7 presents the research conclusions and future recommendations.

2 Literature Review

2.1 Conventional Combustion in Direct Injection Diesel Engine

2.1.1 The Four-Stroke Diesel Engine Cycle

The conventional four-stroke Direct Injection (DI) diesel engine undergoes four strokes per cycle characterised by the linear vertical motion of the piston depicted in Figure 2-1. In a cycle, air enters the chamber in the induction stroke and is then compressed by the piston's upward motion in the compression stroke. Fuel injection can occur during the compression and power stroke. In the power stroke, the piston is forced downwards due to combustion of the fuel-air mixture while inertia causes its upward motion expelling the exhaust gases out of the chamber in the exhaust stroke [18].

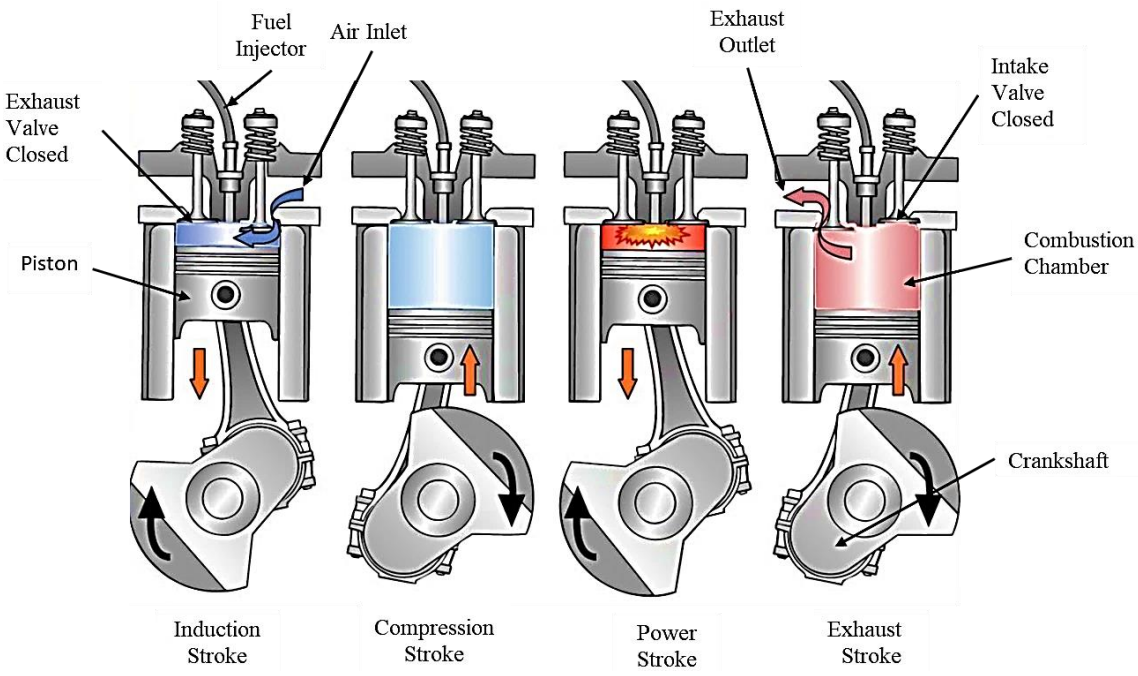

Figure 2-1: Four-stroke DI diesel engine cycle [18]

2.1.2 Heat Release Rate

Figure 2-2 shows a typical Heat Release Rate (HRR) profile produced by diesel combustion, highlighting three co-dependent combustion phases. The Start of Injection (SoI) signifies the time at which fuel injection into the combustion chamber commences. This is followed by an Ignition Delay (ID) which is a period characterised by fuel atomisation, evaporation and mixing with air and residual gas content within the combustion chamber.

Auto-ignition is caused by the increase in the pressure and temperature of air-fuel mixture due to compression. It signifies the Start of Combustion (SoC) and is identified by the first rise in the generated heat release. The three combustion phases are influenced by the duration of the ignition delay.

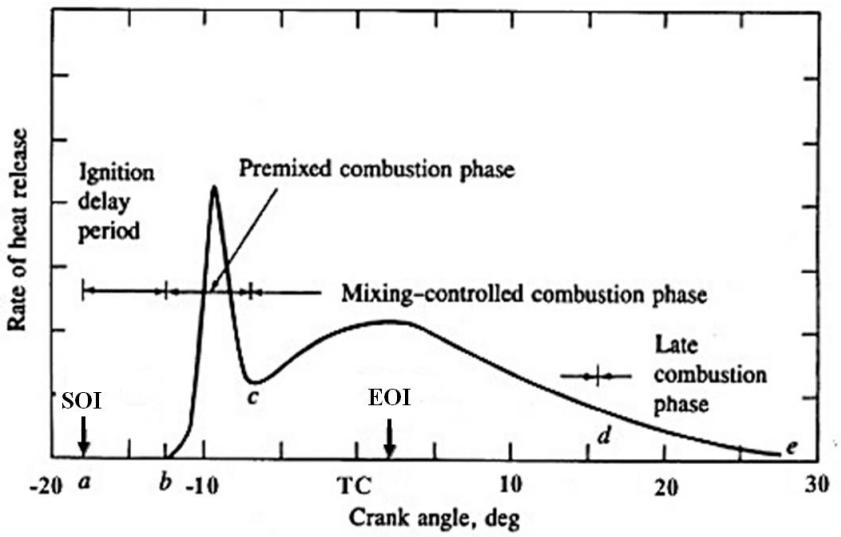

Figure 2-2: Typical HRR profile produced by diesel combustion [18].

The premixed combustion phase is characterised by the air-fuel mixing during the ignition delay period and can be nearly stoichiometric (i.e., local equivalence ratio, $\lambda \approx 1$). It is comprised of mainly lean mixing formations (i.e., local equivalence ratio, $\lambda < 1$). In addition, it is commonly characterised by a rapid rise in the in-cylinder pressure and temperature caused by sudden and high HRR. This combustion phase usually results in high Indicated Mean Effective Pressure (IMEP), combustion noise and NOx emissions. This is due to the presence of higher oxygen content and in-cylinder temperature during this period.

The diffusion/mixing controlled combustion phase is characterised by the rate of air-fuel mixing. The mixing formations in this phase are usually rich (i.e., local equivalence ratio (λ) > 1) since newly introduced parcels of fuel droplets evaporate much faster due to higher in-cylinder temperature resulting in shorter residence time to mix with the air to form a stoichiometric/lean mixture. This mixing and remixing process results in a slower rate of heat release generally observed in this phase compared to the premixed phase. This combustion phase usually results in high PM, soot, and CO emissions due to insufficient oxygen.

The late combustion phase involves partial oxidation of the remaining fuel left after the end of the mixing-controlled combustion phase. The combustion temperature in this phase is relatively low compared to the first two phases and results in the termination of the combustion process [18]. The characteristics of each phase and thus the emissions formation is linked to the nature of the local and global mixture formation within the combustion chamber. Thus, careful control of fuel injection quantity and timing can aid in optimising different combustion phases through an improved local air-fuel equivalence ratio, λ; wherein a $\lambda = 1$, $\lambda < 1$ and $\lambda > 1$ represent stoichiometric, rich, and lean combustion, respectively [18].

2.2 Diesel Engine Emissions

2.2.1 Nitrogen Oxide (NOx) Emission

Nitrogen oxide emissions also referred to as "NOx emissions" are family of nitrogen-based emissions consisting of about 70-90% Nitric Monoxide (NO) and about 10-30% Nitrogen Dioxide (NO_2) with negligible amounts of nitrous oxide N_2O [19]. NOx emissions are highly regulated globally due to their negative environmental and health effects. NOx is a major exhaust emission produced by diesel engines, formed due to the reaction of atmospheric nitrogen with oxygen in the presence of temperatures in excess of 1500K [19]. NOx emissions are higher in diesel engines compared to gasoline engines due to their higher combustion temperatures.

2.2.1.1 NOx Formations

2.2.1.1.1 Thermal NOx formation

Thermal NOx formation is regarded as the predominant process in NOx formation during combustion. It is caused by the reaction of dissociated atmospheric molecular nitrogen with oxygen in the presence of high temperatures. NOx formation occurs in the flame front as well as the burnt gases; however, its formation in the burnt gas region is more pronounced due to higher local temperatures.

The thermal NOx formation rate increases with increasing temperature. Its reaction mechanism is accurately expressed by the extended Zeldovich mechanism seen in equations 2.1, 2.2 and 2.3[19].

$$N_2 + O \leftrightarrow NO + N \ : k_1 \quad (2.1)$$

$$O_2 + N \leftrightarrow NO + O : k_2 \quad (2.2)$$

$$OH + N \leftrightarrow NO + H : k_3 \quad (2.3)$$

Equations 2.1 and 2.2 were developed by Zeldovich while Lavoie et al [19] identified equation 2.3 through spectroscopy. Equation 2.1 represents the rate restrictive step of the reaction mechanism. It is significantly fast and characterised by activation energy required for the decomposition of the stable triple-bond molecular atmospheric nitrogen and thus highly temperature dependent. Equation 2.2 represents the reaction of a nitrogen atom with oxygen to form NO. Equation 2.3 represents the formation of NOx from the oxidation of nitrogen atom by hydroxyl radicals (OH) to form NO and hydrogen atom at near-stoichiometric conditions.

Reactions k_1, k_2, and k_3 in the mechanism are fully reversible. Furthermore, the kinetics of the mechanism is such that, the NOx formation timescale is comparable and sensitive to the combustion duration, residence time, oxygen content and the increase of in-cylinder temperature [19].

More also, from equations 2.1, 2.2 and 2.3, it can be seen that the thermal nitric oxide formation is mainly determined by only five chemical species (O, H, OH, N and O_2) (i.e. the effects of oxygen, hydrogen and nitrogen radicals) but not by the fuel being used. Nevertheless, an investigation by Hellier and Ladommatos [20] on biodiesel NOx emission suggested that thermal NOx formation can also be influenced by the fuel properties and characteristics.

2.2.1.1.2 Prompt NOx Formation

Prompt NOx formation also known as the *Fenimore NOx* is dominant under fuel-rich conditions, short residence time and in temperature regions of about 1000K and lower. It occurs during the premixed combustion phase by the “attack” of intermediate hydrocarbon fragments specifically CH and CH_2 excess in fuel rich conditions on the nitrogen N_2. This reaction yields fixed species of nitrogen such as Nitrogen Monohydride NH, Hydrogen Cyanide HCN, Dihydrogen Cyanide H_2CN and Cyano radical *CN, all of which can oxidise into NO. Its reaction mechanism is seen in equation (2.4) [19].

$$N_2 + CH \leftrightarrow HCN + N \quad (2.4)$$

$$O_2 + N \leftrightarrow NO + O$$

$$OH + HCN \leftrightarrow CN + H_2O$$

$$CN + O_2 \leftrightarrow NO + CO$$

2.2.1.1.3 Fuel NOx Formation

Fuel NOx formation is caused by the oxidation of fuel species containing nitrogen. During combustion, nitrogen within the fuel is released as a free radical, which forms N_2 or NO. However, due to the very small amounts of nitrogen present in fuels such as diesel and biodiesel, NOx formation from the fuel is negligible. Nevertheless, it should be noted that fuel NOx can increase significantly when nitrogen containing fuel additives such as dispersants are used in high concentration [19].

2.2.1.2 Environmental and Health Effects of NOx Emission

Figure 2-3 shows the effects of acid rain on vegetation and aquatic wildlife. Regarding its environmental impact, NOx emissions are reported to contribute to acid rain formation by reacting with atmospheric water molecules, destruction of the stratospheric ozone layer thus increasing ultraviolet radiation exposure and the formation of ground-level or tropospheric ozone by reacting with volatile organic compounds (VOC)'s. Acid rain mostly affects aquatic bodies such as lakes and streams and thus endangering aquatic life.

Regarding its wildlife impact, some fish eggs have been reported to die at pH levels of 5 while adult fish die at even lower pH levels. Although frogs may tolerate pH of 4, their prey, mayflies die in such pH environments. Regarding vegetation, acid rain causes the removal of vital soil minerals and nutrients required by the plants to grow. It offsets the pH balance through the leaching of aluminium in the soil into the water bodies. It also strips foliage nutrients which results in brown leaves that prevent sunlight absorption. These issues lead to weakness and death of the plants. There are reports of the loss of species diversity, change in ecological balance, reduced plant growth rate, etc due to ground level ozone[21], [22].

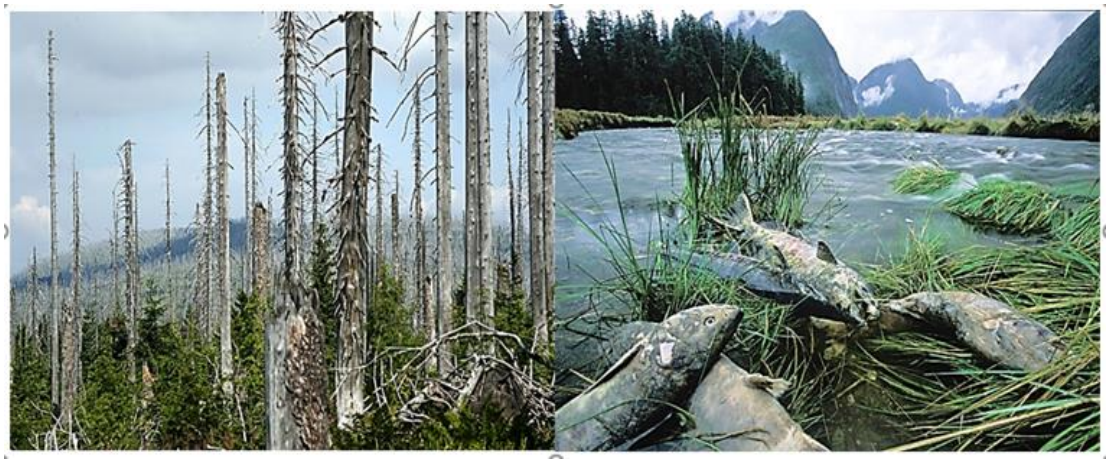

Figure 2-3: Effects of acid rain due to NOx emissions on vegetation and aquatic wildlife

Figure 2-4 shows the effects of NOx emissions on human health. The health effects of acid rain are mostly related to the respiratory and cardiovascular systems. They include lung damage, increased breathing difficulties and increased onset of asthma, COPD as well as heart conditions. More also, there have been reports of DNA mutation, premature death, and damage to the skin from prolonged exposure [23].

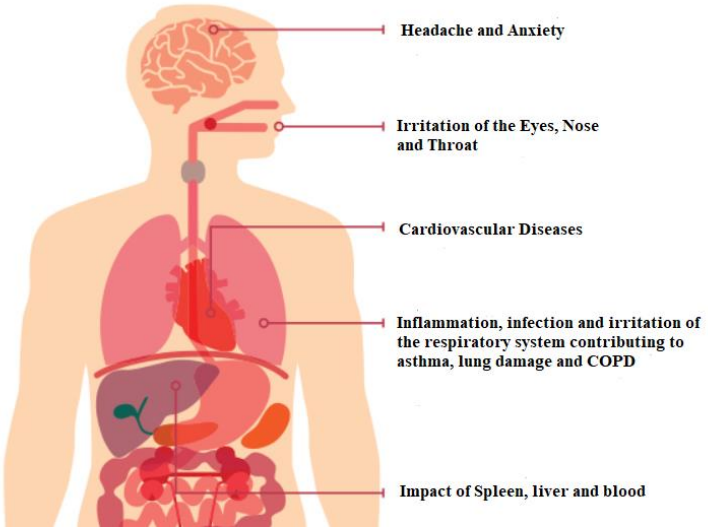

Figure 2-4: Health effects of NOx emissions [23]

2.2.2 Particulate Matter (PM) Emission

Particulate matter (PM) is one of the significant emissions produced by diesel engines wherein approximately 0.2% to 0.5% of the fuel mass injected for combustion is emitted as small particulates of about 0.1μm in diameter. It comprises of carbonaceous particles also known as soot, sulphate particles and soluble organic compounds as illustrated in Figure 2-5. Soot which is an accumulation of

carbonaceous particles is produced in high temperature and fuel rich regions of the combustion flame due to the nucleation of heavy molecules, incomplete combustion, and insufficient oxygen. When formed in the premixed combustion phase, it is depleted due to oxidation in oxygen rich regions from the atomic oxygen attack onto carbonaceous particles in high temperature conditions. Hence, the amount of soot oxidation technically determines the particle emission characteristics and performance of the engine.

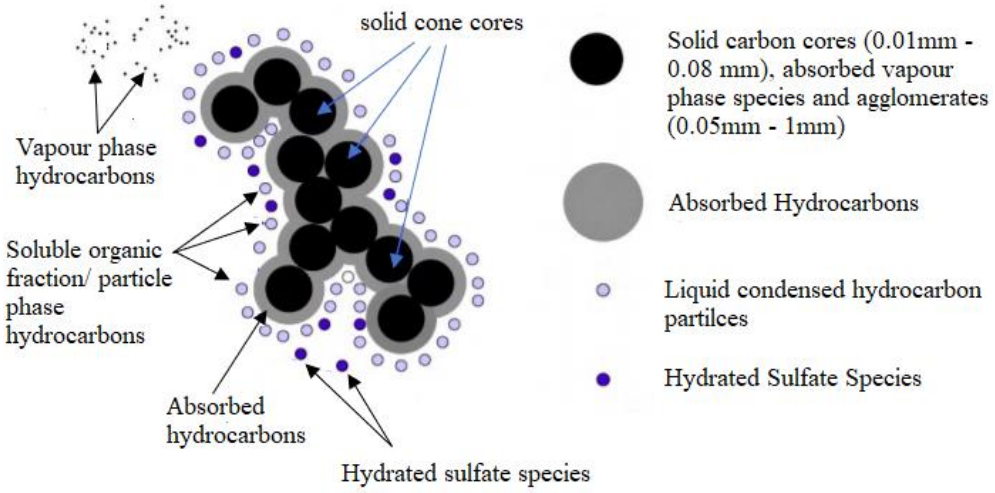

Figure 2-5: Diesel exhaust particles [24]

Soot formation is characterised by a gas to solid conversion reaction wherein particle formation involves physical and chemical processes such as the formation and growth of large aromatic hydrocarbons, conversion of the aromatic hydrocarbons to particles, primary particle coagulation and the accumulation of gaseous components to form soot in the solid phase exhibiting a non-uniform physical and chemical topology as depicted in the soot model proposed by Dec [25] shown in Figure 2-6 [26].

Reports on these reactive conversion processes show that large aromatic rings from the aliphatic species are formed as the fuel molecule is split into predominantly acetylene radicals usually in two dimension (2D) that grow as hydrogen is removed in the reaction. After that, the molecules become three dimensional (3D) primary particles through coagulation experiencing surface growth as illustrated in Figure 2-6 [27]–[30]. Although these reports are based on the investigation of premixed combustion, they also support the suggestion that a similar process occurs in diffusion combustion, with the difference that diffusion flame is predominantly driven by inhomogeneous turbulent mixing [31]. In addition, parameters such as combustion

temperature and pressure, residence time and local air-fuel ratio (i.e., the carbon-oxygen and carbon-hydrogen ratios) are significant to soot formation.

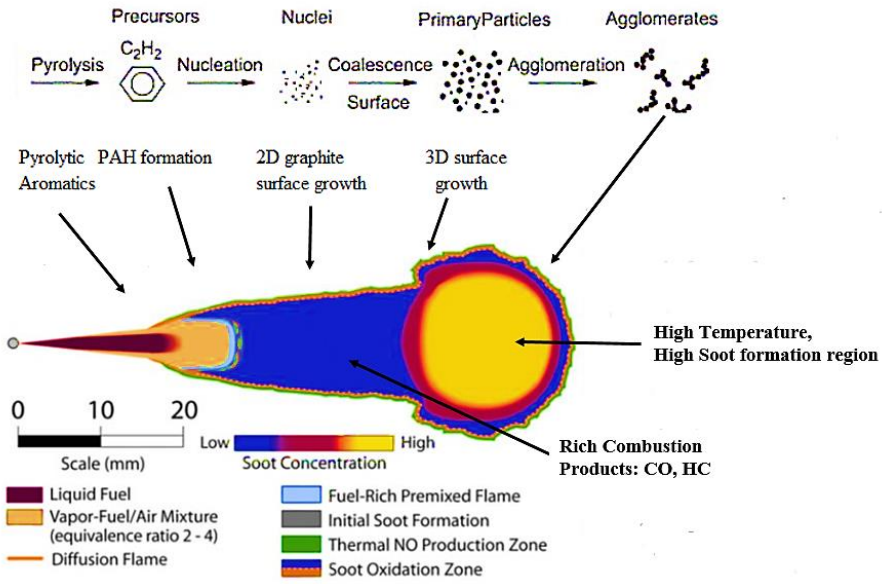

Figure 2-6: Dec's mixed-controlled combustion conceptual model of soot formation along with thermal NOx formation [26]

2.2.2.1 Environmental and Health Effects of PM Emission

Figure 2-7 shows some health effects of PM. PM can be grouped by size into two fine and coarse particles. The fine particles, $PM_{2.5}$ have a diameter less than 2.5μm and the larger coarse particles, PM_{10} have diameters ranging between 2.5 and 10 μm. $PM_{2.5}$ can penetrate deep into the lungs causing serious respiratory problems because they are finer and easily respirable when compared to PM_{10}. The health effects of PM include irritation of the nose, throat and eyes, headache, reduced lung function, respiratory inflammation, irritation and the onset of lung diseases such as asthma, lung cancer and obstructive pulmonary disease. In addition, PM affects the environment through the contribution to smog which hinders visibility and aggravates respiratory disfunction. PM contributes to acid rain by combining with sulphuric acid and ground-level ozone respectively [32], [33].

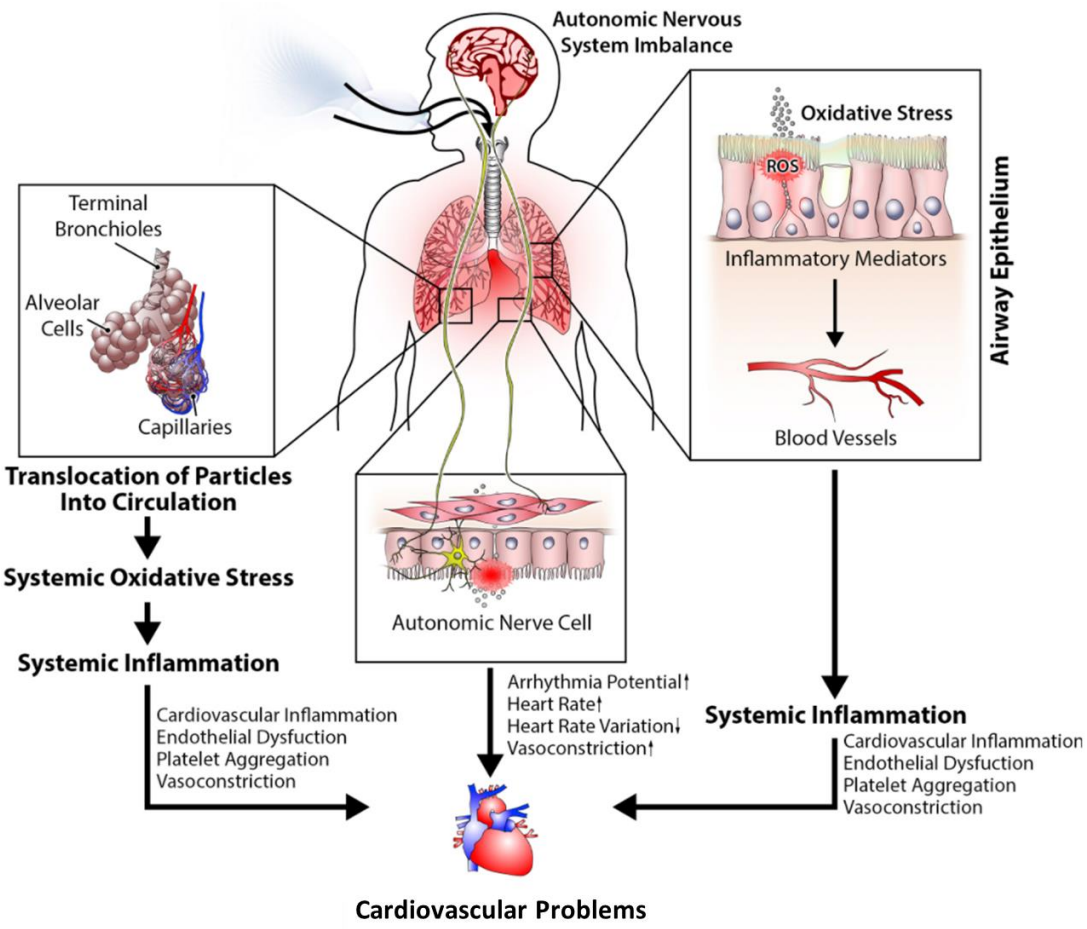

Figure 2-7: Health effects of PM emissions [34]

2.2.3 Unburned Hydrocarbon (uHC) Emission

Unburned hydrocarbon (uHC) emissions produced in diesel engines are mainly associated to very lean mixtures. Here, lean mixtures lead to reduced flammability due to over mixing and/or rich fuel mixtures due to insufficient oxygen. It is generated due to unburned fuel trapped within the piston crevices, in-cylinder flame-quenching caused by flame extinguishing near cold boundaries and wall wetting under cold start conditions [35].

2.2.3.1 Environmental and Health Effects of Unburned Hydrocarbon

Unburned Hydrocarbons are hazardous in the presence of sunlight due to the formation of photochemical smog. They also result in ground level ozone both of which result in health effects such as irritation of the eyes, severe respiratory issues and death under long exposure as well as environmental effects such as reduced productivity in vegetation.

2.3 Methods of Improving Emissions and Performance

2.3.1 Piston Bowl Geometry

Piston bowl geometry is an important factor when considering improvements to engine performance and emissions, due to its influence on air-fuel mixing in the combustion chamber. In addition, it influences combustion characteristics and emissions formation within the combustion chamber and thus, it is considered a primary emission reduction method. It has continued to gain attention especially due to its advantages over aftertreatment technologies besides its positive impact on emissions. Here, improvements to piston bowl geometry often come without the additional weight, cost of materials and storage considered in the application aftertreatment technologies. Therefore, it is an attractive method of emissions reduction in automotive engines. Piston bowl geometry influences combustion characteristics and emissions formation by promoting in-cylinder turbulence required for improved air-fuel mixing through tumble motion. Despite this, piston bowl geometry is classed as an engine hardware which implies that its control towards improved performance and emissions is limited. Many investigations have been performed in the course of its advancement.

Jaichandra and Annamalaib [36] investigated the effects of piston bowl geometry on combustion and emissions characteristics. Their investigation showed that engine performance and emissions were correlated to the geometry of the piston bowl used in the combustion chamber. The results of their investigation also showed that an improved piston bowl geometry led to improvements in in-cylinder air-fuel mixing which in turn, had a direct impact on heat release rate and emissions formation.

The investigations of Soni and Gupta [37], [38] focused on the effects of optimising piston bowl geometry on air-fuel mixing as well as engine performance and emissions through CFD simulations that were supported by engine experiments. Their results showed that the injection of fuel into regions of high air turbulence caused by an improved piston bowl geometry resulted in higher fuel efficiency, as well as lower CO, uHC and soot emissions. The findings from their investigation were also supported by Gaffor and Gupta [39].

The earlier research work by Montajir et al., [40] showed that piston bowl geometries with a round surface at the side and base walls provided a larger surface area for fuel spray droplet parcels closer to the bowl wall to interact with air thus reducing uHC emission that arose form wall wetting. Furthermore, these geometries assisted close-wall vortices which exerted shear stress on the wall impinged particles that caused them to move towards the middle of the piston bowl which was rich in air.

Li et al., [12] investigated the effects of shallow depth, omega and hemispherical re-entrant piston bowl geometries on diesel engine performance and emissions using biodiesel fuel under medium engine load conditions. In their investigation, the omega re-entrant bowl was observed to be more effective at forming strong tumble turbulence which resulted in lower CO emissions compared to the shallow depth and hemispherical re-entrant piston bowl geometries.

Soni and Gupta [41] investigated the effects of hemispherical piston bowl on the in-cylinder performance characteristics of a diesel engine fuelled with diesel-methanol blends through 3D CFD simulation. Their results showed that although the re-entrant bowl achieved better in-cylinder mixture formation and as a result, improved combustion efficiency, it also produced the highest NOx emissions. Here, higher NOx emissions were attributed to the increase in combustion temperatures due to improved mixture formation thus promoting greater premixed combustion.

Venkateswaran et al., [42] investigated the effect of re-entrant bowl on the engine performance of a turbocharged diesel engine operating at full load condition. The authors reported that turbulent kinetic energy generated as a result of the tumble created by the bowl wall produced improved combustion and engine performance for indicated fuel consumption and soot emissions. Kahn et al., [43] investigated the influence of toroidal re-entrant, toroidal and hemispherical piston bowls on the combustion and emissions characteristics of a direct injection diesel engine. The toroidal re-entrant piston bowl was reported to generate a more improved mixture formation and as a result, improved fuel combustion with the highest in-cylinder mean pressure, temperature, heat release and the lowest fuel consumption, compared to the other piston bowls. Although, the toroidal re-entrant piston bowl produced the lowest soot emissions, NOx emission was higher.

Considering the advances made in more recent investigations, Guo et al., [44] performed a CFD optimisation study on piston bowl geometry for a heavy-duty diesel engine with the focus on reducing NOx emission while avoiding engine power and thermal efficiency penalties. Their study explored 100 piston bowl designs which were narrowed down to 32 bowl designs including 3 spray angles. The final piston bowl design selected resulted in a 17% and 41% reduction in NOx and soot emissions respectively with no penalties to engine power and fuel consumption. In addition, their results showed that reducing the oxygen rich regions surrounded by high temperature mixing formations caused NOx emissions to reduce. Furthermore, the results also showed that bowl assisted combustion towards the centre of the combustion chamber caused engine power to increase and soot emissions to decrease.

Pastor et al., [45] investigated the effects of a novel stepped lip-wave piston bowl geometry on the combustion characteristics and soot emission formation in a light-duty diesel engine against the re-entrant and stepped lip piston bowl geometries. The results of the investigation showed that the novel piston bowl geometry had soot emissions that were similar to the stepped lip bowl geometry while the soot emissions for the re-entrant bowl was observed to be higher than both. Their investigated confirmed the viability of yet another piston bowl configuration that aided improved emissions.

Temizer and Cihan [46] studied the effects of a Standard Combustion Chamber (SCC) and Modified Combustion Chamber (MCC) piston geometries on combustion and emissions characteristics of a DI diesel engine. The results of their study showed that the MCC geometry caused a homogenous mixing formation which resulted in an improved combustion as well as lower CO and NOx emissions compared to the SCC. Furthermore, the addition of hydrogen resulted in a 32% and 6% reduction in NOx and CO emissions for the MCC piston geometry compared to the SCC which had an 11% and 3% reduction, respectively. Figure 2-8 presents some piston bowl geometries commonly used in diesel engines.

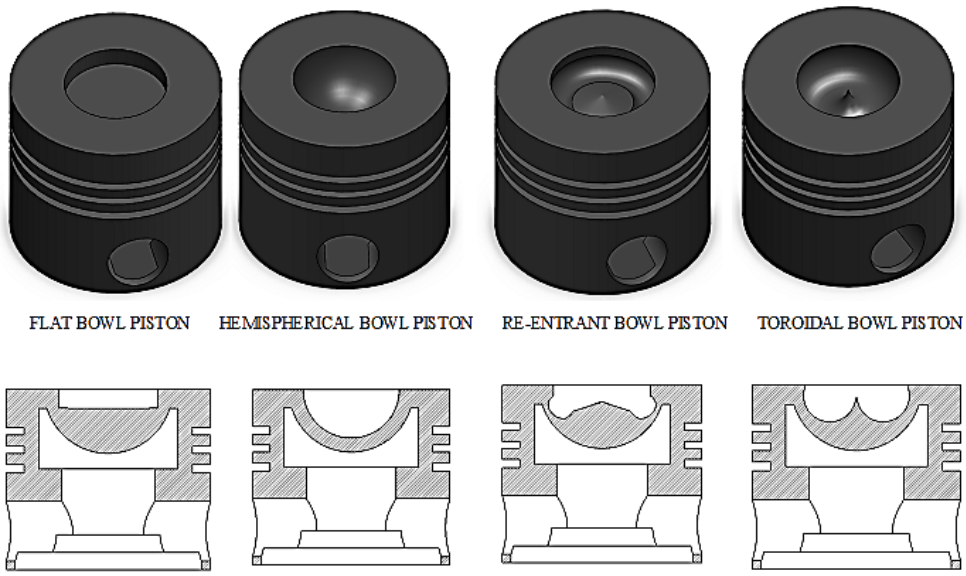

Figure 2-8: Piston crown geometries currently used for improved in-cylinder mixture formation [38], [41], [47], [48]

2.3.2 Fuel Injection

The effects of fuel injection on CI engine performance and emissions have been the subject of several investigations. Combustion characteristics and phasing are highly influenced by the spatial and temporal distribution of the injected fuel with respect to the combustion chamber residence temperature and pressure. The single fuel injection is a simple strategy which involves the delivery of the fuel load in a single event in a working cycle. The control over combustion phasing when using this strategy is generally poor. This is because apart from other parameters such as injection pressure, combustion phasing is greatly influenced by the Start of Injection (SoI) timing and injection rate which occur only once per working cycle and before other critical aspects of combustion such as ignition delay period.

Inadequate control over combustion phasing is a major challenge which results in high engine emissions and combustion noise despite any accompanied improvements in performance [10]. Advancements in modern High-Pressure Common Rail (HPCR) fuel injection systems and Electronic Control Units (ECU) have provided the possibility of a greater control over combustion phasing by using multiple injection strategies. Multiple injection strategies provide greater control over the spatial and temporal distribution of fuel wherein the total fuel load is injected in a series of controlled events rather than a single event. Therefore, a better governance over the

state of air-fuel mixture formation, ignition delay, combustion phasing and the resultant performance and emissions characteristics can be achieved.

Successful implementation of fuel injection strategies especially multiple injections involves an understanding of the effects of injection timings, ratios, pressure, the influence of in-line back pressure as well as the fuel type used. Most of these parameters are controllable which provides an avenue for optimisation even during engine runtime. However, using a multiple injection strategy introduces complexity and requires optimisation under different engine operating conditions. This is because besides the interaction between these injection parameters, there is also the interaction with in-cylinder engine hardware such as number of fuel injector nozzles, spray angle and piston bowl geometry which cannot be adjusted during engine runtime.

Amongst the aforementioned injection parameters, the effects of spray angle, injection timing and multiple injection strategy are presented in the following sections.

2.3.2.1 Fuel Injector Spray Angle

Khan et al., [43] investigated the effects of fuel injection spray angle on fuel efficiency. Their investigation showed that fuel efficiency increased compared to baseline results due to improved air-fuel mixing. They observed that in-cylinder air-fuel mixing improved when the spray angle was adjusted to target regions of highly turbulent resident air. They also observed improvements to IMEP and soot results when both injector spray angle and piston bowl geometry were adjusted. In addition, they found that spray angle also contributed to spray-wall impingement under high fuel injection pressure which caused high uHC emission and ISFC.

Soni and Gupta [47] numerically investigated the effects of spray angle and piston bowl geometry on a diesel engine fuelled with diesel and diesel-methanol blends at medium and full loads. Their investigation showed that the combined enhancement of spray angle and piston bowl geometry caused a reduction in ISFC, as well as CO and soot emissions and an increase in NOx emissions. They attributed this observation to larger portions of the fuel droplets and vapor being trapped in highly turbulent air which resulted in high heat release and combustion temperatures. Interestingly, the findings of Soni and Gupta [47] also supported an earlier investigation carried out by

Lim and Min [49] wherein lower soot emissions and reduced wall wetting were observed when the piston bowl and spray angle were adjusted.

Gainey et al., [50] studied the effects of three spray angles (i.e. 150°, 118°, and 60°) and two piston bowl geometries (i.e. re-entrant and shallow piston bowls) on the performance and emissions of a diesel engine. Their findings on the sole effects of spray angle revealed that the 150° spray angle provided the best control over combustion and elongated the combustion duration over 1.8 times, the 118° spray angle provided a negligible control over combustion and the 60° spray angle provided no control over combustion. Their findings also revealed that the 150° spray angle and shallow bowl combination maintained a high control over combustion duration, while the 118° and 60° spray angle and shallow bowl combinations had no control over combustion.

This behaviour was attributed to the low surface-to-volume ratio of the shallow bowl compared to the re-entrant bowl which resulted in less natural thermal stratification. Therefore, it was suggested that re-entrant bowl with a wide spray angle could improve effective combustion control.

2.3.2.2 Fuel Injection Timing

Fuel delivery into the combustion chamber either as a single or multiple event is governed by fuel injection timing usually measured in microseconds (μs) or Crank Angle Degrees (CAD). Fuel injection commences at the Start of Injection (SoI) and continues over a time interval known as the injection duration at the end of which fuel injection is terminated. The dwell angle is an additional injection timing parameter which is considered in the case of multiple injections per working cycle. It has been defined differently by a few researchers. It is defined in Ahn Tuan Hoang [51], as the period between the end of the previous injection and the start of the next injection while in Herfatmanesh et al., [52] it was defined as the time period between the start of the previous injection and the start of the next injection. Fuel injection timing and duration significantly affect air-fuel mixture formation, ignition delay, combustion phasing and emissions characteristics with respect to in-cylinder temperature and pressure.

Considering controllability, fuel injection timing can be either retarded or advanced with respect to its initial time and cylinder TDC. The advancement of fuel injection timing sees the fuel injected earlier and farther away from the TDC in comparison to the initial injection timing. It has been closely linked to longer ignition delay, improved air-fuel mixing and spray wall impingement. Lower pressure and temperature are the in-cylinder conditions at the time of early injections. Such in-cylinder conditions promote longer ignition delay due to lower fuel evaporation rate. Although longer ignition delay facilitates improved air-fuel mixing, it can lead to spray wall impingement due to lower fuel evaporation rate. Consequently, advanced timings can cause high heat release rates, greater premixed combustion, high combustion temperatures, high NOx and uHC emissions but lower soot emissions.

The retardation of fuel injection timing sees the fuel injected later and closer to the TDC in comparison to the initial injection timing. It has been closely linked to shorter ignition delay and improved fuel evaporation due to higher in-cylinder temperature closer to TDC. Nevertheless, the available oxidation time for carbon and CO is also short causing a rise in soot emissions. Moreover, shorter ignition delay often leads to lower NOx emissions due to less pronounced premixed combustion phase. Therefore, careful optimisation of injection timing can be used to achieve a desired balance in the NOx-Soot trade off, as well as enhanced ISFC and reduced combustion noise.

2.3.2.3 Fuel Injection Strategy – Multiple Injection

Multiple injection strategy offers the flexibility to control combustion and emissions characteristics. Parameters/terminologies such as dwell angle, injection ratio, pilot and pre injection, main injection as well as post injection are used to define and implement multiple injection strategies. Despite the inconsistency observed in the use of these terminologies, the main injection refers to the event in which the bulk of the total fuel quantity is injected. The pilot and pre injection refer to the events that occur before the main injection in which about 5% to 10% of the total quantity is injected. The late and post injections refer to the events that occur after the main injection in which about 10% to 20% of the total quantity is injected. An illustration of these injection events is presented in Figure 2-9 [53].

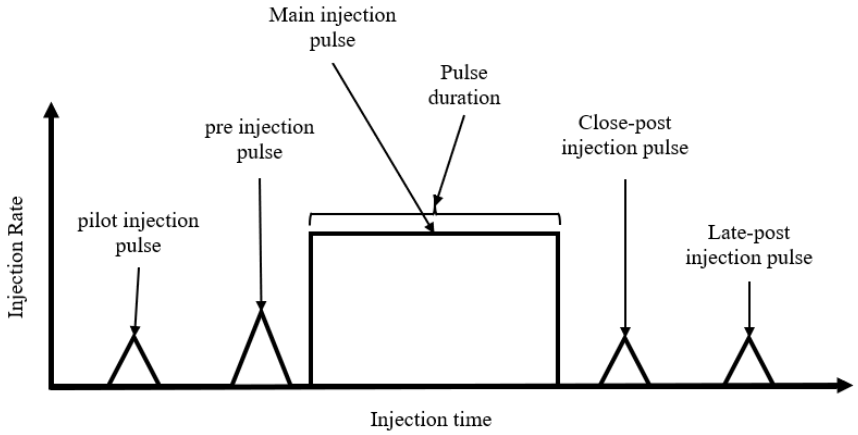

Figure 2-9: A multiple fuel injection strategy event of diesel engine cycle [53]

Despite the improvements in performance and emissions achieved through the use of multiple injection strategy, optimisation of the fuel injection system and fuel injection strategy requires further research and development.

Herfatmanesh et al., [52] investigated the effects of fuel line pressure wave and dwell angle in split injection strategies on diesel engine performance and emissions. Their investigation revealed that fuel line pressure fluctuations affected the actual injected fuel quantity of the second injection in the case of two consecutive injections. This in turn, influenced air-fuel mixture formation, combustion phasing, performance, and emissions. They suggested that these fluctuations could reduce the control over combustion phasing which was initiated by the multiple injection. Moreover, their findings also revealed that dwell angle also influenced combustion phasing and could be used besides injection duration, to dampen the effects of fuel line pressure fluctuations.

Herfatmanesh et al., [54] investigated the effects of split injection ratios in an optical single cylinder diesel engine. Their findings showed that even when the total fuel quantity was split in either even or uneven twin ratios such as 50:50, 70:30 and 30:70 for both high and low loads, subsequent injection pulses and their injection timings were still significantly influenced by the dwell angle due to the presence of fuel line pressure fluctuations. They observed that very short dwell angles such as 5 °CA resulted in a single injection with a considerably larger fuel quantity injected due to a crossover of injection timing between the two injection events.

D’ Stefano et al., [55] investigated the effects of multiple injection strategies with EGR rates on the performance and emissions of a low C.R. Euro 5 diesel engine. In their investigation a pilot-Main (pM) injection strategy was analysed and compared to a rate-shaped mains injection strategy implemented in the form of double pilot and boot injections. They found that the rate-shaped main injection offered a negligible influence on reducing NOx and soot emissions. Moreover, the pilot and boot injections both resulted in reduced combustion noise. Apart from this, they observed from a DoE optimisation of the pM injection strategy that splitting the injection aided in entrapping air inside the fuel clouds thereby forming locally leaner mixture formation and allowing increased EGR rates which caused lower Soot and NOx emissions.

Asadi et al., [56] numerically investigated the effects of ethanol-diesel and biodiesel-diesel blended fuels using multiple injection strategies on a diesel engine. Both ethanol and biodiesel were blended with diesel at 10% and 20% each while the multiple injection strategy involved a 20% and 30% pilot injection quantity of the total fuel load in each fuel blend case for two injection timings. Their findings on the effects of multiple injection timings showed that while both the pilot injection quantity and injection timings significantly influenced combustion phasing, the effects of the former were found to be more crucial. Their findings also suggested that the fuel type used in operating the engine influenced the injection timing and strategies adopted.

Aziz et al., [57] investigated the influence of multiple injection strategies on the gross indicated efficiency, as well as CO and uHC emissions of a diesel engine fuelled with methanol under Partially Premixed Compression Ignition (PPCI) mode. Their investigation revealed that the gross indicated efficiency could be increased while simultaneously reducing uHC and CO emissions with multiple injection strategies compared to single injection strategy.

Panda and Ramesh [58] investigated the effects of methanol to diesel energy share and injection timing on the combustion stability, efficiency and emissions of a single cylinder CI engine using single pilot and double pilot multiple injection strategies. Their results showed that in the case of single pilot multiple injection strategy, an increase in the methanol to diesel energy share of about 43% caused NOx and smoke

emissions to reduce. This was attributed to high latent heat of vaporisation of methanol. The increase in methanol to diesel energy share also led to improved premixed combustion and thermal efficiency. Their results showed that in the case of double pilot multiple injection strategy, combustion stability was improved with the methanol to diesel energy share increase up to 50% while NOx and smoke emissions reduced by 49% and 91%, respectively. A reduction in NOx emission by an additional 14.5% was obtained when methanol to diesel energy share increased to 53%. Their results suggested that double pilot multiple injection strategy has the potential to provide improved performance, emissions and combustion stability compared to single pilot multiple injection strategy.

The study on the combined effects of EGR and split injection to further reduce NOx by Montgomery and Reitz [59] showed that NOx emission could be further reduced through the reduction of peak combustion temperatures but with an increase in soot emissions due to inadequate amount of oxygen compared to the application of split injection alone. Park et al., [60] studied the effects of multiple fuel injections to find that pilot fuel injection reduced ignition delay by reducing premixed combustion and peak heat release rate, while post fuel injection contributed to the oxidation of soot emission by 40%.

Shayler et al., [61] investigated the effect of three split fuel injection strategies (i.e., 70:30, 55:45, and 50:50 ratios) with EGR rates of 10% to 25% on a heavy-duty diesel engine. Their results showed that NOx and soot emissions were reduced simultaneously across all three multiple injection strategies. The reduced soot emission was attributed to improved air-fuel mixing which caused higher in-cylinder temperatures during the diffusion combustion. The reduced NOx emission was attributed to lower oxygen content due the use of EGR.

Mobasheri et al., [11] studied the effect of dwell angle in split injection strategies. Their study revealed that the dwell angle of 20 CAD was optimal regarding the operating conditions used and lead to the simultaneous reduction of soot and NOx emissions.

Yang and Zeng [62] investigated the effect of natural gas injection timing and pilot injection quantity in a split injection strategy on the combustion and emissions

characteristics of a dual-fuel engine. Their investigation showed that both the injection timing of natural gas as well as split injection strategy had major influences on the combustion and emission characteristics. They revealed that improvements could be made to the premixed combustion phase of natural gas when its injection timing is retarded. Furthermore, their results showed that the tested split injection strategy diminished diesel pilot combustion, however, this could be improved with advanced diesel pilot injection timing.

The benefits of multiple injection strategies as presented in various investigations have shown its significant influence over combustion characteristics and consequently, performance and emissions. Many of these investigations have focused on the effects of multiple injection strategy as a standalone phenomenon and few have focused on the combined effects of multiple injection strategy and its interaction with piston bowl geometry.

Regarding this frontier, Kershawani and Gupta [63] numerically investigated the effects from split injection and piston bowl geometry on engine performance and emissions. Their investigation involved six piston bowl geometries and three injection ratios which yielded 18 configurations of varying pilot injected fuel quantity up to 15% of the total injected quantity. Furthermore, the investigation was performed at a constant single engine load, compression ratio and speed. They also performed an optimisation study based on their findings to obtain a suitable piston bowl geometry and injection ratio for the tested engine.

Despite the insight their investigation provided on the interaction between split injection strategy and piston bowl geometry, it was observed to be lacking the consideration of injection timing which according to many investigations imposes a significant influence over combustion characteristics and emissions formation. Apart from that, their investigation and optimisation were limited to finding an optimal injection ratio and piston bowl geometry solution for a single engine load.

2.3.3 Multiple Fuel Injection Strategies in Alternative Combustion Modes

Multiple fuel injection strategies such as the double injection has been used either alone or with alternative fuels to achieve some Low Temperature Combustion (LTC) (i.e., alternative) modes in the search for improved CI engine performance and reduced emissions. Figure 2-10 shows the Equivalence Ratio-Temperature (Eq-T) regions of alternative advanced combustion modes compared to Conventional Diesel Combustion (CDC). The Eq-T regions of these combustion modes influence their respective performance and emissions. These modes are discussed in the following sections.

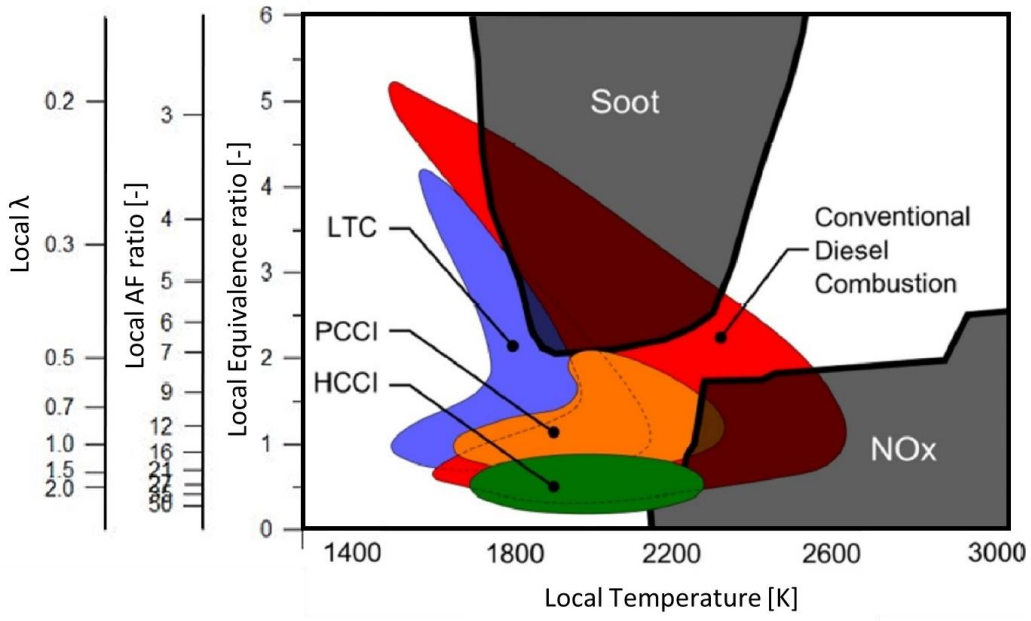

Figure 2-10: The Eq-T chart of conventional and advanced diesel combustion modes [64]

2.3.3.1 Premixed Charge Compression Ignition (PCCI)

The PCCI mode is an evolution from the HCCI mode, broadly aimed at overcoming HCCI's drawbacks while reducing NOx and soot emissions simultaneously. The PCCI mode involves the combustion of premixed air-fuel mixture at temperatures between about 1650K and 2400K, thus, producing lower NOx and soot emissions compared to the CDC mode. Fuel injection strategy with respect to in-cylinder charge temperature and pressure plays a critical role in the initiation of the PCCI mode. Early fuel injection often results in high uHC and CO emissions due to wall wetting whereas late fuel injection can result in high soot emissions due to insufficient time available for air-fuel mixing [65].

Multiple injection strategies provide a good control for the application of PCCI mode. The state of the in-cylinder air-fuel mixture is governed by the injection of fuel in multiple intervals. Therefore, ignition delay, start of combustion and combustion characteristics can be better controlled. In addition, EGR can be used to prolong the ignition delay to enhance air-fuel mixing at lower temperatures for simultaneous reduction of NOx and soot emissions. Nevertheless, some reports have shown that the use of high EGR levels results in high CO and uHC emissions [66], [67].

Shim et al., [8] performed a comparative investigation on the single fuel HCCI, PCCI and dual fuel PCCI combustion modes with a focus on combustion characteristics, thermal and combustion efficiency, as well as emissions. Their investigation was performed on a heavy-duty single cylinder engine under stable operating conditions. Their results on the single fuel and dual fuel PCCI modes showed that both modes simultaneously reduced NOx and PM emissions to levels below Euro 6 regulations without the use of aftertreatment systems. In their investigation, single fuel PCCI mode exhibited poor control over combustion phasing due to incomplete combustion which resulted in much higher CO and uHC emissions, about 38 times that of the CDC mode. Its low efficiency was also attributed to incomplete combustion, therefore, the addition of high EGR rates over 40% and multiple injection strategies was suggested to improve thermal efficiency.
Their report on the dual fuel PCCI mode showed that it offered an easier and better control over combustion phasing and duration which resulted in a 43.5% higher Indicated Thermal Efficiency (ITE) compared to the CDC mode as well as a 14.3% reduction in CO_2 emission. Nevertheless, it showed uHC emissions which although was lower than that of the single fuel PCCI and HCCI modes, it was about 7.8 times higher than that of the CDC mode.

Bhiogade and Suryawanshi [68] recently performed a numerical investigation on the effects of PCCI and EGR on engine performance and emissions. In their investigation, an externally prepared vaporised diesel was used to create a port premixing formation which was introduced into the combustion chamber along with EGR to prolong ignition delay. The results of their investigation showed that this PCCI setup resulted in an increase in CO and uHC emissions as well as a 43.57% reduction in NOx

emissions. In addition, this PCCI setup resulted in a 1.9% lower Brake Thermal Efficiency (BTE) compared to the CDC mode.

2.3.3.2 Reactivity Charge Compression Ignition (RCCI)

The RCCI mode offers better control over ignition delay, start of combustion and combustion phasing while maintaining reduced NOx and soot emissions. It involves multiple fuel injection strategies generally using multiple fuels of different reactivities. These fuels are injected into the combustion chamber at specific intervals to control the in-cylinder reactivity of air-fuel mixture, thus combustion phasing. In this configuration, lower reactivity fuel is injected into the cylinder early in the compression stroke to mix with the in-cylinder charge to form a homogenous mixture after which the fuel with higher reactivity is injected later in the compression stroke or early in the power stroke to initiate and control the combustion [65].

This method of fuel injection results in the formation of not just different air-fuel ratios but also different reactivities. The change of reactivity controls the start of combustion at different times and rates as combustion proceeds from regions with higher reactivities towards regions of lower reactivities. Moreover, the higher the difference in fuel reactivity the better the in-cylinder performance even at higher loads due to better control over combustion phasing and heat release rate. This results in some advantages such as longer premixed combustion phase, lower pressure rise rate, lower emissions even at higher loads and higher thermal efficiency. Nevertheless, different fuel blends are required to achieve an adequate RCCI mode especially at different operating conditions and engine loads [65].

Poorghasemi et al., [69] carried out a numerical investigation on the effects of fuel injection spray angle and pressure, premixed ratio and injection pulse on the performance and emissions of a light duty RCCI engine fuelled with diesel and natural gas. The report showed that these parameters had a significant effect on RCCI combustion characteristics. A 5% increase in indicated thermal efficiency was observed when the timing of the first fuel injection was retarded by 4 CAD and its pressure was reduced from 400bar to 350bar. However, indicated thermal efficiency was reduced by 4% when spray angle was reduced from 144 to 100 degrees and injection timing was advanced by 6 CAD. In addition, uHC and CO emissions were

reduced besides NOx emission by increasing natural gas fraction, increasing the fuel fraction in the first injection and advancing the start of injection.

Ansari et al., [70] carried out an experimental investigation on the effect of fuel reactivity using High Reactive Diesel (HRD) and Ultra Low Sulphur Diesel (ULSD) having cetane numbers of 85 and 49, respectively, with methane fuel as the fuel of low reactivity in RCCI and conventional diesel combustion modes. A 1.9L inline 4-cylinder turbocharged CI engine that was modified for dual-fuel operation at an engine speed and IMEP of 1500 rpm and 8bar, respectively, was used for the investigation. The cetane number was reported to be the most significant factor to influence uHC and CO emissions. It was also reported that extended combustion duration, reduced in-cylinder peak pressure and thus noise as well as reduced Maximum Rate of Pressure Rise (MPRR) were attributed to the larger difference in the reactivity between the two fuels used.

Singh et al., [71] performed a comparative study of the engine performance and emissions characteristics of the PCCI and RCCI modes against the CDC mode using a single cylinder engine at four engine loads and an engine speed of 1500 rpm. The RCCI mode was operated using a diesel-methanol pair for high and low reactivity, respectively, while the CDC and PCCI modes were operated using diesel. Their results revealed that the RCCI offered a better and more stable control over combustion phasing compared to the CDC and PCCI modes. This resulted in the RCCI having similar thermal efficiency to the CDC mode at baseline load and even higher efficiency at higher loads compared to the CDC and PCCI modes. In addition, the RCCI exhibited lower exhaust gas temperature, lower combustion noise and engine knock compared to the CDC and PCCI modes. Regarding emissions, the RCCI produced lower NOx but significantly higher uHC emission compared to the CDC and PCCI modes.

Ghaffarzadeh et al., [72] investigated the effects of direct injection biodiesel-CNG and diesel-CNG dual fuel combustion modes in a modified single cylinder RCCI engine. Their findings showed that the SOI timing of the liquid fuel was crucial for the performance and emissions. Thermal efficiency and NOx emissions increased while uHC and CO emissions reduced when the SoI timing of the liquid fuel was advanced.

Hasankola et al., [73] numerically investigated the effects of Inlet Valve Closing (IVC) temperature, 293K to 353K, and EGR rate, a 0% to 25%, on the performance and emissions of a dual fuel natural gas-diesel RCCI engine. In this investigation, natural gas was port injected as the low reactivity fuel and diesel was directly injected into the combustion chamber as the high reactivity fuel. The results showed that the maximum heat release rate, in-cylinder pressure, NOx and soot emissions reduced as the EGR rate increased. In contrast, maximum heat release rate, in-cylinder pressure, NOx and soot emissions increased as the IVC temperature increased. Their results suggest that IVC temperature and EGR rate can significantly alter the combustion phasing of an RCCI engine.

Mabadi et al., [74] investigated the enhancement of hydrogen energy share in an RCCI engine. In their investigation, diesel and syngas enriched natural gas were the fuels used to achieve high and low reactivity while EGR was introduced to stabilise and achieve LTC. The syngas consisted of an 80:20 ratio of hydrogen and CO. The results of their investigation revealed that a 40.43% increase in hydrogen energy share was obtained with an engine power trade off of about 1%. Further improvements to engine power over 4% resulted in a hydrogen energy share of about 27.05%. These two hydrogen energy shares also led to the reduction of hydrocarbon fuel consumption by 46.6% and 33.86% respectively. Finally, the gross indicated efficiency was reported to be over 50%.

Bae and Kim [75] reported that the DME fuel spray injection structure was key to its improved fuel atomisation, evaporation and thus, improved combustion. The authors assessed DME spray structure under three ambient pressure conditions; below saturated vapor pressure condition (atmospheric condition) wherein it exhibited the flash boiling phenomenon, ambient pressure condition wherein it exhibited a similar shape to diesel spray but with a wider spread and the critical pressure condition wherein the ambient pressure was beyond the critical pressure.

Kim [76] reported that while DME can be easily changed to liquid phase at about 298K which is advantageous for storage; it evaporates as temperatures approach that of steady engine operating temperatures around 353K to 373K. This causes problem in piezo fuel injectors as hydraulic couplers tend to malfunction when filled with DME in gaseous form. Nevertheless, Xu et al., [77] reported improvements in DME

injection in back pressure insensitivity and piezo injection when using a novel common rail type fuel injection system. Sasaki et al., [78] suggested the need for nozzle hole optimisation when using DME due to cavitation inside the nozzle, thus restricting nozzle flow rate as a result of its low vapour pressure and boiling.

2.4 Algorithms and Methods used in solving Optimisation Problems

The optimisation of engine performance and emissions has become widely recognised as part of engine design and modification processes. Here, optimisation methods and algorithms are applied to a set of engine parameters which lead to an improvement in engine performance and emissions. Optimisation can be performed either by parametric study, using optimisation algorithms or a combination.

Regarding the optimisation algorithms, they work by applying a set of systematic rules with the aim of converging either at the solution of a problem function or at an approximated solution of the problem function. The process involves an objective function which represents the set of parameters to be optimised, a set of design variables that are simultaneously analysed by the optimisation algorithm, and a set of constraints imposed on the objective function. Design variables can be continuous, discrete, or binary wherein the problem function can have a combination of these variables while the objectives can be conflicting. Algorithms used in solving optimisation problem functions are generally grouped into non-evolutionary algorithms and evolutionary algorithms.

2.4.1 Optimisation by Parametric Study

Optimisation by parametric study is widely used in arriving at optimal solutions and may be considered as the initial stage of optimisation. It is a manual approach to optimisation that is based on human knowledge of the input parameters (i.e., design or input variables), the search space and their effects on the selected output parameters. Here, human knowledge and experience guides the adjustment of the design variables within their search space towards a set of optimal values that yield either a single or multiple optimal solutions with respect to a set objective or objectives through successive simulations.

Nao Hu [92], applied optimisation by parametric study in obtaining an optimal dynamic response for a HPCR injector to improve injection characteristics for a

marine diesel engine. Here, three variables namely control piston diameter, inlet passage diameter and outlet passage diameter were studied while the injector opening delay, closing delay and fuel injection mass were the output parameters observed. Furthermore, optimisation by parametric study was also applied by Nao et al., [93] in obtaining optimal reductions in NOx and soot emissions and specific fuel oil consumption for a marine diesel engine. Here, the design variables were injection timing, swirl ratio, spray angle, nozzle protrusion length, bowl diameter, centre crown height and toroidal radius.

Both reports showed that this method has the advantage of being guided by human knowledge and experience of the problem being optimised wherein subsequent simulations are based on the analysis of previous results. Thus, optimal solutions can be obtained quickly. However, the reports also showed that this method is only effective when considering a small set of design variables, search space and number of objectives (i.e., ≤ 3). Using this method, the optimisation efficiency is reduced with the following:

- a higher number of design variables and search space (i.e., ≥ 3)
- a higher number of objectives considered (i.e., ≥ 3) and
- a higher number of conflicting objectives.

2.4.2 Optimisation by Non-Evolutionary Methods

Optimisation by non-evolutionary and evolutionary methods involve the use of computational algorithms that offer a systematic approach to obtaining an optimal solution instead of applying human governance. For these methods, the human element of the optimisation process is completely replaced by an algorithm. Therefore, these methods do not have the drawbacks/limitations of the parametric study. Furthermore, it means that they can be applied to a problem with a larger set of design variables, search space and multi-conflicting objectives. These methods can be categorised into design of experiments (i.e., optimisation by sampling algorithms) and gradient-based algorithms.

2.4.2.1 Design of Experiments (DoE's)

DoE is an organised way of constructing the connection between input and output parameters in order to analyse the factors that contribute to minimisation,

maximisation, and trade-offs in a problem. Thus, it can effectively be used in studying the impact of individual variables on the overall behaviour of a system's response by obtaining the highest quantity of information on them while reducing the number of simulations. Generally, a set of design points for which the simulations should be assessed is outlined wherein the design variables are referred to as "factors" and the specific value assigned to a factor is referred to as a "level".

The factors have lower and upper bounds which describes a hypercube while its numerical stability can be increased by scaling them to a range between +1 and -1. Then statistical tools such as regression analysis and Analysis of Variance (ANOVA) are applied to identify the sensitivity of the variable to the response. DoE's can be used either to screen design variables to ascertain the dependency of a response parameter on a design variable or to find a good starting point for a design optimisation algorithm. Some DoE sampling algorithms include the Full Factorial Design, Orthogonal Arrays, Sobol Sequence [94] and Latin Hypercube [95].

2.4.2.1.1 Latin Hypercube (LH)

In this DoE sampling method, the design space for each factor is divided into n levels equally wherein a single design point is placed on each level of every factor. Hence, $n!$ permutations of n levels are possible for the individual factors. Apart from that, the design matrix for the LH consists of a single column determined by an arbitrarily chosen permutation of n levels for each factor. Moreover, correlations between the columns may exist as the matrix is generated arbitrarily. For a row in the design matrix n^k combinations are possible and have an equivalent chance of occurrence.

The LH has a good space filling property as more combinations for each factor can be studied, thus, several levels and consequently several combinations may be studied for each factor wherein the number of design points used may be chosen at will. In addition, an independency is kept amongst the variables wherein the input variables are randomly selected within the distribution from each interval only once, thus avoiding unwanted correlation in the design points which is a drawback of the Sobol sequence. Nevertheless, the probability of missing some design regions tends to increase as the number of design points decrease while the n dimensional unit of the hypercube slows down the algorithm [96].

2.4.2.2 Gradient Based Algorithms

Gradient based (non-evolutionary) algorithms use derivatives to locate the optimum solution of the problem function. Three main steps; the search direction, step size and convergence need to be performed before the design variables are updated. The various types of this algorithm differ mainly by the way in which they solve for the search direction. They are fast and widely used for single and multi-dimensional problems. Nevertheless, they are only good with gradient, continuous and smooth problem functions and are susceptible to finding the local minimum rather than the global minimum of the problem function. Details of some of these methods such as the Newton's method, Steepest Descent method, Quasi-Newton method and Non-Linear Programming by Quadratic Lagrangian (NLPQL) are presented in the literature [97], [98].

2.4.3 Optimisation by Evolutionary Methods

Gradient free (evolutionary) algorithms do not use derivatives but rather natural heuristic search methods and as such can be used for problem functions that are discrete, discontinuous, noisy, or non-differentiable. Although they are useful for problems that are difficult for gradient-based algorithms, they are slower in comparison. Most gradient free algorithms are global minimum finders and although they can find many good solutions and local minima, many of them are stochastic and thus, may not guarantee the global optimum solution. Some gradient free algorithms include the Nelder-Mead (N-M) [99], Particle Swarm Algorithm (PSA) and Genetic Algorithm (GA) family.

2.4.3.1.1 Genetic Algorithm (GA)

GAs are algorithms that simulate nature's evolutionary process of "survival of the fittest" based on Darwin's theory. Holland [100] first proposed the concept of GA and together with Goldberg [101] became the frontrunners who suggested its application in engineering optimisation problems. GA is a search method that uses the fitness attributes of earlier designs to produce new designs with a movement of the designs' evolution towards yielding better solutions as its primary goal.

The search procedure for GA is initialised with several randomly generated designs. The number of designs evaluated in each generation is called the population size and each design is called a gene. The genes generated are encoded in mathematical expressions such as real numbers or binary strings and are evaluated to provide a set of solutions called a set of individuals. Moreover, the objective function is called the fitness function. Furthermore, the set of individuals is improved by producing their offspring's and applying the principle of survival of the fittest wherein their fitness is tested to yield a new set of individuals (solutions) with corresponding new genes characterised by a higher chance of survival and reproduction with respect to the fitness function.

Newly generated genes undergo genetic modifications using mutation, selection, and crossover to determine their level of fitness based on the objective function as well as to produce the next set of individuals and genes. A crossover modification among the evaluated designs gives high possibility of the designs with better fitness merit to survive to the next generation and drives the population towards the local minimum or maximum using crossover points. A mutation modification involves introducing random changes to parts of a gene (i.e., its design variables or chromosomes) which provides increased diversity and randomness of the genes and thus their solutions by avoiding trapping at the local minima and maxima [102], [103].

Hence, the parameters that influence crossover and mutation are vital to the performance of GAs in terms of avoiding local trapping and achieving optimality, thus, arriving at an improved set of results at termination [14][15].

The various GAs within the GA family of algorithms such as the (micro) μ-GA, Non-dominated Sorting Genetic Algorithm (NSGA), Adaptive Range Multi-Objective Genetic Algorithm (ARMOGA), etc are formed based on different methods of gene coding, crossover, and mutation function creation. Apart from that, GAs are widely applied to multi-objective optimisation problems as Multi-Objective Genetic Algorithms (MOGA's) [96], [104],[105], [106], [107].

2.4.4 Pareto Optimality and Objective Merit Function

Multi-objective optimisation problems consist of sub-objectives which have different magnitudes of conflicting interests. Hence, they yield a set of optimal solutions rather

than a single solution. The concept of "optimum" for multi-objective optimisation problems is called the Pareto optimum. Pareto optimality indicates a state achieved wherein a set of solutions obtained cannot be outperformed by other solutions within the multi-objective function space. Using Figure 2-11 as an illustration of pareto optimality, the set of solutions [a, b, c, d, e, f] make up the pareto optimal set of solutions because they are not outperformed by the other solutions [g, h, i, j, k, l, m, n, o] with respect to minimising objective 1 and 2. Apart from that, dominance is a terminology generally associated with Pareto optimality.

In Figure 2-11, solutions a - f are dominant while solutions g - o are dominated. Here, a solution is said to be dominated when at least one of its objectives is worse compared to other solutions within the multi-objective space. Thus, Pareto optimal solutions can be considered as dominant solutions. In addition, dominant solutions are grouped to form the Pareto front.

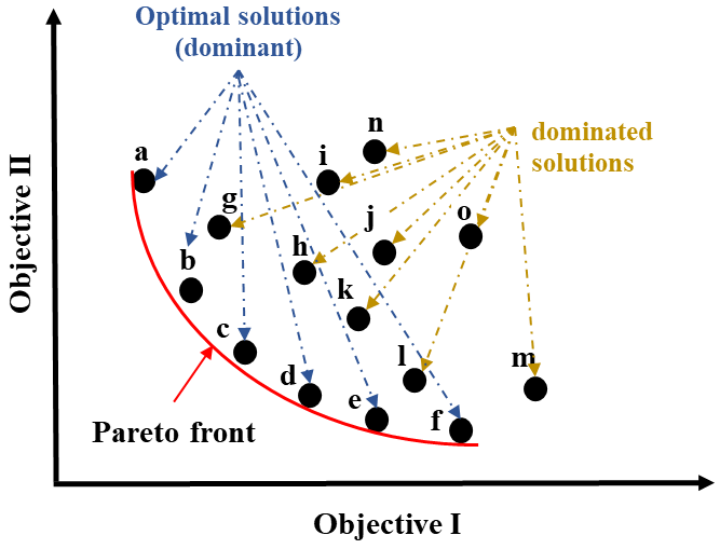

Figure 2-11: Illustration of Pareto optimum for two objectives

A merit function can be used to implement the magnitudes of the respective sub-objectives within a multi-objective function. Equation 2.5 shows the weighted sum method which is generally used in assigned merit to each sub-objective thereby transforming the multi-objective function into a single objective function.

$$Objective = \sum_{i=1}^{k} \mu_i O_i \qquad (2.5)$$

Where μ_i and O_i are the weighting factor of each sub-objective function and sub-objective, respectively.

2.4.5 Regression Analysis and Modelling

Regression analysis involves the use of statistical modelling to estimate the relationship between a set of independent (input) variables and dependent (response) variables by means of a mathematical model or function that best fits the relationship. Regression analysis and modelling can be performed in various forms which include simple and multiple linear regression, logistic regression, polynomial regression, ridge regression, support vector regression etc [108]. In addition, various regression algorithms can be used to implement any of the regression forms on a dataset. Since engine optimisation studies usually involve the generation of relatively large datasets, the relationship between the engine design parameter space and response space can be modelled through regression analysis.

Furthermore, regression modelling of such engine datasets can also be used for the prediction of engine response solutions based on a given set of design inputs parameters using the estimate mathematical model.
Currently, the development of regression algorithms and improvements in computational power has paved the way for increased application of regression analysis with regards to engine optimisation studies in the form of regression-based optimisation.

Regression-based optimisation involves the use of the regression mathematical model which estimates the relationship between the set of design input parameters and response parameters to provide an individual or a set of optimal solutions with respect to the optimisation objective function. Here, the provided optimal solutions especially for the response parameters are predicted optimums (i.e., estimations of the true optimal solutions).
The workflow of a regression-based engine optimisation begins with the regression analysis and modelling of the engine data using a regression algorithm with the aim of obtaining a mathematical model that best describes the relationship between the design input and response spaces. The mathematical model coupled with an optimisation algorithm that searches for optimal solutions is then used to perform the optimisation process for a set optimisation objective function. Regression-based optimisations are fast since the optimisation process utilises statistical functions (i.e., Response Surface Methodology (RSM) [109]). Therefore, they are useful in tackling

complex multi-objective optimisation problems that involve costly computational simulations such as 3D CFD wherein the accuracy of the predictions from the optimisation process depends on the accuracy of the regression mathematical model.

Since regression modelling as well as RSM only generates a predicted response, a prediction error or residual (i.e., the difference between the predicted response and the true response) always exists. Thus, validating the predicted response by performing the actual simulation with the real solver is good practice [110]. Besides the residual, the performance of a regression model can be assessed using metrics which include coefficient of determination (R^2) [111], correlation coefficient (R), Mean Square Error (MSE), Mean Absolute Error (MAE), Mean Absolute Percentage Error (MAPE) and Maximum Absolute Error (MaxAE) [17], etc.

Furthermore, the robustness and accuracy of the regression mathematical model can also be influenced by the regression algorithm used in the modelling process. In regard to this, various regressions which include interpolating methods such as Shepard method, K-Nearest method [112], Radial Basis Function method [113] and the Kriging method [114] as well as approximating methods such as Polynomial SVD method [115], Stepwise Regression method [116], Gaussian Processes method [117] and Neural Networks [118]–[121] have been used for regression modelling of linear and non-linear relationships. More also, methods such as the Support Vector Regression (SVR) through the use the Support Vector Machine (SVM) method have been noted to excel at highly complex non-linear relationships apart from the Kriging, Gaussian, and Neural Network methods.

2.5 Review on IC Engine Optimisation

There have been various studies on the use of optimisation algorithms in improving diesel engine performance and emissions. Some studies reported improvements when using the DoE-3D CFD approach which involves the application of a DoE sampling algorithm to provide exploration points within the design space and the simulation of these points using the 3D CFD solver. Taghavifar et al., [122] reported reduced NOx emission for a 1.8L diesel engine when the Sobol sequence DoE sampling method was applied to obtain the optimal injection strategy and combustion chamber

geometry. Here, the optimal case was found after 22 3D CFD engine simulations and comprised of a lower injection angle and a smaller bowl volume.

The effectiveness of this approach is limited due to the circumstance that DoE algorithms are not setup to find optimal solutions (i.e., exploitation) but are rather setup to sample the design space (i.e., exploration). Therefore, the identification of optimal solutions is not deliberate as with the Optimser-3D CFD approach which is more commonly applied and has been reported to also provide improvements to engine performance and emissions. With the Optimiser-3D CFD approach, the optimiser algorithm drives to obtain optimal solutions based on learning which is done by assessing the CFD simulation results of selected suggested designs. Therefore, the design space is exploited for optimal solutions in a deliberate manner. This approach can also involve using DoE's to sample the space prior to using the optimiser.

Taghavifar [123] studied the use of multi-objective Nelder-Mead algorithm with the Latin Hypercube sampling method to obtain optimal piston and injector parameters for improved combustion noise, indicated torque and swirl ratio for a 1.8L diesel engine. In this case the optimal case was found at 27 runs with simultaneous reduction in emissions and improvements in performance. Chen et al.,[124] investigated the use of multi-objective NLPQL algorithm with orthogonal sampling method in the optimisation of a combustion chamber and injection parameters for an 8.9L Cummins diesel engine. Here, simultaneous reduction in NOx and soot as well as reasonable performance characteristics were obtained.

Navid et al., [13] applied multi-objective Nelder-Mead algorithm with Sobol sequence and Latin Hypercube DoE sampling methods to obtain optimal bowl and injector parameters for improved indicated torque, combustion noise and swirl ratio in a 1.8L diesel engine. It was found that although similar results with deviation of less than 1% were observed when using both sampling methods, they both achieved their respective results in 7 runs and 27 runs, respectively.

Navid et al., [14] studied and compared the difference between Multi Objective evolutionary Genetic Algorithm (MOGA) and multi-objective non-evolutionary NLPQL optimisation methods for a 1.8L diesel engine. This investigation aimed to obtain the optimal design values for the following variables, inner distance of the

bowl wall, bowl radius, injection spray angle and injector half spray cone angle with ISFC, IMEP, NOx emission and spray droplet diameter set as the objectives. It was observed from the study that a closer inner wall distance of the bowl resulted in higher engine efficiency, deeper bowl with a more circular shape resulted in lower NOx emissions due to a higher swirl motion. It was also observed that the NLPQL and MOGA achieved the best design at 41 runs and 84 runs, respectively, with the deviation of less than 2% in their NOx emission results in favour of MOGA.

Hu et al., [15] also studied the comparison between the NLPQL and MOGA for the optimisation of a 4-cylinder marine diesel engine in terms of NOx, soot and SFOC. Here, the authors reported that the NLPQL produced a best design case that resulted in NOx emissions higher than that of the baseline run thus, failing to achieve optimisation at 17 runs attributed to improper weights whereas the MOGA obtained a best design case reducing NOx and soot emissions considerably at 14 runs. It was also observed that better results were obtained when both algorithms were combined. Bozza et al., [16] applied the MOGA-II in optimising the performance of a light-duty diesel engine equipped with a HPCR fuel injection system and observed that it was able to yield optimal results for NOx, IMEP and combustion noise based on five design variables of fuel injection strategy.

Li et al., [126] performed a 3D CFD multi-objective optimisation that was focused on improving methanol-diesel blend injection characteristics for enhanced performance and emissions of a diesel engine fuelled with direct pilot diesel and main methanol injections. In their investigation, methanol injection pressure and nozzle diameter, as well as two diesel/methanol spray interval angles, α in the XZ plane and β in the XY plane were the four design parameters. The characteristics of combustion, performance and emissions were the objectives analysed. Their findings showed that engine performance and emissions were significantly affected by methanol nozzle diameter and injection pressure. At a constant injection duration of methanol, the combination of larger nozzle diameter and lower injection pressure resulted in lower peak pressure, HRR and NOx emissions while uHC, CO and soot emissions increased. In addition, an α and β methanol spray of 2° and 15°, respectively, led to improvements in the fuel economy and emissions.

Liu et al., [128] performed a multi-objective optimisation of diesel fuel injection parameters of a dual-fuel engine fuelled with diesel and natural gas using GA. The results of their investigation showed that almost all the non-Pareto and Pareto solutions exhibited soot levels below the Euro 6 limit. However, only a few non-Pareto and Pareto solutions exhibited NOx levels below the Euro 5 limit. The Pareto front designs were dominated by open piston bowl geometries.

Various investigations previously discussed as well as others [129]–[136] have demonstrate the benefits of multi-objective optimisation in engine development especially from the application of GAs in the Optimiser-3D CFD approach. However, in many of these reports, the required computational cost was observed to limit their application especially when utilising a GA as the optimiser due to their relatively slower convergence compared to the non-evolutionary and gradient based algorithms.

From some of these studies, the optimisation process was found to utilise a large set of CFD simulated designs to adequately sample the design space for the GA-CFD optimisation which in turn increased the computational cost required.

An additional factor of challenge was the types of engine design parameters considered for optimisation and the approach to their stand-alone or combined optimisation. The combined optimisation of controllable and fixed engine parameters (hardware) raises the issue of finding an adequate optimisation technique or approach. Addressing these parameters further increased the complexity of the optimisation process and consequently the computational requirement. However, only a few investigations have been carried out on this frontier despite the acknowledgement of its importance.

Shi et al., [249] presented the two-step approach and the consistent approach in an attempt to tackle this issue. Some conclusions from their investigation provided insight on the hierarchy of the considered parameters as well as effective approaches towards optimisation. Nevertheless, their investigations were limited to single fuel injection strategy and piston bowl geometry even with the use of the advanced CONDOR server computational system which suggested that the consideration of an optimisation approach was also impacted by the computational cost involved.

The investigation by Ge et al., [250] which formed the basis of the optimisation study by Shi et al, [249] suggested piston bowl geometry optimisation should be carried out under high or full engine load conditions due to the higher sensitivity of engine performance and emissions to piston bowl geometrical attributes under these engine load conditions. However, as with Shi et al., [249], their study was also limited to single injection strategy and piston bowl geometry and did not consider multiple injection strategies and the additional complexities involved.

The application of surrogate/regression models via the optimiser-surrogate approach have been shown to greatly reduce the required computational cost which in turn, promotes the inclusion of more prime design parameters in optimisation studies. However, the computational cost reduced here is that of the cost required for design exploitation and not from training the models. From various studies involving the use of optimiser-surrogate approach and regression modelling, relatively large design sets of 200 to 400 designs have been reportedly required for training and validation to achieve an accurate model which are expensive from either engine experiments CFD simulations [246]–[248].

In the study by Lotfan et al., [17], the combination of the NSGA-II and Artificial Neural Network (ANN) was used in optimising CO and NOx emissions for a direct injection dual-fuel engine. A Multi-Layer Perception (MLP) network was trained on 400 experimental data to predict the values of output parameters, NOx and CO emissions based on the input parameters, engine speed, intake temperature, diesel mass flow rate, CNG mass flow rate and power output. The NSGA-II was applied to this network to find the Pareto optimal solutions of the problem. The results showed that the ANN successfully modelled the emission characteristics with 0.9953 and 0.9969 as the correlation factors for CO and NOx, respectively, while the MAPE was less than 0.2.

Roy et al., [111], investigated the potential of ANN in predicting the performance and emissions of a single cylinder four stroke diesel engine under varying EGR rates. In this study, an ANN model was trained using 70% of 441 experimental test data while 15% of the data was used for the model validation and 15% was used to test the model network performance. The study showed that the developed ANN model could predict the characteristics of the output parameters BTE, BSFC, PM, CO and NOx

emissions accurately with correlation coefficient (R) values ranging from 0.987 to 0.999 and MAPEs ranging from 1.1% to 4.57%.

Costa et al., [125] explored a methodology for the multi-objective optimisation of a diesel engine piston bowl employing a GA and ANN combination and finally, 3D CFD simulation. The study aimed to leverage the fast-calculative nature of artificial neural networks in obtaining Pareto optimal solutions for a multi-objective optimisation problem and then confirming the best solutions using 3D engine CFD simulations. The study showed that the inclusion of ANN to conventional GA-3D CFD simulation optimisation significantly reduced the computational time while generating Pareto solutions for NOx, soot and IMEP.

Jabbr et al., [127] performed a numerical CFD multi-objective optimisation of hydrogen-diesel fuel mixture ratios for CI engine performance and emissions. In the optimisation, EGR, diesel injection timing and various ratios of hydrogen were the design parameters investigated. Their findings showed that a 37.5% increase in hydrogen ratio caused a 22% increase and 32,5% decrease in NOx and soot emissions at the baseline, respectively. However, NOx and soot emissions experienced a simultaneous reduction at an optimal operating condition of 4% EGR, 30°bTDC diesel SoI timing and about 13% hydrogen ratio. The results were obtained from the application of ANN, GA and regression analysis.

Tara et al., [251] employed a dataset of 335 3D CFD simulated designs in training a regression model and combined it with the NSGA-II to predict the relationship between seven injection design parameters and the response parameters of indicated efficiency, NOx, CO, and HC emissions. The results showed that the RSM-NSGA-II successfully reduced NOx, CO, and HC by 22.3%, 44.9%, and 47.1%, with a consequence of 37.5% in maximum pressure rise rate while indicated efficiency improved by 11.5%.

In the regression-GA multi-objective optimisation study by Costa et al., [252], 81 DoE designs used for training the RBF model were generated through 3D CFD simulation. It was noted in their investigation that each design required approximately 24 hours for completion and estimated about 2100 hours to generate the designs during optimisation if the GA designs were generated with 3D CFD simulations.

The studies which featured regression/surrogate models revealed that the capability of a regression model in mapping the relationship between the input (i.e., design) and a set of output responses (i.e., multi-objective) is correlated to factors such as the size and diversity of the generated design dataset. Generally, the source design dataset size should be such that it reasonably reflects the dimensionality (i.e., number of design parameters) and grid resolution (i.e., step size) of the design space. The studies also revealed that the diversity and dimensionality of the design space can also influence the performance of the trained regression model.

Whilst there is some evidence of successful applications of DoE algorithms over design spaces with relatively low and high dimensionalities for training and testing regression models, some reports have also highlighted the limitation of this approach especially when using relatively smaller design datasets (i.e., lower than 200 designs) in the search for reduced computational cost.

In the investigation by Shi [253] which employed a relatively medium design dataset size of 120 designs for nine design parameters, the trained regression model was reported to make predictions that were sufficient in replacing CFD simulations for the performance objectives but insufficient for the emissions objectives. This observation was attributed to dimensionality to design dataset size ratio of the design space. In addition, it appeared that the diversity provided by the DoE could be detrimental to the regression modelling as it could lead to low visibility of the relationship between the design parameters and objective responses. Furthermore, the complex relationship between the design parameters and some response parameters such as soot emission was observed to contribute to a poor visibility and consequently poor predictive capability of some regression models.

The initial findings by Shi [253] also led them to towards further optimisation investigations using MOGA-II generated designs in training four regression methods for comparison. Interestingly, this revealed improvements in the predictive capability of the tested regression methods due to generational dynamic learning. Their investigation also showed that the regression methods exhibited different behaviours due to diversity and dimensionality of the dataset.

Therefore, it is obvious that even with the negligible computational cost and time required by regression/surrogate modelled designs over 3D CFD simulated designs, the regression-based optimisation still incurs a significant computational cost due to the number of CFD simulated designs required to achieve reasonable diversity within the design space and for adequate training and validation. It is clear that although the accuracy of a regression model is important, reducing the computational cost and time associated with obtaining the training and validation design dataset is also vital for the feasibility and scalability of its engine optimisation process application. Hence, striking a balance between an accurate and reliable regression model as well as a training design dataset size which incurs lower computational cost is important.

Towards this end, more recent endeavours some of which feature the application of Super leaners (i.e., the use of multiple surrogate/regression models) within unique strategies to reduce computational cost have been explored. Moiz et al., [144] developed a machine learning-genetic approach called the ML-GA involving a Super Learner model which yielded improvements in engine ISFC. They reported that the ML-GA model enable the reduction of computational cost by about 75% when compared to a GA-CFD optimisation approach which used the malschain μGA. Although the ML-GA was trained using 2084 CFD simulated designs which required a runtime of about 336 hours, it was later found to only require about 300 designs. On the other hand, the GA-CFD approach required 784 3D CFD simulated designs to converge wherein each design simulation required a runtime of about 12hours when using 128 processors from a supercomputer.

Owoyele et al., [145] developed an AutoML-GA approach that utilised an automated hyperparameter tuning functionality to improve the quality of the ML model which consequently reduced the number of CFD simulated functions required and thus, reduced computational cost significantly. More recently, Owoyele et al., [146] developed the ActivO algorithm for accelerating simulation-driven engine design. In their report, an improvement of about 1.9% in ISFC was gained using the ActiveO approach which utilised a weak and stronger leaner trained in an active loop to perform effective exploration and exploitation of the design space for optimum solutions. The improvement obtained required 88 CFD simulated designs wherein each CFD design required 8.3hours of runtime reducing computational cost and time

by about 5.5 times when compared to the CFD- μGA by Moiz et al., [144] earlier discussed.

Although these studies, [145], [146] showed that computational cost could still be further reduced, it is worth noting that the optimisation process was limited by providing a single optimal solution to reducing ISFC and did not show any evidence towards the provision of more than one optimal solution which is a more attractive avenue for engine development because it presents more options towards improving engine design for realistic operations.

2.6 Concluding Remarks

A review on the combustion and emissions characteristics of CI engines was performed. Besides seeking improvements in performance, reducing CI engine emissions to even sub-regulation levels is significant now more than ever due to their adverse health and environmental effects.

Combustion phasing and the resultant performance and emissions hinge on the characteristics of air-fuel mixture and its interaction with the resident in-cylinder charge temperature, pressure, and density. Therefore, identification of ways by which combustion characteristics and phasing can be controlled is rather important.

The pursuit for achieving greater combustion control, has led to investigations on some advanced methods and technologies currently used to improve performance and reduce emissions with minimal penalties. The advantages of aftertreatment systems such as SCR, DOC, DPF and NOx absorbers support their current mandatory application. However, their contribution to the increased weight and operational cost of CI engines is a notable drawback. Furthermore, they only control downstream emissions after formation and do not provide any way of reducing emissions at source (i.e., within the combustion chamber).

The improvement and optimisation of in-cylinder and combustion chamber parameters is still trending. The application of EGR is very beneficial to increasing thermal efficiency and reducing NOx emissions. Nevertheless, this is often at the expense of a loss in engine power and an increase in CO, uHC and soot emissions. The investigations carried out on the effects of piston bowl geometry clearly show its

significance to improving the state of air-fuel mixing by assisting in-cylinder turbulence to improve combustion and reduce NOx and soot emissions.

The investigations performed on the effects of fuel injection timing, injection spray angle and injection strategy show that they greatly influence combustion phasing through spatial and temporal distribution of the injected fuel within the combustion chamber. Advancements in fuel injection is currently drawing attention because of the significant improvements gained without the drawbacks experienced with aftertreatment systems. With the constant technological enhancements made to the HPCRs and ECUs, multiple fuel injection strategies offer tremendous advantages in terms of combustion and emissions control which can be further complemented through the application of EGR, miller cycle, LTC modes and alternative fuels.

Identifying adequate setups for various engine parameters is currently achieved by using computational optimisation and statistical algorithms along with engine CFD simulations. This provides a time and cost-effective approach of finding optimal solutions to engine parameters of interest compared to engine experiments. The use of optimisation approaches such as surrogate-3D CFD (regression-based approach) over the more common GA-3D CFD approach provides reduced computational cost with minimal drawbacks in robustness. However, these methods still incur quite significant computational cost primarily from the CFD simulated designs they require for sufficient modelling. This has led to new endeavours involving super learner surrogate-Gas, automated hyperparameter tuning and the ActiveO approaches which all show significant computational savings.

Based on the various papers reviewed, researchers have been more focused on the optimisation of either hardware or controllable engine parameters with crossovers in the combined optimisation of piston bowl geometry and single fuel injection strategy at single and multiple fuel loads as well as multiple fuel injection strategy at single loads. There are fewer works on the optimisation of more complex interactions such as multiple injection strategy and piston bowl geometry at multiple fuel loads. This can be attributed to the complexity involved in mapping such interactions especially in finding suitable piston bowl geometry for various optimal multiple injection strategies at multiple fuel loads. It would be interesting to explore new optimisation approaches that enable the consideration of both engine parameters for optimisation.

3 Experimental Procedure and CFD Modelling Approach

This chapter presents a brief description of the experimental procedure which generated the engine data used to validate the 3D CFD engine model. In addition, it also presents details of the CFD software utilised in this research, and a description of the 3D CFD engine modelling approach which involved the piston bowl geometry configuration, mesh generation and sensitivity test, simulation configuration and the model validation.

3.1 Experimental Procedure

The experimental setup and procedures upon which the CFD model in this research work was built and validated were performed by Herfatmanesh et al., [147], [148]. A Ricardo Hydra Single Cylinder diesel engine was used to perform the experiments used in validating the engine CFD model. The details of its description, specifications and fuel injection system are presented in Appendix A, subsection A1.1 and A1.3.

According to the reports, [147], [148], the procedure for the experimental analysis met the health and safety standards set to prevent any accidents in the engine laboratory. The engine room was inspected for any spillages and leakages before every engine run. The engine room was ventilated throughout the experimental process. The engine was heated using the cooling and lubrication systems for one hour before the engine operation commenced as detailed in Appendix A subsection A1.2. The engine was motored to 1500 rpm and the heater fitted to the air intake was switched on. The heater was used to heat the intake air to 100℃ and to prevent overheating it was only switched on when the engine was running as detailed in Appendix A subsection A1.4.

Fuel injection timing and quantity as well as engine start-up were controlled using the EC-Lab software. Engine firing was carried out for a few cycles to achieve a stabilised combustion before in-cylinder pressure recording started. Experimental data collection as detailed in Appendix A section A2 was performed using the LabVIEW data acquisition software.

3.2 IC Engine CFD Software Packages

Computational Fluid Dynamics (CFD) is a very useful non-destructive method of analysis that can be used for fluid dynamics related studies and investigations of various systems. Engine CFD modelling and simulation is useful as a predictive, cost effective and time saving tool in studying engine performance and emissions characteristics of existing and new designs [79]. Various 1D and 3D CFD solvers have been used in predicting engine performance and emissions for various fuels, fuel blends and operating conditions to drive engine development as discussed, the literature review. Generally categorised as either commercial or open source, some of these software packages include Ricardo Wave, KIVA, AVL Fire, Star ICE, ANSYS IC Engine, ANSYS Forte', Converge, OpenFOAM, Lotus Engine Simulation, GT-Power, and AVL Boost wherein each has their advantages and disadvantages according to their respective competence for different types of studies.

The comparative work on various engine CFD packages by Azad et al., [65] showed that the selection of an engine CFD package for simulation studies is influenced by the various factors. Some of these factors include the type of study, the engine detail available, the computational resources available for an adequate simulation run time, availability of technical support as well as the extent of the software application in the research field. Regarding the simulation type, engine CFD package is the 3D CFD simulations are known for providing more in-depth results compared to 1D CFD simulations, however they achieve this at the expense of significantly longer computational time and resources [80]–[89].

3.2.1 AVL Fire CFD Solver Package

The CFD solver package used for the research investigations is AVL Fire and more specifically, the Engine Simulation Environment (ESE) Diesel module. AVL Fire is a powerful thermo-fluid and dynamics CFD tool whose rapid development was established through the support of a wide range of engine test data designed for various aspects of IC engine simulation and analysis. As a result, it has been extensively used in research and development of IC Engines. ESE Diesel offers a comprehensive implementation that comprises of pre and post processing workflows as well as a solver program that can effectively generate predictive solutions for in-cylinder IC engine simulations [90].

This software was selected for this study based on the consideration factors stated earlier. AVL Fire was found to work sufficiently without engine information such as valve geometry and valve linear translation specifications which other packages such as ANSYS IC Engine and Forte', and Star ICE require.

AVL also has an extensively published capability of handling 3D CFD simulations and accurate predictions for the injection and combustion of diesel fuel as well as other alternative liquid and gaseous fuels. Regarding its pre-processing workflow, it is known for its robust 2D and 3D mesh generation that is useful in dynamic meshing. The Fire solver uses a two-stage pressure correction method that provides good stability with first, second and third order accuracy schemes.

The FIRE solver algorithm resolves the conservative governing and transport equations for chemical species, turbulence, and scalar quantities, such as mixture fraction, flame surface density, etc. It performs this process by using a fully conservative finite volume method where all the dependent variables such as pressure, density, turbulent kinetic energy, dissipation rate, etc are evaluated at the computational centre of the individual cells created during the meshing process. Its Semi-Implicit Method for Pressure-Linked Equations (SIMPLE) Euler or Pressure Implicit with Splitting of Operators (PISO) schemes are used to discretise the rate of change of the convection term. In addition, it is applicable to turbulent flows at all flow speeds [31][91].

Furthermore, it offers a range of mathematical models for solving fuel injection spray, break-up, evaporation, in-cylinder turbulence, mixing phases, combustion, and emissions formation. Most notably is its k-zeta-f turbulence model which has been reported to produce highly robust and accurate turbulence modelling and prediction. Its post-processing workflow is performed for 2D and 3D result formats, as well as data visualisation of the results.

The AVL Fire package was obtained through a university partnership program for free which also included provisions for technical support from AVL technical engineers who oversaw the development and application of the software. In addition, its extensive application in industry and research created a community of researchers and engineers with experience of its application in the research field which was

difficult to get for open-source packages and some commercial packages such as ANSYS, and Star ICE.

Considering its fit for optimisation purpose, AVL Fire application with 3rd party packages such as MATLAB and modeFRONTIER for further post processing, and data analytics was found to be sufficient for the scope of the research as seen in its application when coupled to MATLAB and involved via a DOS Batch scripting within the modeFRONTIER platform in Chapter 6 and 7.

3.3 3D CFD Modelling Approach

Figure 3-11 shows the CFD modelling approach used in this investigation implemented within AVL Fire. The process commenced with the adaption of the actual engine specifications presented in Table 9-1 into the ESE Diesel module. The general engine parameters required by the software module included the cylinder layout, number of cylinders, cylinder bore and stroke as well as the desired compression ratio. In addition, the piston displacement as function of crank radius, connecting rod length, and piston pin offset were also included.

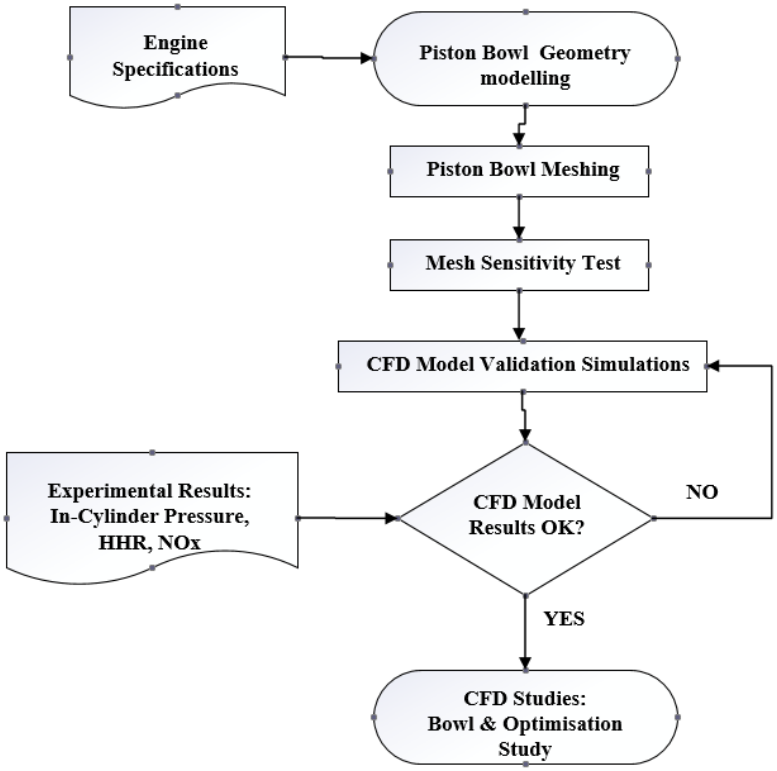

Figure 3-1: Flowchart showing the processes involved in the CFD modelling approach

3.3.1 Piston Bowl Geometry Configuration

The configuration of the piston bowl geometry involved the declaration of the parameters for the bowl-in-piston, and injector according to the engine specifications. The modification of the bowl-in-piston started with a geometry template in the 2D sketcher which was imported from the ESE Diesel library. The TDC clearance, bowl radius and bowl depth were defined with respect to the piston bowl parameters stated in Table 8-1 of appendix section 8.1. Although the modifications resulted in the slight increase of the actual compression ratio to 16.015:1, this deviation was resolved to meet the desired compression ratio of 16:1 through the automatic adjustment of the clearance volume as a function of the desired compression ratio. This adjustment was negligible due to the negligible difference between the actual and desired compression ratios.

Furthermore, the parameters which defined the injector were specified based on the injector parameters stated in Table 8-2 of appendix section 8.1. In addition to these parameters, an injector nozzle position in the z-coordinate of 1.4mm, and a nozzle hole half outer cone angle of 7.5° were also included.

The author of the engine experiment referred to the actual bowl-in-piston as the shallow rectangular piston bowl. However, in this research, it was referred to as the Flat Re-entrant Bowl (FRB). Figure 3-2 shows the 2D cyclic boundary view of the FRB model to be used in engine CFD simulation with the characteristics of the Ricardo Hydra single cylinder engine.

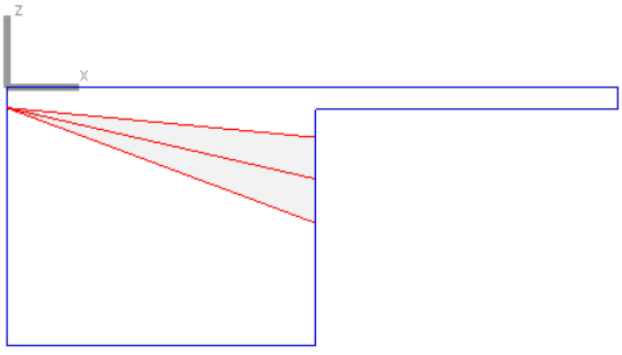

Figure 3-2: Cyclic Boundary view of the FRB showing its injector spray cone

3.3.2 Mesh Generation and Sensitivity Test

The meshing process commenced after the piston bowl geometry was configured. This process involved two sub-processes which were the 2D and 3D meshing processes, respectively. The 2D meshing involved two boundary layers such that each boundary layer had a thickness of 0.2mm. In addition, an average cell size of 1.3mm was used to form a coarse mesh having approximately 41144 cells at TDC. The 3D meshing involved 25 subdivisions in angular direction with a distribution factor of 1. A mesh inspection was automatically performed by the software during the mesh generation to find overlapping cells due to their tendency to cause divergence.

A mesh sensitivity analysis was performed to ensure the numerical results are independent of the mesh size. During the analysis, the effect of reducing the average cell size of model mesh on its simulation results and time was observed. Seven different cell sizes were examined, and their predicted in-cylinder pressures results were analysed as shown in Figure 3-3. In addition to in-cylinder pressure profile, the simulation run time and deviations at the peak pressure were also considered.

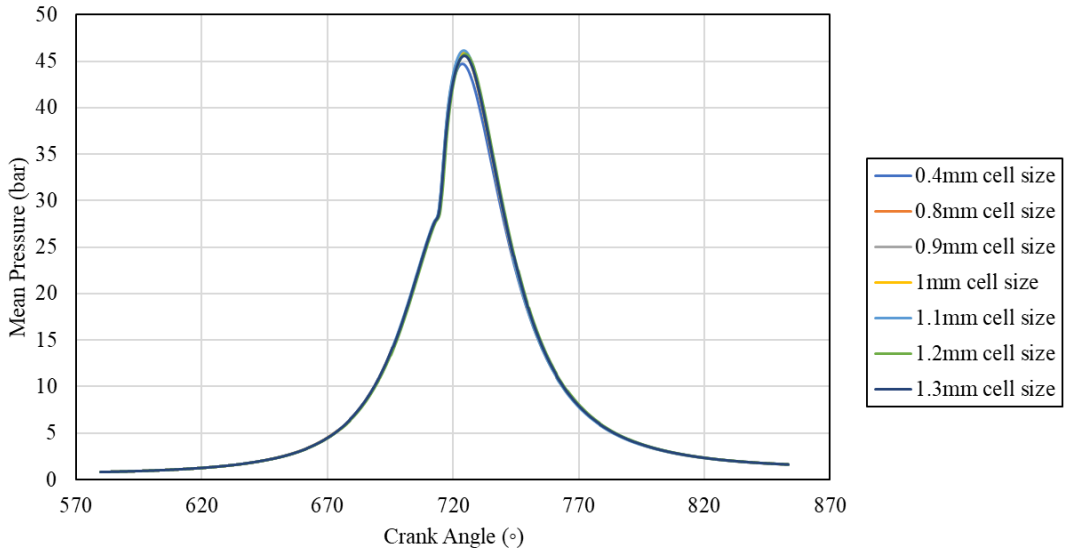

Figure 3-3: In-cylinder pressure showing mesh sensitivity

Pressure stability was observed as the cell size was reduced from 1.3mm to 0.4mm. A peak pressure of about 45.8bar was observed for cell sizes 1.0mm, 0.9mm and 0.8mm before reducing to about 44.7bar for the cell size 0.4mm. Apart from that, simulation time was observed to increase as the cell size reduced. Finally, the 0.8mm cell size was selected for the CFD model as it provided an acceptable in-cylinder pressure

profile with a simulation time of approximately 8 hours compared to the 0.4mm cell size which had a simulation time of almost 12 hours.

Figure 3-4 shows the model with the fine mesh having the 0.8mm cell size and consequently, 57000 and 176575 hexahedral cells at TDC and BDC respectively. A 60° sector of the geometry was used for CFD model and its simulations due to the bowl symmetry and central location of the injector in order to save time in mesh generation and simulation. This analysis was carried out using a computer workstation with an Intel Core i7 processor and 32 Gigabytes of RAM.

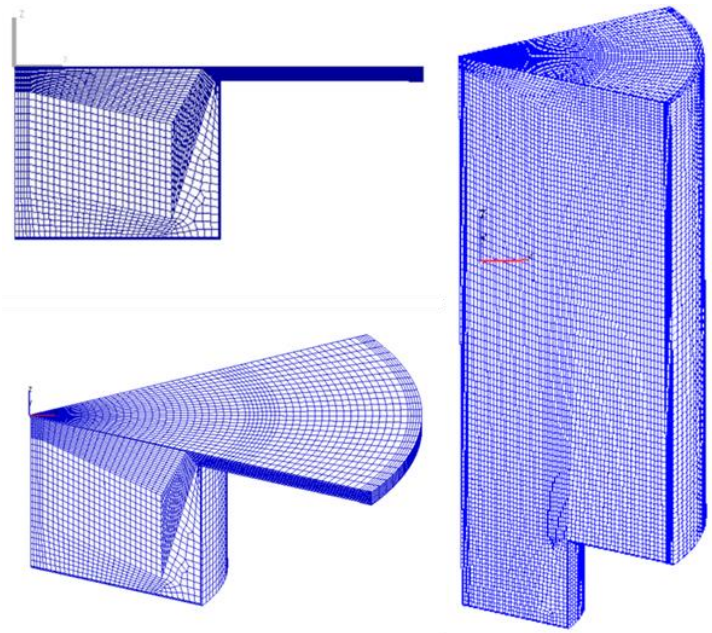

Figure 3-4: 2D (Top), 3D mesh cell distribution at TDC (Bottom) and at BDC (Side)

3.4 Simulation Configuration.

AVL Fire simulates engine High-Pressure (HP) cycle from the Intake Valve Closing (IVC) time to the Exhaust Valve Opening (EVO) time, thus these parameters were specified. The in-cylinder boundary temperature boundary conditions for chamber head and piston were specified based on similar literature. In addition, the initial conditions at IVC which included, air pressure and temperature, a turbulent kinetic energy, dissipation rate and length scale of $10m^2/s^2$, $1732m^2/s^3$ and 0.003m respectively were used in addition to a swirl/tumble ratio of 2100/min.

More also, the SIMPLE/PISO discretization scheme was applied for the AVL Fire solver which calculated the boundary values on extrapolation, the derivatives based on the Least Square Fit as well as the governing equations and Sub-Models described

in Appendix B sections B1 and B2, respectively. In addition, the hybrid wall treatment and standard wall function for wall heat transfer were also applied. The default values for the simulation underrelaxation factor for momentum, pressure, turbulent kinetic energy and dissipation rate, energy, mass source, viscosity, and species transport equations were used based on an AVL technical directive.

Furthermore, the MINMOD relaxation and central differencing schemes for the momentum and continuity equations respectively while the convergence is setup for a minimum of 10 and a maximum of 60 iterations per crank angle while the reduction of residuals for pressure and momentum is kept at 1×10^{-2} as further reduction led to negligible differences in the results. The Diesel Nozzle Flow model was used for nozzle flow simulation with its C_1 and C_2, constant values of 0.57 and 5.43 respectively. The calculation step is set to 0.2° CA to emphasize on accuracy during fuel injection as well as match the time step data reading of the experimental data. Finally, an output criteria was written for to obtain 2D and 3D output results from the simulation.

3.5 Model Validation

The experimental data presented in Herfatmanesh [149] and obtained from the single cylinder diesel engine was used in validating the CFD model. Here, the model was validated against single and double injection strategies to provide certainty that the fuel injection strategies and their resulting engine performance could be accurately predicted. The numerical results were obtained assuming the temperatures for cylinder and piston head as 570K, and the temperatures for cylinder wall liner, intake air charge and fuel as 470K, 300K, and 350K, respectively. Table 3-1 shows the operating conditions at which the validation process was performed for the single and double injection strategies.

Table 3-1: Operating conditions of CFD model validation

Intake Valve Closure (IVC)	140.4°bTDC
Exhaust Valve Opening (EVO)	133.4°aTDC
Engine Speed	1500 rpm
Engine Load	36% and 72%
Fuelling Demand	$10mm^3$ and $20mm^3$
Single Injection Strategy	
Start of Injection (SoI) and (Case Code)	15°bTDC (Si-1) and 10°bTDC (Si-2)
Double Injection Strategy	
Start of 1^{st} Injection (SoI-1)	20°bTDC and 15°bTDC
Dwell Angle	10°CA
Injection Ratios	50:50, 70:30 and 30:70

3.5.1 Single Injection

Figure 3-5 shows the comparism of the numerical and experimental results for in-cylinder pressure and Heat Release Rate (HRR) for the single injection strategies. It is evident that the predicted results for in-cylinder pressure and HRR for both cases were in good agreement with the experimental data.

Regarding the deviations of the CFD results, the predicted in-cylinder pressure profiles for both cases had slightly lower peak pressure values with negligible differences at the start of the fuel injection. This was mainly attributed to engine blow-by and in-cylinder charge leakage from the optical window seals near TDC, thus affecting the in-cylinder thermodynamic conditions before, during and after combustion.

The predicted HRR profiles for both cases had minor differences at the start of fuel injection and at the start of combustion which resulted in minor differences in combustion duration. The deviations were attributed to the variations in in-cylinder thermodynamic conditions caused by the lower thermal conductivity of the quartz

windows on the sides of the engine cylinder while the local deviations at the end of combustion were due to the HRR sensitivity to slight changes in the in-cylinder pressure profile.

In-cylinder charge leakage has reportedly resulted in in-cylinder air quantity variations more prominent at advanced fuel injection timings compared to retarded injection timings which influences the available air for soot oxidation. In addition, the lower thermal conductivity of quartz in comparison to aluminium has been reported to result in a higher build-up of in-cylinder temperature, thus, influencing temperature related parameters especially for late injection timings. Nevertheless, the predicted emission results were within the acceptable limits

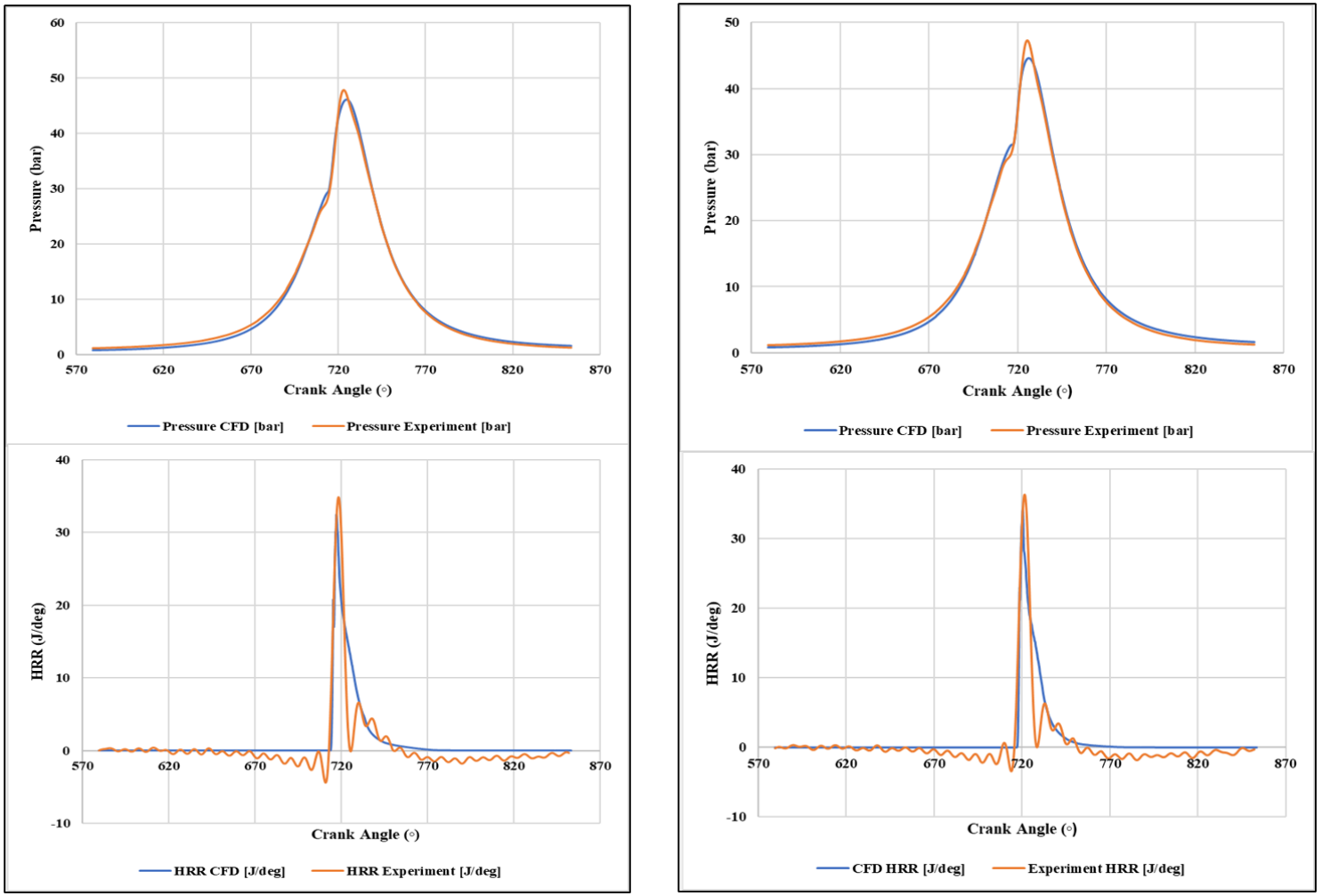

Figure 3-5: Comparism of numerical and experimental in-cylinder pressure (top) and HRR (bottom) data for Si-1(left) and Si-2(right)

Figure 3-6 shows the comparison of the predicted and experimental NOx and Soot emissions for the tested single injection strategies. The predicted results for Si-1 and Si-2 cases are in good agreement with the experimental data. Si-1 had a higher predicted NOx of about 2.5% and a lower predicted soot of about 10% compared to the experimental data while Si-2 had lower predicted NOx and soot emissions of about 6.5% and 2.9% compared to the experimental data, respectively. The deviations were attributed to the influence of uncertainties such as the fuel injection duration due to delays in needle opening and closing and particularly, in-cylinder air content at the start of fuel injection due to in-cylinder charge leakage and the thermal conductivity of the quartz optical windows.

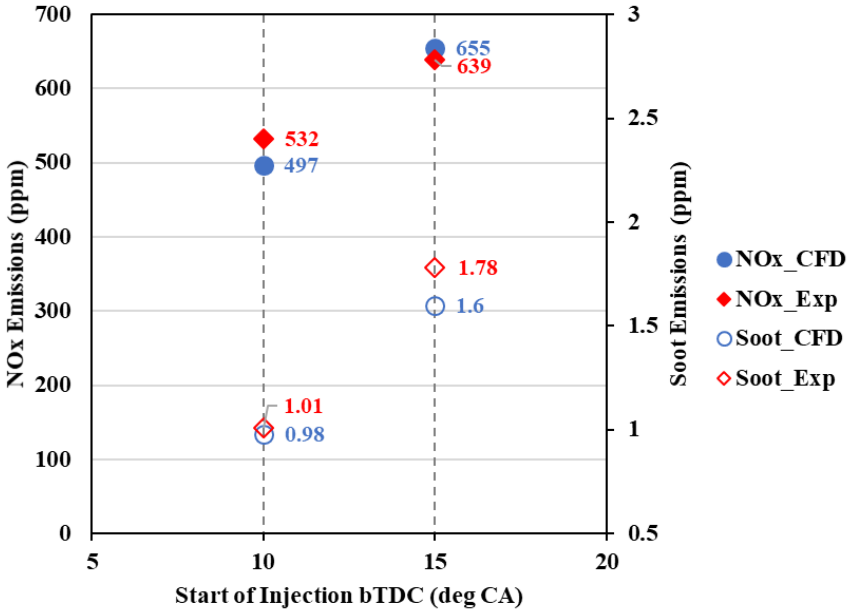

Figure 3-6: Comparism of numerical and experimental NOx and Soot emission data for Si-1 (15°bTDC) and Si-2 (10°bTDC) at low load

3.5.2 Double Injection

Figure 3-7 to Figure 3-9 show the comparism of the numerical and experimental results for in-cylinder pressure and HRR for the double injection strategies at low and high load respectively. Close similarities were observed between the predicted results and experimental data for the pressure and HRR profiles while exhibiting with slightly larger deviations compared to the single injection strategies. The deviations observed were attributed to the greater uncertainty over the actual fuel injection quantities injected. According to reports on multiple injection strategies, [150], fuel line pressure waves can affect the quantity of the second injection. Since these variations cannot be fully accounted for in engine CFD, such deviations between the predicted results and experimental data can occur, however, the observed differences were within the acceptable limits.

Figure 3-10 shows the comparison of the predicted and experimental NOx and Soot emissions for the tested double injection strategies at low and high load. The predicted emissions were observed to also be in good agreement with the experimental data for all the tested double injection strategies. Slight deviations were observed in the 70:30 injection ratio cases at low load wherein the numerical NOx for the SoI-1 20bTDC and SoI-1 15bTDC strategies were about 0.57% and 0.38% lower than their respective experimental comparisms respectively.

However, slightly larger deviations were observed in the 50:50 injection ratio cases. This behaviour was not evident in the soot emissions compared which exihibited relatively moderate deviations which nevertheless were still within acceptable limits.

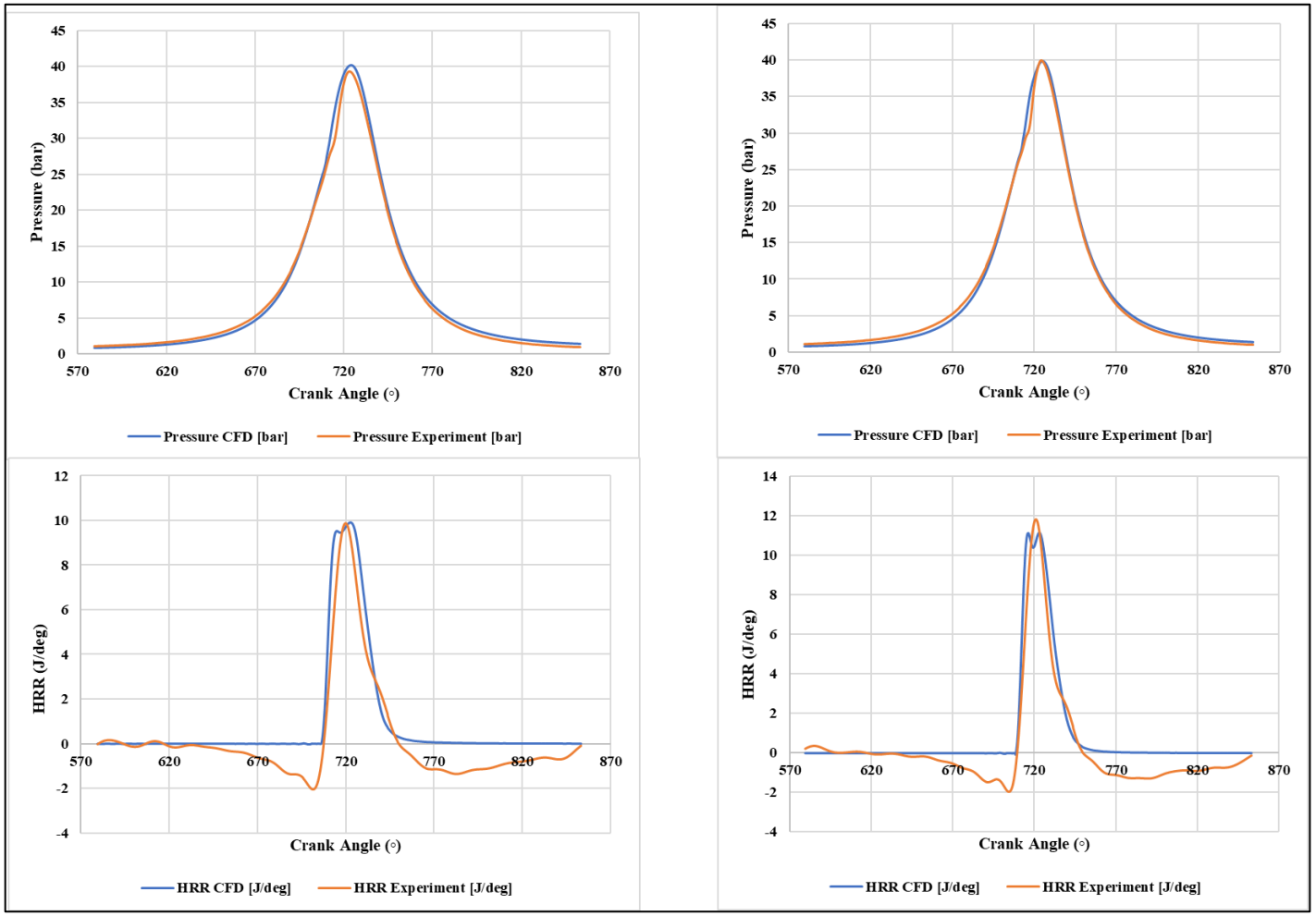

Figure 3-7: Comparism of numerical and experimental in-cylinder pressure (top) and HRR (bottom) for 5050 ratio, SoI-1 20°bTDC (left) and SoI-1 15°bTDC (right) at low load

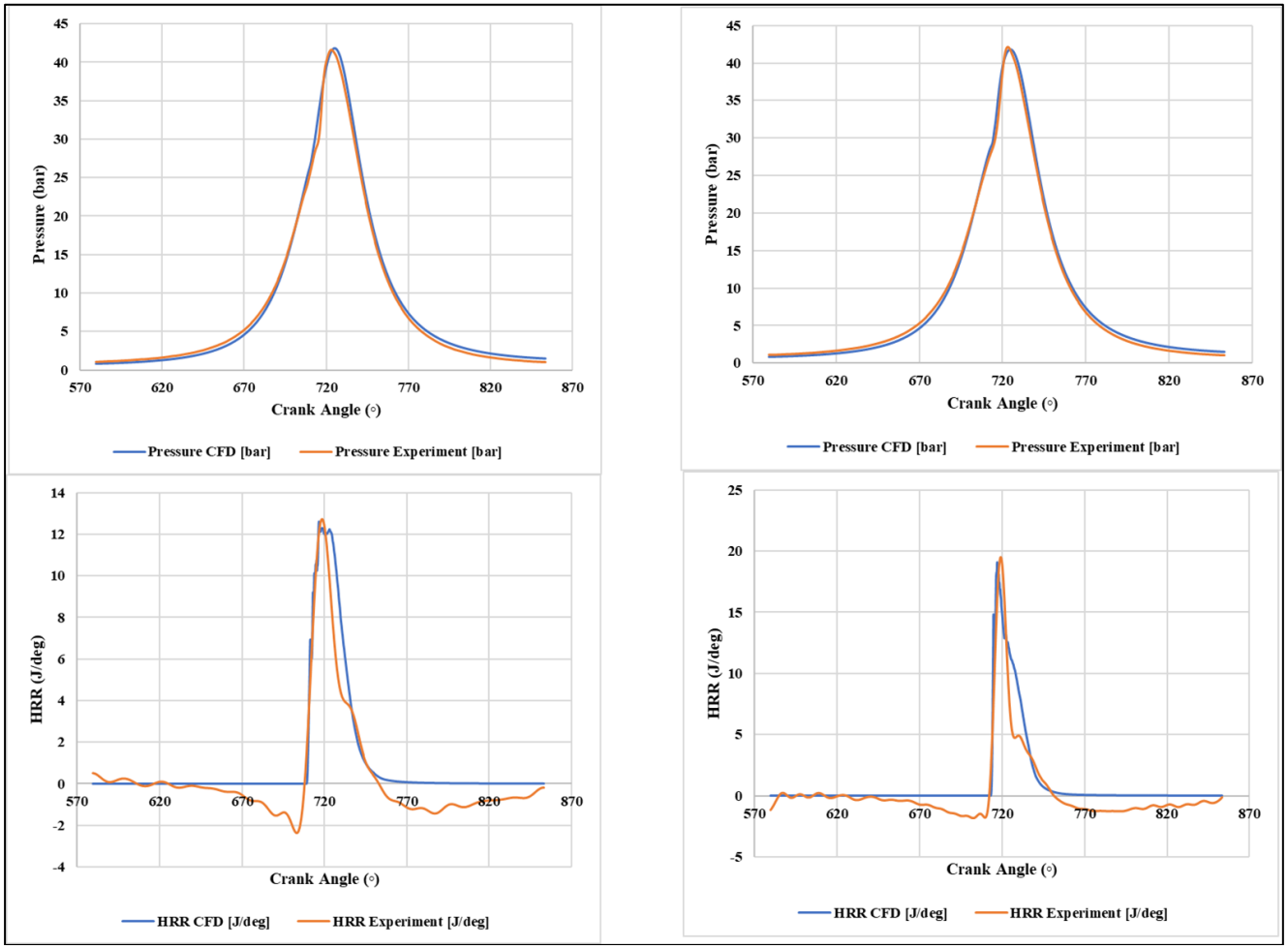

Figure 3-8: Comparism of numerical and experimental in-cylinder pressure (top) and HRR (bottom) for 7030 ratio SoI-1 20°bTDC (left) and SoI-1 15° bTDC (right) at low load

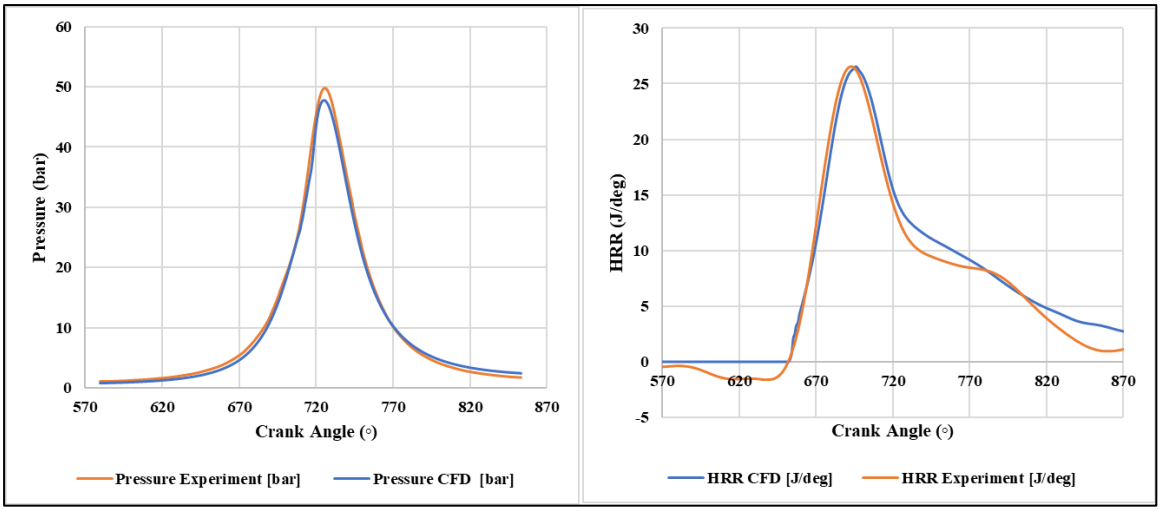

Figure 3-9: Comparism of numerical and experimental in-cylinder pressure (left) and HRR (right) for 3070 ratio SoI-1 20° bTDC at high load

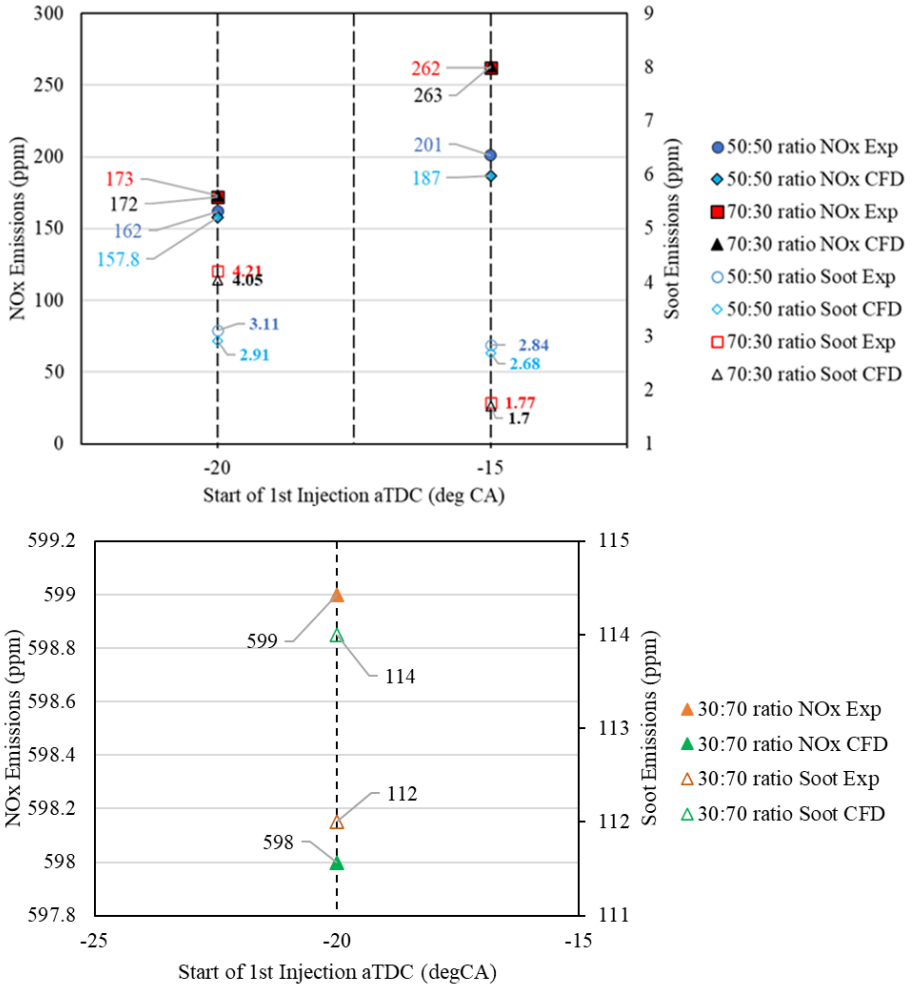

Figure 3-10: Comparism of numerical and experimental NOx and Soot emission data at low load 50:50 and 70:30 ratios (top) and at high load 30:70 ratio (bottom)

The validation process demonstrated that the CFD model could accurately predict the in-cylinder pressure, HRR and combustion and emissions characteristics of single and double injection strategies despite the existence of minor deviations attributed to uncertainties mostly linked to injection characteristics and the in-cylinder thermodynamic conditions of optical diesel engines as reported by Kashdan and Thirouard [151] and Pastor et al.,[152].

3.6 Concluding Remarks

The setup and validation of the 3D CFD engine model to be used in predicting the in-cylinder pressure, HRRs and combustion and emissions characteristics of a Ricardo hydra single cylinder diesel engine were presented. The setup and validation processes were implemented in AVL Fire using the ESE Diesel module. The computational sub-models employed in this investigation were selected based on the available information in the literature and through an extensive model validation and optimisation regime.

A 60° sector of the Ricardo Hydra engine piston bowl geometry was modelled to reduce the computational time and resources. Nevertheless, the results obtained represent the entire piston bowl geometry and chamber. A mesh sensitivity analysis involving 7 cell sizes was performed to obtain an optimal cell size that provided good prediction accuracy and repeatability with reasonable simulation runtime. The mesh cell size of 0.8mm was found to meet these criteria. The 3D engine CFD model was validated against experimental in-cylinder pressure, HRR, NOx and Soot emissions data which was obtained from the Ricardo hydra single cylinder engine.

The model was validated against two single fuel injection strategies presented as Si-1 and Si-2. From the validation performed at 50:50 ratio SoI-1 20bTDC and SoI-15bTDC, CFD NOx and soot deviations were less than 7%. From the validation performed at 70:30 ratio SoI 20bTDC and 15bTDC, CFD NOx and soot deviations were less than 0.7% whereas the CFD NOx and soot deviations for the validation performed at 30:70 ratio were less than 0.7%. The validation proved that the model was acceptable for simulating the combustion and emission characteristics of the engine despite the highlighted uncertainties.

4 Effects of Piston Bowl Geometry and Injection Strategy at Low Load

4.1 Investigated Piston Bowl Geometries and Double Injection Strategies

Three re-entrant piston bowl geometries each with distinctive geometrical attributes were considered for this investigation. The first was the Flat Re-entrant Bowl (FRB) from the Ricardo Hydra single cylinder diesel engine which was adopted for the 3D engine CFD model validation. The second and third were two Omega Re-entrant Bowl (ORB) geometries referred to as ORB1 and ORB2. The 2D geometry and 3D mesh cell distribution for the FRB, ORB1 and ORB2 are presented in Figure 4-1 whereas their mesh characteristics are presented in Table 4-1. It is important to note that the compression ratio and piston bowl volume of ORB1 and ORB2 were kept constant and equal to that of the FRB, the benchmark geometry. Their differences were in their respective bowl re-entrance curvature.

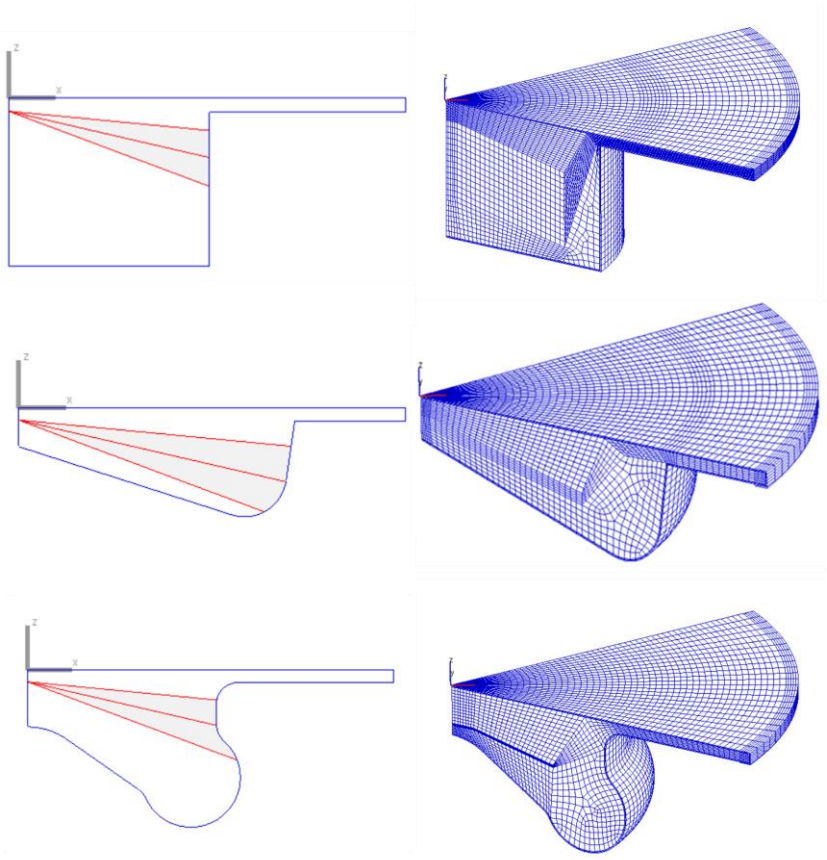

Figure 4-1: 2D geometries (left) and 3D mesh orientations (right) of the FRB (top), ORB1 (middle) and ORB2 (bottom)

Table 4-1: Comparism of the mesh characteristics for FRB, ORB1 and ORB2

Mesh Characteristics at TDC	**Bowl Geometries**		
	FRB	**ORB1**	**ORB2**
Number of cells	57000	33675	40900
Number of faces	2280	1347	1636
Number of boundary faces	208	172	194
Piston bowl volume (m^3)	2.45571×10^{-5}	2.45571×10^{-5}	2.45571×10^{-5}

The double injection strategy is the multiple injection strategy investigated in this research work to observe the influence of injection timing, and injection ratio at a constant dwell angle across the three piston bowl geometries. Table 4-2 presents the characteristics of the double injection strategies along with the operation conditions considered in the investigation at low load.

Table 4-2: Double Injection Strategy and Operating Conditions at Low Load

Intake Valve Closure (IVC)	140.4°bTDC
Exhaust Valve Opening (EVO)	133.4°aTDC
Engine Speed	1500 rpm
Fuel Demand	$10mm^3$/cycle
Start of 1st Injection (SoI-1)	20°bTDC to 5°aTDC sweep with 5° increment
Dwell Angle	10°CA
Injection Ratio	50:50 and 70:30

The dwell angle of 10°CA defined as the time interval between SoI-1 and the Start of the 2nd injection (SoI-2). In addition, this is implemented for two injection ratios. Therefore, 12 configurations were investigated for each piston bowl geometry at one engine load and a total of 72 configuration across both low and high engine loads. Furthermore, each configuration was represented by a codename which indicated its setup. For instance, ORB1-LL-5050-(20b,10b)TDC represented a configuration in which the ORB1 geometry was used at low load with a 50:50 injection ratio strategy and the first and second fuel injections at 20°bTDC and 10°bTDC, respectively.

4.2 Combustion Analysis at Low Load

4.2.1 50:50 Injection Ratio

The influence of the FRB, ORB1 and ORB2 geometries on in-cylinder pressure under the 50:50 injection ratio is shown in Figure 4-2. From the pressure results of the LL-5050-(20b,10b)TDC, LL-5050-(15b,5b)TDC and LL-5050-(10b,0)TDC, the FRB exhibited the highest peak pressures of about 42.5bar, 38.9bar and 34.2bar, respectively, compared to ORB1 and ORB2. In the LL-5050-(5b,5a)TDC case, it resulted in a double peak pressure profile while in the LL-5050-(0,10a)TDC and LL-5050-(5a,15a)TDC cases, it exhibited a similar profile trend and a slightly higher pressure rise after TDC compared to ORB1 and ORB2. ORB1 and ORB2 exhibited similar in-cylinder pressure profile trends and peaks in all the cases except for the LL-5050-(10b,0)TDC case were ORB1 exhibited a higher peak pressure level.
From these results, the FRB seemed to promote higher in-cylinder peak pressure levels compared to ORB1 and ORB2 due to the promotion of air-fuel mixing formations that generated higher HRR's compared to ORB1 and ORB2.

The influence of the FRB, ORB1 and ORB2 on the HRR results under the 50:50 injection ratio is depicted in Figure 4-3. From the results of LL-5050-(20b,10b)TDC, LL-5050-(15b,5b)TDC and LL-5050-(10b,0)TDC, the FRB exhibited the highest peak HRR of about 13.08J/deg, 14.9J/deg and 14.08J/deg, respectively, compared to ORB1 and ORB2. The peak HRRs were exhibited in the diffusion combustion phase. This demonstrated that the combustion was predominantly driven by diffusion mixtures. Despite the similarity in pressure trend observed in the cases for ORB1 and ORB2, the HRR results for ORB2 exhibited higher peak over a similar duration. This suggested that ORB2 promoted higher HRR levels compared to ORB1.

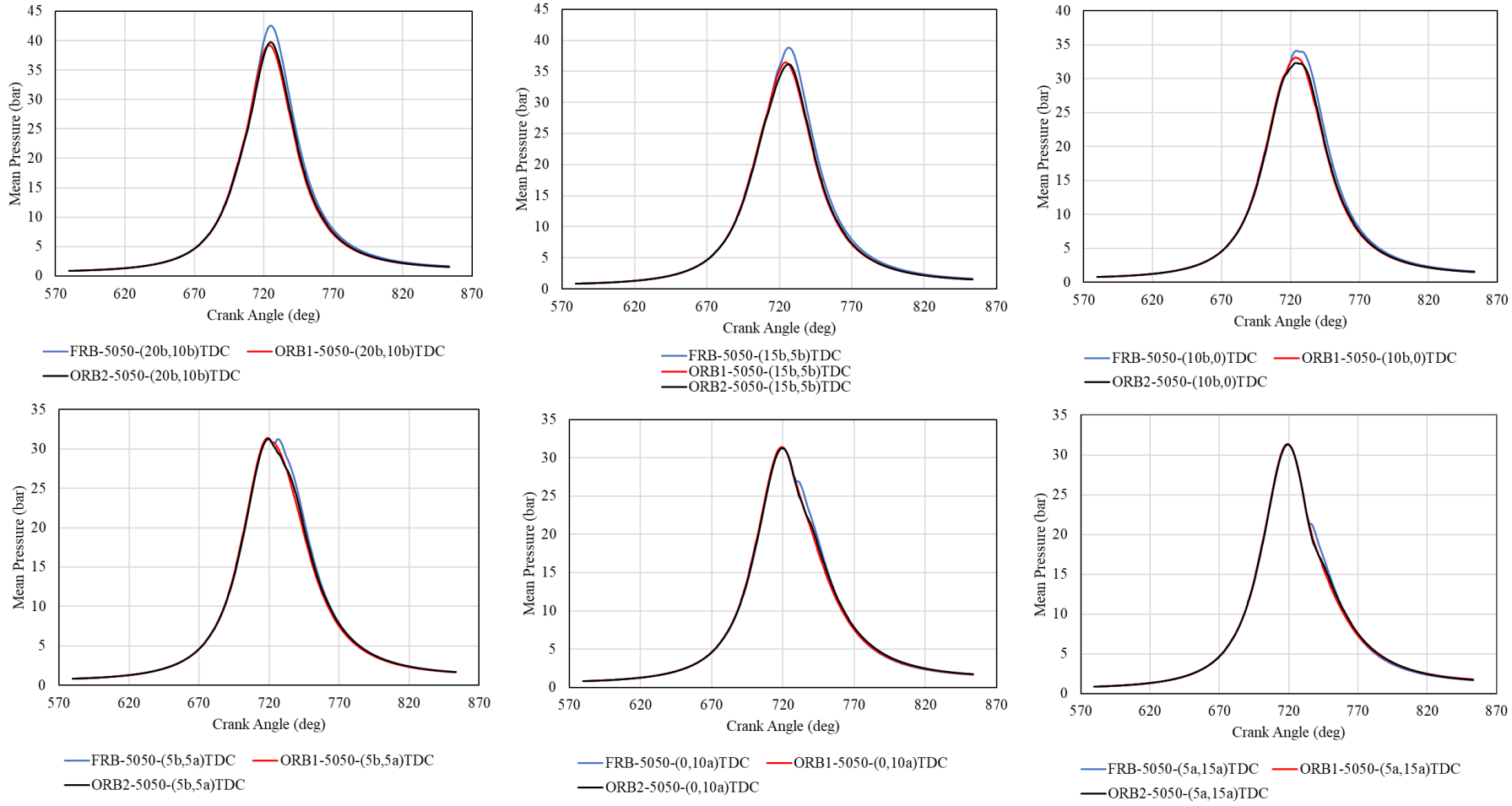

Figure 4-2: In-cylinder pressure data for FRB, ORB1 and ORB2 under 50:50 injection ratio at low load

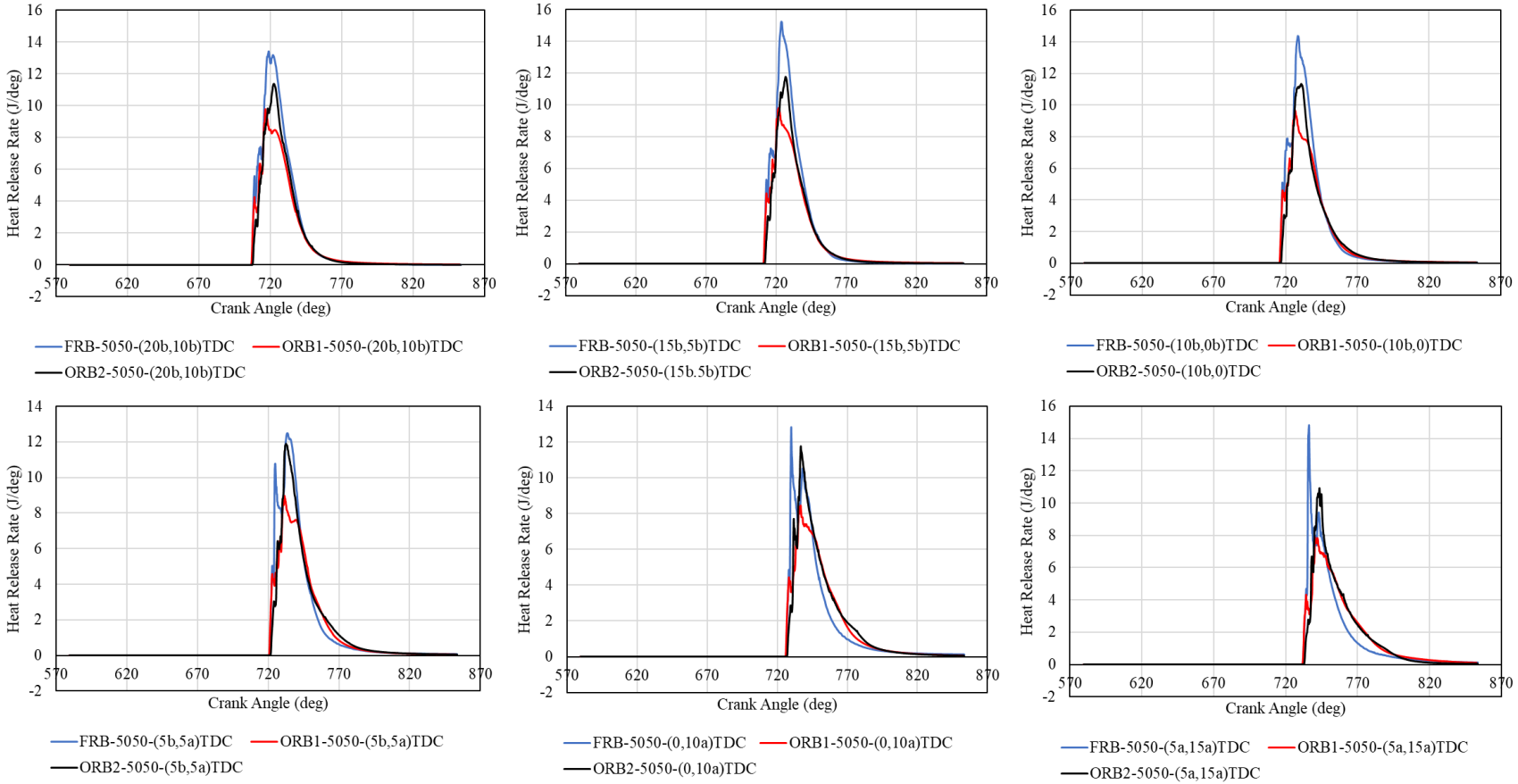

Figure 4-3:In-cylinder HRR profiles for FRB, ORB1 and ORB2 under 50:50 injection ratio at low load

The pressure and HRR behaviour of the FRB was explored further by analysing its equivalence ratio for the LL-5050-(15b,5b)TDC case, presented in Figure 4-4. Injected fuel parcels during and after the first injection event were isolated to a relatively small region close to the piston bowl side wall and remained relatively in the same region with minimal dispersion even during and after the second injection event. Later on, relatively rich mixtures seemed to move towards the squish region at 50% heat release while at 90% heat release, improved air-fuel mixtures had occurred, and the bulk mixture formations had split with a portion moving towards the base of the piston bowl; a characteristic attributed to fluid flow during the expansion of the chamber volume.

Combustion in the presence of such rich mixtures observed in the results especially during the second injection event contributed to high levels of diffusion combustion, high combustion temperatures and consequently high combustion pressure also observed around those times with respect to TDC in the pressure and HRR profile results. It can be seen that the area of the mixing front especially close to the piston bowl side wall was relatively small due to the FRB having a poor degree of re-entrance curvature which hindered the mixing front from stretching under the influence of in-cylinder turbulent fluid flow. While it was apparent that the poor re-entrance curvature of the FRB contributed to improved air-fuel interaction during the second injection event, this event involved the delivery of 50% of the total injection fuel quantity close to TDC which was spatially and temporally characterised by high temperatures and lower residual oxygen content, thus, contributing to a further rise in diffusion HRR.

The HRR results of ORB1 and ORB2 showed a gradual rise in HRR for all the cases with slight fluctuations while those of the FRB showed a steeper rise in HRR with a more pronounced separation of the end and start of the premixed and diffusion phases, respectively. This suggested that ORB1 and ORB2 promoted a smoother transition between the combustion phases compared to FRB due to the influence of their respective re-entrance curvatures.

Furthermore, HRR trend and peak levels remained relatively the same across each case for ORB1 and ORB2, respectively, compared to FRB which exhibited more

obvious shifts in trend and peak levels under the same fuel injection conditions. The behaviour of the bowl geometries with higher degrees of re-entrance curvature especially ORB2 was thus further analysed through its equivalence ratio results for the LL-5050-(0,10a)TDC case as shown in Figure 4-5. The results showed that the injected fuel parcels especially during and after the second injection event were distributed into two main portions upon encountering the bowl wall which further promoted an increase in the surface area of the mixing front, a characteristic which was promoted by the re-entrance curvature of ORB2. Therefore, rapid fuel-air interaction and mixing could occur.

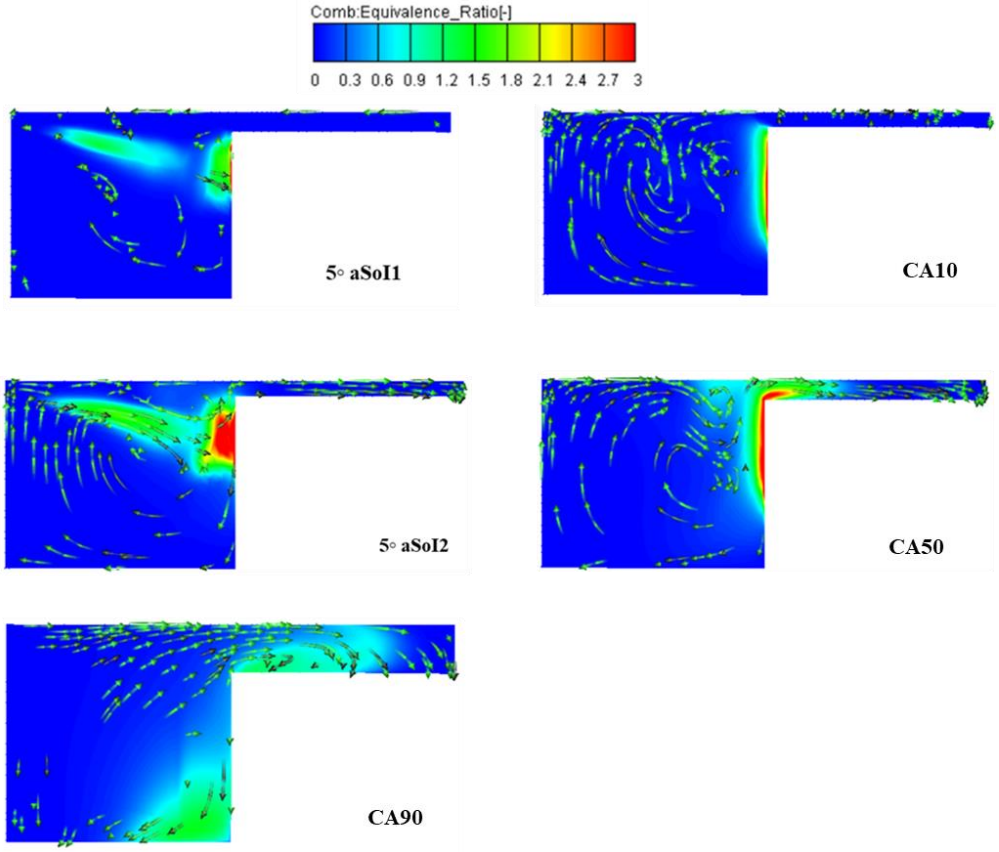

Figure 4-4: Equivalence ratio distribution of FRB for the LL-5050-(15b,5b)TDC case including CA10, CA50 and CA90

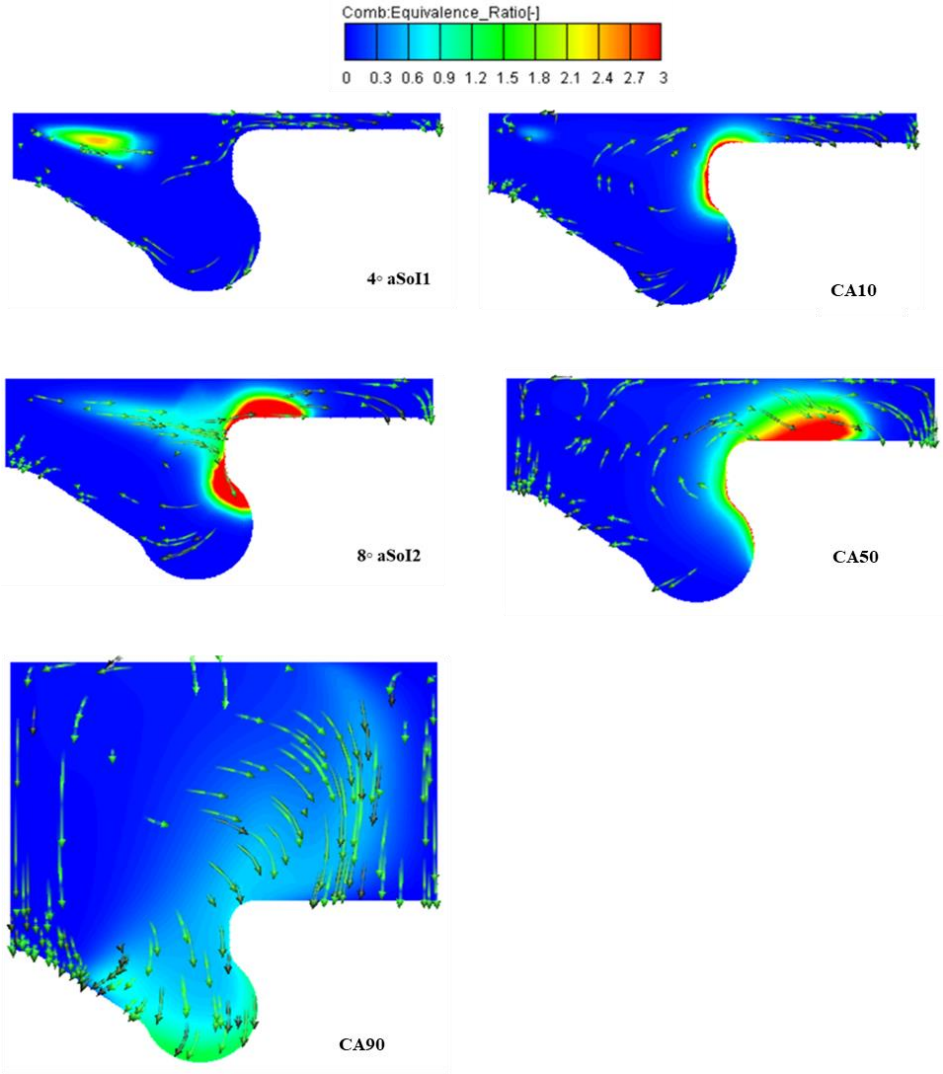

Figure 4-5: Equivalence ratio distribution of ORB2 for the LL-5050-(0,10a)TDC case including CA10, CA50 and CA90

The influence of injection timing retardation on in-cylinder pressure and HRR for all three bowl geometries was also analysed as illustrated in Figure 4-2 and Figure 4-3, respectively. From Figure 4-2, the influence of injection timing retardation was obvious from the peak pressure levels for each bowl geometry. Analysis of the results showed that ORB1 and ORB2 which had similar pressure trends and peak in-cylinder pressures in all the cases decreased by about 7.59% as fuel injection was retarded from LL-5050-(20b,10b)TDC to LL-5050-(15b,5b)TDC and about 10.95% as fuel injection was retarded from LL-5050-(15b,5b)TDC to LL-5050-(10b,0)TDC.

On the other hand, the peak in-cylinder for FRB decreased by about 11.76% and 8% for the retardation cases. Apart from that, peak in-cylinder pressure remained relatively constant at about 32.6bar for all three bowl geometries as injection was retarded from LL-5050-(5b,5a)TDC to LL-5050-(5a,15a)TDC for all three bowl

geometries. ORB1 and ORB2 also exhibited similar pressure trends and peak levels in these cases even after TDC. However, the FRB exhibited a slight deviation compared to ORB1 and ORB2 during the expansion stroke which were attributed to the effect of its geometry.

From Figure 4-5, ORB1 and ORB2 showed more similarities in their overall trends but still with noticeable differences compared to FRB in the HRR results due to the influence of injection retardation. During the first three retardations, ORB1 and ORB2 both resulted in similar gradual rise in HRR levels which remained fairly constant. In fact, an overall view of the HRR results showed that their profiles were relatively similar over the range of injection retardation. However, the FRB exhibited obvious separation between the premixed and combustion phases which grew opposingly as injection was retarded.

More also from Figure 4-5, the magnitude of premixed combustion and diffusion combustion increased and decreased, respectively, for the FRB under injection timing retardation from LL-5050-(5b,5a)TDC to LL-5050-(5a,15a)TDC. This behaviour was less present in the first three cases, compared to the last three cases in which a significant shift from a predominant diffusion phase peak HRR to a predominant premixed phase HRR under retardation was observed for FRB. The behaviour of the FRB in the first three cases was attributed to the interaction between the piston bowl geometry, injection timing and injection ratio with respect to spatial and temporal temperature and pressure distributions in the combustion chamber.

The FRB exhibited relatively low premixed HRR levels in the first three cases because although the first injection event occurred during spatial and temporal conditions such as high oxygen content, other conditions such as low air density and the poor re-entrance curvature hindered the formation of more premixed combustion at higher HRR levels. As the fuel injection retarded, air density increased during the first injection event despite the negative impact of the bowl geometry on air-fuel mixing, therefore, premixed combustion levels increased.

On the other hand, the FRB also exhibited the highest levels of HRR in the diffusion phase in the first three cases because although the second injection event occurred

during spatial and temporal conditions such as higher chamber temperature, pressure and air density to promote faster air-fuel reactions, other conditions such as a depleted oxygen content in the residual air in addition to the delivery of 50% of the total fuel quantity during the second injection event resulted in high diffusion HRR levels. In addition, the fuel injected during the second event was injected into burning region (i.e., combustion due to first injection) which resulted in fuel rich (diffusion) combustion with negligible to no time to form a premixed mixture.

As the fuel injection retarded from LL-5050-(5b,5a)TDC to LL-5050-(5a,15a)TDC, the FRB showed increasingly high premixed combustion HRR over diffusion combustion phase respectively because the second injection event also began to occur in conditions of lower air density and chamber temperatures thereby reducing the rate of diffusion heat release despite the deployment of 50% fuel load during the event. Interestingly, the HRR results of ORB1 and ORB2 did not show such behaviour even remotely. Their behaviour was attributed to the influence of the higher bowl re-entrance curvatures which played a role in controlling the combustion phasing compared to FRB.

Considering the late combustion phase, FRB showed a higher decrease in HRR levels compared to ORB1 and ORB2 which suggested that although it promoted the highest peak HRR levels, ORB1 and ORB2 promoted longer heat release and combustion duration. There seemed to be no correlation between the extent of bowl re-entrance curvature and high peak HRR since the FRB with the smallest degree of re-entrance curvature and ORB2 with the largest degree of re-entrance curvature produced the highest and second highest HRR’s, respectively.

4.2.2 70:30 Injection Ratio

The influence of the FRB, ORB1 and ORB2 geometries on in-cylinder pressure under the 70:30 injection ratio can be seen in Figure 4-6. Although the three bowl geometries exhibited similar in-cylinder pressure profiles in all the cases, the FRB exhibited the highest peak pressures of about 44.5bar, 41.2bar and 36.2bar for LL-7030-(20b,10b)TDC, LL-7030-(15b,5b)TDC and LL-7030-(10b,0)TDC respectively. Peak pressures in LL-7030-(5b,5a)TDC, LL-7030-(0,10a)TDC and LL-7030-(5a,15a)TDC were similar for the three bowl geometries while more obvious deviations were observed in their second peak levels wherein the FRB exhibited the highest local peak pressure levels compared to those of ORB1 and ORB2 that showed close similarity in trend and peak levels.

The influence of the FRB, ORB1 and ORB2 on the HRR results under the 70:30 injection ratio can be seen in Figure 4-7. An overview of the HRR results showed relatively higher HRR levels occurring in the premixed combustion phase compared to the diffusion combustion phase. This was attributed to the effects of injection ratio in which 70% of the total fuel quantity was injected during the first injection event. The deviations exhibited by each bowl geometry in each case was due to their individual influence on the combustion characteristics and phasing. ORB2 exhibited the highest peak HRR in the premixed combustion phase while those of ORB1 and FRB were exhibited in the diffusion combustion phase for cases LL-7030-(20b,10b)TDC and LL-7030-(15b,5b)TDC. This behaviour was attributed to the higher degree of re-entrance curvature of ORB2 which promoted improved air-fuel mixture formations compared to FRB and ORB1 after TDC.

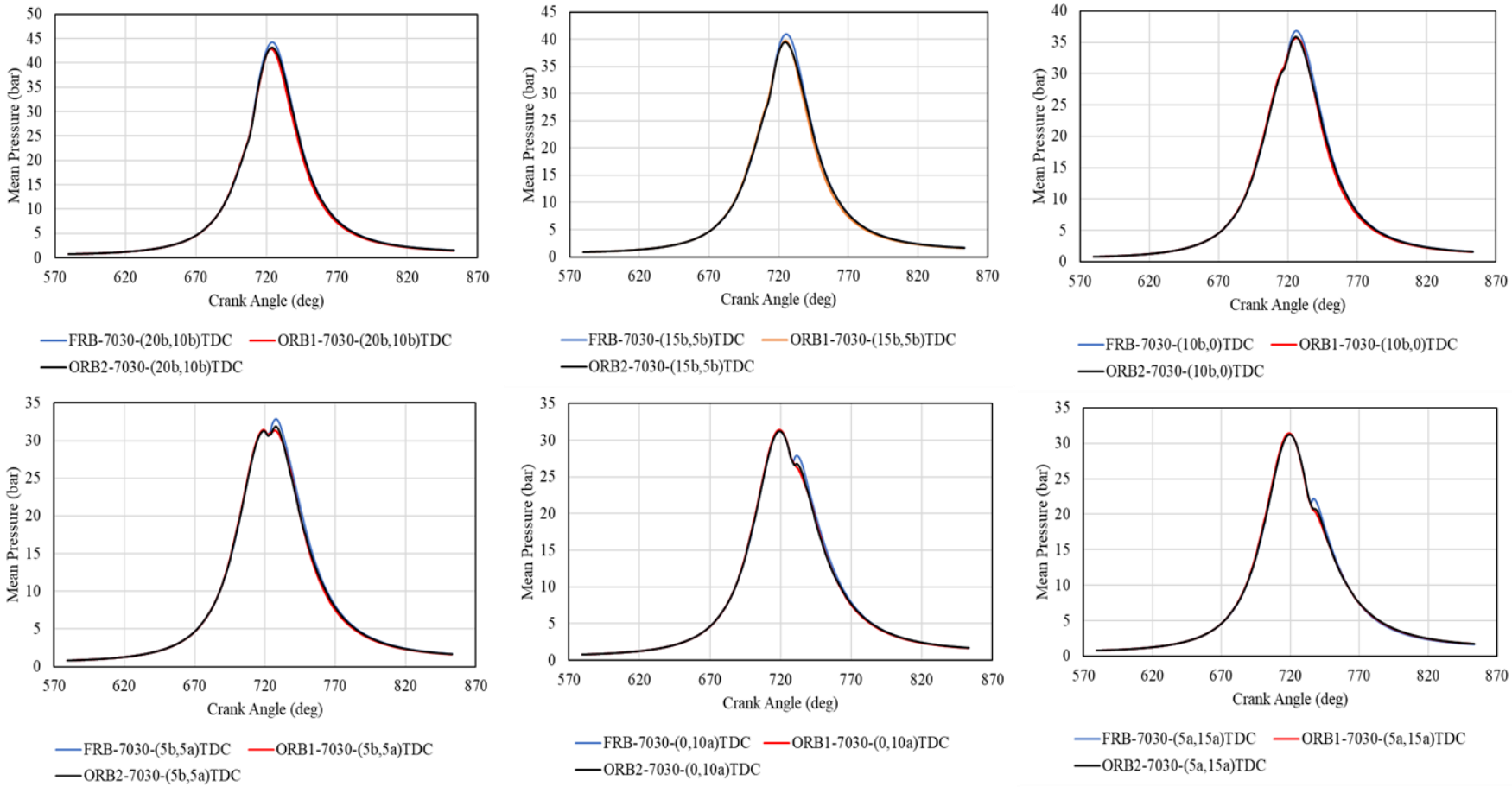

Figure 4-6: In-cylinder pressure data for FRB, ORB1 and ORB2 under 70:30 injection ratio at low load

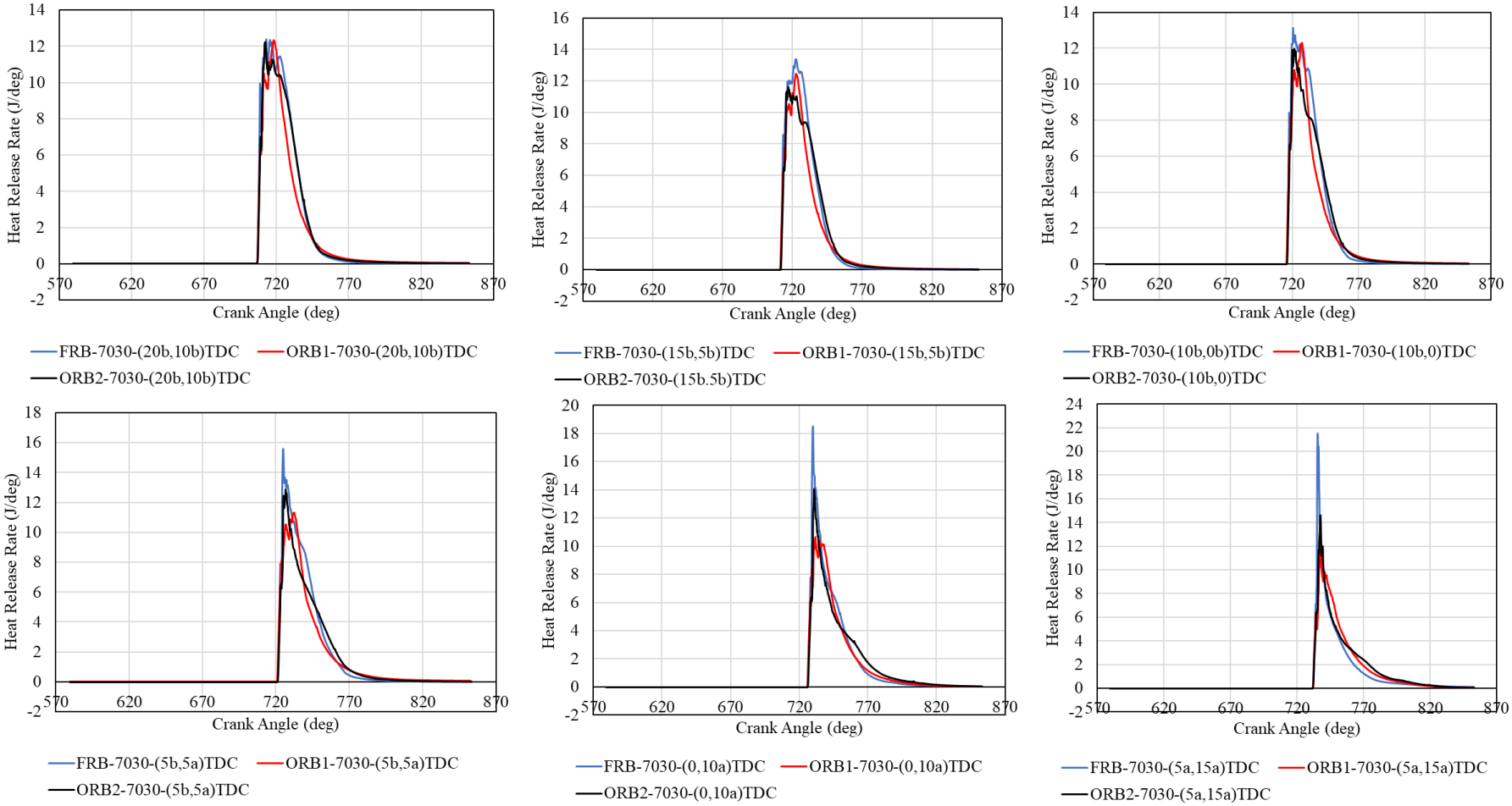

Figure 4-7: In-cylinder HRR profiles for FRB, ORB1 and ORB2 under 70:30 injection ratio at low load

The pressure and HRR behaviour of ORB2 was explored further by analysing its equivalence ratio for the LL-7030-(0,10a)TDC case, presented in Figure 4-8. Besides the influence of the in-cylinder conditions such as turbulent air motion represented by the streamlines and high air density, the injected fuel parcels during and after the first injection event close to the bowl side wall were also influenced by the degree of re-entrance curvature. This caused the spread of the injected fuel towards the squish and bowl base regions at 10% heat release and consequently a large mixing front area for improved air-fuel interaction.

At 50% heat release the bulk of the fuel formation which moved towards the bowl base earlier, had experienced significant interaction with air causing leaner mixture formations. In addition to that, 50% heat release occurred during the expansion stroke wherein turbulent air motion caused more air to move towards the squish region thereby contributing to the oxidation of the fuel mixture in that region. The influence of the conditions stated earlier also contributed to the combustion behaviour at 18 CA after the second injection event which carried 30% of the total fuel load as well as the chamber mixing dynamics at 90% heat release. Therefore, lower levels of diffusion HRRs were present in ORB2 as seen in the HRR results which was evident especially in LL-7030-(10b,0)TDC.

The in-cylinder pressure and HRR results due to injection timing retardation can also be analysed from Figure 4-6 and 4-7, respectively. Form Figure 4-6, the influence of injection retardation was only present at the peak pressure levels of FRB, ORB1 and ORB2. An overview showed that peak in-cylinder pressure decreased under retardation from LL-7030-(20b,10b)TDC to LL-7030-(5b,5a)TDC for all the bowl geometries and remained constant as the injection timing was retarded further from LL-7030-(0,10a)TDC to LL-7030-(5a,15a)TDC.

Considering the profile trends from the geometries, all three geometries exhibited similar pressure trends but with the FRB having slightly higher peak pressure levels compared to ORB1 and ORB2 which had similar peak levels for the first three cases. In LL-7030-(5b,5a)TDC, FRB also exhibited the highest peak pressure level while ORB1 and ORB2 peak pressure levels were all similar after TDC. The pressure profile trend and peak levels for FRB, ORB1 and ORB2 were constant under retardation from LL-7030-(0,10a)TDC to LL-7030-(5a,15a)TDC except for the

deviation observed for the FRB pressure results in both cases which was attributed to the influence of its geometry.

Injection retardation through the last three cases showed behaviours in the HRR results which were different from those of the first three cases for the bowl geometries seen in Figure 4-7. The FRB exhibited the highest peak HRR levels in the premixed phase. In addition, its peak HRR levels were observed to increase significantly with each retardation from LL-7030-(5b,5a)TDC to LL-7030-(5a,15a)TDC. Apart from the contribution of the fuel injection ratio, this behaviour was also attributed to the interaction between its geometry and the spatial and temporal in-cylinder conditions during the injection events as previously discussed for the 50:50 injection ratio scenario.

Interestingly, this behaviour was not observed for the HRR results exhibited by ORB1 and OBR2 both of which seemed to exhibit HRR levels in the premixed and diffusion combustion phases which remained fairly constant as the fuel injection timing was retarded. This suggested that the presence of adequate bowl re-entrance curvature promoted a more stable combustion phasing. Although no correlation between the degree of re-entrance curvature and HRR results was observed, the results showed that ORB2 promoted more HRR levels compared to ORB1.

The behaviour of ORB2 was explored further through its equivalence ratio for the LL-7030-(0,10a)TDC case as depicted in Figure 4-8. The injected fuel parcels during and after the first injection event, closer to the bowl side wall, were influenced by turbulent fluid motion represented by the streamlines and the bowl re-entrance curvature apart from other conditions such as air density. This resulted in the formation of stretched mixing front area that promoted air-fuel interaction and thus improved premixed formation and HRR. Furthermore, these characteristics also influenced the second fuel injection event thus contributing to the presence of relatively low HRR levels in the diffusion phase.

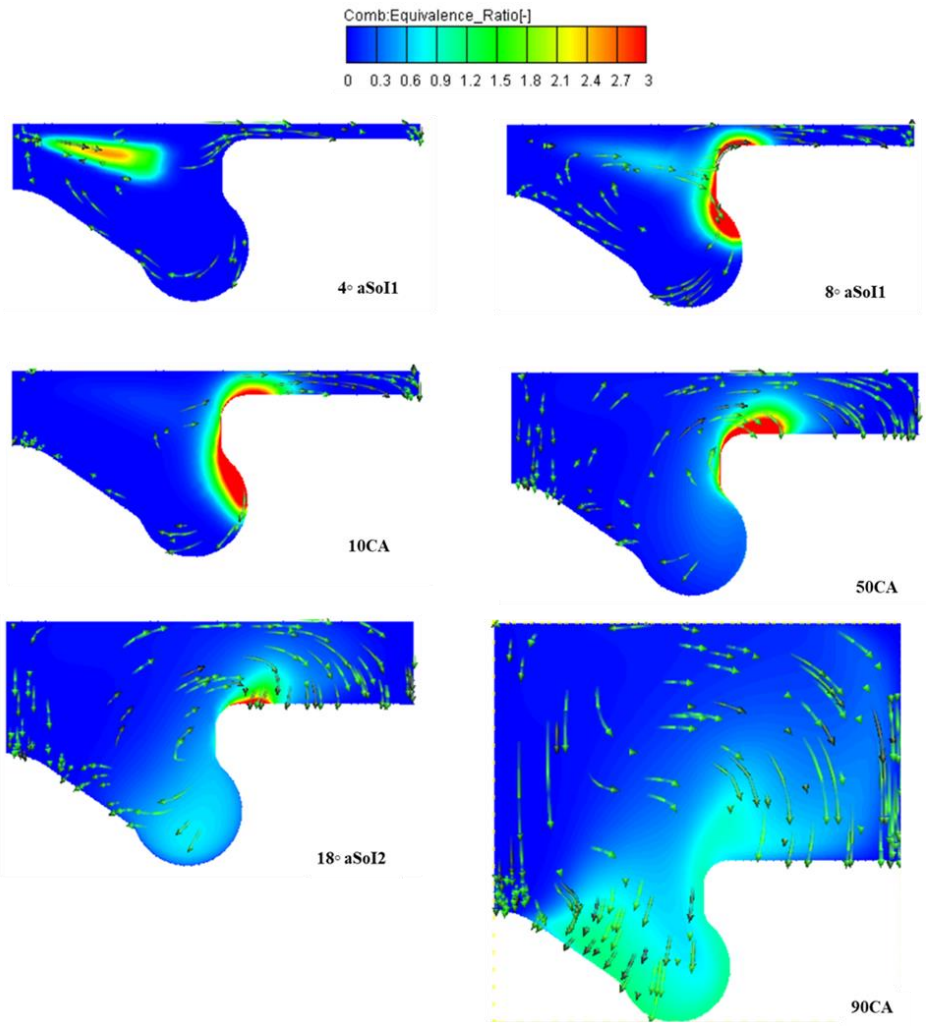

Figure 4-8: Equivalence ratio distribution of ORB2 for the LL-7030-(0,10a)TDC case including CA10, CA50 and CA90

4.2.3 Comparison of 50:50 and 70:30 Injection Ratio Cases

The influence of the FRB, ORB1 and ORB2 under the 50:50 and 70:30 injection ratios were compared to analyse their effect on the combustion process. Under the 50:50 injection ratio, fuel injection was equally split over the two injection events. However, the 70:30 injection ratio involved an unequal split of the injected fuel quantity with 70% of the total quantity injected in the first event and 30% injected in the second event. This difference was observed to affect the combustion characteristics for all three bowl geometries.

The in-cylinder pressure results of the bowl geometries for both injection ratios were compared. In the first four cases, all three bowl geometries exhibited higher peak pressure levels for the 70:30 injection ratio compared to the 50:50 injection ratio. This

was because more fuel was injected during the first injection event for the 70:30 injection ratio compared to the injected fuel quantity during the first injection event for the 50:50 injection ratio which resulted in enhanced air-fuel interaction and higher HRR's which promoted pressure rise. All three bowl geometries exhibited the same peak pressure levels in the last two cases under both injection ratios due to late combustion occurring after TDC. Nevertheless, the influence of the higher fuel quantity of the first injection event for the 70:30 injection ratio was still observed in the form of higher-pressure levels during the expansion stroke after TDC compared to the results for the 50:50 injection ratio.

An analysis of the individual bowl geometries showed that the FRB exhibited the highest peak pressure levels in the first four cases for both injection ratios. Interestingly, a significant deviation in the peak pressure levels of the FRB and those of ORB1 and ORB2 in the first three cases was present for the 50:50 injection ratio whereas this deviation was smaller for the 70:30 injection ratio in which the peak pressure levels of the three bowl geometries were closer. This suggested that the FRB promoted higher in-cylinder pressures in the first four cases and thus, improved pressure dependent performance compared to ORB1 and ORB2.

The HRR results of the three bowl geometries for both injection ratios were also compared. In the first three cases, the FRB exhibited higher peak HRR levels for the 50:50 injection ratio compared to the 70:30 injection ratio. Moreover, its peak HRR levels were present in the diffusion phase for the 50:50 injection ratio and were observed in the premixed phase for the 70:30 injection ratio. The behaviour observed for the 70:30 injection ratio was attributed to enhanced air-fuel interaction due to the availability of more fuel in the first injection event under the same spatial and temporal in-cylinder conditions.

The close HRR results of ORB1 and ORB2 seen for the 50:50 injection ratio was also observed for the 70:30 injection ratio. While a larger deviation between the peak HRR levels of the FRB and those of ORB1 and ORB2 was observed for the 50:50 injection ratio, the peak HRR levels of all three bowl geometries were much closer under the 70:30 injection ratio. This suggested that heat release rate and combustion phasing

was more sensitive to the FRB geometry than the geometry of ORB1 and ORB2 due to the influence of its geometry as previously discussed .

In the last three cases, the sensitivity of HRR to the FRB geometry due to the influence of the injection ratio was more obvious. The presence of more fuel quantity in the first injection event for the 70:30 injection ratio seemed to exacerbate the growth of the HRR peak levels in the premixed phase which was already improved due to the effects of the spatial and temporal in-cylinder conditions as the fuel injection timing was retarded compared to the behaviour observed under the 50:50 injection ratio. FRB seemed to contribute significantly to the observed trend in contrast to ORB1 and ORB2. This suggested that HRR and combustion phasing was less sensitive to ORB1 and ORB2 despite the injection ratio and thus they could provide better control over combustion. This notion was further strengthened from the comparism of the geometries under both injection ratios during injection timing retardation.

4.3 Performance Analysis at Low Load

In-cylinder engine performance analysis was done considering IMEP, ISFC and combustion noise. While many investigations have considered the first two parameters, few studies have included the last of these parameters in the focus of consideration despite its link to in-cylinder combustion behaviour Costa et al., [125]. According to the work by Torregrosta et al., [153] combustion noise is attributed to the in-cylinder excitation during combustion. Here, the features which influence combustion such as the piston bowl and chamber wave reflection as well as HRR affect pressure fluctuations which in turn contribute to the generation of combustion noise especially at auto-ignition time. Since pressure and HRR rise also contribute to the in-cylinder pressure trend behaviour and consequently IMEP, the relationship between combustion noise and IMEP if any was also explored in this work.

4.3.1 50:50 Injection Ratio

Table 4-3 presents the IMEP, ISFC, and combustion noise performance results of FRB, ORB1 and ORB2 at low load for the 50:50 injection ratio based on the injection

timings investigated. The relationship between the IMEP-ISFC results for the three bowl geometries was further analysed as shown in Figure 4-9.

From Figure 4-9, results showed that an increase in IMEP correlated with a decrease in ISFC for each bowl geometry. The influence of injection timing retardation from LL-5050-(20b,10b)TDC to LL-5050-(5a,15a)TDC resulted in the decrease and increase of IMEP and ISFC levels, respectively.

The FRB exhibited the highest IMEP levels in all the cases except for LL-5050-(0,10a)TDC and LL-5050-(5a,15a)TDC cases in which ORB2 exhibited the highest IMEP levels. The IMEP levels exhibited by ORB1 and ORB2 were similar and largely lower than those of the FRB as the injection timing was retarded from LL-5050-(20b,10b)TDC to LL-5050-(5b,5a)TDC. Nevertheless, the IMEP levels for all three bowl geometries were similar in the last two cases. This indicated that the FRB promoted significantly higher IMEP levels and consequently lower ISFC levels compared to ORB1 and ORB2 under earlier injection timings but exhibited similar IMEP and ISFC performance levels to ORB1 and ORB2 under later injection timings. Here, the FRB exhibited IMEP levels of about 25% and 20.7% higher than that of ORB1 and ORB2, respectively, for LL-5050-(20b,10b)TDC (i.e., the case with the earliest injection timing) as opposed to exhibiting a loss of about 2.2% and 2%, respectively, for ORB2 as the injection timing was retarded from LL-5050-(20b,10b)TDC to LL-5050-(5b,5a)TDC.

Figure 4-9 showed that the FRB yielded the highest IMEP levels for about 66% of injection timings considered and similar IMEP levels to ORB1 and ORB2 only in the last two injection timings. Although this was attributed to its very high HRR levels caused mostly most fuel rich combustion, the overall IMEP trend for the FRB seemed to have a steeper negative gradient trend as injection timing was retarded compared to ORB1 and ORB2. This suggested that ORB1 and ORB2 could yield relatively high IMEP levels over the same retardation range compared to FRB.

This IMEP behaviour observed for ORB1 and especially ORB2 was attributed to the combustion behaviour formed due to the interaction between their respective bowl re-

entrance curvatures and the fuel injection retardation encompassed in the mixing front.

As previously depicted in the equivalence ratio results, the high degree of re-entrance curvature of ORB1 and especially ORB2 gave rise to a large mixing front which grew with time, improved air-fuel mixing and promoted a gradual transition from premixed combustion to diffusion combustion. This gradual transition could also contribute to sustaining pressure build ups and thus, high IMEPs especially at retarded injection timings which was not observed for FRB wherein the switch from predominantly premixed combustion to predominantly diffusion combustion due to its lack of a large mixing front seemed to limit its IMEP levels more under retardation.

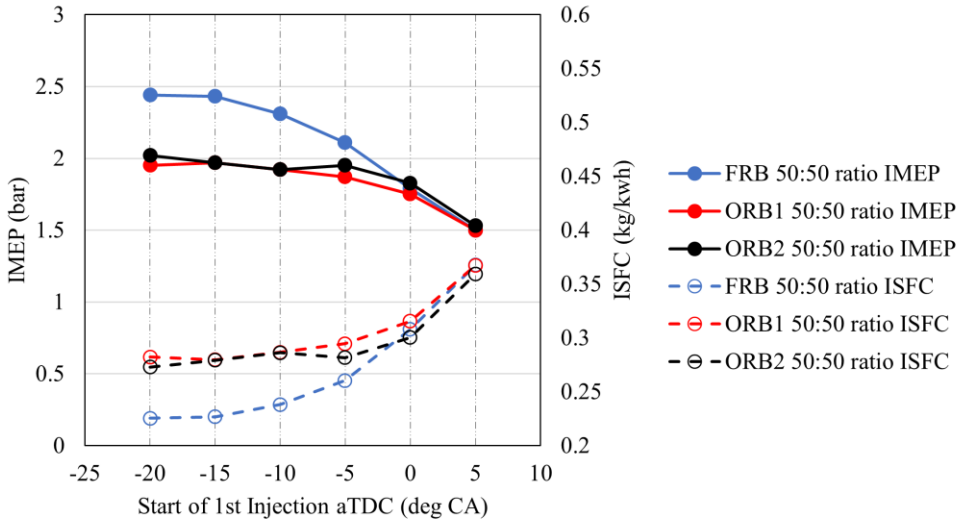

Figure 4-9: IMEP vs ISFC for FRB, ORB1 and ORB2 under 50:50 injection ratio at low load

ORB2 exhibited higher IMEP levels compared to ORB1 by about 3.5%, 4.2%, 4.5% and 2% for LL-5050-(20b,10b)TDC, LL-5050-(5b,5a)TDC, LL-5050-(0,10a)TDC and LL-5050-(5a,15a)TDC, respectively, while both geometries had equal IMEP levels for LL-5050-(15b,5b)TDC and LL-5050-(10b,0)TDC cases. Again, as observed in the HRR results, FRB with the smallest degree of re-entrance curvature and ORB2 with the highest degree of re-entrance curvature resulted in the highest and second highest IMEP levels, respectively. This suggested that both degrees of re-entrance could promote high IMEP levels. It also implied that an increase in bowl re-entrance curvature caused lower IMEP levels due to a more gradual HRR due to improved air-fuel mixing.

The relationship between the IMEP and combustion noise was analysed and presented in Figure 4-10. The results showed that a decrease in IMEP correlated with a decrease in combustion noise for each bowl geometry under injection retardation from LL-5050-(20b,10b)TDC to LL-5050-(5a,15a)TDC. The reduction of combustion noise levels observed during injection retardation as well as between the different piston bowl geometries was negligible and was only exaggerated to show the influence of injection timing and piston bowl geometry on the parameter.

Under retardation, fuel injection occurred either closer to TDC during the compression stroke or after and further away from TDC during the expansion stroke. The former instance caused shorter air-fuel mixing time which resulted to slower pressure rise and thus lower IMEP levels. This also contributed to smaller wave generation and reflection throughout the chamber and thus, lower combustion noise. In addition, wave propagation was further hindered by higher fluid density closer to TDC during compression. In the latter instance, pressure rise due to combustion was hindered by the volume expansion of the chamber which resulted in lower IMEP levels. Furthermore, in-cylinder wave reflection was hindered due to the wave propagation over a larger chamber volume and the piston bowl geometry surface which ,oved further away from TDC during the expansion stroke. Thus, combustion noise reduced.

ORB1 and ORB2 exhibited similar combustion noise levels which were lower than those of the FRB for all the injection timings. The FRB exhibited higher combustion noise levels in LL-5050-(0,10a) TDC and LL-5050-(5a,15a)TDC compared to ORB1 and ORB2 despite having a higher and lower IMEP level compared to ORB1 and ORB2 in the former case and having the same and lower IMEP level compared to ORB1 and ORB2 in the latter case. This highlighted the influence of piston bowl geometry on combustion noise. This suggested noise wave propagation could be influenced by bowl geometry wherein flatter bowl surfaces such as the FRB promoted more wave reflection whereas surfaces of ORB1 and ORB2 promoted the dilution of wave throughout the chamber.

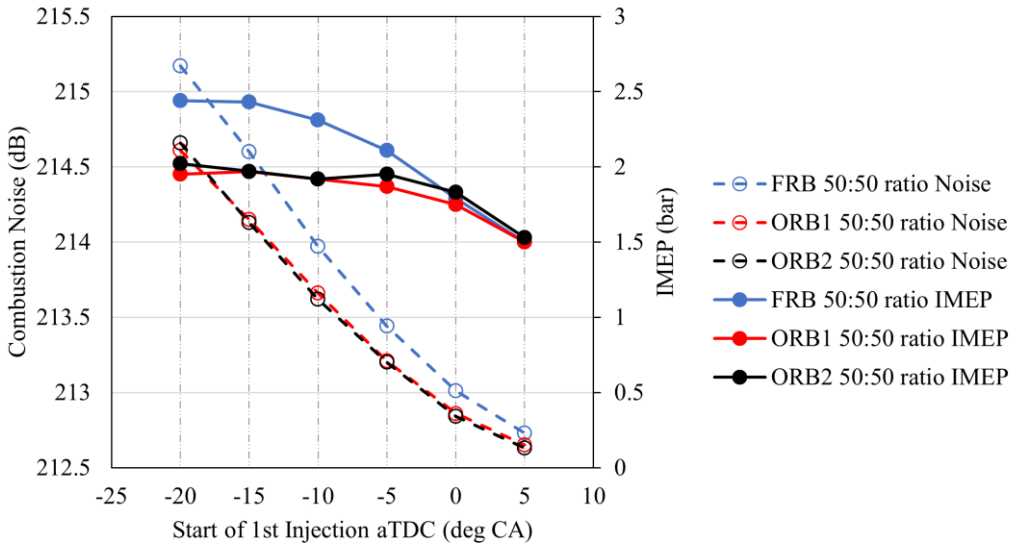

Figure 4-10: Combustion noise vs IMEP for FRB, ORB1 and ORB2 under 50:50 injection ratio at low load

4.3.2 70:30 Injection Ratio

The influence of the FRB, ORB1 and ORB2 on IMEP, ISFC and combustion noise under the 70:30 injection ratio at low load can be seen in Table 4-3. An increase in IMEP correlated with a decrease in ISFC as seen in the table. This behaviour was also exhibited under the influence of injection timing retardation as seen in Figure 4-11. It can be seen from the results that IMEP and ISFC exhibited decreasing and increasing trends, respectively, as the injection timing was retarded from LL-5050-(20b,10b)TDC to LL-5050-(5a,15a)TDC for all three bowl geometries.

The three bowl geometries showed larger deviations in IMEP levels at earlier injection timings and similar IMEP levels at later injection timings . Although negligible, the IMEP levels for ORB2 seemed to be closer to those of the FRB than those of the ORB1 which was different from the trend observed under the 50:50 injection ratio. The results showed that the FRB consistently had higher IMEP levels compared to ORB1 and ORB2 with the exception of LL-7030-(5a,15a)TDC wherein ORB2 had a negligibly higher IMEP level compared to FRB.

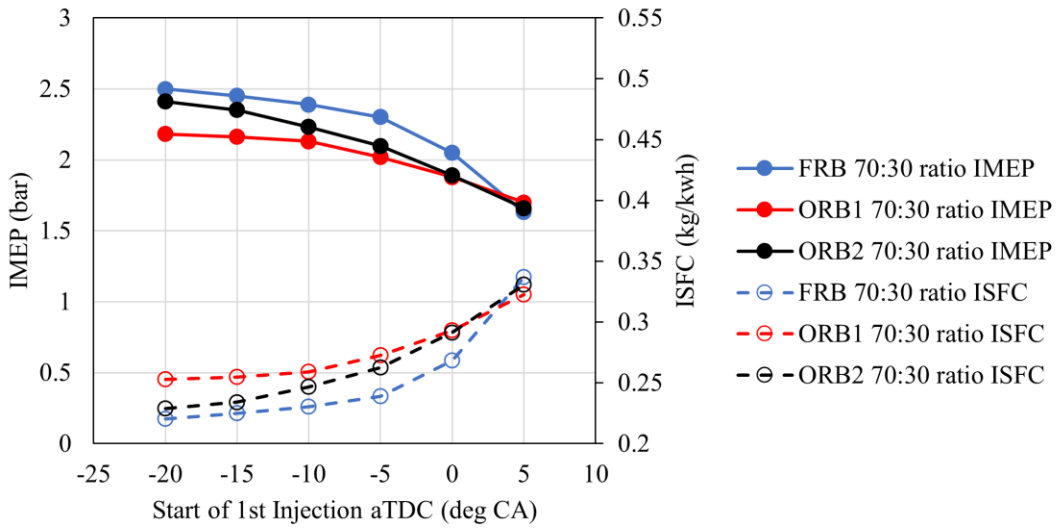

Figure 4-11: IMEP vs ISFC for FRB, ORB1 and ORB2 under 50:50 injection ratio at low load

The FRB exhibited the highest IMEP levels throughout the cases while ORB2 exhibited higher IMEP levels compared to ORB1 in all the cases except for LL-7030-(5a,15a)TDC. This suggested that both the FRB and ORB2, two bowl geometries with very different degrees of re-entrance curvature, promoted high IMEP levels. Although increased bowl re-entrance curvature exhibited by the ORB2 could also contribute to improved IMEP and ISFC, such improvements were either similar or lower compared to the FRB. Again, this behaviour could be attributed to the more gradual HRR exhibited by the ORB2 cases due to improved air-fuel mixing generated by its bowl re-entrance curvature.

Figure 4-12 shows the IMEP-Noise relationship as a function of injection timing. Here, both IMEP and combustion noise levels for the three bowl geometries were seen to reduce as the injection timing is retarded. This behaviour was attributed to the same phenomena also seen for the 50:50 injection ratio wherein shorter air-fuel mixing time associated with later fuel injection timing caused a lower pressure rise as more combustion occurred towards the end of the compression stroke and into the expansion stroke. Lower IMEP levels corresponded with lower peak in-cylinder pressures in this regards as seen in the in-cylinder pressure results. Furthermore, the reduction in combustion noise was also associated with the pressure rise due to the reduced pressure fluctuations.

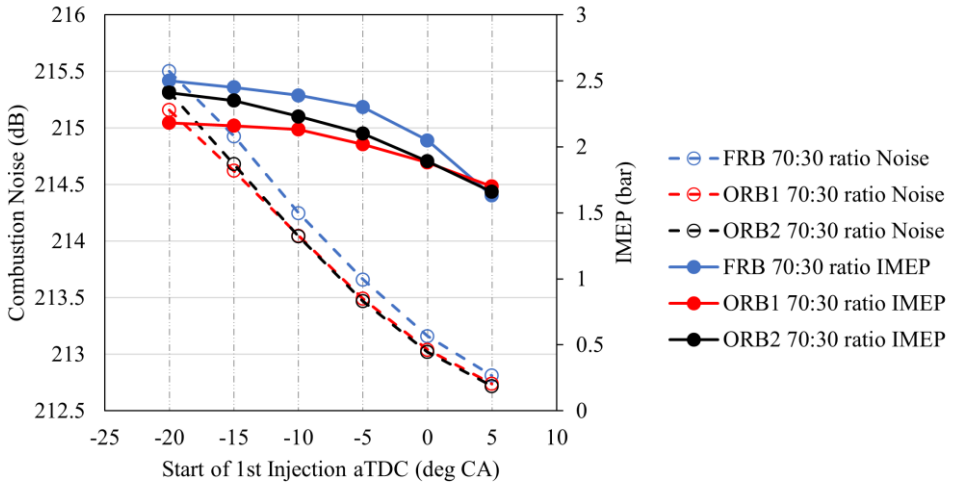

Figure 4-12: Combustion noise vs IMEP for FRB, ORB1 and ORB2 under 50:50 injection ratio at low load

4.3.3 Comparison of 50:50 and 70:30 Injection Ratios Cases

The IMEP, ISFC and combustion noise results for the FRB, ORB1 and ORB2 under 50:50 and 70:30 injection ratios were compared through a cross analysis of their respective results presented in Table 4-3. The comparison showed that the cases under the 70:30 injection ratio exhibited higher IMEP and combustion noise and lower ISFC compared to the respective cases under the 50:50 injection ratio. This behaviour was attributed to the injection of 70% of the total fuel quantity during the first injection under the 70:30 ratio which caused higher HRR levels especially in the premixed combustion phase compared to the 50:50 injection strategy. Here, the production of higher HRR levels over slightly longer durations under the 70:30 ratio promoted higher combustion temperatures and in-cylinder pressures, consequently leading to higher IMEP levels.

The IMEP results of the FRB under the 50:50 and 70:30 ratios suggested that it promoted higher IMEP levels compared to ORB1 and ORB2. However, this was at the expense of slightly increased combustion noise. The IMEP results of ORB2 under the 50:50 and 70:30 ratios suggested that it promoted lower combustion noise and relatively high IMEP levels. In fact, a comparison of the performance of the three bowl geometries under both injection ratios showed that ORB2 exhibited IMEP levels closer to those of the FRB with lower combustion noise similar to those of ORB1.

Table 4-3: Performance results for FRB, ORB1 and ORB2 at low load

Case ID	FRB			ORB1			ORB2		
	IMEP (bar)	ISFC (kg/kwh)	Combustion Noise (dB)	IMEP (bar)	ISFC (kg/kwh)	Combustion Noise (dB)	IMEP (bar)	ISFC (kg/kwh)	Combustion Noise (dB)
LL-5050-(20b,10b)TDC	2.44	0.2256	215.17	1.95	0.2824	214.61	2.02	0.2729	214.66
LL-5050-(15b,5b)TDC	2.43	0.2266	214.6	1.97	0.2795	214.15	1.97	0.2790	214.13
LL-5050-(10b,0)TDC	2.31	0.2383	213.97	1.92	0.2867	213.66	1.92	0.2865	213.62
LL-5050-(5b, 5a)TDC	2.11	0.2605	213.44	1.87	0.2945	213.21	1.95	0.2817	213.20
LL-5050-(0, 10a)TDC	1.79	0.3079	213.01	1.75	0.3152	212.86	1.83	0.3002	212.84
LL-5050-(5a,15a)TDC	1.5	0.3673	212.73	1.5	0.367	212.65	1.53	0.3591	212.63
LL-7030-(20b,10b)TDC	2.5	0.2204	215.5	2.18	0.2527	215.16	2.41	0.2286	215.32
LL-7030-(15b,5b)TDC	2.45	0.2248	214.93	2.16	0.2546	214.62	2.35	0.2340	214.68
LL-7030-(10b,0)TDC	2.39	0.2302	214.25	2.13	0.2588	214.05	2.23	0.2465	214.04
LL-7030-(5b,5a)TDC	2.3	0.2387	213.66	2.02	0.2726	213.49	2.10	0.2623	213.47
LL-7030-(0,10a)TDC	2.05	0.2683	213.16	1.88	0.293	213.04	1.89	0.2916	213.02
LL-7030-(5a,15a)TDC	1.63	0.3369	212.81	1.7	0.3226	212.74	1.66	0.3307	212.72

4.4 Emissions Analysis at Low Load

The in-cylinder NOx and Soot emissions for all the injection strategies considered at the 50:50 and 70:30 injection ratios for the FRB, ORB1 and ORB2 geometries at low load were analysed. The effects from air-fuel mixing as well as the formed mixing fronts due to the interaction between influence the respective re-entrance curvatures and the injection strategies on the emission outputs and trends at constant and retarding injection timings are studied.

4.4.1 50:50 Injection Ratio

Table 4-4 presents the NOx and soot emissions of the piston bowl geometries for the 50:50 injection ratio.

An overview of the table results showed that the NOx and soot emissions were attributed to two interactions, the interaction between the bowl geometries and injection ratio at constant injection timing as well as the interaction between the bowl geometries and injection ratio at injection timing retardation.

Table 4-4: 50:50 injection ratio emissions results for FRB, ORB1 and ORB2 at low load

Case ID	**FRB**		**ORB1**		**ORB2**	
	NOx (ppm)	**Soot (ppm)**	**NOx (ppm)**	**Soot (ppm)**	**NOx (ppm)**	**Soot (ppm)**
LL-5050-(20b,10b)TDC	369.86	4.27	36.43	8.14	57.94	4.42
LL-5050-(15b,5b)TDC	234.6	4.04	25.80	9.08	35.8	5.08
LL-5050-(10b,0)TDC	158.38	8.96	15.94	9.05	25.73	6.12
LL-5050-(5b, 5a)TDC	111.32	21.27	9.73	8.45	24.56	9.28
LL-5050-(0, 10a)TDC	39.24	29.8	6.95	7.81	13.54	9.07
LL-5050-(5a,15a)TDC	7.114	23.8	3.54	6.89	7.93	1.28

In regard to the interaction between the bowl geometries and injection ratio at constant injection timing, the results showed that the FRB and ORB1 exhibited the highest and lowest NOx emissions respectively whereas the highest and lowest soot emissions were exhibited by the FRB and ORB2 respectively at each injection timing strategy except LL-5050-(5a,15a)TDC.

Considering the NOx emissions, Figure 4-13 presents the chamber temperature distribution and NOx formation of the FRB to illustrate the effect of this interaction. The results showed that the circulation and distribution of the mixtures were restricted to the top of the chamber and bowl side wall with no movement towards air rich regions at the centre of the chamber. This effect was attributed to the lack of a bowl re-entrance curvature could promote improved mixture distribution. The results also show that in-cylinder turbulence causes air movement towards the top region of the chamber which further isolated fuel rich mixtures to regions with depleting rich air mixtures. The resulting consequence was the formation of temperature hotspots as seen in the temperature results which exhibited a correlation with the regions of high NOx formations as seen in the NOx results.

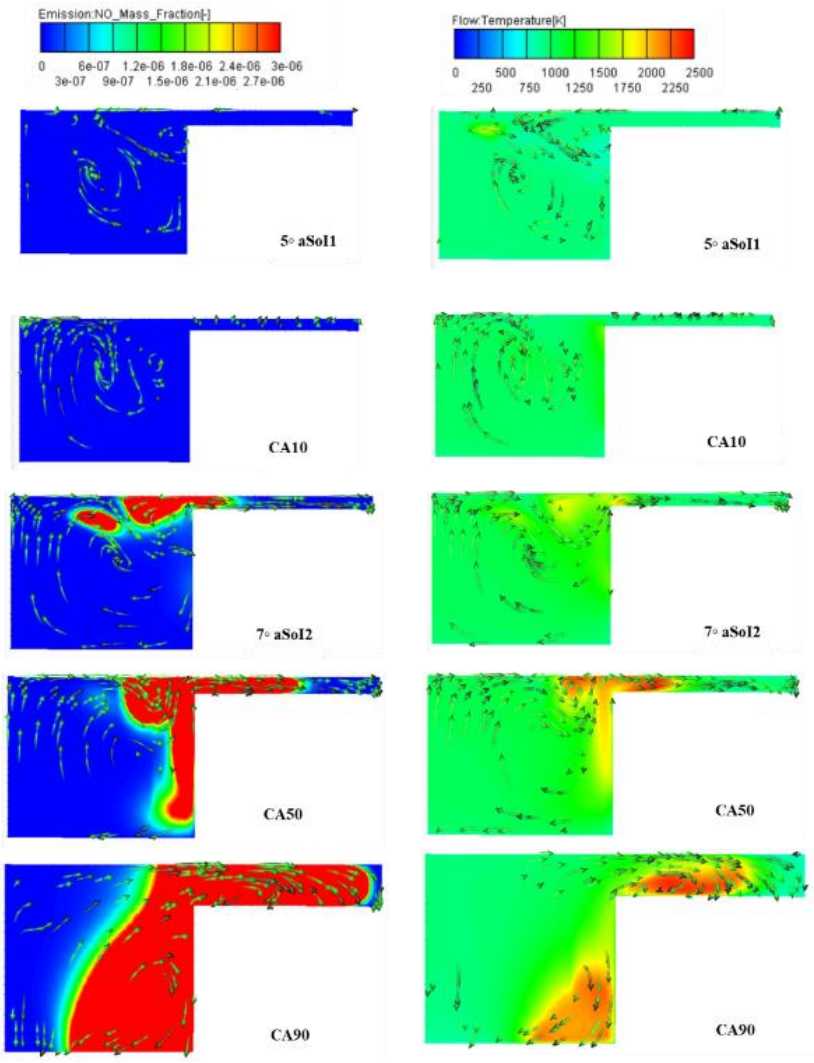

Figure 4-13: NOx and in-cylinder temperature distribution of FRB for the LL-5050-(15b,5b)TDC case including CA10, CA50 and CA90

Considering the soot emissions, Figure 4-14 presents the chamber soot formation of the FRB due to this interaction. The soot behaviour is analysed using the LL-5050-(15b,5b)TDC case and showed that the restriction of fuel rich mixtures previously observed as consequently promoting NOx formation were also observed to occur and promote soot formation. Here, the presence of fuel rich mixtures led to high diffusion HRR's and combustion which promoted soot formation. This behaviour was also attributed to the injection ratio in which 50% of the total fuel load was injected in the second injection event, introducing a relatively large quantity of fuel into a fuel rich diffusion combustion of the first injection event.

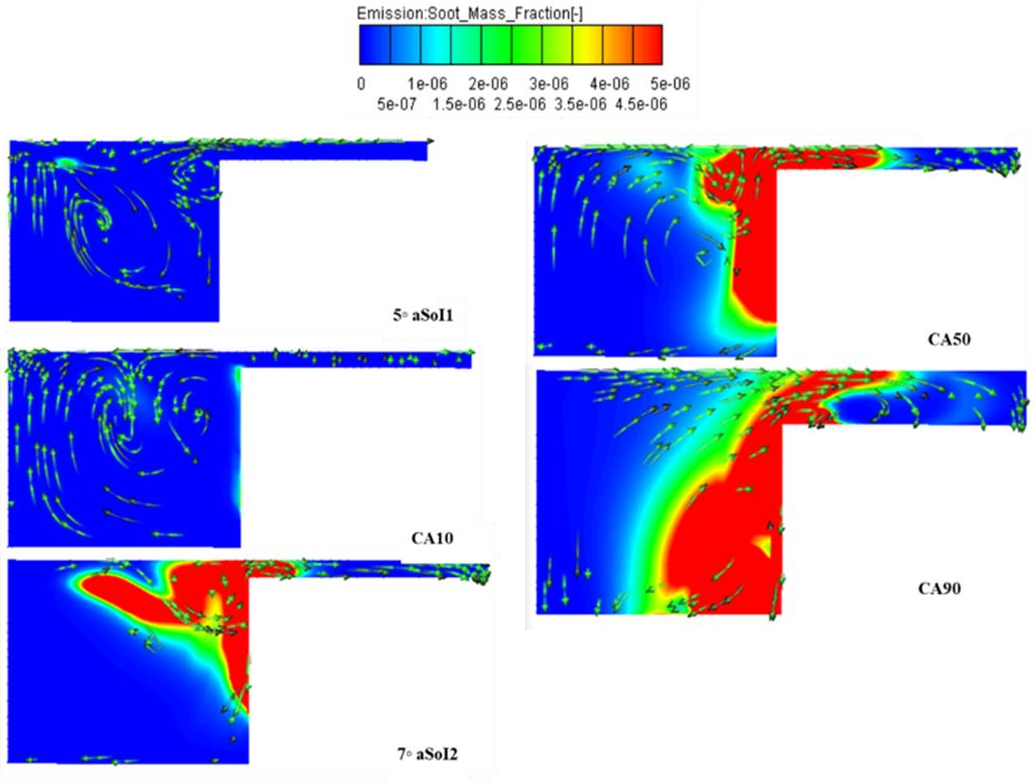

Figure 4-14: Soot distribution of FRB for the LL-5050-(15b,5b)TDC case including CA10, CA50 and CA90

The NOx and soot emission behaviour of the FRB also suggested that the interaction between the injection ratio and ORB1 and ORB2 re-entrance curvatures also resulted in their significantly lower NOx and soot emissions which were more pronounced in comparism to the FRB.

Considering ORB1 and ORB2 NOx emissions, ORB1 exhibited lower NOx emission in all the cases compared to ORB2. This behaviour was attributed to the effect of their respective re-entrance curvatures and mixing fronts which affected the movement and

distribution of air-fuel mixtures and formations which in turn influenced the generation of premixed mixtures, and high temperature hotpots all of which affected NOx formation. The higher NOx emissions exhibited by ORB2 were attributed to the generation of high combustion temperatures in the presence of high oxygen content from high levels of HRR's caused by more premixed combustion as its re-entrance bowl curvature promoted more air-fuel mixing.

Considering ORB1 and ORB2 soot emissions, ORB1 also exhibited higher soot emission in all the cases compared to ORB2 except for LL-5050-(0a,10a)TDC. This behaviour was also attributed to the effect of their respective re-entrance curvatures and mixing fronts which affected the movement and distribution of air-fuel mixtures and formations which in turn influenced the generation of fuel rich diffusion mixtures as well as high combustion temperature regions which affected soot oxidation and formation. The lower soot emissions exhibited by ORB2 for majority of the cases was attributed to its improved utilisation of the available oxygen in the chamber as a result of its higher bowl re-entrance curvature which led to improved air-fuel mixing thus, causing less fuel rich diffusion mixing and combustion.

The interaction between the bowl geometries and injection ratio at injection timings retardation can be seen in Figure 4-15.
The NOx trends in the figure showed that NOx emission reduced as the injection timings retarded from LL-5050-(20b,10b)TDC to LL-5050-(5a,15a)TDC for all three bowl geometries. The FRB exhibiting the highest NOx levels during injection timing retardation, whereas ORB1 and ORB2 were closer and significantly lower with the NOx levels for ORB1 lower than those of ORB2 over the injection retardation range. This behaviour was attributed to the reducing time for air-fuel mixing as well as faster fuel evaporation as a result of higher residence in-cylinder temperatures and pressures as injection occurred closer to TDC. This resulted in shorter ignition delays, reduced premixed mixture formations and combustion as well as HRR's all of which suited the reduction of NOx formations. In addition, NOx emission reduced for injection timings further into the expansion stroke due to an increasing chamber volume which contributed to lower in-cylinder temperature.

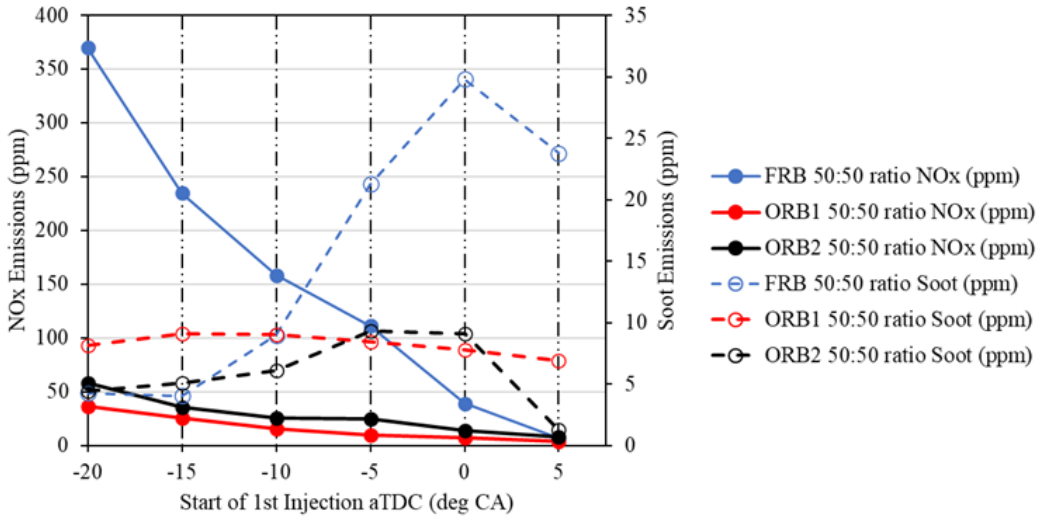

Figure 4-15: NOx vs soot emissions for FRB, ORB1 and ORB2 under 50:50 injection ratio at low load

The soot trends in the figure showed that soot emissions for FRB increased as injection timing was retarded from LL-5050-(20b,10b)TDC to the LL-5050-(0, 10a)TDC after which further injection retardation led to lower soot levels. The soot levels for ORB2 increased as injection timing was retarded from LL-5050-(20b,10b)TDC to the LL-5050-(5b,5a)TDC and remained similar at LL-5050-(0, 10a)TDC after which is reduced with further retardation. ORB1 exhibited relatively similar soot levels. This behaviour was attributed to the reducing time for air-fuel mixing which resulted in increased fuel rich diffusion combustion especially for injection timing retardations up to LL-5050-(0, 10a)TDC. The behaviour seen in the last injection retardation was attributed to the break-up of large fuel rich mixtures by turbulence in an increasing chamber volume and reducing temperature which reduced diffusion mixing and allowing more fuel oxidation which resulted in lower soot formation.

Besides the general trends observed for NOx and soot emissions due to injection timing retardation, the results in the figure also showed that the bowl geometries each exhibited different emissions trends of varying levels .

Considering the NOx emissions to this regard, Figure 4-15 showed that besides the FRB exhibiting the highest NOx levels, it also exhibited the most obvious NOx reduction of the three bowl geometries with a drop in NOx levels of over 300ppm over the range. Its observed NOx reduction behaviour was attributed to an

improvement in its chamber mixture distribution as its mixing front grew under injection retardation.

Here, injection retardation caused fuel injection at moments when the chamber volume was smaller due to piston compression. This increased the potential of the poor mixing front to promote more air-fuel mixing especially at rich air regions and rich fuel regions at the bowl base and thus increased the chamber temperature distribution and reduced temperature hotspots which suited lower NOx formation.

Figure 4-15 showed that ORB1 and ORB2 exhibited significantly lower NOx levels compared to the FRB as injection timing was retarded from LL-5050-(20b,10b)TDC to LL-5050-(0,10a)TDC mainly due to the additional influence of bowl re-entrance curvature while similar NOx levels were observed for all three bowl geometries at LL-5050-(5a,15a)TDC case mainly due to the influence of injection timings with negligible contributions from the bowl geometries. This showed that the influence of entrance curvature was stronger at earlier injection timings and had greater influence over mixing formations and thus, combustion compared to injection timing which was the opposite effect and influence at latter injection timings.

ORB1 had lower NOx levels compared to ORB2 which showed that whilst a high degree of re-entrance curvature promoted lower NOx formation, the effect of increasing the degree of re-entrance in reducing NOx was limited to an extent. Here, the higher NOx levels of ORB2 were attributed to improved air-fuel mixing from its larger mixing front along bowl side and base walls as well as during and just after the first injection event as well as higher HRR’s and combustion temperatures caused by more diffusion mixing and combustion when the second injection event occurred in the fuel rich mixtures of the first injection event closer to the bowl side wall. Figure 5-16 shows the equivalence ratio of ORB1 and ORB2 which illustrates this behaviour in ORB2 and its absence in ORB1.

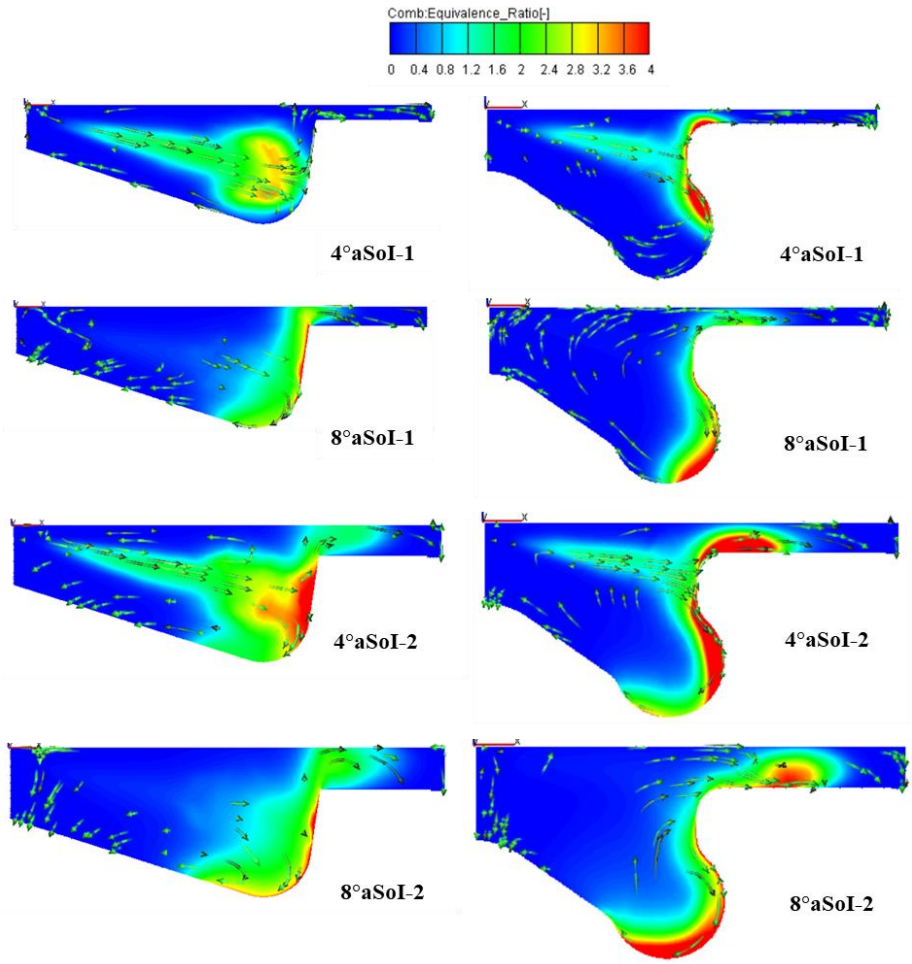

Figure 4-16: Equivalence ratio distribution for ORB1 and ORB2 at LL-5050-(5b,5a)TDC

Considering the soot emissions due to these interactions, Figure 4-15 showed that the soot levels for FRB and ORB2 were closer and significantly lower than that of ORB1 by about 84% at LL-5050-(20b,10b)TDC. Retardation of the injection timing to LL-5050-(15b,5b)TDC caused a decrease in the FRB soot level by about 5%, as well as an increase in the ORB1 and ORB2 soot levels by about 11.5% and 14.9% respectively. FRB soot levels were observed to significantly increase as the injection timing was retarded from LL-5050-(10b,0)TDC to LL-5050-(0,10a)TDC which was different for ORB1 and ORB2 wherein the former exhibited relatively similar soot levels and the latter exhibited higher soot level at LL-5050-(5b,5a)TDC but remained relatively similar at LL-5050-(0,10a)TDC. All three bowl geometries were observed to exhibit reduced soot levels at the last injection retardation compared to the immediate previous injection timing.

The poor re-entrance curvature of FRB hindered air-fuel mixing and limited fuel oxidation within the chamber. At earlier injection timings this effect and soot emission consequence was limited due to the availability of more time for improved air-fuel mixtures to be formed in an increasing chamber density due to compression of the chamber. However, as injection timing retarded, limited air-fuel mixing as well as the injection of a relatively larger fuel quantity in the second injection event promoted more diffusion fuel rich mixing and combustion which in turn increased soot formation with negligible influence from the poor mixing front formed. Nevertheless, injection retardation predominantly in the expansion stroke also caused an improvement of air-fuel mixing due to in-cylinder turbulence which as seen in the equivalence ratio results causes an increase in the mixing front.

The improved re-entrance curvatures of ORB1 and ORB2 increased air-fuel interaction compared to the FRB which resulted in their lower soot levels under injection timing retardation. ORB2 exhibited the lowest soot levels for 4 out of the 6 injection retardation timings considered which showed the effect of its re-entrance curvature and resultant mixing front. A high degree of re-entrance curvature permitted more movement of fuel mixtures towards air rich regions in the chamber which in turn promoted an improved air-fuel mixture for ORB1 and ORB2. However, in-cylinder air turbulence behaviour at times closer to TDC could negatively affect the movement of fuel rich mixtures closer to the bowl side wall of the ORB2 by moving bulk air towards that region which tended to trap fuel mixtures of the second injection event in the fuel mixtures of the first injection event as seen in Figure 4-16 which increased diffusion mixing and combustion as well as soot formation. This behaviour suggested that the influence of increasing the re-entrance curvature to reduce global soot formation was limited and was positive for most of the injection strategies considered and only negative in few injection strategies. The similar levels of soot exhibited throughout the range of injection timings by ORB1 showed that its bowl re-entrance curvature led to similar mixing front behaviours for the individual injection strategies. this also showed that soot emissions could be controlled over the range of injection timings.

4.4.2 70:30 Injection Ratio

Table 4-5 presents the NOx and soot emissions of the FRB, ORB1 and ORB2 for the 70:30 injection ratio.

An overview of the table results showed that the NOx and soot emissions were attributed to the interaction between the bowl geometries and injection ratio at constant injection timing as well as the interaction between the bowl geometries and injection ratio at injection timing retardation.

Table 4-5: 70:30 injection ratio emissions results for FRB, ORB1 and ORB2 at low load

Case ID	FRB		ORB1		ORB2	
	NOx (ppm)	Soot (ppm)	NOx (ppm)	Soot (ppm)	NOx (ppm)	Soot (ppm)
LL-7030-(20b,10b)TDC	455.85	2.71	117.37	7.17	121.76	5.23
LL-7030-(15b,5b)TDC	218.2	3.37	82.75	7.7	77.44	6.15
LL-7030-(10b,0)TDC	126.11	3.8	51.67	8.14	38.15	7.05
LL-7030-(5b,5a)TDC	103.9	4.3	23.08	8.52	21.45	7.89
LL-7030-(0,10a)TDC	69.58	12.6	10.83	8.89	12.32	10.85
LL-7030-(5a,15a)TDC	12.95	17.8	5.16	8.13	6.44	12.62

Regarding the interaction between the bowl geometries and injection ratio at constant injection timing, the results showed that the FRB exhibited the highest NOx emissions in all the cases as well as the lowest soot emissions in all the cases except for LL-7030-(0,10a)TDC and LL-7030-(5a,15a)TDC in which it exhibited the highest soot levels compared to ORB1 and ORB2.

The emission consequences of this interaction in the FRB were analysed further with Figure 4-17 presenting its resultant equivalence ratio, as well as its NOx and soot formations for LL-7030-(15b,5b)TDC. The equivalence results showed that the fuel delivered during the first injection event settled at the bowl side wall with no movement towards the bowl base or top of the chamber which showed again that the lack of re-entrance curvature on the FRB hindered improved fuel distribution.

The NOx results during these periods were negligible due to lower levels premixed formations as well as lower combustion temperature. The soot results also showed

that relatively small quantities of soot formation were present which high soot concentrations in small quantities located in the spray.

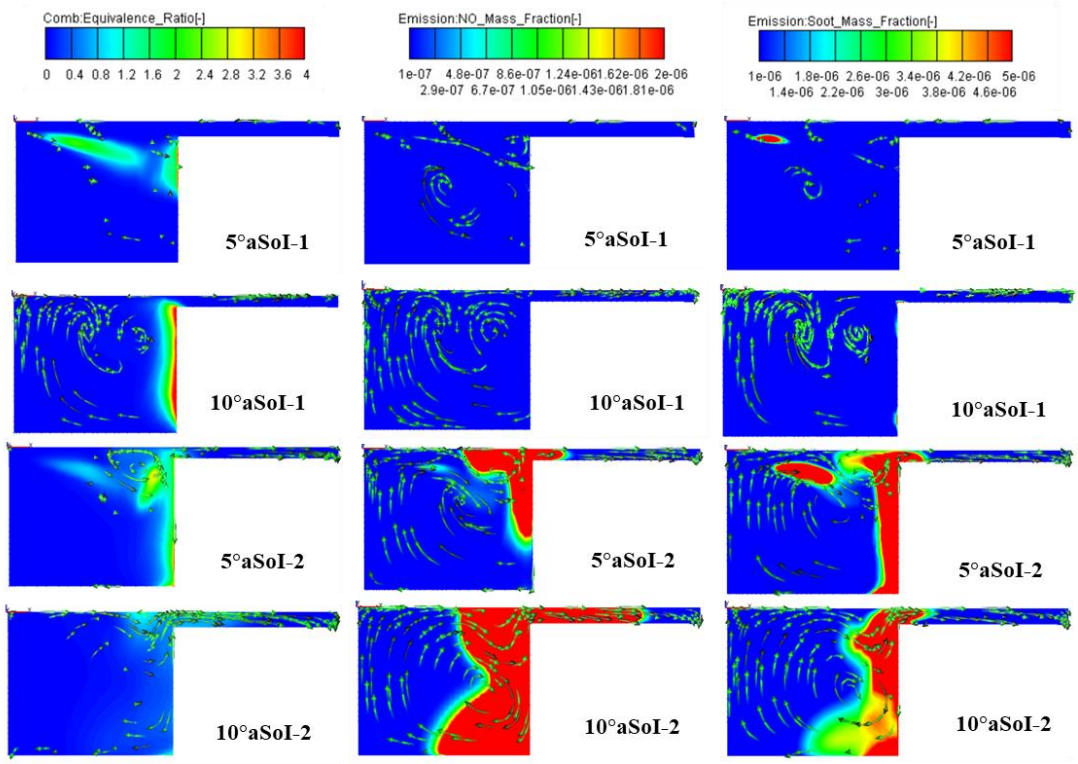

Figure 4-17: Equivalence ratio, NOx, and soot formation for FRB at LL-7030(15b,5b)TDC at low load

Furthermore, the results showed more obvious NOx and soot formations during and after the second injection event. The obvious NOx formations began to form just before, during and after the second injection event since the second injection event was shorter than the first. These formation occurred due to the presence of larger quantities premixed mixtures largely from the air-fuel mixing from the first injection event. Further NO formation was facilitated in regions of the chamber characterised by leaner and premixing formations observed at the chamber top and base corner in the presence of higher combustion temperatures.

In addition, the distribution of the soot formations closely aligned with that of the equivalence ratio during and after the second injection event. High soot concentrations were observed closer to the chamber top whereas lower soot concentrations were observed closer to the bowl base corner due to better premixing. The poor re-entrance curvature limited the distribution of fuel mixtures towards the centre of the bowl especially in the dwell angle and after the second injection.

The contribution of the FRB re-entrance bowl and mixing front to the NOx and soot emissions formed suggested that the interaction between the injection ratio and re-entrance curvatures of ORB1 and ORB2 also resulted contributed to their emissions which were significantly lower NOx and soot emissions.

ORB1 and ORB2 NOx emissions were significantly lower than that of the FRB. This was attributed to the effect of their more pronounced re-entrance curvatures which improved air-fuel mixing in a more controlled manner. High quantities of premixed formations promoted to NOx formation as seen with the FRB. However, with ORB1 and ORB2, the mixing formations could be better controlled via adequate distribution of the fuel mixtures throughout the chamber such that lower combustion temperatures occurred through the avoidance of temperature hotspots which in turn, controlled the extent of NOx formed.

The soot emissions for ORB1 and ORB2 were also significantly lower compared to FRB. This was also attributed to the effect of their more pronounced re-entrance curvatures which improved air-fuel mixing and thus caused an improved fuel oxidation. As seen in previous instances, the re-entrance of the fuel mixtures more so in ORB2 than ORB1 due to its higher re-entrance resulted in further dispersal of the fuel mixtures which aided a faster oxidation towards a leaner chamber mixture.

The interaction between the bowl geometries and injection ratio at injection timings retardation can be seen in Figure 4-18.
The NOx trends in the figure showed that NOx emission reduced as the injection timings retarded from LL-7030-(20b,10b)TDC to LL-7030-(5a,15a)TDC for all three bowl geometries. The FRB exhibited the highest NOx levels during injection timing retardation, whereas those of ORB1 and ORB2 were significantly lower and similar over the injection retardation range. The NOx trends were attributed to the reducing time for available for adequate air-fuel mixing as well as faster fuel evaporation as a result of higher residence in-cylinder temperatures during injection retardation. This caused reduced premixed formation and combustion and HRR’s which consequentially resulted in lower combustion temperatures and thus, reduced NOx formations. Injection retardation into the expansion stroke also caused a reduction in

NOx formation due to an increasing chamber volume which contributed to lower in-cylinder temperature.

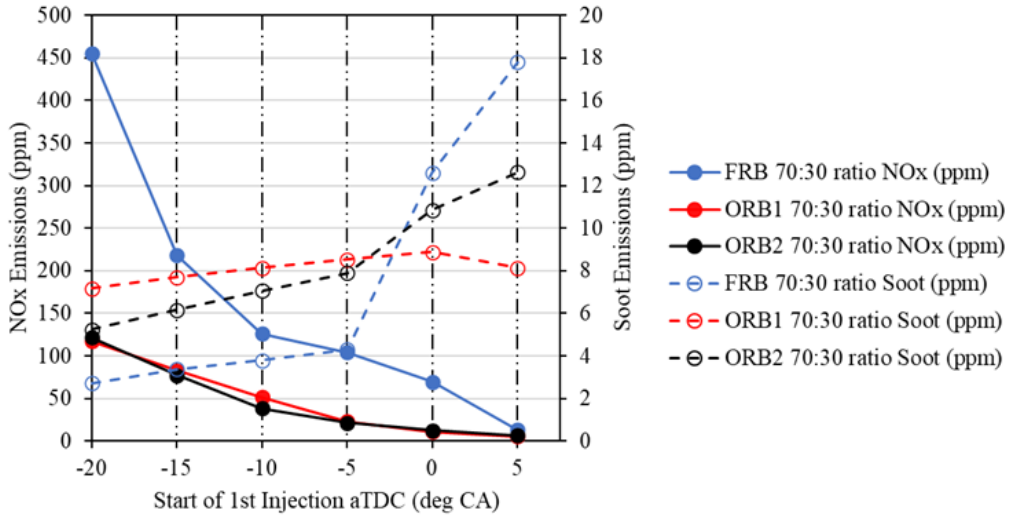

Figure 4-18: NOx vs soot emissions for FRB, ORB1 and ORB2 under 70:30 injection ratio at low load

The soot trends in the figure showed that soot emission for the FRB and ORB2 increased as injection timing was retarded from LL-7030-(20b,10b)TDC to the LL-7030-(5a, 15a)TDC. The ORB1 also exhibited increasing soot levels during injection retardation up to LL-7030-(0,10a)TDC after which further retardation from LL-7030-(0,10a)TDC to LL-7030-(5a,15a)TDC resulted in soot reduction. The trend was attributed to the formation of more diffusion and fuel rich mixtures caused by poor air-fuel mixing which worsened during retardation especially for FRB and ORB2. Here, retardation caused a shorter time for improved air-fuel mixing. In addition, diffusion combustion was promoted by the occurrence of the second injection event in the combustion of the first injection event which introduced 70% of the total fuel load.

The behaviour seen in the last injection retardation for ORB1 was attributed to the break-up of large fuel rich mixtures by turbulence in an increasing chamber volume and reducing temperature which reduced diffusion mixing and allowing more fuel oxidation in combination with a shallow re-entrance of fuel mixtures from the first injection event which limited diffusion mixing between fuel mixtures from both injection events and consequentially resulted in lower soot formation.

Besides the general trends observed for NOx and soot emissions due to injection timing retardation, the results also showed that the bowl geometries each exhibited different emissions trends of varying levels.

Considering the NOx emissions to this regard, Figure 4-18 showed that besides the FRB exhibiting the highest NOx levels, it also exhibited the most obvious NOx reduction of the three bowl geometries with a drop in NOx levels of over 400ppm over the range. Its observed NOx reduction behaviour was attributed to an improvement in its chamber mixture distribution as its mixing front grew under injection retardation.

Here, injection retardation caused fuel injection at moments when the chamber volume was smaller due to piston compression. This increased the potential of the poor mixing front to promote more air-fuel mixing especially at rich air regions and rich fuel regions at the bowl base and thus increased the chamber temperature distribution and reduced temperature hotspots which suited lower NOx formation.

Figure 4-18 also showed that ORB1 and ORB2 exhibited significantly lower and closer NOx levels compared to the FRB for the injection timing retardation from LL-7030-(20b,10b)TDC to LL-7030-(0,10a)TDC and closer NOx levels were observed for all three bowl geometries at LL-7030-(5a,15a)TDC. This supported the initial notion made for the 50:50 injection ratio that the influence of entrance curvature was stronger at earlier injection timings and had greater influence over mixing formations and thus, combustion compared to injection timing which was the opposite effect and influence at latter injection timings.

ORB1 had higher NOx levels compared to ORB2 at the retarded injection timings of LL-7030-(15b,5b)TDC, LL-7030-(10b,0)TDC and LL-7030-(5b,5a)TDC as well as higher soot levels compared to ORB2 in all the cases except for LL-7030-(0,10a)TDC and LL-7030-(5a,15a)TDC which was attributed to their respective control of the air-fuel mixing formations. From the equivalence ratio results of both bowl geometries presented in Figure 4-19, the ORB1 promoted high NOx due to mushroom mixing front which aided air-fuel interaction on almost all sides observed after the first and second injection events compared to ORB2. In ORB2 wall impingement due to the close proximity of its side wall to the nozzle caused the mixing front to move along

the bowl wall towards the top and bottom. This caused the level of air-fuel mixing to be constrained and in turn reduced NOx formations.

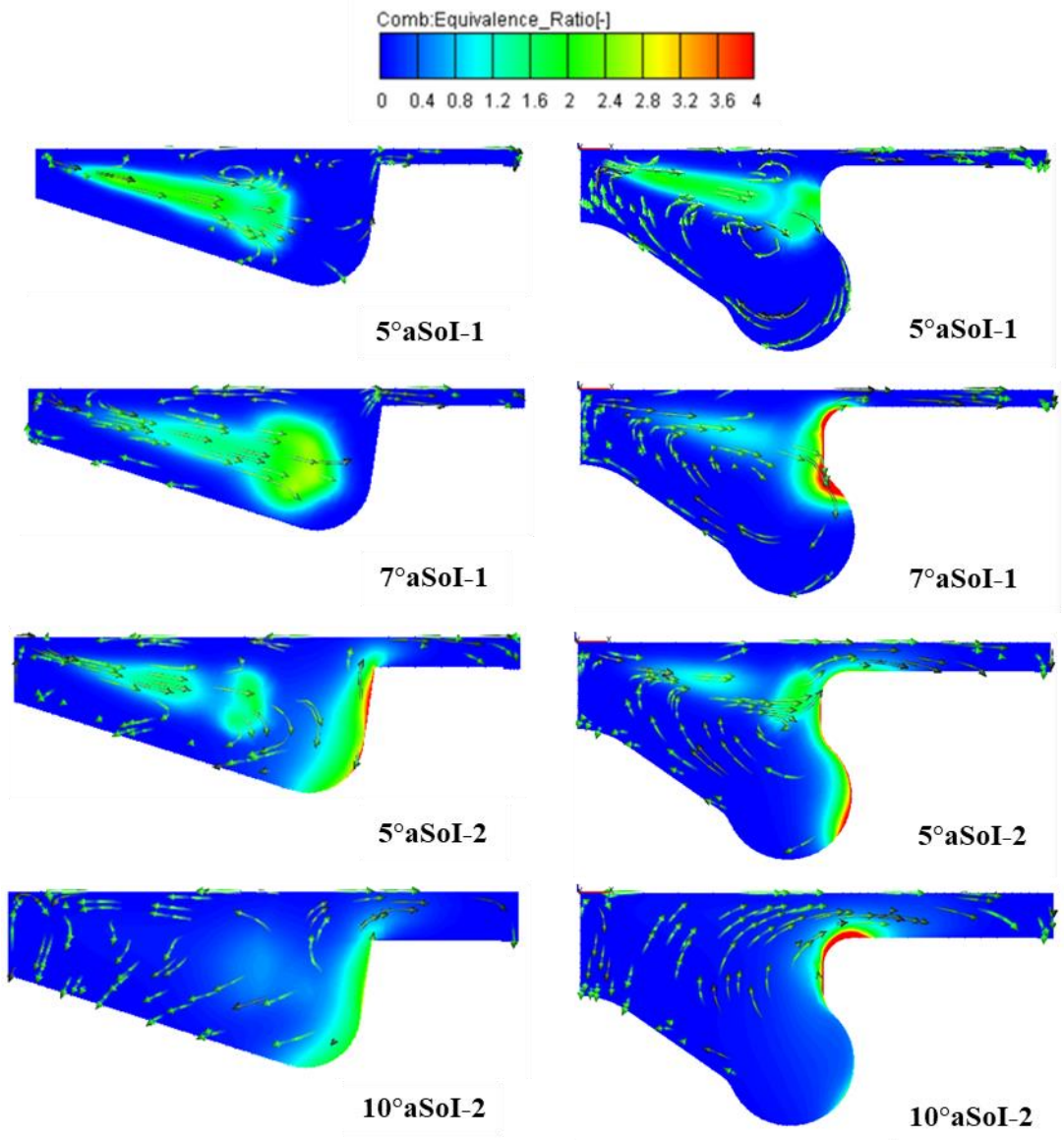

Figure 4-19: Equivalence ratio of ORB1 and ORB2 at LL-7030-(5b,5a)TDC

Considering the soot emissions due to this interaction, Figure 4-18 showed that the soot levels for all three bowl geometries increased with injection retardation from LL-7030-(20b,10b)TDC to LL-7030-(0,10a)TDC after which further injection retardation to LL-7030-(5a,15a)TDC caused further increase in soot levels for FRB and ORB2 while the soot levels for ORB1 decreased.

The poor re-entrance curvature of FRB impeded air-fuel mixing and fuel oxidation within the chamber especially during the first injection event. At advanced injection timings this effect and soot emission consequence was limited due to the availability of more time for improved air-fuel mixing. However, as injection timing retarded,

limited air-fuel mixing as well as the injection of a relatively larger fuel quantity in the first injection event promoted high diffusion fuel rich mixing and combustion which in turn increased soot formation. Injection retardation into the expansion stroke seemed to cause further increase in soot emissions due to the increasing chamber volume which hindered close reactions between air and fuel parcels thereby forming regions of very lean mixtures and regions of very rich mixtures which promoted further diffusion mixing and combustion.

Moreover, ORB1 and ORB2 exhibited lower soot levels for the same injection retardation range which was attributed to their improved re-entrance curvatures which increased air-fuel interaction.

ORB2 exhibited lower soot levels compared to ORB1 for the first 4 injection retardations which showed the effect of its re-entrance curvature and resultant mixing front. The higher re-entrance curvature of ORB2 permitted more movement of fuel mixtures towards air rich regions in the chamber which in turn promoted an improved air-fuel mixing and fuel oxidation as well. However, in-cylinder air turbulence behaviour at LL-7030-(0,10a)TDC and LL-7030-(5a,15a)TDC excited by its re-entrance curvature caused the second injection event to occur in regions were fuel rich mixtures were present which decreased fuel oxidation. Since the ORB1 had a shallow bowl re-entrance in comparism to ORB1, diffusion mixing and combustion from the interaction between the two injection events was limited which caused lower soot emissions.

4.4.3 Comparison of 50:50 and 70:30 Injection Ratios Cases

Comparison of the emissions data under the 70:30 and 50:50 injection ratios demonstrated that ORB1 and ORB2 exhibited higher NOx emissions for the 70:30 ratio compared to the 50:50 ratio as the injection timing was retarded. Interestingly, the FRB exhibited a different trend wherein NOx emissions were higher in the 70:30 ratio in all the cases except for LL-7030-(15b,5b)TDC, LL-7030-(10b,0)TDC and LL-7030-(5b,5a)TDC which exhibited lower NOx levels compared to their respective cases under the 50:50 injection ratio. The observed trend for the majority of the cases under the 70:30 ratio was attributed to the injection of larger fuel quantity during the first injection compared to the 50:50 ratio. Here, at respective injection timings, the presence of a larger fuel quantity intensified the characteristics that led to higher NOx

emissions e.g., larger premixed combustion durations and peak HRR levels due to enhanced air-fuel mixing. This in turn led to higher combustion temperatures and consequently higher NOx emissions.

Considering the comparison of soot emission between the 70:30 and 50:50 ratios, the FRB exhibited lower soot levels for the 70:30 ratio compared to the 50:50 strategy. ORB1 exhibited this same trend as the FRB in all the cases except for LL-7030-(5a,15a)TDC which exhibited a higher soot level than the respective 50:50 case. ORB2 also exhibited the same trend as the FRB in all the cases except for the LL-7030-(0,11a)TDC and LL-7030-(5a,15a)TDC cases which had higher soot levels than their respective 50:50 cases. The lower soot levels exhibited by the majority of the cases was attributed to reduced diffusion mixing formations and combustion which occurred as a result of to the relatively smaller fuel injection quantity during the second injection event for the 70:30 injection ratio strategies compared to the 50:50 strategies.

4.5 Concluding Remarks

The study presented in this chapter investigated the effects of the interaction between double injection strategy and piston bowl geometry on engine performance and emissions at low load. It focused on the 50:50 and 70:30 injection ratios over a range of six double injection strategies for the FRB, ORB1 and ORB2 piston bowl geometries, respectively.

The investigation showed that the interaction between the different bowl geometries and injection ratios at constant or varying injection timings had varying impact on combustion behaviour due to different air utilisations during air-fuel mixing. This consequently resulted in the various differences in the in-cylinder performance and emissions observed. The influence of the injection ratios at constant injection timings on in-cylinder performance and emissions were investigated. The injection strategies with the 70:30 injection ratio resulted in consistently higher IMEP levels, NOx levels and slightly higher combustion noise levels, along with lower ISFC and soot levels compared to the same injection strategies with the 50:50 injection ratio for all three bowl geometries.

The influence of retarding injection timing with the 50:50 and 70:30 injection ratios on in-cylinder performance and emissions were investigated. The results showed that with both injection ratios, the IMEP, combustion noise and NOx levels reduced while the soot and ISFC levels increased during injection timing retardation for low load conditions. This observation in addition to the observation from the influence of injection ratios showed that fuel injection characteristics had more influence on in-cylinder performance and emissions compared to that of piston bowl geometries.

The influence of the geometries on in-cylinder performance and emissions were also investigated. Considering IMEP levels at low load conditions, the FRB had the highest IMEP levels compared to ORB1 and ORB2 in majority of the injection strategies with 50:50 and 70:30 injection ratios. The largest difference in IMEP levels compared to ORB1 and ORB2 respectively were 25.1% and 20.79% in LL-5050-(20b,10b)TDC. ORB1 exhibited the highest IMEP levels in LL-7030-(5a,15a)TDC whereas ORB2 exhibited the highest IMEP levels for the same injection strategy but with the 50:50 injection ratio. Although the FRB exhibited higher IMEP levels , this was at the consequence of significantly higher NOx levels in all the injection strategies and higher soot levels in a few cases compared to ORB1 and ORB2. Besides these, its combustion noise levels were marginally higher.

5 Effects of Piston Bowl Geometry and Injection Strategy at High Load

5.1 Investigated Piston Bowl Geometries and Double Injection Strategies

The three re-entrant piston bowl geometries FRB, ORB1 and ORB2 as well as the double injection that were considered at low load were also investigated at high load. However, at high load the fuel demand was double that of the demand at low load as seen in Table 5-1.

Table 5-1: Double Injection Strategy and Operating Conditions at High Load

Intake Valve Closure (IVC)	140.4°bTDC
Exhaust Valve Opening (EVO)	133.4°aTDC
Engine Speed	1500 rpm
Fuel Demand	20mm^3/cycle
Start of 1st Injection (SoI-1)	20°bTDC to 5°aTDC sweep with 5° increment
Dwell Angle	10°CA
Injection Ratio	50:50 and 70:30

5.2 Combustion Analysis at High Load

5.2.1 50:50 Injection Ratio

The in-cylinder pressure results for the 50:50 injection ratio cases at high load are presented in Figure 5-1. An overview of the results showed ORB1, ORB2 and FRB exhibited similar pressure profile trends and obvious varying differences in their peak pressure levels in all cases except for HL-5050-(15b,5b)TDC and HL-5050-(10b,0)TDC where they exhibited much closer similarities in peak levels. Moreover, ORB1 and ORB2 exhibited closer similarities for most of the cases which was attributed to the close similarity in their bowl re-entrance curvatures compared to the FRB which caused them to have more similar combustion behaviours compared to the FRB.

In HL-5050-(20b,10b)TDC, the close similarity shared between the ORB1 and ORB2 was present as observed in their in-cylinder pressure trends and peak levels. Also in

this case, the FRB exhibited the lowest peak pressure for the HL-5050-(20b,10b)TDC which was attributed to lower air-fuel mixing formation due to the interaction between the injection strategy and its bowl geometry which lacked a re-entrance curvature. The behaviour seen in the pressure results in HL-5050-(20b,10b)TDC was not observed for HL-5050-(15b,5b)TDC and HL-5050-(10b,0)TDC wherein all three bowl geometries exhibited similar pressure trends and peak levels. The similarity observed in these cases suggested that the pressure differences induced by the different bowl geometries for the same injection strategy was minimal.

In HL-5050-(5b,5a)TDC, HL-5050-(0,10a)TDC and HL-5050-(5a,15a)TDC ORB1 and ORB2 exhibited similar pressure trends and peak levels. While the FRB also exhibited similar pressure trends, its second peak level were clearly higher compared to those of ORB1 and ORB2. Here, this behaviour could be also attributed to the presence of re-entrance bowl curvatures for ORB1 and ORB2 which contributed to a more gradual air-fuel mixing and more controlled heat release and a lack thereof in the FRB which contributed to a lesser controlled heat release generation which translated to higher pressure levels presented.

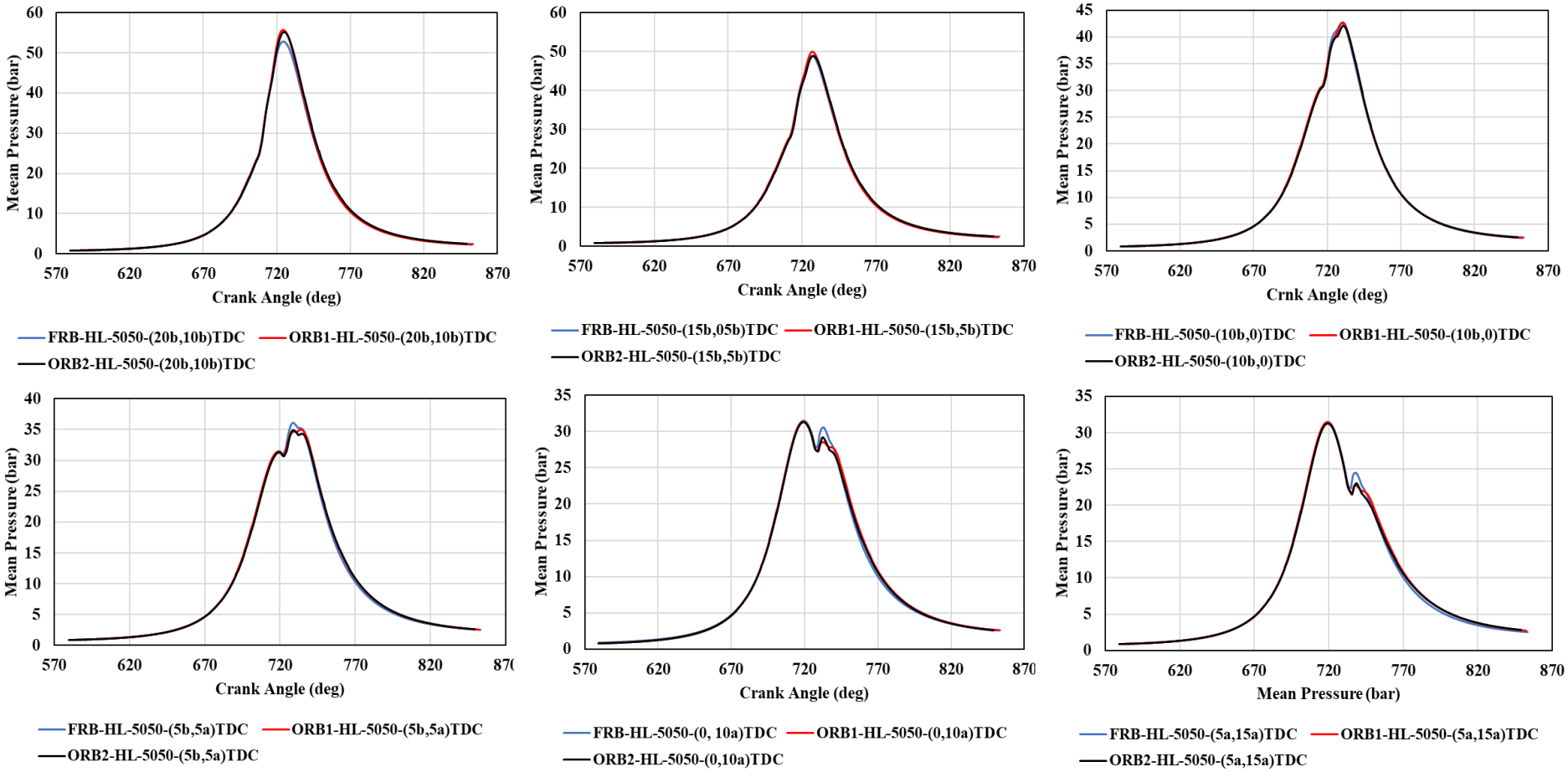

Figure 5-1: In-cylinder pressure data for FRB, ORB1 and ORB2 under 50:50 injection ratio at high load

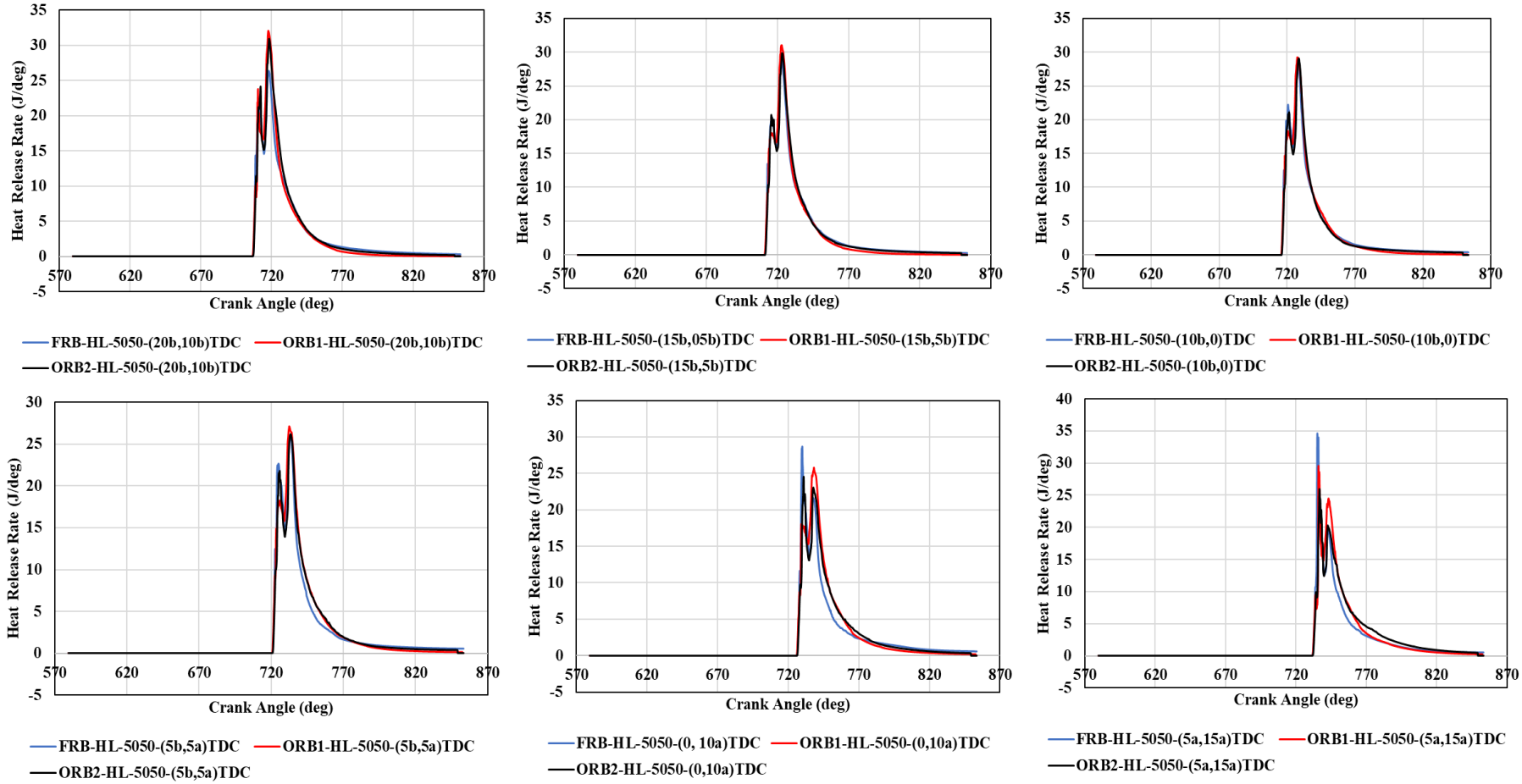

Figure 5-2: In-cylinder HRR profiles for FRB, ORB1 and ORB2 under 50:50 injection ratio at high load

The HRR results of the 50:50 injection ratio cases at high load are presented in Figure 5-2. An overview of the results showed that the three bowl geometries exhibited peak HRR in the diffusion combustion phase in HL-5050-(20b,10b)TDC, HL-5050-(15b,5b)TDC, HL-5050-(10b,0)TDC and HL-5050-(5b,5a)TDC. This behaviour was largely attributed to the influence of the injection ratio which involved the injection of 50% of the total fuel load during the second injection event.

Injection of 50% total fuel load during the first injection event occurred at in-cylinder residence time characterised by relatively lower temperature, pressure and in-cylinder air density compared to residence time close to TDC. This contributed to the formation of premixed mixtures in the earlier stages of heat release and combustion as well as the formation of a large quantity of fuel rich diffusion mixtures due to the second fuel injection event occurring in the mixing process of the first injection event. Here, the introduction of additional fuel into the mixing formations of the first injection further promoted fuel rich diffusion mixing and consequently high diffusion HRR's.

The overview of the results also showed that the HRR trend behaviour changed due to injection retardation with HL-5050-(0,10a)TDC considered as the switching point wherein the FRB and ORB2 exhibited peak HRR in the premixed combustion phase while ORB1 exhibited peak HRR in the diffusion phase. In addition, peak HRR occurred in the premixed combustion phase in HL-5050-(5a,15a)TDC which was attributed to the first injection event occurring closer to TDC and into an expansion of the cylinder characterised by a reducing cylinder density, pressure and temperature which increased the tendency of a longer ignition delay therefore promoting the formation of more premixed mixtures and consequently high premixed HRR and combustion.

The additional consideration of the interaction between the piston bowl geometries and injection strategy provided further insight into the various combustion behaviours observed. In HL-5050-(20b,10b)TDC, ORB1 and ORB2 exhibited similar and higher HRR profiles in the premixed and diffusion combustion phases compared to the FRB. This was attributed to the influence of their bowl re-entrance curvatures which had higher radii compared to FRB. The large radius curvatures of ORB1 and especially

ORB2 promoted in-cylinder turbulence and air-fuel mixing by causing large mixing fronts along their bowl walls. This improved mixing during the first injection leading to more premixtures and thus higher HRR's in the premixed combustion phase for ORB1 and ORB2.

Improved mixing also implied a better mixing reaction rates of the rich formation especially during the second injection. These two characteristics contributed to the promotion of high HRRs in the diffusion combustion phase for ORB1 and ORB2. Nevertheless, the diffusion phase exhibited by ORB2 was lower compared to the FRB.

In contrast, the lower peak HRR of the FRB in the diffusion combustion phase of HL-5050-(20b,10b)TDC was attributed to a combined interaction of a poor in-cylinder turbulence generated from its poor bowl re-entrance curvature and the injected fuel quantity during the second injection. Here, the poor mixing turbulence contributed to a smaller reaction of the relatively large newly introduced fuel in the presence of low oxygen content which led to reduced diffusion mixing formations and consequently a diffusion combustion with lower HRR levels.

Furthermore, the FRB exhibited a similar HRR profile to ORB1 and ORB2 in the late combustion phase for HL-5050-(20b,10b)TDC, as well as HL-5050-(15b,5b)TDC and HL-5050-(10b,0)TDC cases. However, its HRR profile in the late combustion phase for HL-5050-(5b,5a)TDC, HL-5050-(0,10a)TDC and HL-5050-(5a,15a)TDC exhibited a steeper profile indicating a shorter late combustion. This was attributed to the combined influence of the FRB's bowl orientation and fuel injection quantity during the second injection wherein the poor re-entrance curvature of the FRB led to poor mixing reaction for combustion and thus, a shorter combustion. In addition, the HL-5050-(0,10a)TDC case involved a second fuel injection in the expansion stroke characterised by an increasing chamber volume and lower in-cylinder temperature both of which limited diffusion mixing, consequently leading to a shorter combustion in the diffusion phase.

These mixing behaviours are further demonstrated through the equivalence ratio distribution of HL-5050-(20b,10b)TDC for FRB, ORB1 and ORB2 presented in Figure 5-3.

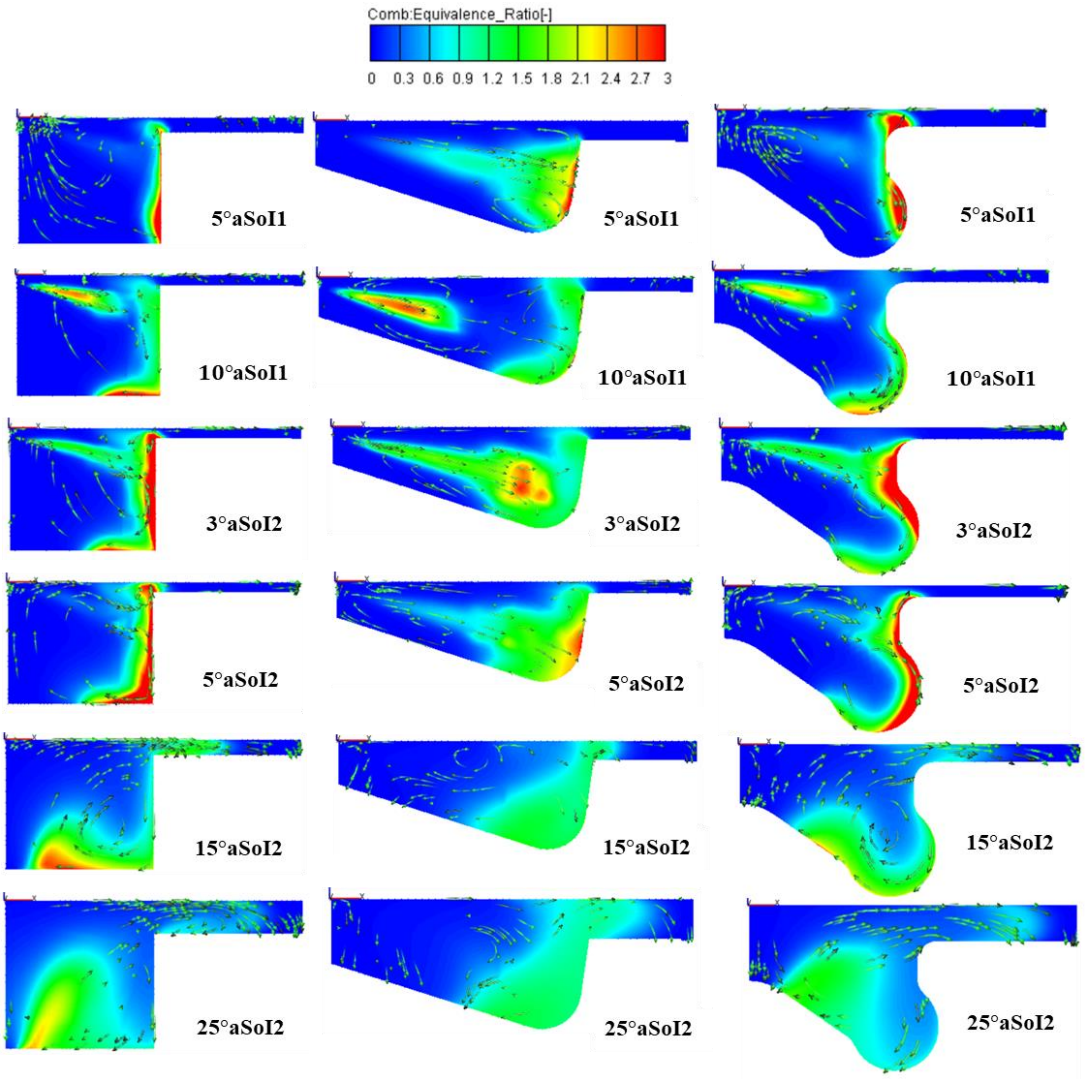

Figure 5-3: Equivalence ratio distribution of FRB, ORB1 and ORB2 for the HL-5050-(20b,10b)TDC

Figure 5-4 and Figure 5-5 show the equivalence ratio distribution of HL-5050-(0,10a)TDC for ORB1 and ORB2. From the results, it can be seen that the re-entrance curvature radius of ORB2 causes enhanced air-fuel mixing and a larger mixing front area which causes a more gradual rise in HRR and consequently lower peak HRR compared to ORB1. The re-entrance curvature radius of ORB1 promotes improved air-fuel mixing adequate for a quicker rise in HRR and consequently higher peak HRR. Furthermore, the higher HRR of ORB1 is promoted by more localised mixing formation and movement in the bowl region which causes localised increase in the HRR, combustion temperature and pressure compared to the large movement inside and outside the bowl region of ORB2.

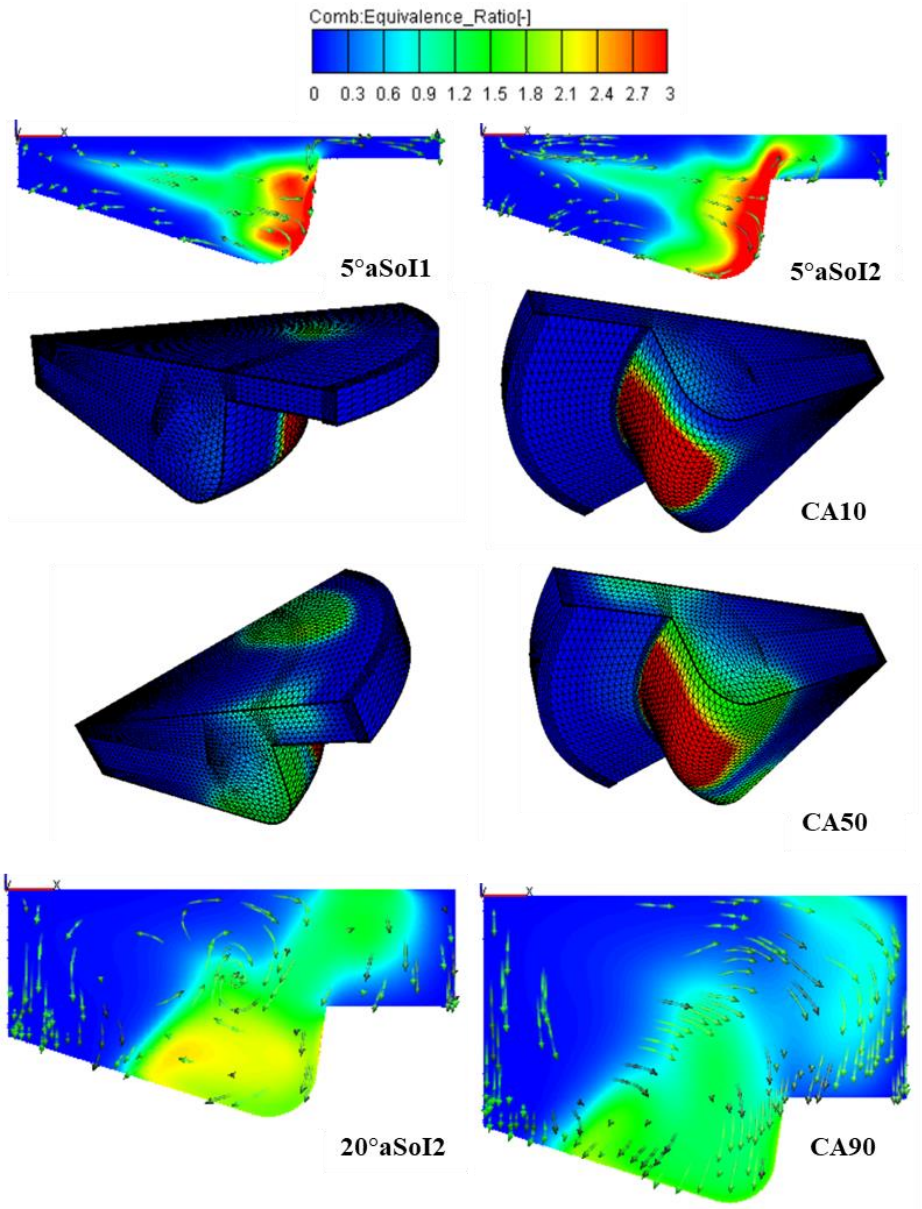

Figure 5-4: Equivalence ratio distribution of ORB1 for the HL-5050-(0,10a)TDC case including CA10, CA50 and CA90

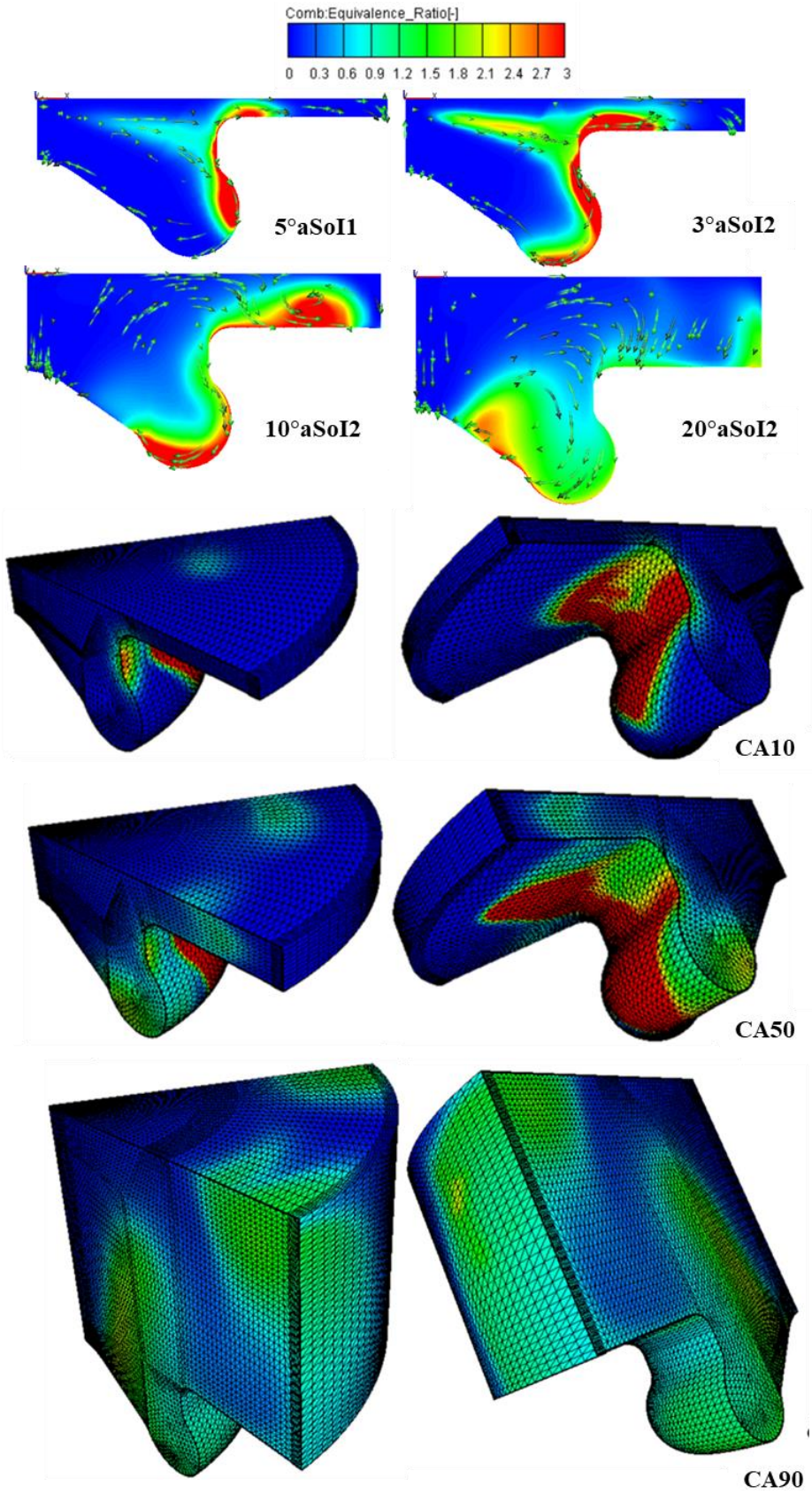

Figure 5-5: Equivalence ratio distribution of ORB2 for the HL-5050-(0,10a)TDC case showing CA10, CA50 and CA90

Furthermore, in the case of HL-5050-(0,10a)TDC, the FRB exhibited the highest peak HRR in the premixed combustion phase and a similar peak HRR in the diffusion combustion phase compared to ORB2 whereas ORB1 exhibited the lowest peak HRR in the premixed combustion phase and the highest peak HRR in the diffusion phase. This trend was also observed in HL-5050-(5a,15a)TDC except that in this case, the FRB exhibited an even higher peak HRR in the premixed combustion phase and ORB1 exhibited the second highest peak HRR in the premixed combustion phase as well as the highest peak HRR in the diffusion combustion phase.

The HRR behaviour of the three bowl geometries for HL-5050-(5b,5a)TDC, HL-5050-(0,10a)TDC and HL-5050-(5a,15a)TDC cases was attributed to the interaction between fuel injection timing and the squish region of the chambers. Here, retarded fuel injection timing resulted in the late initiation of combustion in the expansion stroke. In addition, fuel injection occurred in the squish region which is characterised by high oxygen content. Peak HRR was lower for ORB1 and ORB2 especially for HL-5050-(0,10a)TDC and HL-5050-(5a,15a)TDC cases due to improved air-fuel mixing which caused a more gradual rise in HRR. The increasing volume as well as lower in-cylinder pressure experienced in the expansion stroke also contributed to improved premixing and hence a high HRR peak in the premixed combustion phase.

The effects of the interaction between the piston bowl geometry and the 50:50 injection ratio injection ratio under injection timing retardation can also be observed in Figure 5-1 and Figure 5-2. Peak in-cylinder pressure was lower as the injection timing was retarded especially from HL-5050-(20b,10b)TDC to HL-5050-(5b,5a)TDC. In HL-5050-(0,10a)TDC and HL-5050-(5a,15a)TDC cases peak in-cylinder pressure remained at about 31.2 bar for all three bowl geometries while the difference exhibited by each bowl geometry was noticed at the second pressure peaks in these cases. The first peaks signify the motoring pressure while the second peaks are attributed to the commencement of combustion and the consequential rise in in-cylinder HRR, temperature and pressure after TDC in the expansion stroke.

The results clearly showed that during injection retardation from HL-5050-(20b,10b)TDC to HL-5050-(5b,5a)TDC, the highest peak HRR was exhibited in the diffusion combustion phase for all three bowls. However, both diffusion and

premixed combustion phases shared close peak HRR levels with the highest peak experienced in the premixed combustion phase for the HL-5050-(0,10a)TDC case. In the case of HL-5050-(5a,15a)TDC, the highest peak HRR was exhibited in the premixed combustion phase with a clear distinction from the diffusion peak. The results suggested that as injection timing was retarded, diffusion combustion peak HRR reduced while premixed combustion peak HRR increased with a shorter duration.

From the results of the cases under the 50:50 injection ratio, the FRB and ORB1 exhibited higher disparities in the shift between the premixed and diffusion combustion phase as injection timing was retarded. Interestingly, ORB2 exhibited a rather controlled shift which suggested that it promoted a better control over combustion phasing. It exhibited the highest degree of re-entrance curvature which seemed to generate sufficient in-cylinder turbulence to promote adequate HRR in the premixed and diffusion combustion phases.

5.2.2 70:30 Injection Ratio

The in-cylinder pressure results for the 70:30 injection ratio cases at high load are presented in Figure 5-6. An overview of the results showed that ORB1, ORB2 and FRB exhibited similar trends in pressure profiles and varying differences in their peak pressure levels in all cases except for HL-5050-(15b,5b)TDC and HL-5050-(10b,0)TDC where they exhibited much closer similarities in peak pressure levels. Moreover, ORB1 and ORB2 exhibited closely similar pressure trends in HL-7030-(20b,10b)TDC compared to the FRB. ORB1 also exhibited the highest peak pressure levels of the three bowl geometries while that of ORB1 and FRB were much closely similar in HL-7030-(15b,5b)TDC and HL-7030-(10b,0)TDC.

In HL-7030-(20b,10b)TDC, the FRB exhibited the lowest peak pressure level compared to ORB1 and ORB2. Although the pressure trends and peak levels for ORB1 and ORB2 were similar, ORB1 exhibited a slightly higher-pressure trend and peak level compared to ORB2. This suggested that the combustion behaviour from both geometries were attributed to the impact the difference in their respective re-entrance curvatures had on promoting high heat release and combustion. In HL-7030-

(15b,5b)TDC and HL-7030-(10b,0)TDC, ORB1 exhibited the highest peak pressure levels which were slightly higher than those of FRB and ORB2 that were more similar. This observation of the pressure profile for ORB1 in both injection cases was attributed to the generation of higher heat release due to its air-fuel mixing behaviour which was different for the FRB and ORB2. Regarding the FRB and ORB2, their similar pressure trends and peak levels were attributed to different causes.

Concerning the FRB, its comparatively low peak pressure was attributed to its lack of a re-entrance curvature which hindered improved air-fuel mixing and heat release for an increased pressure. Concerning the ORB2, its lower peak pressure was attributed to improved air-fuel mixing caused by its very high re-entrance curvature which promoted more gradual heat release and consequently caused a gradual pressure rise.

In HL-5050-(5b,5a)TDC, the three bowl geometries had similar pressure rise and fall trends with differences at their peak levels wherein ORB1 exhibited the highest peak pressure which was negligibly higher than that of the FRB and noticeably higher than that of ORB2. This suggested that ORB1 and FRB promoted higher in-cylinder pressure due to their induced air-fuel mixing behaviour compared to ORB2 which promoted a more gradual heat release and thus, gradual pressure rise due to improved air-fuel mixing. In HL-5050-(0,10a)TDC, FRB exhibited the highest peak pressure which was slightly higher than the motoring peak pressure as well as the peak pressure levels for ORB1 and ORB2. FRB was also observed to exhibit slightly lower pressure fall trend compared to ORB1 and ORB2.

In HL-5050-(5a,15a)TDC, the peak in-cylinder pressure was the peak motoring pressure due to the fuel injection events occurring well after TDC in the expansion stroke. ORB1 and ORB2 exhibited very similar peak pressure levels which were slightly lower compared to the peak level for the FRB during combustion. The behaviour ORB1 and ORB2 was attributed to the more gradual rise in heat release and combustion due to the improved air-fuel mixing induced by their re-entrance curvatures which was absence in the FRB and thus caused a harsher and quicker heat release which translated to a slightly higher peak pressure.

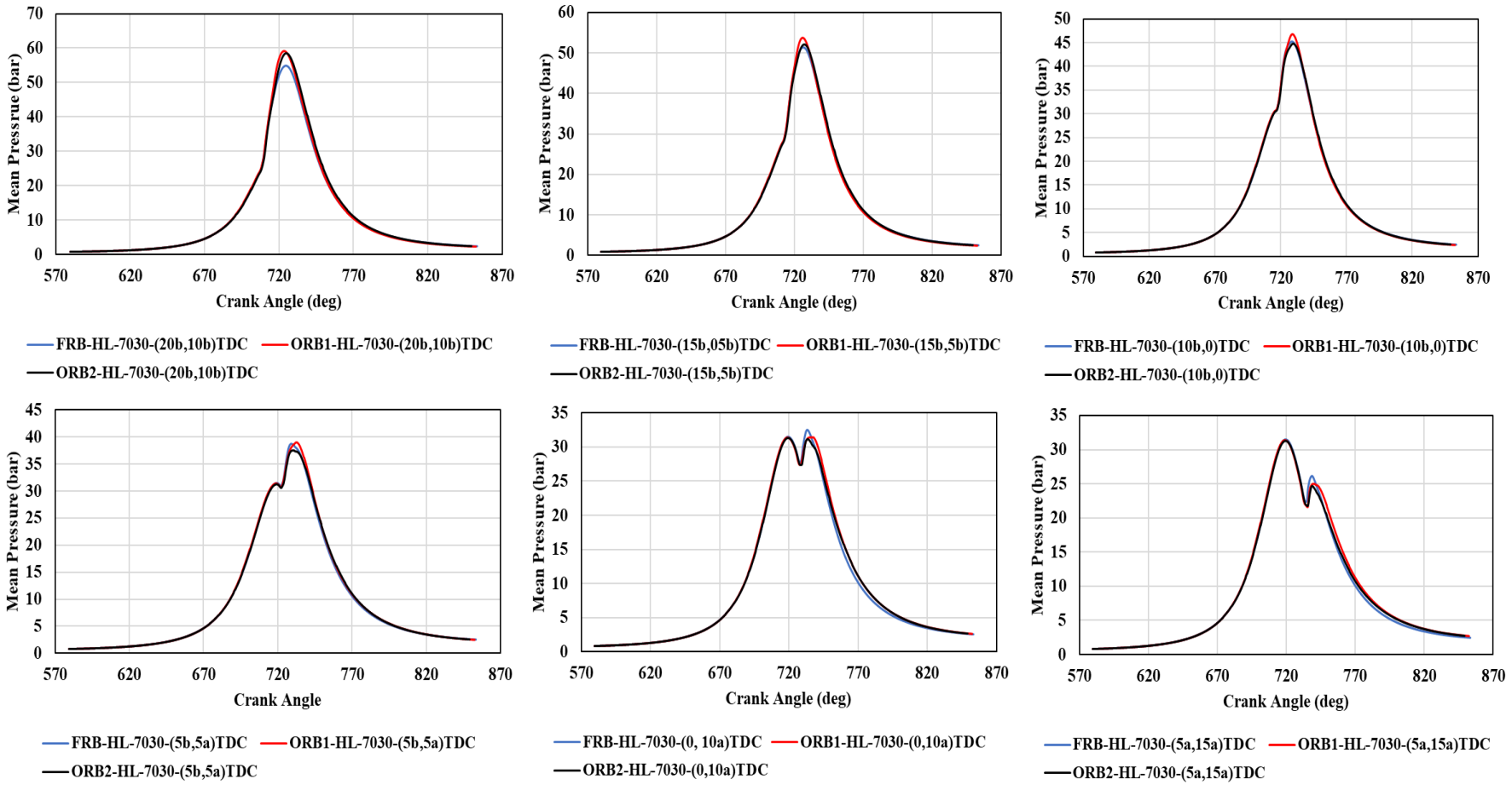

Figure 5-6: In-cylinder pressure data for FRB, ORB1 and ORB2 under 70:30 injection ratio at high load

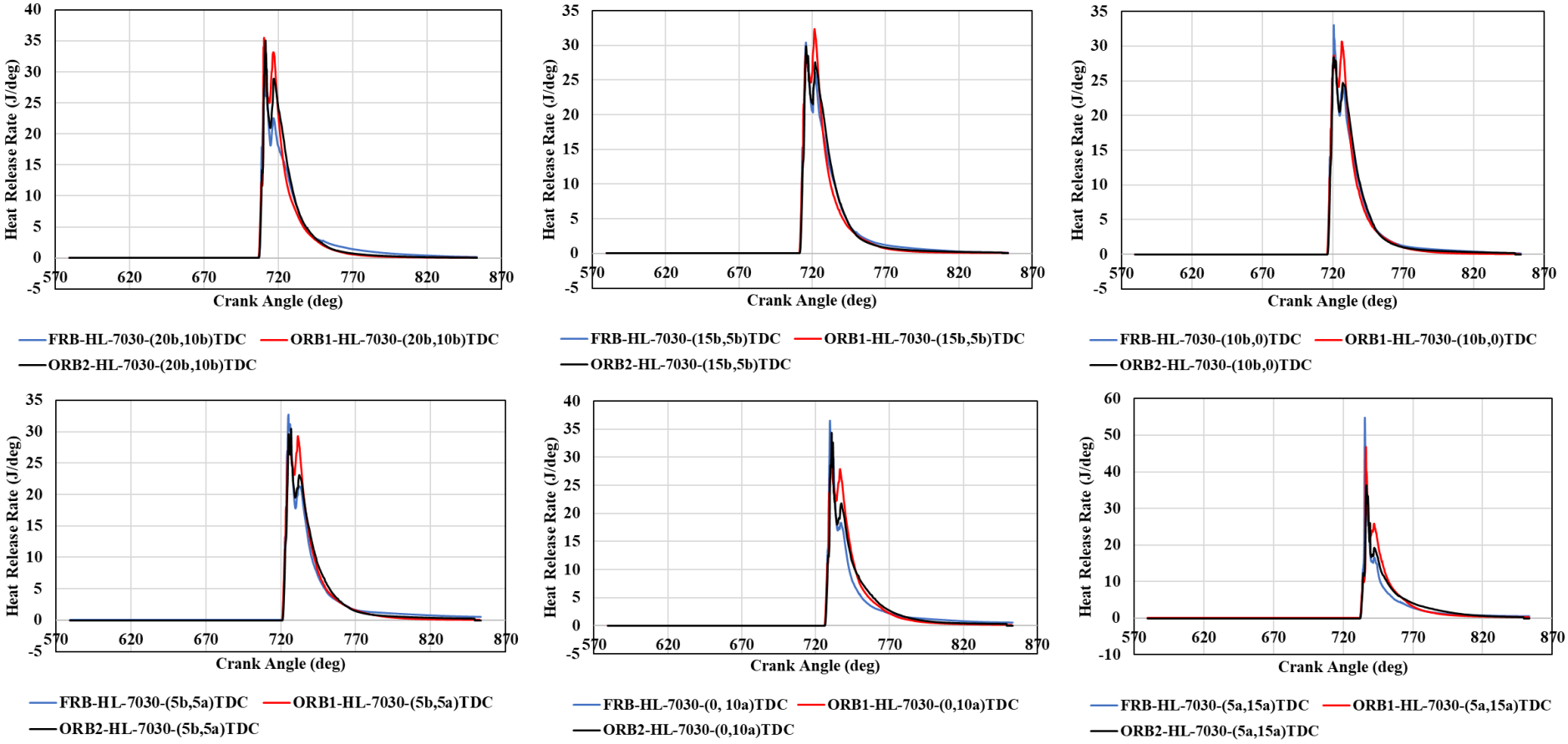

Figure 5-7: In-cylinder HRR profiles for FRB, ORB1 and ORB2 under 70:30 injection ratio at high load

The HRR results of the 70:30 injection ratio cases at high load are presented in Figure 5-7. An overview of the results showed that while the FRB and ORB2 exhibited peak HRR levels in the premixed combustion phase for all the cases, ORB1 exhibited peak HRR levels in the diffusion combustion phase for all the cases except for HL-7030-(20b,10b)TDC and HL-7030-(5a,15a)TDC wherein its peak HRR levels were in the premixed combustion phase. The HRR behaviour exhibited by majority of the bowl geometries in most of the cases in which peak HRR was predominantly in the premixed combustion phase was attributed to the influence of the injection strategy.
The 70:30 injection strategy involved the delivery of 70% of the total fuel load during the first injection event which caused the mixing of more fuel with the available air and consequentially contributed to an increase formation of premixed mixtures, as well as high premixed heat release and combustion. The HRR behaviour exhibited by ORB1 in which it generated peak HRR levels in the diffusion phase was attributed to the interaction between the shallow bowl re-entrance curvature and injection strategy for the injection timings considered.

The three bowl geometries exhibited different HRR trends in each of the cases. In HL-7030-(20b,10b)TDC, ORB1 and ORB2 had closely similar peak HRR levels with that of ORB1 negligibly higher. The peak HRR levels for both geometries were higher compared to that of the FRB. In the diffusion phase of HRR, ORB1 and FRB exhibited the highest and lowest peak HRR levels. This behaviour in HRR trend was due to the interaction between each piston bowl geometry and the injection strategy. ORB1 and ORB2 are characterised by higher re-entrance curvatures with that of ORB2 the highest. Improved bowl re-entrance contributed to improved air-fuel mixing, increased premixed formations, HRR's and premixed combustion compared to the FRB which had no re-entrance curvature.

The HRR trend of ORB1 in the diffusion phase was attributed to its shallow re-entrance curvature compared to that of ORB2 and its influence on the incoming fuel from the second injection event. Due to its shallow re-entrance curvature, global movement of rich fuel mixtures from the first injection event was limited. This resulted in the generation of further rich fuel mixtures due to the second injection event occurring into the mixing formations already present in the chamber. In the case

of FRB, the peak diffusion HRR was the lowest of the three geometries due to the migration of rich fuel mixtures to the base of its bowl which permitted a leaner mixing of the second injection event. Figure 5-8 presents the equivalence ratio distribution of the three bowl geometries for HL-7030-(20b,10b)TDC illustrated their air-fuel mixing behaviours which resulted in the HRR behaviour presented.

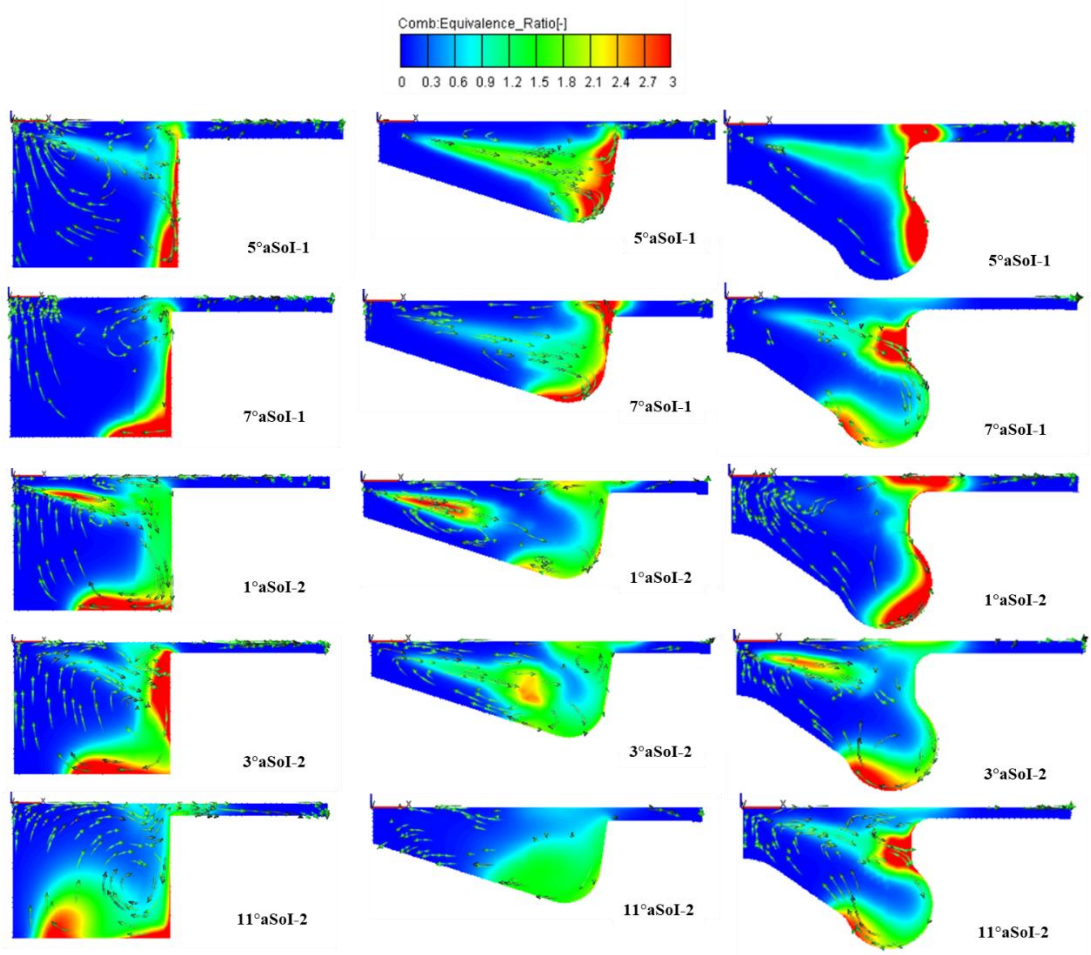

Figure 5-8: Equivalence ratio distribution of FRB, ORB1 and ORB2 for the HL-7030-(20b,10b)TDC

The results from ORB1 and ORB2 also suggested that bowls with re-entrance curvatures could also facilitate diffusion mixing wherein a shallow re-entrance as seen in ORB1 interacted with the second injection event to lead to higher fuel rich diffusion HRR's compared to a deep re-entrance as seen in ORB2. Consequently, this presented a correlation between bowl re-entrance curvature and the extent of diffusion mixing.

The influence of the three bowl geometries and injection timings under the 70:30 injection ratio is also be observed from the pressure and HRR results presented in Figure 5-6 and Figure 5-7, respectively.

From Figure 5-6, in-cylinder peak pressure was observed to reduce, and the formation of double pressure peaks became obvious as the injection timing was retarded.

The reduction of peak in-cylinder pressure occurred as injection timing retarded until peak pressure was motoring pressure. The formation of double peak in-cylinder pressure was observed in HL-7030-(0,10a)TDC and then HL-7030-(5a,15a)TDC as injection timing retarded from HL-7030-(5b,5a)TDC.

The reduction of the peak in-cylinder pressure was because of the faster fuel evaporation due to higher in-cylinder temperature and pressure closer to TDC which limited the time available for adequate air-fuel mixing which limited the HRR at peak levels required for increased peak pressure. The formation of double pressure peaks was due to the extensive retardation of the injection timing to TDC and after TDC into the expansion stroke due to combustion occurring in the expansion stroke. Here, the first peak pressure was the motoring pressure whereas the second peak pressure was caused by combustion.

From Figure 5-7, the HRR results supported this notion by providing further insight on the combustion behaviour of each bowl geometry under the same injection timing. Here, for most of the cases peak HRR was observed in the premixed combustion phase, no correlation between bowl re-entrance curvature and peak HRR was obtained as in the FRB and ORB2 produced higher peak HRR in some cases while FRB and ORB1 produced higher peak HRR in other cases.

Interestingly, peak HRR reduced under injection retardation from HL-7030-(20b,10b)TDC to HL-7030-(0,10a)TDC. However, HL-7030-(5a,15a)TDC produced the highest peak HRR with the FRB and ORB1 exhibiting 54.5J/deg and 46.8J/deg, respectively. This was attributed to the injection of 70% of the total fuel quantity at a time closer to TDC where in-cylinder temperature, density and pressure were favourable for the formation of improved premixtures with respect to bowl orientation.

The HRR results of the FRB, ORB1 and ORB2 for the HL-7030-(5a,15a)TDC case suggested that the ORB2 and FRB promoted very HRR peak levels whereas ORB2 promoted more controlled peak HRR levels. The peak HRR levels exhibited by ORB2 compared to the FRB and ORB1 was attributed to its re-entrance curvature inducing a more gradual heat release rise while the lesser degrees of bowl re-entrance curvature in ORB1 and FRB resulted in a faster rise in HRR. This supported an earlier notion that improved bowl re-entrance curvature could promote high premixed combustion HRR due to improved air-fuel mixing as well as lower peak HRR in the premixed combustion phase due to gradual heat release rate.

Moreover, the HRR results demonstrated an interesting characteristic for the FRB. The FRB exhibited higher HRR trend in the late combustion phase compared to ORB1 and ORB2 which were similar in earlier injection timings. However, its trend in the late combustion phase began to reduce to a point where it was lower than those of ORB1 and ORB2 which remained closely similar for HL-7030-(5a,15a)TDC.
This suggested that ORB1 and ORB2 characterised by higher bowl re-entrance curvatures led to prolonged combustion at higher HRR levels towards the end of the combustion process compared to FRB. The bowl assisted turbulence which promoted reaction rate was highlighted as a possible cause for the observed trend. Figure 5-9 presents the equivalence ratio results of FRB, ORB1 and ORB2 to illustrate their respective air-fuel mixing behaviour with respect to injection timing retardation from HL-7030-(10b,0b)TDC to HL-7030-(0,10a)TDC.

The results for the three bowl geometries suggested that ORB1 could promote high HRR levels, the FRB was limited by its bowl orientation which caused huge shifts in the premixed and diffusion combustion phases while ORB2 promoted a well-controlled combustion phasing from the premixed phase to the diffusion phase by not having a severe shift even though it experienced very high HRR levels in either phases in some cases.

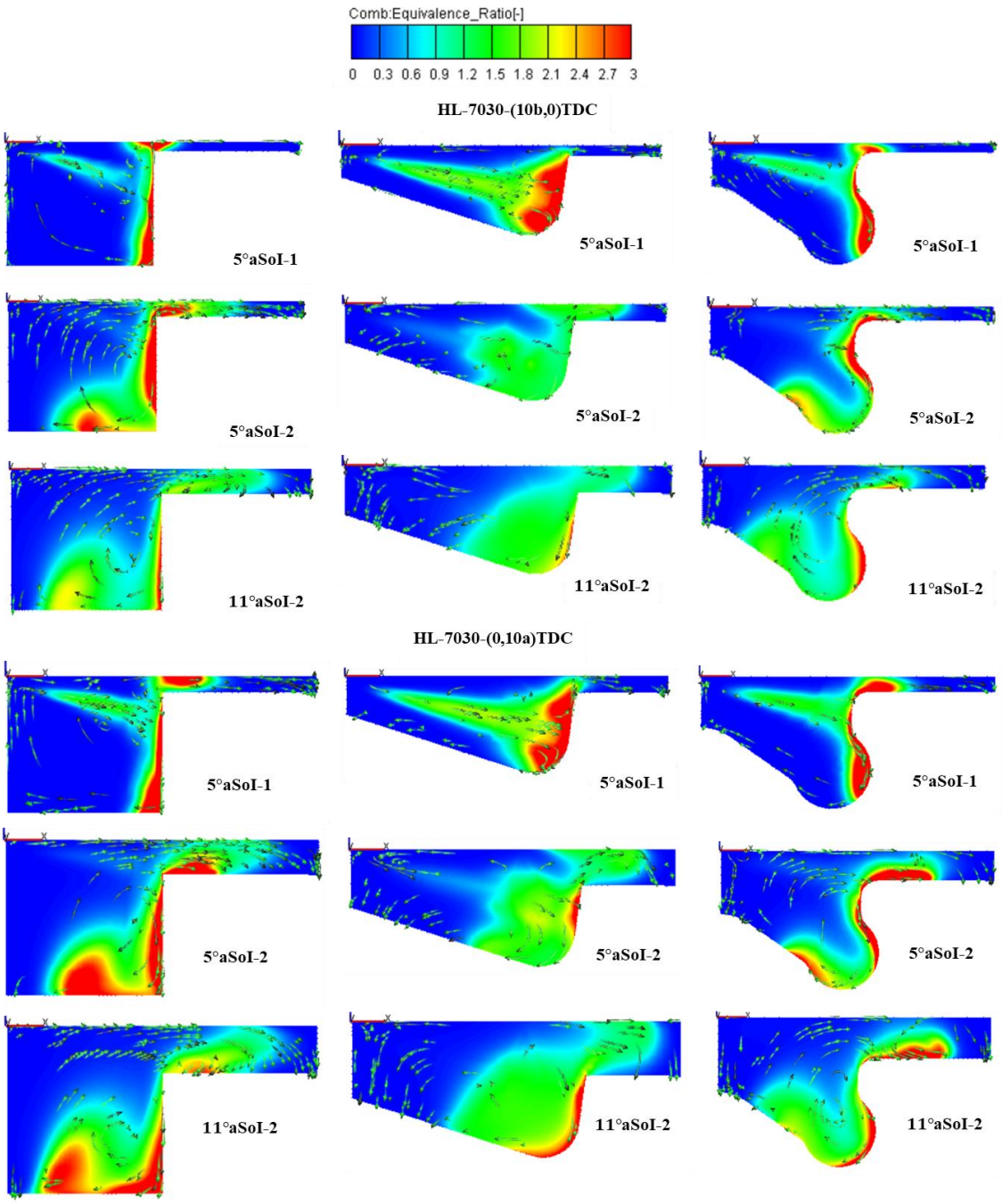

Figure 5-9: Equivalence ratio distribution of FRB, ORB1 and ORB2 for injection timing retardation from HL-7030-(10b,0)TDC to HL-7030-(0,10a)TDC

5.2.3 Comparison of 50:50 and 70:30 Injection Ratios Cases

The behaviour of the three bowl geometries due to the influence of the 50:50 and 70:30 injection ratios could be obtained from a cross comparison of the respective in-cylinder pressure and HRR results. A comparison of the pressure results showed that the cases under the 70:30 injection ratio exhibited higher in-cylinder peak pressures compared to the same cases under the 50:50 injection ratio. This behaviour was due to the injection of 70% of the total fuel quantity during the first injection under the 70:30 ratio compared to the 50:50 injection strategy where 50% of the total fuel quantity was injected during the first injection. A comparison of the HRR results showed that this caused a high rise in HRR levels during the combustion and thus, higher in-cylinder pressures.

Furthermore, the cases under both injection ratios experienced increasing peak HRR levels in the premixed combustion phase where injection timing was retarded the most. Apart from that, the majority of the cases exhibited high peak HRR in the diffusion combustion phase under the 50:50 injection ratio whereas most of the cases under the 70:30 injection ratio exhibited high peak HRR in the premixed combustion phase. Again, this was due to the injection of more fuel during the first injection which promoted improved air-fuel mixing during the first injection under the 70:30 injection ratio.

A comparison of the diffusion HRR levels for the 50:50 and 70:30 ratios showed that although a smaller fuel quantity was injected during the second injection under the 70:30 ratio, both ratios shared similar HRR levels in the diffusion combustion. This was because of the higher accumulated HRR at the end of the premixed combustion phase under the 70:30 ratio which led to the diffusion phase commencing at a high HRR and temperature and contributed to the HRR produced from the second injection.

The results also showed while injection ratio influenced combustion phasing by affecting the extent of HRR from the premixed and diffusion combustion phases, the bowl orientation also significantly contributed to this phenomenon. A comparison of the results exhibited by each bowl geometry suggested that the FRB was most prone to severe shifts in the HRR levels from the premixed and diffusion combustion phases

while ORB1 and ORB2 exhibited better control over combustion phasing. This also implied that the degree of bowl re-entrance curvature contributed to the control of premixed and diffusion combustion levels through the influence of bowl assisted turbulence which promoted improved air-fuel mixing under lean and rich mixtures in advanced and retarded injection timings, respectively.

5.3 Performance Analysis at High Load

5.3.1 50:50 injection ratio

The influence of the FRB, ORB1 and ORB2 on IMEP, ISFC and combustion noise under the 50:50 injection ratio at high load can be seen in Table 5-2. From an overview, an increase in IMEP correlated to a decrease in ISFC. This behaviour is also seen to extend to the influence of injection timing retardation seen in Figure 5-10. Here, IMEP decreased while ISFC increased as the injection timing was retarded from HL-5050-(20b,10b)TDC to HL-5050-(5a,15a)TDC. Furthermore, the influence of injection timing and bowl geometry on IMEP could also be observed from Figure 5-10. While ORB2 exhibited the highest, second highest and lowest IMEP levels of the three bowl geometries as injection timing was retarded from HL-5050-(20b,10b)TDC to HL-5050-(15b,5b)TDC and to HL-5050-(10b,0)TDC, respectively, its IMEP level reduced to a point where it was higher and lower than the IMEP levels of the FRB and ORB2, respectively, as the injection timing was retarded from HL-5050-(5b,5a)TDC to HL-5050-(0,10a)TDC and to HL-5050-(5a,15a)TDC.

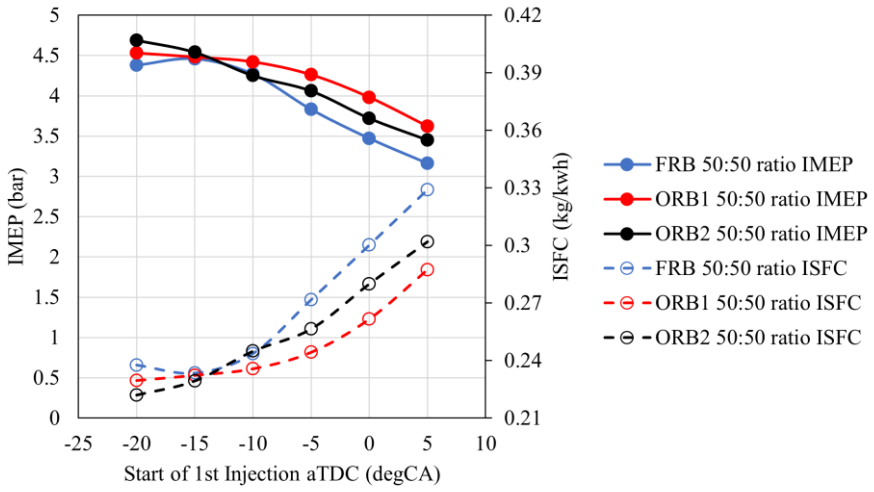

Figure 5-10: IMEP vs ISFC for FRB, ORB1 and ORB2 under 50:50 injection ratio at high load

An overview of the results presented in Table 5-2 showed that none of the bowl geometries exhibited the highest IMEP level in every case. Furthermore, there was no correlation between the highest IMEP level and the degree of bowl re-entrance curvature. However, a correlation between bowl geometries with higher re-entrance curvatures and high IMEP levels was observed. ORB2 and FRB exhibited the highest and lowest IMEP levels in HL-5050-(20b,10b)TDC and HL-5050-(15b,5b)TDC cases. In HL-5050-(10b,0)TDC, ORB1 and ORB2 exhibited the highest and lowest IMEP levels with the ORB2's IMEP level negligibly lower than that of the FRB by about 0.46%.

Apart from that, ORB1 and FRB exhibited the highest and lowest IMEP levels in HL-5050-(5b,5a)TDC, HL-5050-(0,10a)TDC and HL-5050-(5a,15a)TDC cases. In these cases, the ORB2 IMEP levels were correspondingly 4.92%, 6.98%, and 4.92% lower compared to the respective IMEP levels of ORB1. The results showed that ORB1 exhibited a strong promotion of IMEP while ORB2 was second. The IMEP behaviour of ORB1 and ORB2 suggested that high IMEP correlated with high HRR levels and that ORB2 showed lower IMEP levels compared to ORB1 for the majority of the cases due to more gradual HRR rise caused by improved air-fuel mixing as a result of its higher re-entrance curvature. The poor IMEP levels of FRB in comparison to ORB1 was obviously due to lower HRR levels.

Figure 5-11 shows the behaviour of the IMEP and combustion noise for the FRB, ORB1 and ORB2 as a function of injection timing. The IMEP and noise levels generated from each bowl geometry reduced as injection timing was retarded. Here, the noise levels of ORB1 and ORB2 under retardation are closely similar and lower compared to FRB. In addition, the FRB exhibited a noticeably higher noise level when its IMEP level is very similar compared to ORB1 and ORB2 in LL-5050-(5a,15a)TDC. This suggested that apart from the existing correlation between IMEP and combustion noise under injection timing retardation, there exists a correlation between bowl re-entrance curvature and combustion noise. This was seen as the FRB which had the lowest IMEP levels in a majority of the cases exhibited the highest combustion noise levels in those cases however, negligible.

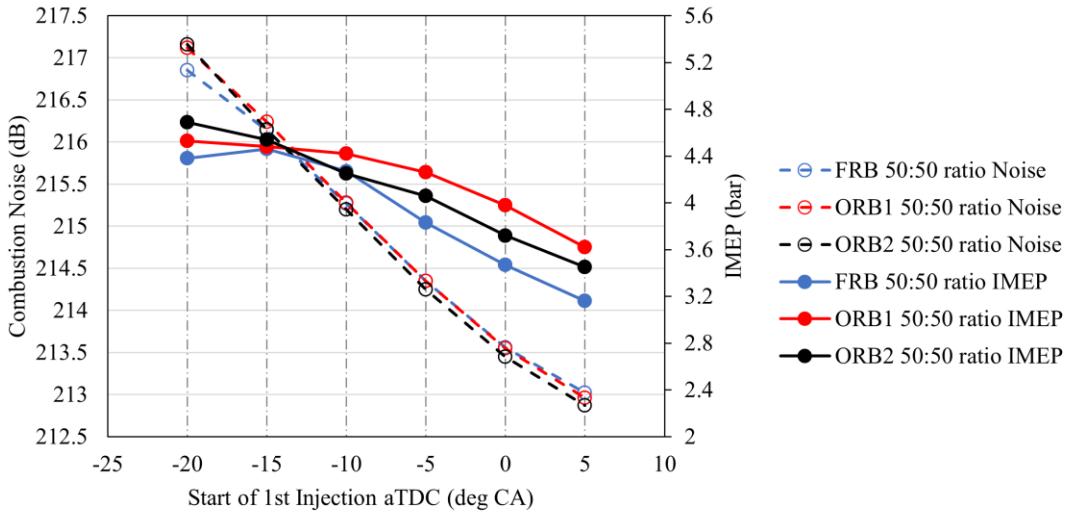

Figure 5-11: Combustion noise vs IMEP for FRB, ORB1 and ORB2 under 50:50 injection ratio at high load

5.3.2 70:30 Injection Ratio

The influence of the FRB, ORB1 and ORB2 on IMEP, ISFC and combustion noise under the 70:30 injection ratio at high load can be seen in Table 5-2. From an overview, an increase in IMEP correlated to a decrease in ISFC. This behaviour was also observed under the influence of injection timing seen in Figure 5-12. Here, IMEP decreased while ISFC increased as the injection timing was retarded from HL-7030-(20b,10b)TDC to HL-7030-(5a,15a)TDC.

ORB2 exhibited the highest IMEP levels as injection timing was retarded from HL-7030-(20b,10b)TDC to HL-7030-(15b,5b)TDC. Its IMEP level reduced to a point where it was higher and lower than the IMEP levels of the FRB and ORB2, respectively, as the injection timing was retarded whilst the IMEP level for ORB1 increased above its levels as the injection timing was retarded beyond HL-7030-(10b,0)TDC.

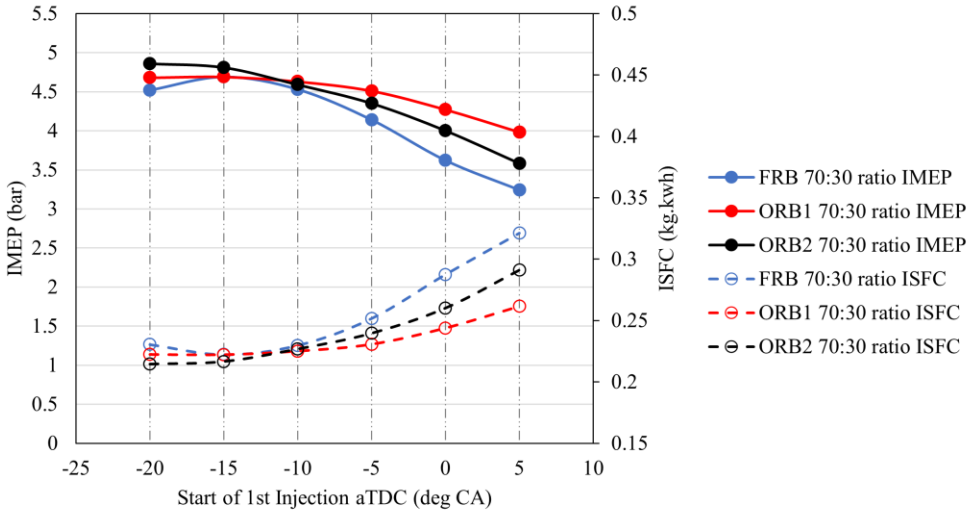

Figure 5-12: IMEP vs ISFC for FRB, ORB1 and ORB2 under 70:30 injection ratio at high load

The results presented in Table 5-2 also showed a correlation between IMEP levels and bowl geometries with higher degrees of re-entrance curvature. ORB2 and ORB1 were seen to exhibit higher IMEP levels compared to FRB with ORB2 exhibiting the highest IMEP level in HL-7030-(20b,10b)TDC and HL-7030-(15b,5b)TDC cases. Interestingly, the FRB and ORB1 exhibited equal IMEP levels for HL-7030-(15b,5b)TDC. Furthermore, ORB1 exhibited the highest IMEP levels of the three geometries in HL-7030-(10b0)TDC, HL-7030-(5b,5a)TDC, HL-7030-(0,10a)TDC and HL-7030-(5a,15a)TDC cases. In these cases, the ORB2 IMEP levels were higher than those of FRB and correspondingly 0.86%, 3.54%, and 10.05% lower compared to the respective IMEP levels of ORB1.

The results showed that ORB1 exhibited a strong promotion of IMEP while ORB2 performed better than FRB. The IMEP behaviour of ORB1 and ORB2 suggested that high IMEP correlated with high HRR levels and that ORB2 showed lower IMEP levels compared to ORB1 for the majority of the cases due to more gradual HRR rise caused by improved air-fuel mixing as a result of higher re-entrance curvature. The poor IMEP levels of FRB in comparison to ORB1 was attributed to its lower HRR levels compared to ORB1 and ORB2. It can be seen that despite the FRB exhibiting the highest HRR peak level in the premixed combustion phase for the HL-7030-(5a,15a)TDC case, this did not result in higher IMEP due to its short duration. Here combustion duration in both phases was observed to influence IMEP levels.

Figure 5-13 shows the behaviour of the IMEP and combustion noise of the three bowl geometries as a function of injection timing. The results showed that IMEP and combustion noise levels for the FRB, ORB1 and ORB2 reduced as injection timing was retarded. Here, the combustion noise levels of ORB1 and ORB2 under retardation exhibited a closer and similar trend which was higher compared to FRB for the HL-7030-(20b,10b)TDC case. However, the FRB and ORB2 combustion noise levels exhibited a closer and similar trend from HL-7030-(15b,5b)TDC to HL-7030-(10b0)TDC, HL-7030-(5b,5a)TDC, HL-7030-(0,10a)TDC and lastly, HL-7030-(5,15a)TDC.

Furthermore, ORB1 exhibited higher combustion noise compared to FRB and ORB2 as the injection timing was retarded. Interestingly, the results showed that while ORB2 exhibited IMEP levels that were closer to ORB1, its combustion noise levels were closer to those of the FRB as injection timing was retarded. This suggested that the IMEP-Noise correlation with bowl re-entrance curvature observed under the 50:50 ratio was also present here even though it was negligible. Here, the FRB which had the lowest degree of re-entrance curvature compared to ORB2 exhibited lower IMEP levels compared to ORB2 as well as higher combustion noise compared to ORB2 however negligible.

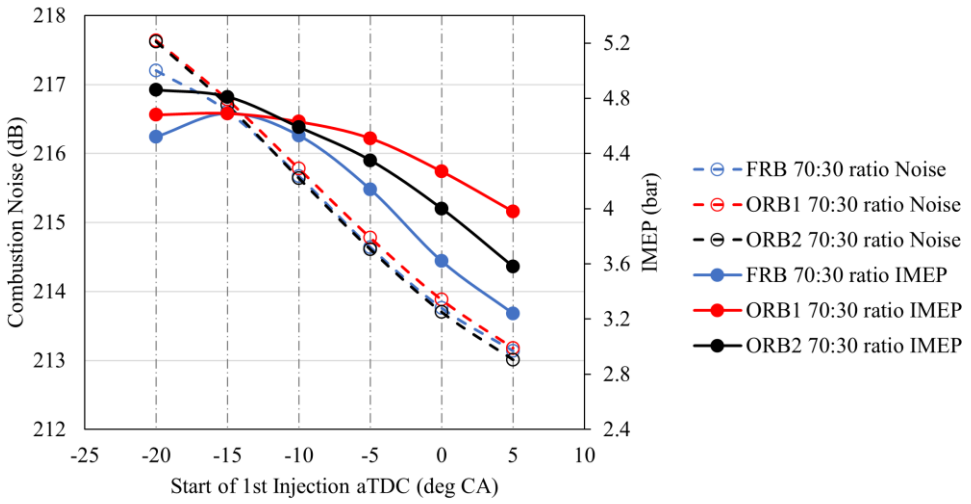

Figure 5-13: Combustion noise vs IMEP for FRB, ORB1 and ORB2 under 70:30 injection ratio at high load

5.3.3 Comparison of 50:50 and 70:30 Injection Ratios Cases

The behaviour of the three bowl geometries due to the influence of the 50:50 and 70:30 injection ratios at high load could be obtained from a cross comparison of the IMEP, ISFC and combustion noise results for each case. A comparison of these performance results showed that the cases under the 70:30 injection ratio exhibited higher IMEP, higher combustion noise and lower ISFC compared to the same cases under the 50:50 injection ratio. The observed trend was attributed to the fact that 70% of the total fuel quantity is injected during the first injection in the case 70:30 injection strategy which caused higher HRR compared to the 50:50 injection strategy. Here, higher HRR levels led to higher combustion temperatures and pressures consequently leading to higher IMEP levels.

Furthermore, the cases under the 70:30 ratio exhibited higher combustion noise levels compared to the same cases under the 50:50 ratio. This behaviour is attributed to the chamber reflection and pressure fluctuation phenomenon previously established in the IMEP-Noise relationship as well as in previous sections.

Table 5-2: Performance results for FRB, ORB1 and ORB2 at high load

Case ID	FRB			ORB1			ORB2		
	IMEP (bar)	ISFC (kg/kwh)	Combustion Noise (dB)	IMEP (bar)	ISFC (kg/kwh)	Combustion Noise (dB)	IMEP (bar)	ISFC (kg/kwh)	Combustion Noise (dB)
HL-5050-(20b,10b)TDC	4.38	0.2376	216.85	4.53	0.2296	217.12	4.69	0.2220	217.16
HL-5050-(15b,5b)TDC	4.46	0.2334	216.14	4.48	0.2323	216.24	4.54	0.2294	216.15
HL-5050-(10b,0)TDC	4.27	0.2436	215.27	4.42	0.2357	215.28	4.25	0.2449	215.20
HL-5050-(5b, 5a)TDC	3.83	0.2717	214.35	4.26	0.2443	214.35	4.06	0.2565	214.25
HL-5050-(0, 10a)TDC	3.47	0.3002	213.56	3.98	0.2616	213.55	3.72	0.2800	213.45
HL-5050-(5a,15a)TDC	3.16	0.3291	213.02	3.62	0.2873	212.96	3.45	0.3020	212.87
HL-7030-(20b,10b)TDC	4.52	0.2304	217.20	4.68	0.2223	217.64	4.86	0.2144	217.62
HL-7030-(15b,5b)TDC	4.69	0.2222	216.61	4.69	0.2221	216.78	4.81	0.2165	216.70
HL-7030-(10b,0)TDC	4.53	0.2297	215.67	4.63	0.2250	215.78	4.59	0.2267	215.64
HL-7030-(5b,5a)TDC	4.14	0.2516	214.64	4.51	0.2306	214.78	4.35	0.2395	214.61
HL-7030-(0,10a)TDC	3.62	0.2874	213.76	4.27	0.2438	213.88	4.00	0.2600	213.70
HL-7030-(5a,15a)TDC	3.24	0.3211	213.14	3.98	0.2615	213.18	3.58	0.2909	213.01

5.4 Emissions Analysis at High Load

The NOx and Soot emissions of the injection cases using the FRB, ORB1 and ORB2 piston bowl geometries for the 50:50 and 70:30 injection ratios were analysed. An overview of the emission results for both injection ratios showed that the NOx and soot emission formations were attributed to two interactions, the interaction between the respective bowl geometries and injection ratio at a constant injection timing and the interaction between the bowl geometries and injection ratio at retarding injection timing.

5.4.1 50:50 Injection Ratio

The NOx and soot emissions exhibited by FRB, ORB1 and ORB2 for the 50:50 injection ratio at high load is presented in Table 5-3. Considering the interaction between the bowl geometries and injection ratio in the individual cases for NOx emissions, the results showed that ORB1 exhibited the highest NOx levels in each of the cases whereas ORB2 exhibited the lowest NOx levels in each of the cases except for HL-5050-(20b,10b)TDC in which FRB exhibited the lowest NOx level.

Table 5-3: 50:50 injection ratio emissions results for FRB, ORB1 and ORB2 at high load

Case ID	**FRB**		**ORB1**		**ORB2**	
	NOx (ppm)	**Soot (ppm)**	**NOx (ppm)**	**Soot (ppm)**	**NOx (ppm)**	**Soot (ppm)**
HL-5050-(20b,10b)TDC	2095.3	45.5	2586.33	2.07	2237.41	10.02
HL-5050-(15b,5b)TDC	1159.5	52.7	1392.22	4.48	1041.03	26.1
HL-5050-(10b,0)TDC	622.43	77.05	807.98	8.21	488.43	56.3
HL-5050-(5b, 5a)TDC	348.67	70.71	479.35	14.25	232.22	57.0
HL-5050-(0, 10a)TDC	224.07	133.4	256.85	39.01	127.59	60.2
HL-5050-(5a,15a)TDC	99.54	131.5	138.68	50.4	60.86	45.2

This behaviour suggested that the bowl re-entrance curvatures influenced combustion behaviour and consequently NOx formation through the air utilisation during air-fuel mixing and mixture temperature distribution within the chamber. The NOx results for ORB1 and ORB2 showed a duality which arises from bowl assisted turbulent air-fuel mixing. Both ORB1 and ORB2 exhibited improved air-fuel mixing and movement of

fuel rich mixtures throughout the chamber compared to the FRB. The duality with regards to the bowl geometries was such that on one hand, improved air-fuel mixing led to higher NOx formation due to the formation of more premixed mixtures which caused high premixed HRR levels, combustion, and thus high combustion temperatures. On the other hand, improved air-fuel mixing also resulted in the more gradual rise in HRR along with relatively lower combustion temperatures which led to lower NOx formation. These two sides of the duality were primarily influenced by the degree of re-entrance curvature.

The behaviour exhibited in ORB1 was clearly the former side of this duality wherein improved air-fuel mixing caused by its bowl orientation, especially the bowl base radius, led to high HRR levels which promoted high combustion temperature thus higher NOx formation. In addition, its bowl re-entrance was shallow which promoted localised movement of mixing formations rather than a globalised movement. Localised movements promoted the presence and isolation of more temperature hotspots which promoted NOx formation reaction. Figure 5-14 shows the ORB1 temperature distribution and NOx formation illustrating this behaviour which can be compared to that of ORB2 presented in Figure 5-15.

The behaviour exhibited in ORB2 was the later side of the duality wherein improved air-fuel mixing caused by its larger and deeper radius of curvature in its bowl base led to leaner mixture formations which resulted in a more gradual HRR and lower combustion temperature that led to lower NOx formation. In addition, its bowl base radius promoted more re-entrance of mixtures into the centre and squish regions of the bowl thus reducing the presence and intensity of temperature hotspots through a better distribution of in-cylinder temperature.

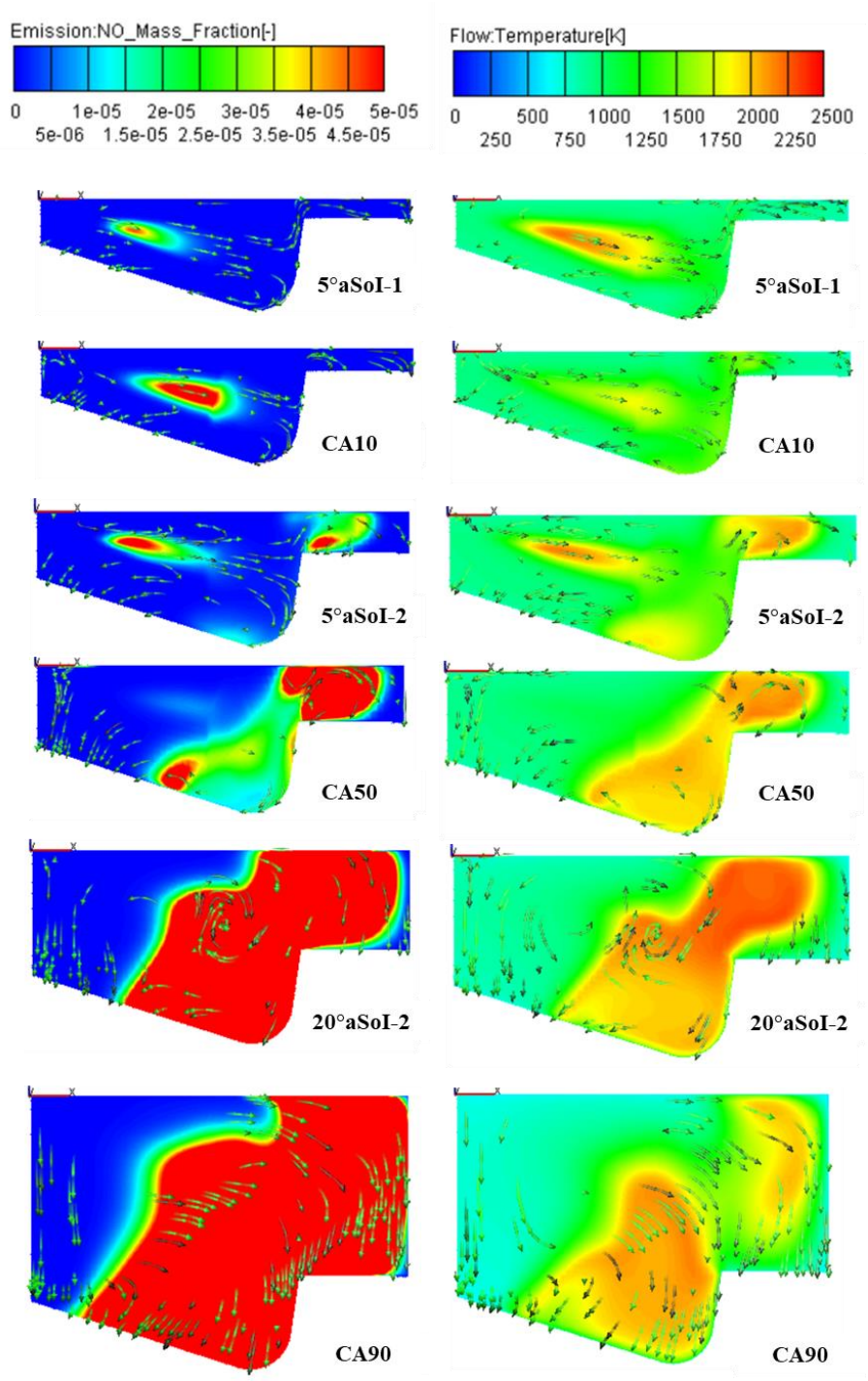

Figure 5-14: NOx and in-cylinder temperature distribution of ORB1 for the HL-5050-(0,10a)TDC case including 10%, 50% and 90% heat release timings

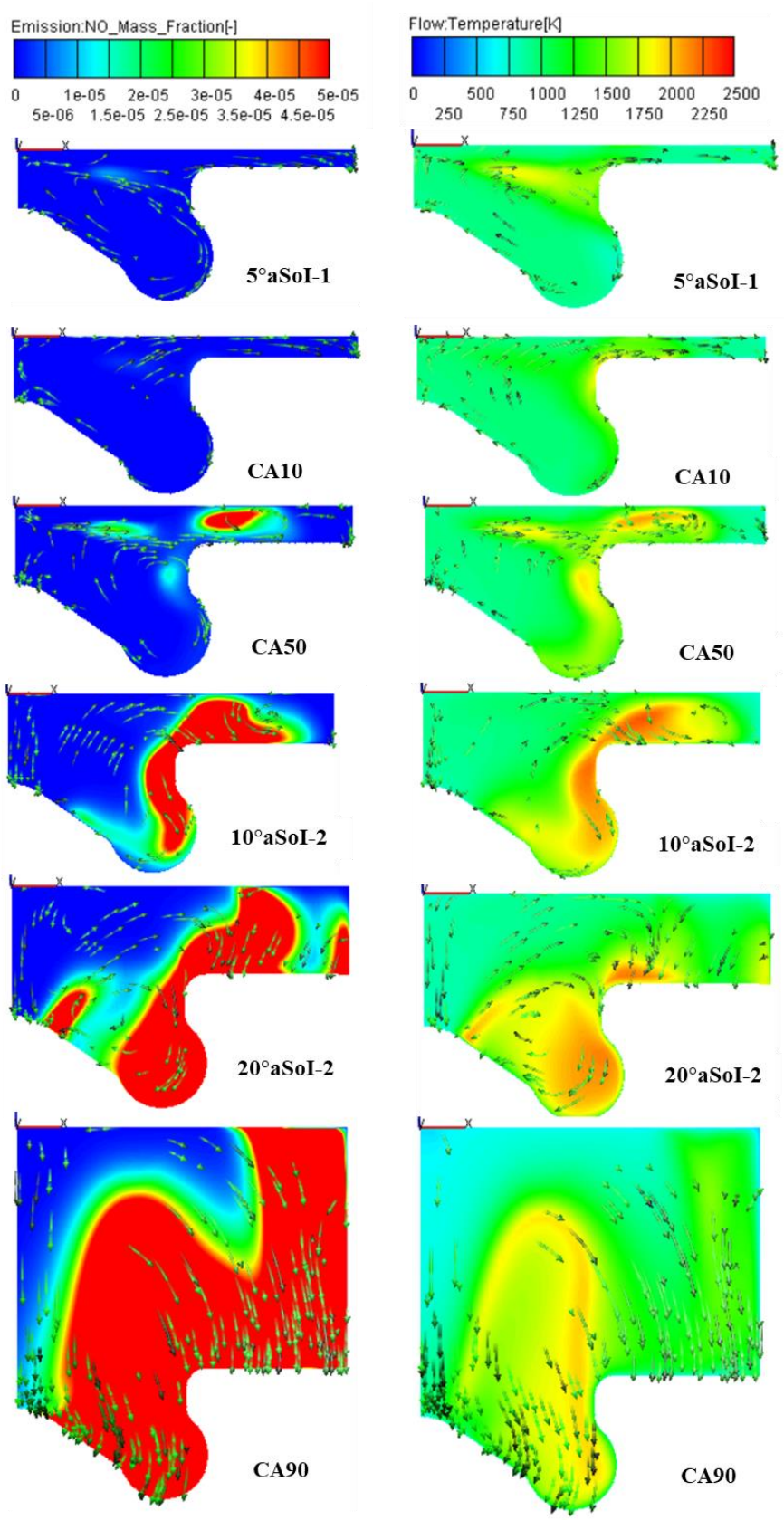

Figure 5-15: NOx and in-cylinder temperature distribution of ORB2 for the HL-5050-(0,10a)TDC case including 10%, 50% and 90% heat release timings

Considering the interaction between the bowl geometries and injection ratio in the individual cases for soot emissions, the results showed the FRB exhibited the highest soot levels for each case whereas ORB1 exhibited the lowest soot level for each case except for HL-5050-(5a,15a)TDC in which ORB2 exhibited the lowest soot level. As previously observed for the NOx formation, this behaviour suggested that the bowl re-entrance curvatures influenced combustion behaviour and consequently the formation of soot through the air-mixing behaviour.

FRB exhibited high soot levels attributed to a lack of re-entrance curvature in its bowl orientation. As seen in the equivalence ratio results for FRB, a lack re-entrance curvature in the FRB caused minimal dispersion of fuel rich mixtures globally throughout the chamber movement contributed to poor fuel oxidation, high diffusion mixing and combustion and consequently promoted the formation of soot. The behaviour of ORB1 in the majority of the cases was attributed to the NOx-soot trade off. In addition, its shallow re-entrance curvature reduced the interaction between the mixing formations from the first injection event and the fuel introduced in the second injection event which resulted in less fuel rich diffusion mixing and thus reduced soot formation. As seen in Figure 5-16, the re-entrance profile of ORB1 results in an outwash which causes the bulk fuel rich mixture to split with a small section surrounded by air at the top of the chamber which promotes further soot oxidation compared to the same time in ORB2 in which less air surrounds the fuel rich mixture at the top of the chamber. The results in the figure also show that well into the expansion stroke the bulk fuel mixture is divided into two portions in ORB1 thus improved fuel and soot oxidation compared to ORB2 wherein the fuel rich mixtures are all together leading to high soot formations .

ORB2 exhibited higher soot levels compared to those of ORB1 which also suggested that piston bowl re-entrance curvature had no direct correlation with soot reduction in every instance. The behaviour exhibited in ORB2 was attributed to fuel rich mixtures of the bowl wall (i.e., opposite the mixing front) as well as the occurrence of the second injection event into fuel mixtures from the first injection event which increased diffusion mixing and thus increased soot formation.

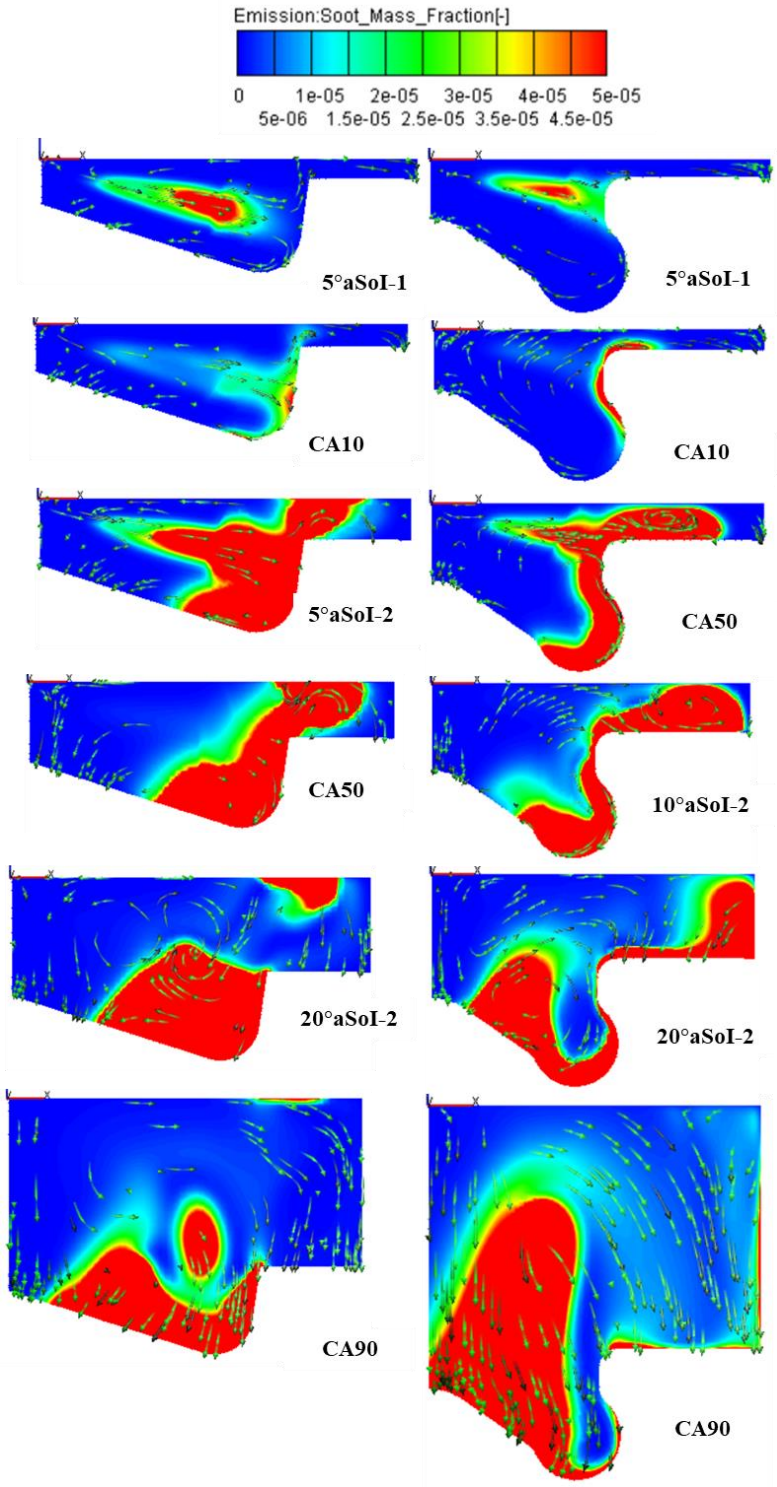

Figure 5-16: Soot distribution of ORB1 and ORB2 for the HL-5050-(0,10a)TDC case including 10%, 50% and 90% heat release timings

Considering the interaction between the bowl geometries and injection ratios at retarding injection timing, Figure 5-17 presents the NOx and Soot emission trends for FRB, ORB1 and ORB2.

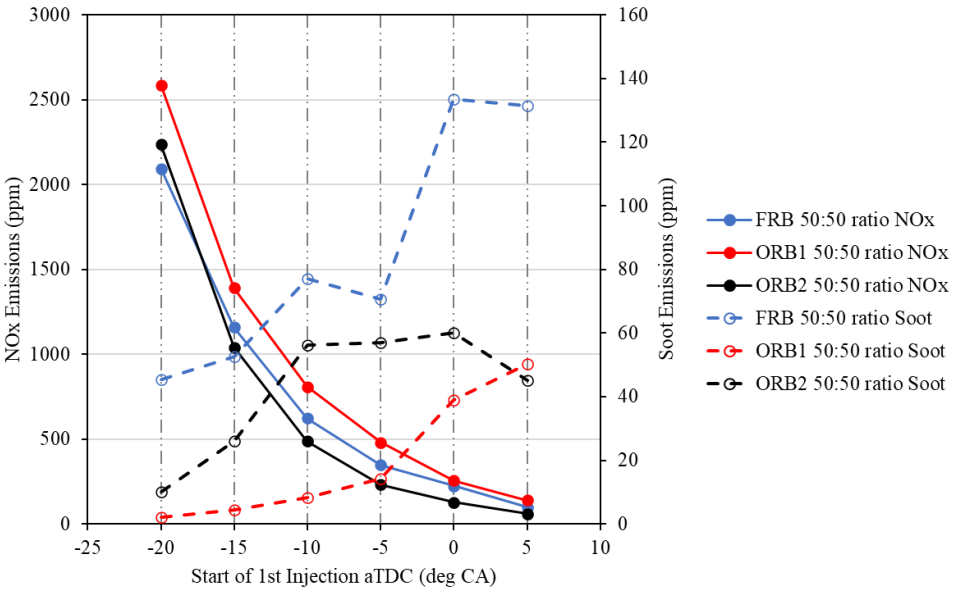

Figure 5-17: NOx vs soot emissions for FRB, ORB1 and ORB2 under 50:50 injection ratio at high load

Regarding the NOx emission trends, the results showed that the NOx levels for all three bowl geometries reduced as injection timing was retarded. This was attributed to improved fuel evaporation closer to TDC due to higher in-cylinder temperature as the fuel injection timing was retarded. This led to shorter ignition delay and insufficient air-fuel mixing time, hence premixed HRR levels were lower which resulted in lower combustion temperatures thus lower NOx emissions for the cases when the fuel injection took place closer to TDC. In the cases when fuel injection occurred after and farther away from TDC, lower NOx emissions were attributed to combustion occurring in lower temperatures due to the increase in in-cylinder volume during the expansion stroke.

Regarding the soot emission trends, the results showed an increasing trend in soot levels for all three bowl geometries as injection timing was retarded. Nevertheless, each bowl geometry exhibited different behaviours at different timings. For the FRB, soot levels increased with a retardation from HL-5050-(20b,10b)TDC to HL-5050-(10b,0)TDC, reduced at HL-5050-(5b,5a)TDC, increased at HL-5050-(0,10a)TDC and slightly reduced at the last retardation to HL-5050-(5a,15a)TDC. For ORB1 and ORB2, soot levels increased throughout the range of injection timing retardation except for the soot level reduction in the last retardation for ORB2.

The results suggested that ORB1 and ORB2 followed a similar trend in their soot levels except for the last retardation step while the FRB followed a contrasting trend.

Nevertheless, the large deviations observed between the FRB, ORB1 and ORB2 implied that the influence of bowl orientation on emissions was significant.

5.4.2 70:30 Injection Ratio

The NOx and Soot emissions exhibited by FRB, ORB1 and ORB2 under the 70:30 injection ratio at high load is presented in Table 5-4. Considering the interaction between the bowl geometries and injection ratio in the individual cases for NOx emissions, the results showed that ORB1 exhibited the highest NOx levels in each of the cases whereas ORB2 exhibited the lowest NOx levels in each of the cases except for HL-5050-(20b,10b)TDC in which FRB exhibited the lowest NOx level also observed in the 50:50 injection ratio results.

Table 5-4: 70:30 injection ratio emissions results for FRB, ORB1 and ORB2 at high load

Case ID	**FRB**		**ORB1**		**ORB2**	
	NOx (ppm)	**Soot (ppm)**	**NOx (ppm)**	**Soot (ppm)**	**NOx (ppm)**	**Soot (ppm)**
HL-7030-(20b,10b)TDC	2366.9	130.51	3844.42	31.99	3146.63	68.48
HL-7030-(15b,5b)TDC	1586.5	138.85	2193.73	46.20	1472.47	68.30
HL-7030-(10b,0)TDC	808.59	133.78	1241.52	49.94	653.51	63.22
HL-7030-(5b,5a)TDC	400.74	134.80	701.53	47.84	347.46	74.86
HL-7030-(0,10a)TDC	272.25	176.31	382.23	56.12	184.01	94.82
HL-7030-(5a,15a)TDC	161.93	138.44	229.57	54.61	72.17	101.23

It seemed from the results that a shallow re-entrance curvature led to an increase in NOx, however, this notion was not plausible considering that FRB had no re-entrance curvature but led to a decrease in NOx levels. ORB1 and ORB2 exhibited increased bowl assisted turbulent mixing provided by their respective bowl re-entrance curvatures especially during the first fuel injection in which 70% of the total fuel load was injected. However, there was a contrasting NOx behaviour exhibited by both geometries which could be attributed to the shape of their respective re-entrance curvature profiles which caused significantly different NOx behaviours.

This was because of the duality which arises from improved air-fuel mixing and the presence of premixtures. This duality is such that improved air-fuel mixing on one hand, promotes high HRR due to premixed combustion leading to high combustion temperatures thus high NOx formation as exhibited by ORB1 while on the other hand, promotes a gradual rise in HRR leading to lower temperature and thus lower NOx formation as exhibited by ORB2. Figure 5-18 presents the NOx and temperature distribution for ORB1 illustrating the NOx formation dependency on temperature hotspots which is linked to the air-fuel mixing behaviour compared to that of ORB2 presented in Figure 5-19.

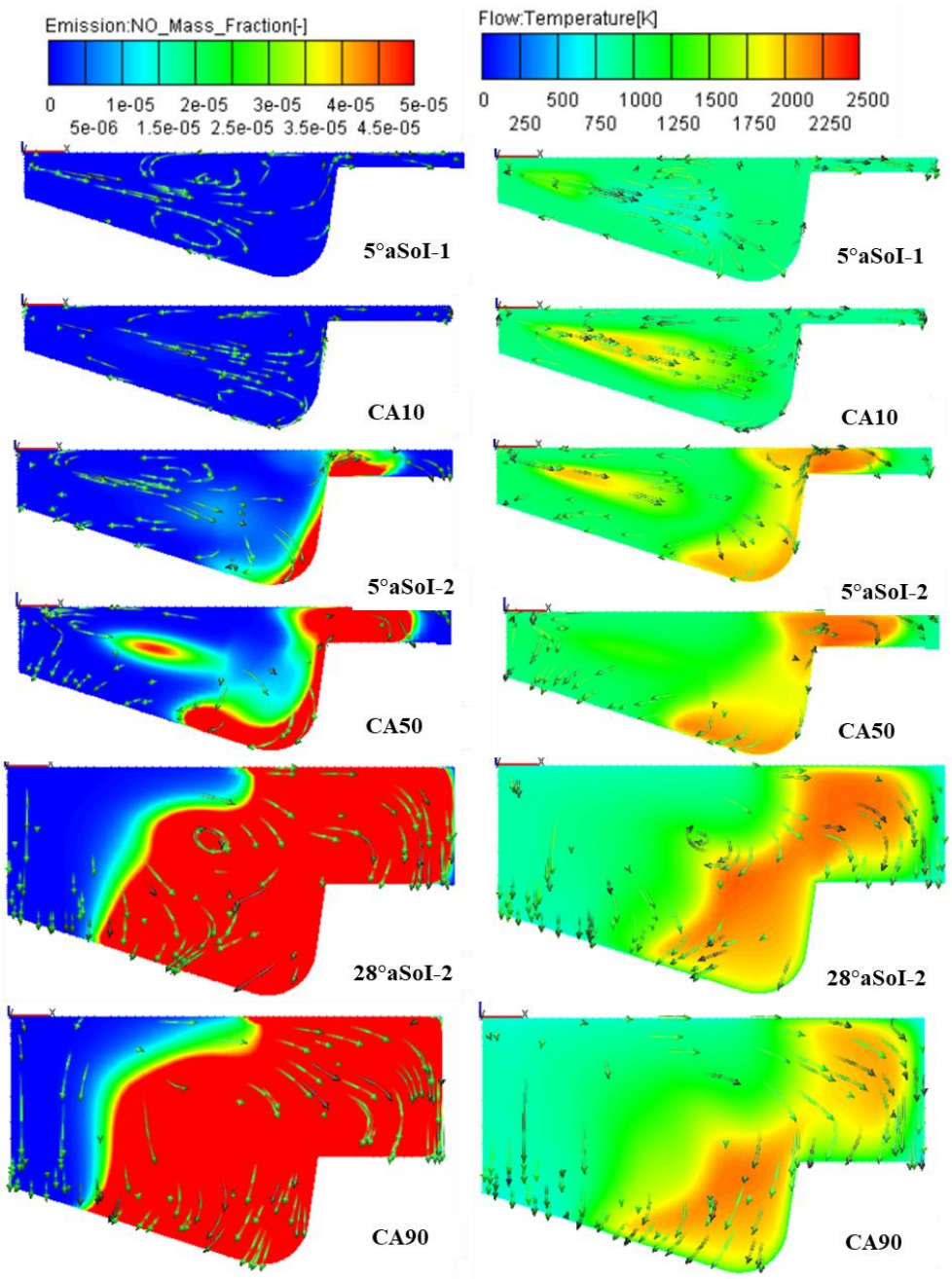

Figure 5-18: NOx and in-cylinder temperature distribution of ORB1 for the HL-7030-(5b,5a)TDC case including 10%, 50% and 90% heat release timings

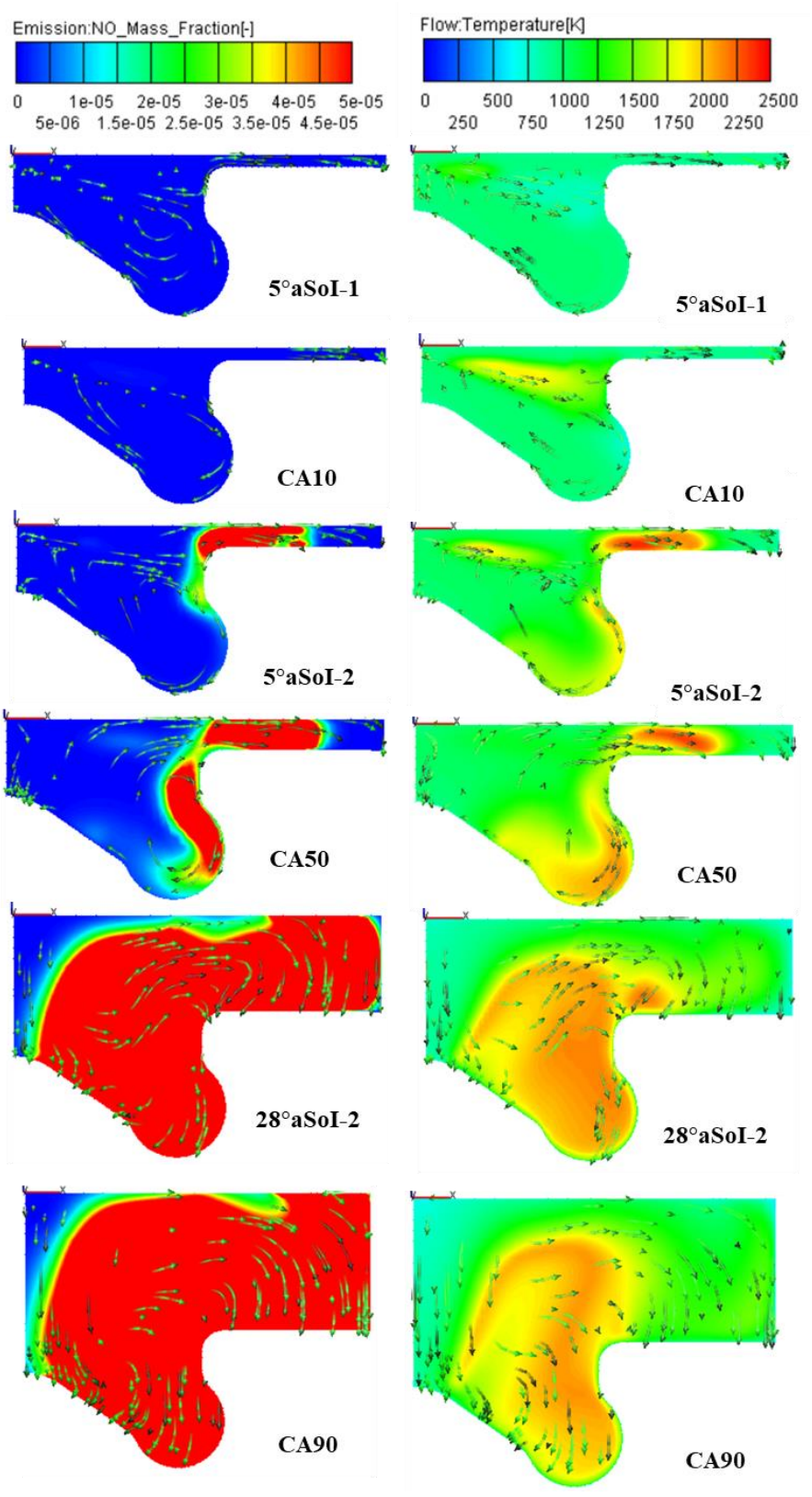

Figure 5-19: NOx and in-cylinder temperature distribution of ORB2 for the HL-7030-(5b,5a)TDC case including 10%, 50% and 90% heat release timings

Another contributing factor was the movement of in-cylinder mixing formations wherein slower and localised movements led to a larger presence of temperature hotspots while faster and more globalised movements led to a smaller presence of temperature hotspots due to enhanced temperature distribution within the chamber. Since ORB1 possessed a shallow re-entrance curvature compared to ORB2, it resulted in a more localised movement of mixing formations thus resulting in higher NOx levels.
ORB2 on the other hand exhibited lower NOx levels compared to ORB1 because its in-cylinder environment resulted in a more gradual HRR rise, lower peak HRR levels as seen in the HRR results and therefore lower combustion temperatures and NOx levels. Furthermore, its bowl orientation provided a more globalised movement of mixing formations compared to ORB1, thereby reducing the quantity of temperature hotspot regions in the chamber, causing improved temperature distribution which also contributed to reduced NOx formation for ORB2.

Considering the interaction between the bowl geometries and injection ratio in the individual cases for soot emissions, the results showed that ORB1 and FRB exhibited the lowest and highest soot levels in all the cases, respectively, except for the HL-7030-(5a,15a)TDC case where, ORB2 and FRB exhibited the lowest and highest soot levels, respectively. Whilst the behaviour of ORB1 was largely attributed to the NOx-Soot trade-off, the FRB's behaviour was due to poor air-fuel mixing caused by its poor bowl re-entrance curvature. The FRB exhibited high soot levels due to the influence of its bowl re-entrance curvature and interaction with the injection ratio.

It can be seen from the equivalence ratio and soot formation results that the FRB's poor bowl orientation resulted in poor air-fuel mixing and hence promoted the formation of rich mixtures and diffusion mixing wherein low oxygen quantities present in the chamber inadequately mixed with the remnant and newly introduced fuel parcels. This in turn led to poor carbon oxidation in high combustion temperature regions thus, high soot formations. Although the results implied that bowls with a high re-entrance curvature led to soot reduction as seen in ORB1 and ORB2, no correlative proportionality between the degree of re-entrance curvature and the extent of soot reduction was formed. While ORB1 and ORB2 were seen to exhibit lower soot emissions due to their higher degrees of re-entrance curvatures compared to the

FRB; ORB2 with a higher degree of bowl re-entrance curvature exhibited higher soot emissions compared to ORB1 as seen in Figure 5-20.

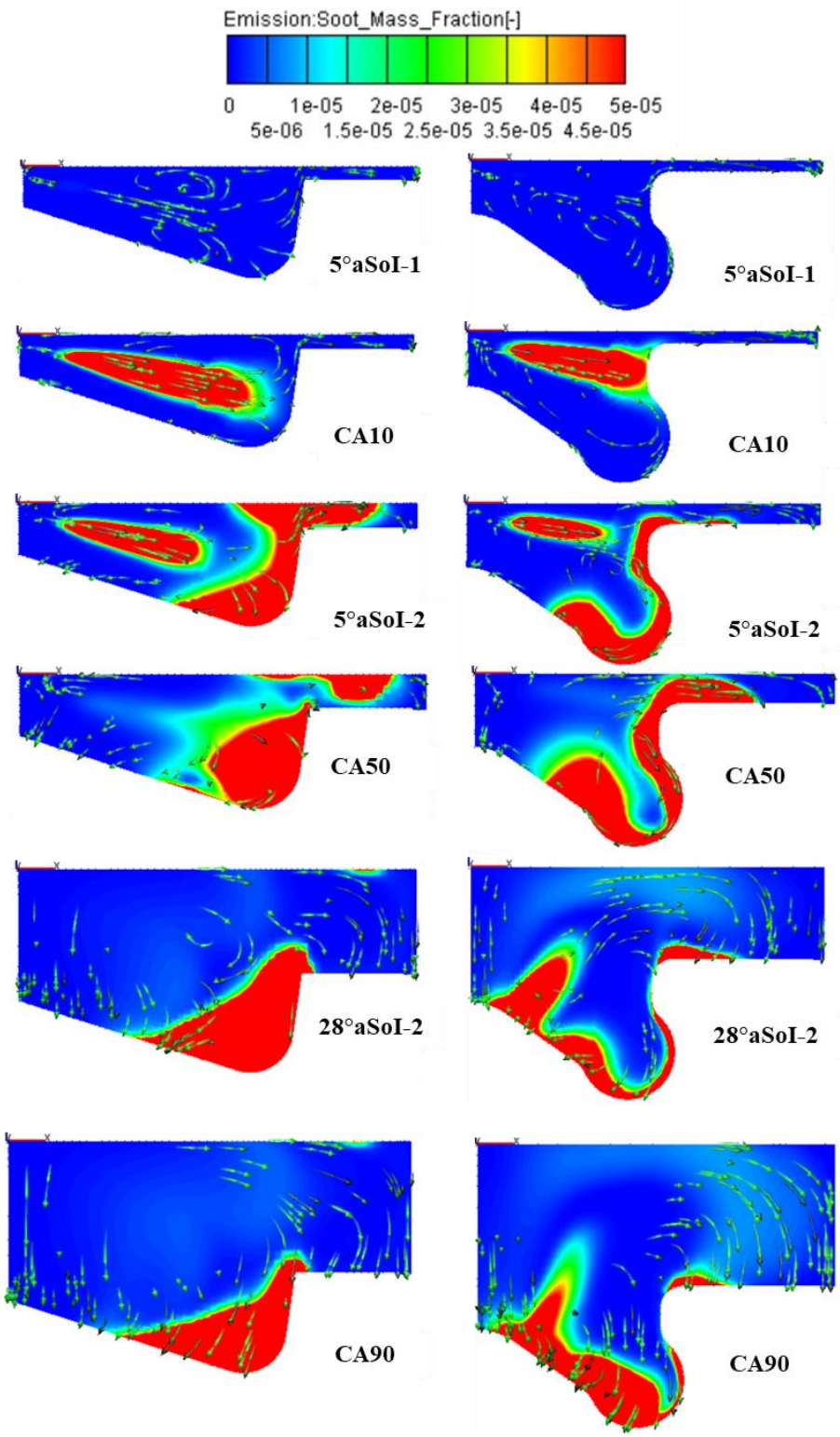

Figure 5-20: Soot distribution of ORB1 and ORB2 for the HL-5050-(5b,5a)TDC case including 10%, 50% and 90% heat release timings

Figure 5-21 shows the NOx and soot emissions for the FRB, ORB1 and ORB2 under the 70:30 injection ratio at high load as a function of injection timing. Considering NOx emissions under injection timing retardation, results showed that NOx levels for all three bowl geometries reduced as injection timing was retarded. This was attributed to improved fuel evaporation due to higher in-cylinder temperatures as the injection timing was retarded towards and closer to TDC. This led to an insufficient air-fuel mixing time as well as shorter ignition delay which caused the formation of smaller premixture quantities and combustion occurring at relatively lower temperatures which consequently contributed to lower NOx emissions. Considering the behaviour of the three bowl geometries, a large deviation was observed between ORB2 and FRB, ORB1 and ORB2 as well as ORB1 and FRB for the HL-7030-(20b,10b)TDC case. However, the deviation between ORB2 and FRB reduced as injection timing was retarded from HL-7030-(15b,5b)TDC to HL-7030-(5a,15a)TDC. This was different for the deviation between ORB1 and ORB2. Here, the deviation between ORB1 and ORB2 remained relatively large until HL-7030-(5b,5a)TDC after which it significantly reduced. This suggested that the retardation of the injection timing was more suitable for ORB2 compared to ORB1.

Considering the soot emissions, results showed that soot levels for all three bowl geometries exhibited a positive gradient as the injection timing was further retarded. The FRB exhibited a relatively similar soot level from HL-7030-(20b,10b)TDC to HL-7030-(5b,5a)TDC before exhibiting a large increase in soot levels at HL-7030-(0,10a)TDC and a decrease in soot levels at HL-7030-(5a,15a)TDC. ORB2 exhibited a relatively similar soot level from HL-7030-(20b,10b)TDC to HL-7030-(10b,0)TDC before exhibiting an increasing soot level from HL-7030-(10b,0)TDC to HL-7030-(5a,15a)TDC. ORB1 exhibited an increase in soot level from HL-7030-(20b,10b)TDC to HL-7030-(10b,0)TDC where the soot level remained relatively constant up to HL-7030-(5b,5a)TDC after which it increased for the HL-7030-(0,10a)TDC case and then remained constant for HL-7030(5a,10a)TDC. Apart from that, the soot levels for ORB1 and ORB2 from HL-7030-(20b,10b)TDC to HL-7030-(5b,5a)TDC exhibited contrasting trends after which they exhibited similar trends.
Nevertheless, the large deviations observed between the FRB and ORB1 and ORB2 implied that the influence of bowl orientation on emissions was significant.

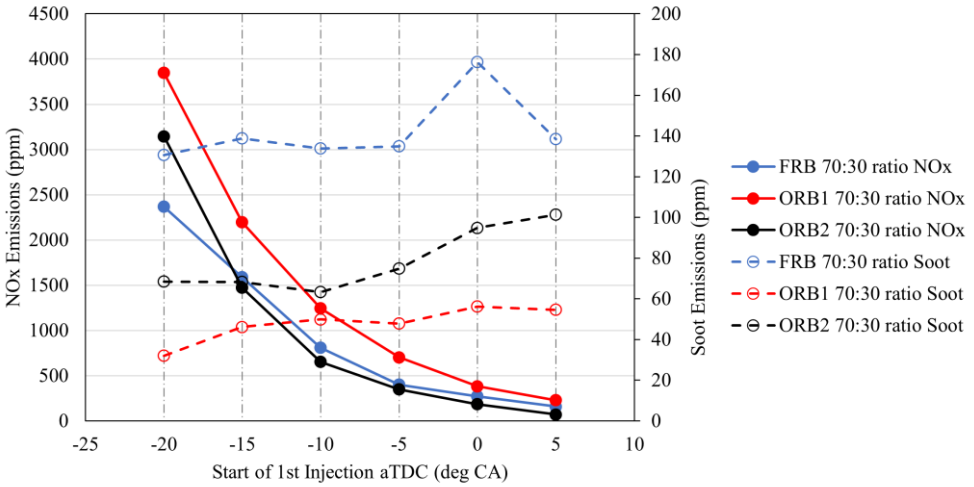

Figure 5-21: NOx vs soot emissions for FRB, ORB1 and ORB2 under 70:30 injection ratio at high load

5.4.3 Comparison of 50:50 and 70:30 Injection Ratios Cases

The NOx and soot emissions exhibited by the FRB, ORB1 and ORB2 under the 50:50 and 70:30 injection ratios at high load can be compared through a cross analysis of the results shown in Table 5-2. The comparison of the results showed that the cases under the 70:30 injection ratio resulted in higher NOx and lower soot emissions compared to the respective cases under the 50:50 injection ratio for all three bowl geometries. This behaviour was attributed to the injected fuel quantities in each injection in the two injection ratios.

In the 70:30 injection ratio, 70% of the total fuel quantity per cycle was injected during the first injection resulting in significantly higher HRR levels which led to higher combustion temperatures and NOx formation compared to the 50:50 injection ratio. The fuel quantity in the second injection was a major factor in the diffusion HRR levels and soot formation since newly introduced fuel parcels influenced the mixing rate and mixing formation. The second injection in the 70:30 injection ratio involved injection of 30% of the total fuel quantity per cycle. Soot formation was lower under this injection ratio compared to the 50:50 injection ratio because there was a smaller quantity of newly introduced fuel to mix with already depleted in-cylinder oxygen content.

ORB1 exhibited the highest NOx levels and lowest soot levels across most of the cases under both injection ratios. ORB2 exhibited the lowest NOx levels in most cases and exhibited soot levels that were between those of ORB1 and FRB for both injection ratios. Under the 50:50 injection ratio, FRB exhibited a negative gradient trend while ORB1 and ORB2 exhibited positive gradient trends as the fuel injection timing was retarded. This was slightly different to their behaviour under the 70:30 injection ratio wherein all three bowl geometries exhibited positive gradient trends with the FRB having the smallest gradient.

5.5 Concluding Remarks

The study presented in this chapter investigated the effects of the interaction between double injection strategy and piston bowl geometry on engine performance and emissions at high load. It focused on the 50:50 and 70:30 injection ratios over a range of six double injection strategies for the FRB, ORB1 and ORB2 piston bowl geometries, respectively. The investigation showed that the interaction between the different bowl geometries and injection ratios at constant or varying injection timings had varying impact on combustion behaviour due to different air utilisations during air-fuel mixing. This consequently resulted in the various differences in the in-cylinder performance and emissions observed. The influence of the injection ratios at constant injection timings on in-cylinder performance and emissions were investigated. The high load investigation showed that injection ratio imposed a stronger influence on performance and emissions compared to the influence of the piston bow geometries which was similar to the low load investigation.

The influence of retarding injection timing with the 50:50 and 70:30 injection ratios on in-cylinder performance and emissions were investigated. The results showed that with both injection ratios, the IMEP, combustion noise and NOx levels reduced while the soot and ISFC levels increased during injection timing retardation for high load conditions. This observation in addition to the observation from the influence of injection ratios showed that fuel injection characteristics had more influence on in-cylinder performance and emissions compared to that of piston bowl geometries.

The influence of the piston bowl geometries on in-cylinder performance and emissions were also investigated. At the high load conditions, ORB1 and ORB2 had higher IMEP levels compared to the FRB in all the injection strategies with ORB1

exhibiting highest IMEP levels in majority of the injection strategies of the 50:50 and 70:30 injection ratios. The largest difference in IMEP levels compared to FRB and ORB2 respectively were 22.8% and 11.58% in HL-7030-(5a,15a)TDC. In contrast to the low load conditions wherein the FRB exhibited obviously higher combustion noise in all the injection strategies accompanied by higher IMEP levels, the combustion noise levels were similar for all three bowl geometries in both injection ratio ratios. Considering the positive correlation between IMEP and combustion noise, this observation showed that ORB1 and ORB2 promoted better performance at high load compared to low load conditions. ORB1 had the highest NOx emissions in all the injection strategies for 50:50 and 70:30 injection ratios with its highest difference of 218% and 41.77% compared to ORB2 and FRB in the HL-7030-(5a,15a)TDC whereas the FRB had the highest soot emissions difference of 190% and 160% compared to ORB2 and ORB1 respectively in HL-5050-(5a,15a)TDC.

6 Piston Bowl Geometry Optimisation (Stage 1 of 2)

6.1 Introduction

The optimisation of the piston bowl geometry is stage 1 of the two-stage optimisation approach presented as the simple schematic workflow of the routine Figure 6.1. This stage involved an optimisation by analysis of the piston bowl geometries based on the inferences made in Chapter 4 for low load and Chapter 5 for high load.

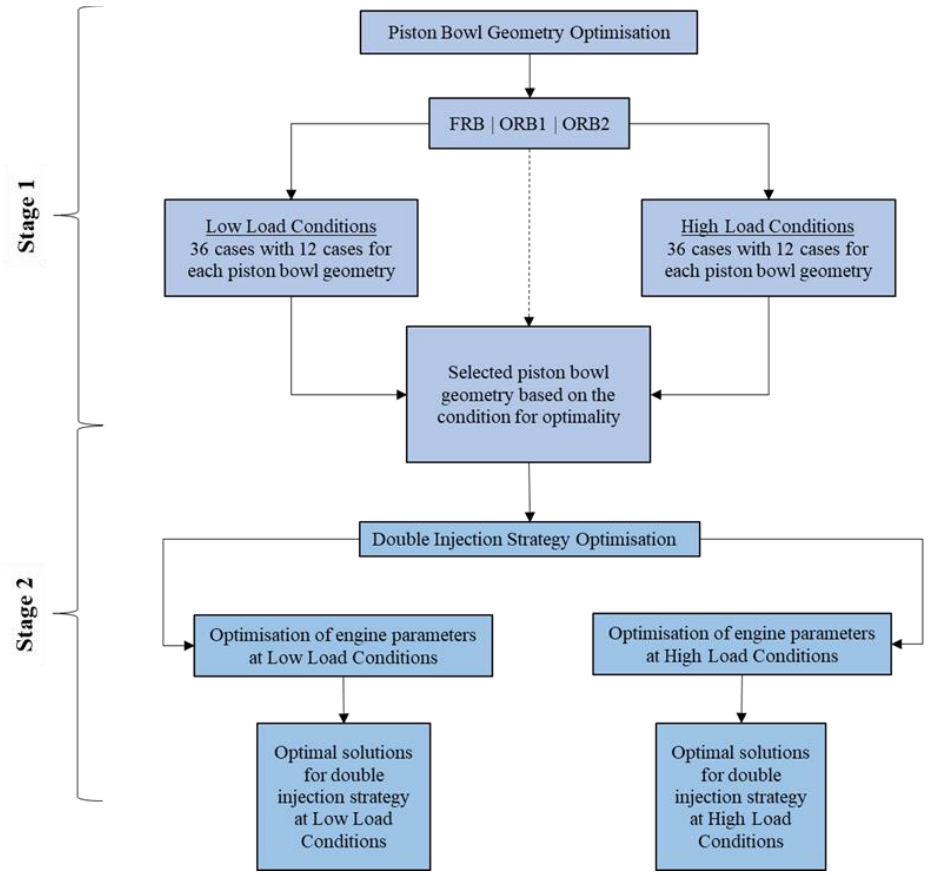

Figure 6-1: Workflow of the two-stage optimisation routine

In this optimisation, 36 design cases were analysed for each engine load. At each load, the double injection strategies considered consisted of six double injection timings for two injection ratios, respectively. The simultaneous optimisation of IMEP as well as minimisation of ISFC, combustion noise, NOx and soot were the set multi-objective criteria. Its focus was on obtaining a piston bowl geometry suitable in providing optimal solutions over a relatively wide range of double injection strategies. Figure 6-2 shows the 3D mesh orientation of the three piston bowl geometries at TDC. Distinctions between the bowl geometries were captured in this work as the degree of re-entrance curvature characterised by the inclination of the bowl base

towards the bowl and chamber top centre, the curvature of the bowl side wall as well as the curvature of the bottom corner which joined the bowl side wall and base as shown in Figure 6-2. Based on this, FRB, ORB1 and ORB2 exhibited the lowest, mid and the highest degrees of re-entrance curvature, respectively.

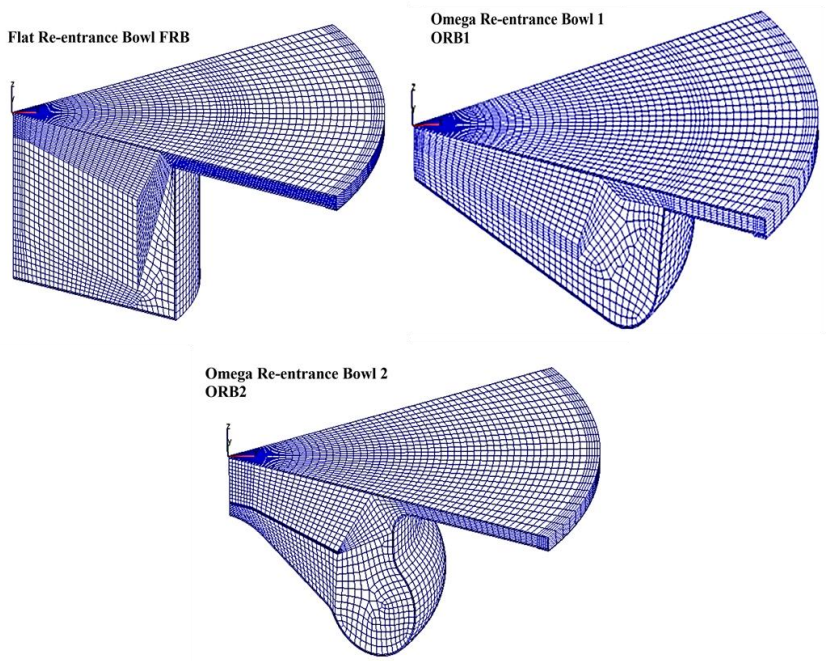

Figure 6-2: 3D mesh orientation of FRB, ORB1 and ORB2 bowl geometries at TDC

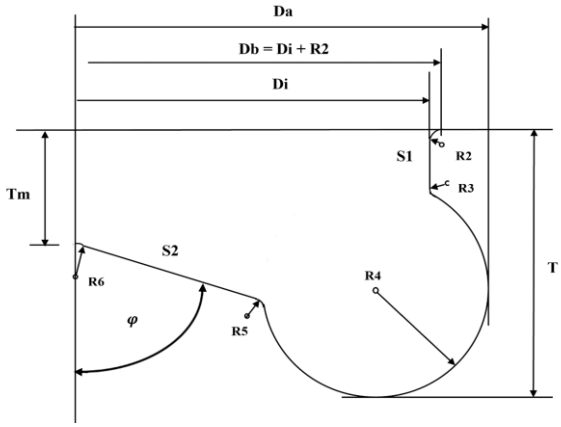

Figure 6-3: Schematic diagram of the piston bowl geometrical attributes

The re-entrance curvature is a vital characteristic of modern piston bowl geometries due to its influence on in-cylinder turbulence mixing, in-cylinder motion and status of near wall mixture (i.e., overly lean, lean, near-stoichiometric, and rich mixtures), oxygen utilisation, chamber temperature distribution within the chamber as well as mixing front area. Figure 6-3 shows the geometrical parameters of the three bowl geometries extracted into Table 6-1.

Table 6-1: Piston bowl geometrical attributes of FRB, ORB1 and ORB2

Parameters	Bowl Geometries		
	FRB	**ORB1**	**ORB2**
Da (m)	0.0434	-	0.05
Db (m)	0.0434	0.06143	0.0469
R2 (m)	-	-	0.0025
R3 (m)	-	-	0.0027
R4 (m)	-	0.0047	0.00581
R5 (m)	-	-	0.0024
R6 (m)	-	-	0.008
S1 (m)	-	0.0067	-
S2 (m)	-	0.02485	0.00237
T (m)	0.0166	0.01066	0.01699
Tm (m)	0.0166	0.00285	0.0052
φ (◦)	90	72.2287	55.1397

The increase in IMEP alongside simultaneous reduction in ISFC, combustion noise, NOx, and soot were the desired multi-objective outcome. Nevertheless, the reduction of NOx and soot emissions while maintaining marginal increase/decrease or similar IMEP, ISFC and combustion noise was also considered as an acceptable outcome.

6.2 Optimisation of Piston Bowl Geometries at Low Load

The multi-objective piston bowl geometry optimisation was captured through the objective spaces presented in Figure 6-4 to Figure 6-10 with the details of their combustion characteristics, performance and emissions previously presented in Chapter 4. It should be noted that the noise levels displayed in the results were closely similar and were only exaggerated to show negligible differences from the bowl geometries. An overview of the results showed no outstanding dominance by one bowl geometry over the other two bowl geometries in all the objective spaces which suggested a strong dependence on the fuel injection strategy despite any improvements made by the piston bowl geometry. The pareto front in the IMEP-NOx objective space seen in Figure 6-4 consisted mostly of FRB and ORB2 strategies

whereas the pareto front of the IMEP-noise objective space seen in Figure 6-5 consisted mostly of FRB strategies with few cases of ORB2 strategies. This showed that while the FRB promoted high IMEP levels accompanied by high NOx at a range of noise levels, ORB2 promoted high IMEP levels with lower NOx at similar noise levels.

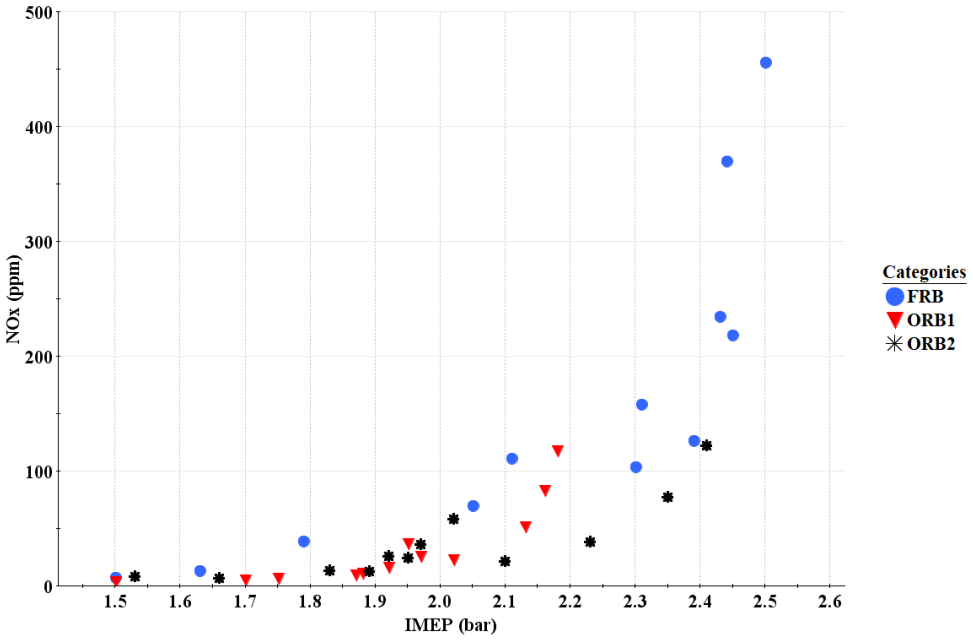

Figure 6-4: IMEP-NOx objective space of FRB, ORB1 and ORB2 at low load

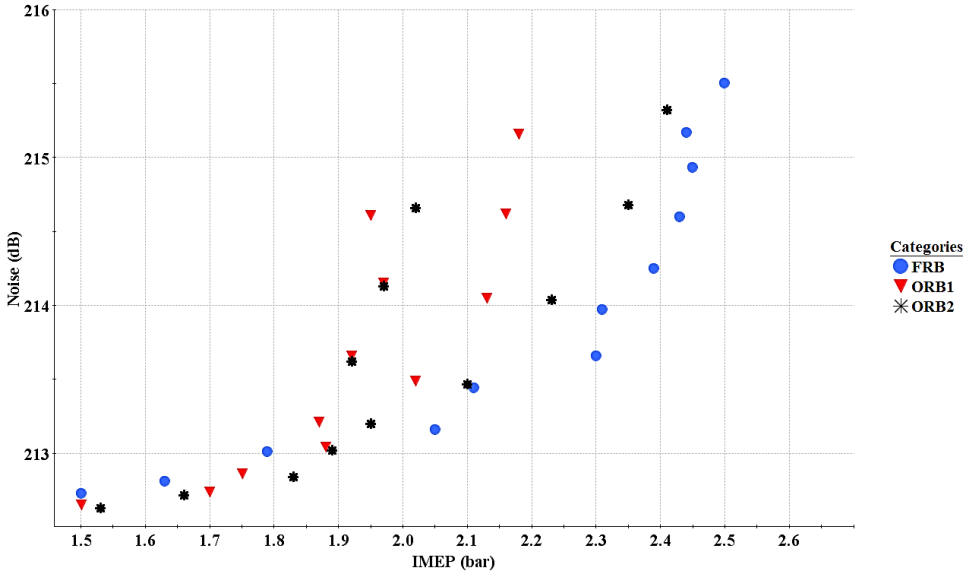

Figure 6-5: IMEP-noise objective space of FRB, ORB1 and ORB2 at low load

The NOx-soot and IMEP-soot objective spaces are presented in Figure 6-6 and Figure 6-7, respectively. In these results, a stratum between the strategies of each bowl

geometry with those of the FRB, ORB2 and ORB1 at the top, middle and bottom of the objective spaces, respectively, was observed. The pareto front of objective space consisted of primarily ORB1 and ORB2 strategies with very few strategies of FRB in the NOx-soot space which indicated that ORB1 and ORB2 were more preferrable compared to the FRB considering IMEP, NOx and soot. More importantly, these results showed that while ORB1 contributed to lower emissions, its IMEP levels were also lower than those of ORB2 which had slightly higher emissions in comparison.

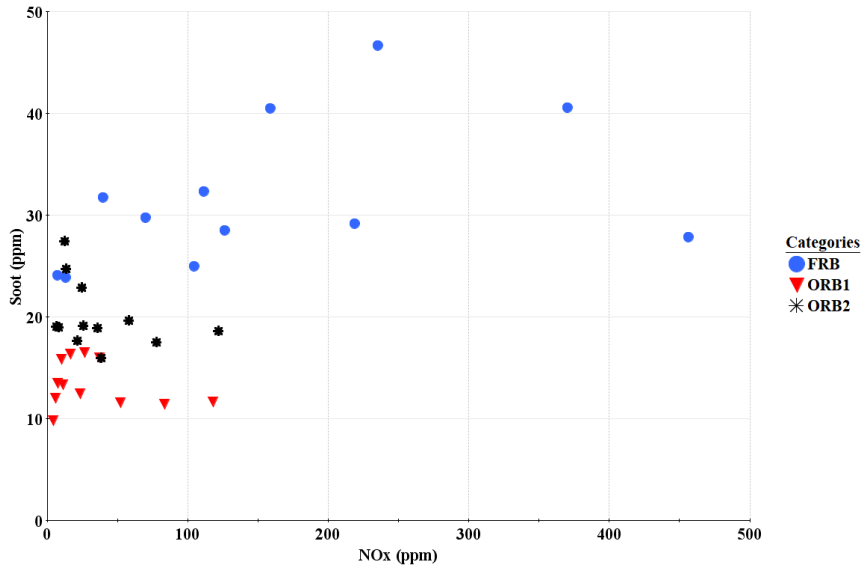

Figure 6-6: NOx-soot objective space of FRB, ORB1 and ORB2 at low load

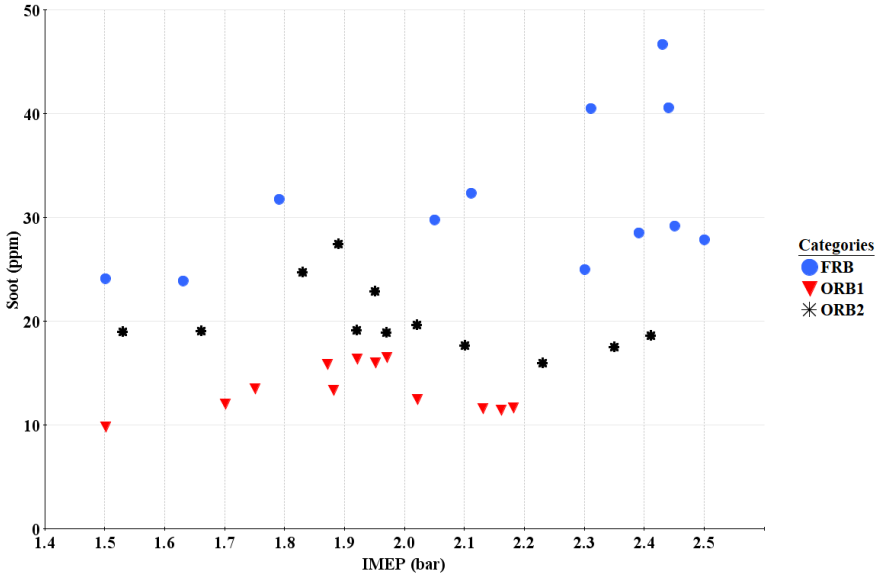

Figure 6-7: IMEP-soot objective space of FRB, ORB1 and ORB2 at low load

The pareto region in the IMEP-ISFC objective space, seen in Figure 6-8, consisted of FRB and ORB2 strategies whereas that of the NOx-noise objective space, seen in Figure 6-9, consisted of ORB1 and ORB2 strategies. Interestingly, the same stratum behaviour seen in the results of the NOx-soot and IMEP-soot spaces was also observed in the Noise-soot objective space, Figure 6-10. This behaviour was suggestively attributed to the soot behaviour of the bowl geometries since it was the common parameter across these objective spaces.

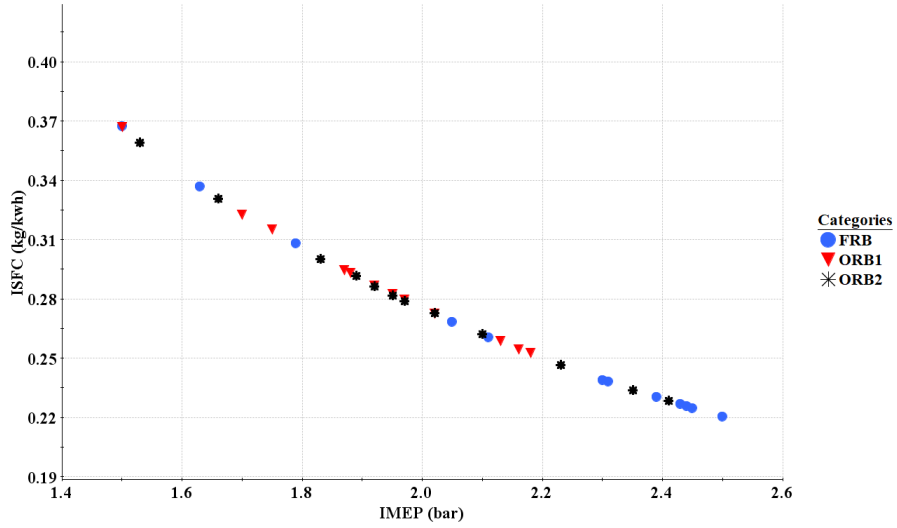

Figure 6-8: IMEP-ISFC objective space of FRB, ORB1 and ORB2 at low load

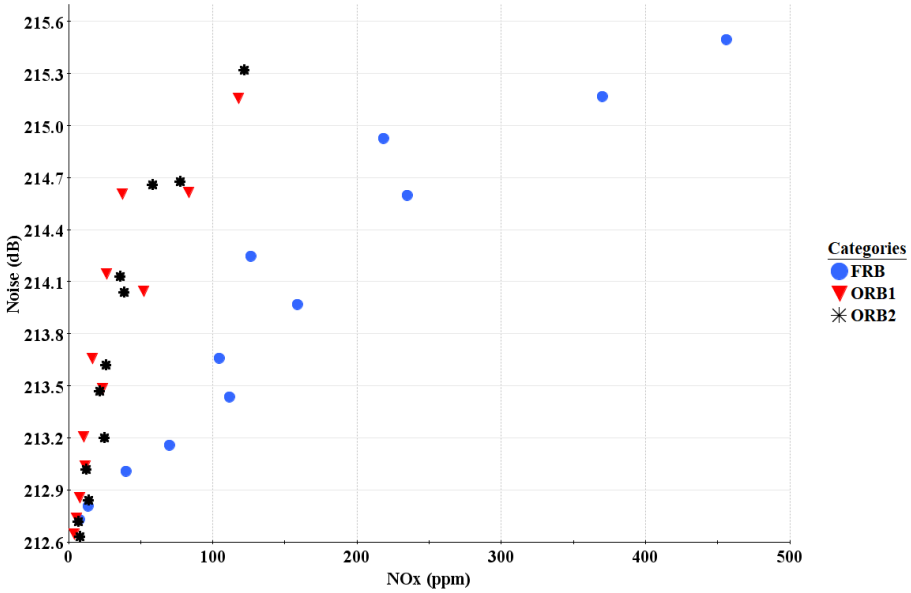

Figure 6-9: NOx-noise objective space of FRB, ORB1 and ORB2 at low load

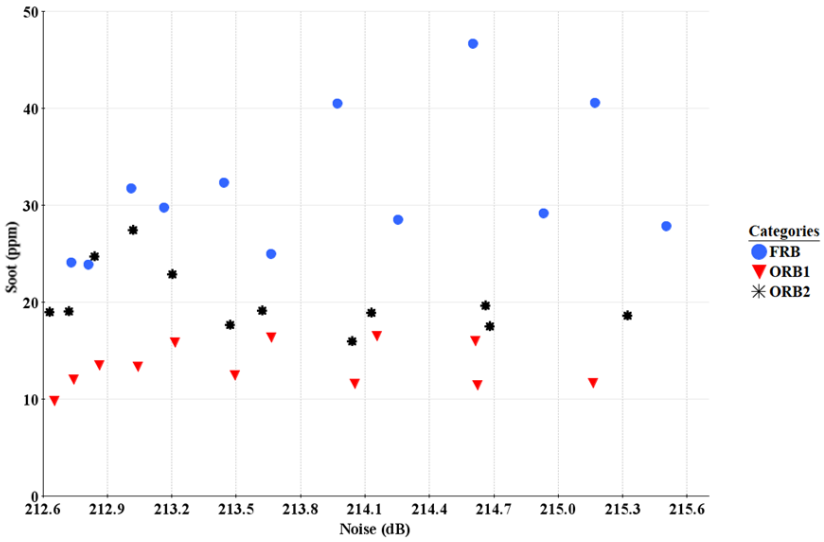

Figure 6-10: Noise-soot objective space of FRB, ORB1 and ORB2 at low load

The results across the aforementioned objective spaces showed that the injection strategies pertaining to FRB and ORB1 highlighted the extremes of the multi-objective space domain compared to ORB2. An observation of the same injection strategies pertaining to the ORB2 showed that it provided acceptable improvements to IMEP and ISFC which were closer to the FRB in some strategies, similar combustion noise levels and considerable reductions in NOx and soot emissions.

6.3 Optimisation of Piston Bowl Geometries at High Load

The multi-objective piston bowl geometry optimisation was captured through in the objective spaces presented in Figure 6-11 to Figure 6-17 with the details of their combustion characteristics, performance and emissions characteristics previously presented in Chapter 5. It should be noted that the noise levels displayed in the results were closely similar and were only exaggerated to show negligible differences imposed by the bowl geometries.

An overview of the results showed no outstanding dominance by one bowl geometry over the other two bowl geometries in all the objective spaces which suggested that despite the improvements provided by each bowl geometry, such improvements were linked to the interaction between the bowl geometry and fuel injection strategy.

The pareto front in the IMEP-NOx objective space seen in Figure 6-11 consisted mostly of ORB2 strategies and very few strategies of ORB1 whereas the pareto front

of the IMEP-noise objective space seen in Figure 6-12 consisted mostly of ORB1 strategies, a few ORB2 strategies and even fewer FRB strategies. This showed that both ORB1 and ORB2 promoted high IMEP levels with ORB1 having negligibly lower Noise levels compared to ORB2.

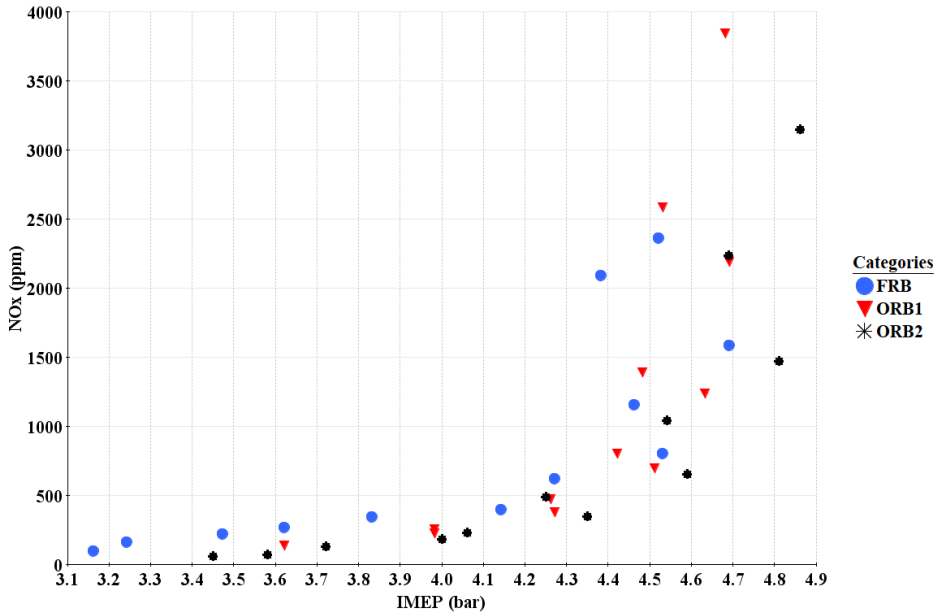

Figure 6-11: IMEP-NOx objective space of FRB, ORB1 and ORB2 at high load

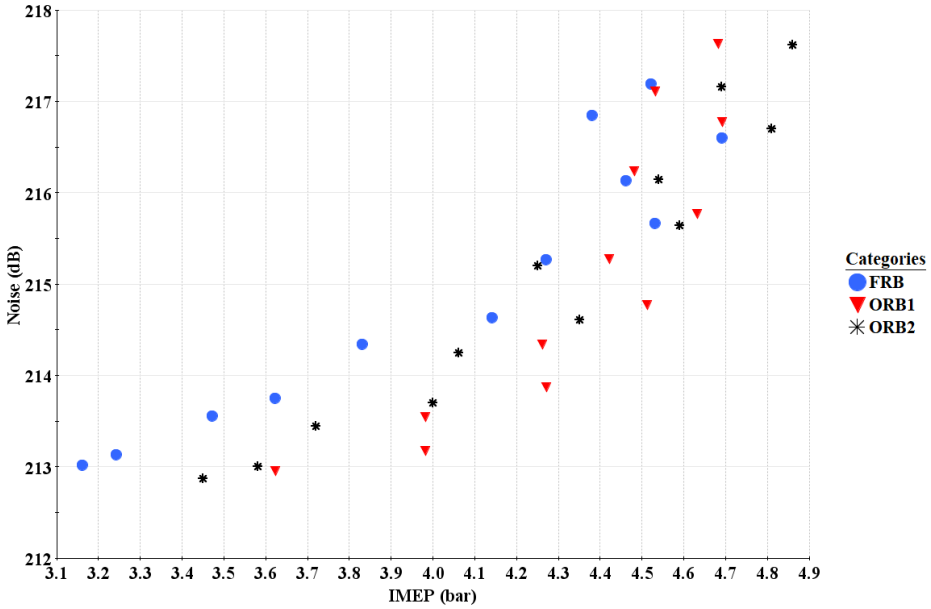

Figure 6-12: IMEP-noise objective space of FRB, ORB1 and ORB2 at high load

The NOx-soot and IMEP-soot objective spaces are presented in Figure 6-13 and Figure 6-14, respectively. In contrast to the results at low load, there was no stratum between the strategies of each bowl geometry. The pareto region of both objective

spaces consisted of primarily ORB1 and ORB2 strategies. These results showed that while ORB1 promoted slightly lower soot and NOx levels, this was accompanied by lower IMEP levels in comparison to ORB2.

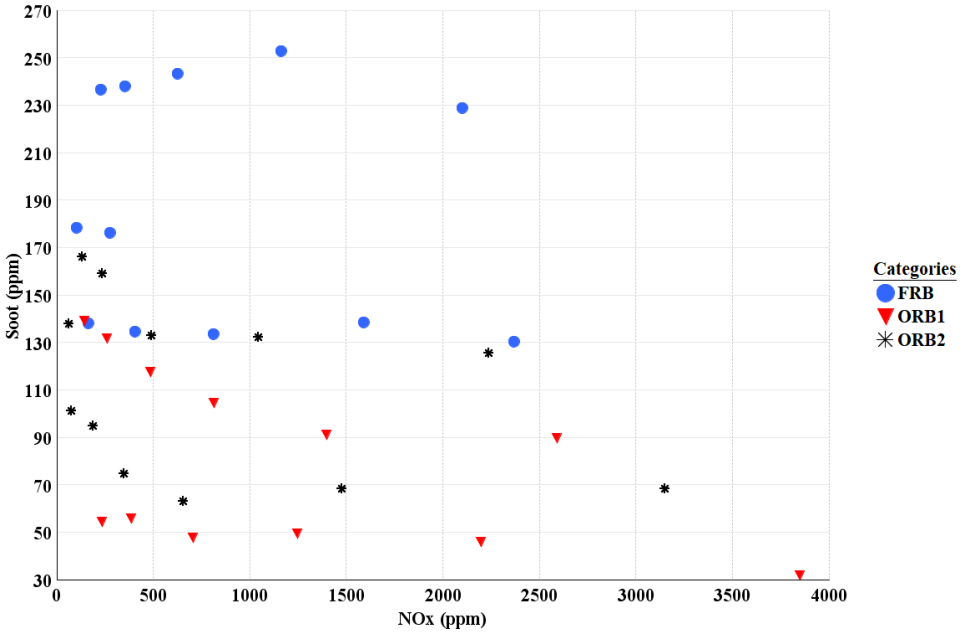

Figure 6-13: NOx-soot objective space of FRB, ORB1 and ORB2 at high load

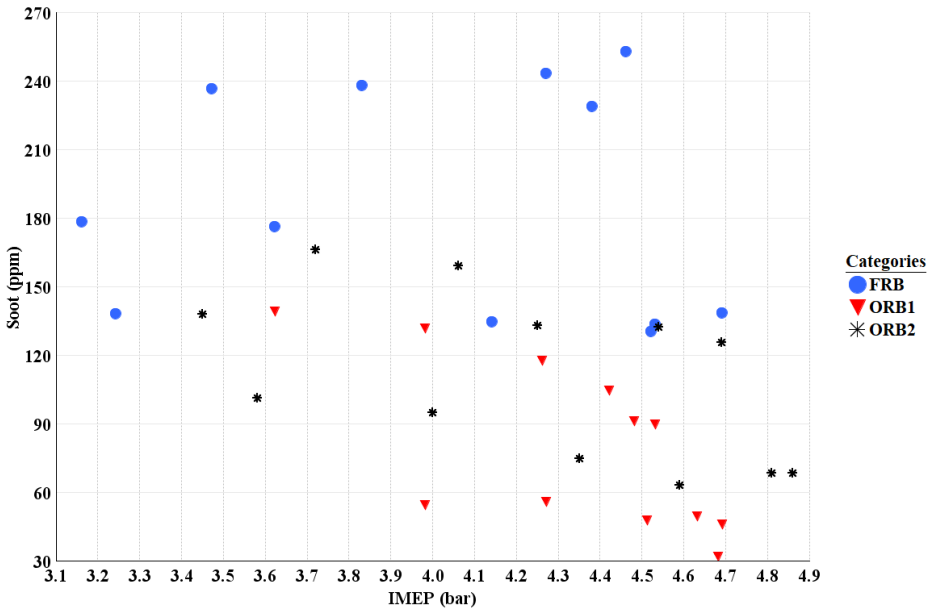

Figure 6-14: IMEP-soot objective space of FRB, ORB1 and ORB2 at high load

The pareto region in the IMEP-ISFC objective space, seen in Figure 6-15, consisted mostly of ORB2 strategies and few strategies of ORB1 which supported the aforementioned observations from Figure 6-13 and Figure 6-14. On the other hand,

Figure 6-16 showed the NOx-noise objective space wherein a stratum was observed for the strategies of the bowl geometries with those pertaining to ORB2 located on the pareto front and those of the FRB and ORB1 further to the right of the ORB2 strategies in the bottom left corner. The presence of the ORB2 strategies at the pareto front showed that it promoted lower NOx out of the three bow geometries with negligibly lower noise levels.

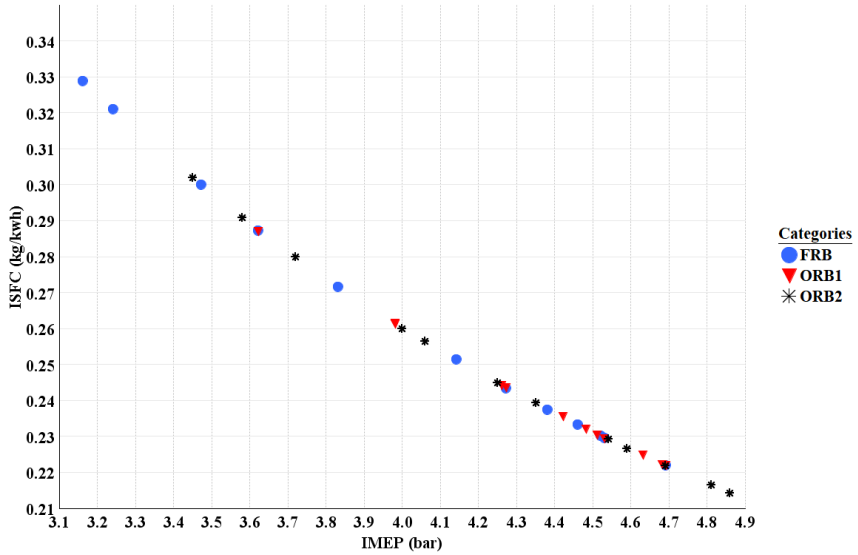

Figure 6-15: IMEP-ISFC objective space of FRB, ORB1 and ORB2 at high load

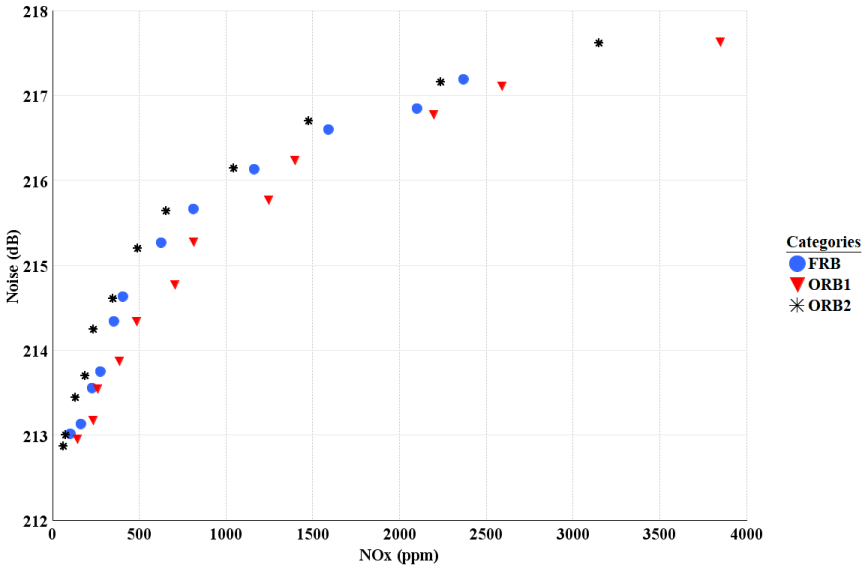

Figure 6-16: NOx-noise objective space of FRB, ORB1 and ORB2 at high load

Figure 6-17 illustrates the Noise-soot objective space. Here, the stratum was also observed with a mixture of strategies pertaining to FRB and ORB2 in the middle of the space while the strategies pertaining to ORB1 and ORB2 were also seen towards

to bottom of the space. Furthermore, although the results clearly demonstrate that ORB1 is more suitable, ORB2 was also considered due to ORB1's lower IMEP.

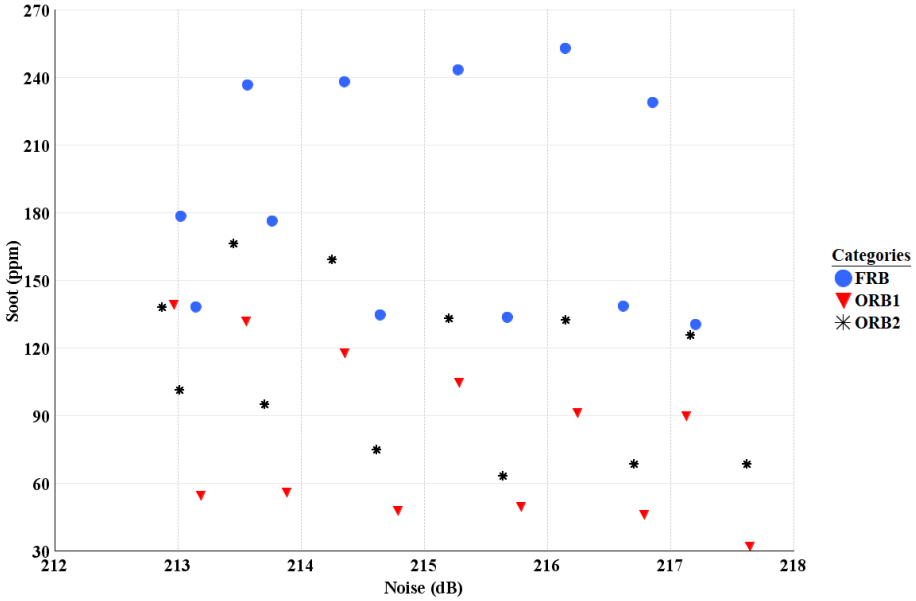

Figure 6-17: Noise-soot objective space of FRB, ORB1 and ORB2 at high load

6.4 Concluding Remarks

In this chapter, the study of the multi-objective optimisation of the piston bowl geometry was performed by analysis of the 36 3D CFD simulated cases at low and high engine loads, respectively. The goal of this optimisation study was to select the best suited piston bowl geometry for low and high load operation to be latter used for the optimisation of double injection strategies in second stage. The optimisation study showed that at high load showed that ORB1 supported improved soot levels compared to ORB2 whereas the performance of the FRB deteriorated compared to the same strategies at low load.

Nevertheless, ORB2 promoted improved levels of IMEP, ISFC and NOx levels with similar combustion noise levels without the drawbacks previously observed in FRB and ORB1. In addition, ORB2 exhibited these characteristics over the range of injection timings and injection ratios considered which demonstrated that it was the preferred and suitable piston geometry to be used during the optimisation of the double injection strategy. The first stage of the optimisation recommended ORB2 piston bowl geometry as the most suitable design due to its ability to control combustion behaviour and thus in-cylinder performance and emissions characteristics

at low and high loads. This led to improvements in performance and emissions with a consideration of the ORB2-7030-(15b,05b)TDC compared to the FRB-7030-(15b,05b)TDC at high load and ORB2-7030-(20b,10b)TDC compared to the FRB-7030-(20b,10b)TDC at low load.

7 Double Injection Strategy Optimisation (Stage 2 of 2)

The double injection strategy optimisation is stage 2 of the two-stage approach of the optimisation workflow process presented earlier in Chapter 6 Figure 6-1. It focused on a range of injection ratios and timings with the ORB2 geometry as the nominated bowl at the same engine loads and multi-objective criteria considered in stage 1. A unique optimisation methodology referred to as the Hybrid Regression-based Technique (HRT) in this research work is proposed and implemented for this process aimed at achieving reliable and accurate optimal strategies at significantly lower computational cost compared to more conventional approaches used in similar studies. Figure 7-1 shows the scheme of this optimisation methodology while Figure 7-2 presents its logical process built using modeFRONTIER.

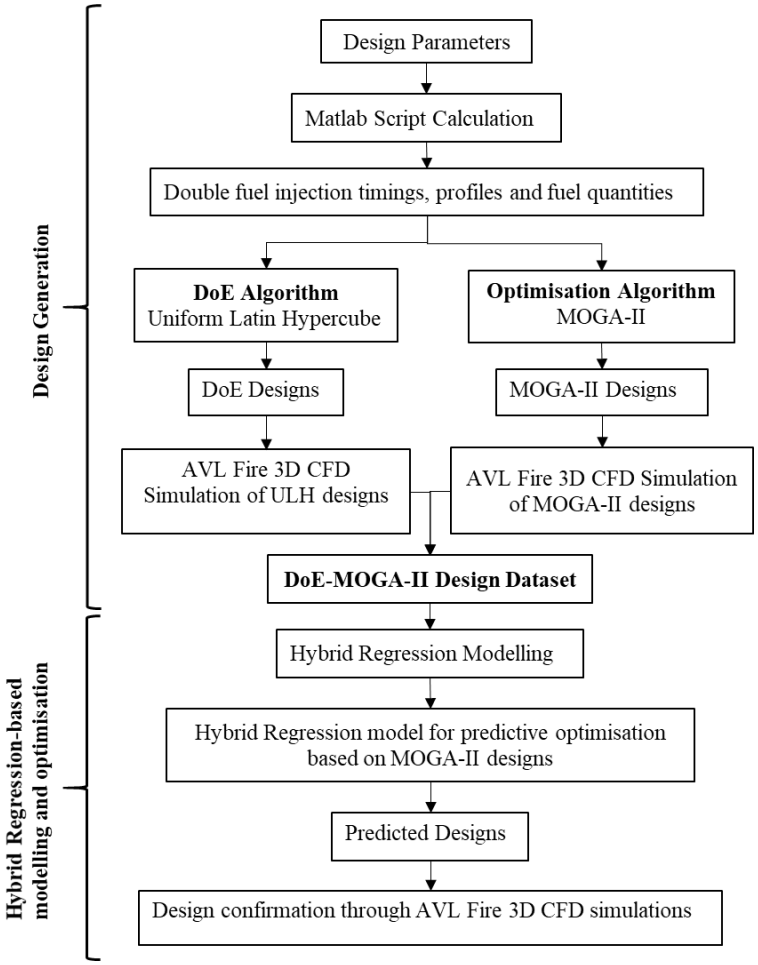

Figure 7-1: Schematic workflow of the hybrid regression-based optimisation routine

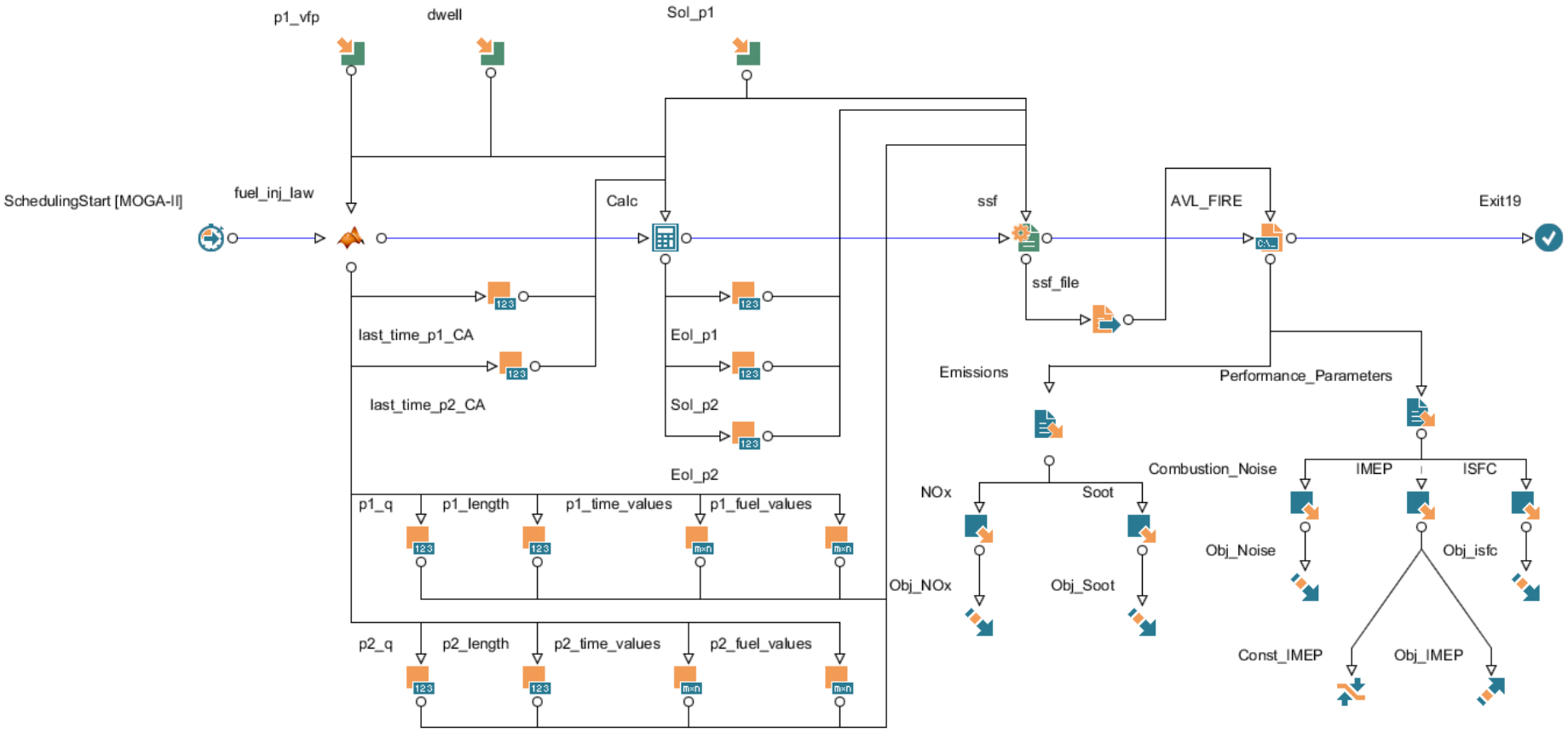

Figure 7-2: Logical process of the hybrid regression-based optimisation routine in modeFRONTIER

7.1 Implementation of the Hybrid Regression-based Technique

7.1.1 Design Input and Output Parameters

In this optimisation process, an injection strategy is referred to as design while its characteristics such as injection timing and injection ratio are referred to as the design input parameters. A double injection strategy has a relatively high dimensionality since it consists of seven design input parameters which include two injected fuel quantities and their respective injection timings, as well as the time interval between the two injection events. This high dimensionality was reduced to three design input parameters namely, the SoI_p1, p1_vfp and dwell angle to decrease to complexity which is associated with high dimensionality design spaces.

These three parameters represented the start of the 1st injection, fuel quantity of the 1st injection as a percentage of the total injected fuel quantity per cycle and the time interval between the start of the 1st injection and the start of the 2nd injection, respectively. These three parameters as well as their integration into the optimisation routine can be seen in Figure 7-2. Table 7-1 presents the domain characteristics of the three design input parameters that was chosen in order to provide a sufficient design space exploration.

Table 7-1: Domain characteristics of the design input parameters for double injection strategy optimisation

Design Parameter	Lower Bound	Upper Bound	Step
p1_vfp (%)	5	95	5
Dwell °CA	8	20	1
SoI_p1 °CA	20°bTDC	10°bTDC	1

The IMEP, ISFC, combustion noise, NOx, and soot solutions of the CFD engine model simulation using a double injection strategy were the target outputs. These parameters are referred to the design output parameters in the optimisation process. The multi-objective outcomes from the first stage were adopted for this optimisation with the addition of a constraint on the IMEP optimisation to a maximum of 10 bar to avoid designs that would lead to excessive mechanical strain on the engine components. Thus, realistic strategies could be achieved while maintaining a reasonable exploration for improved IMEP.

7.1.2 Design Space Exploration: The Hybrid Design Dataset Approach

A common challenge in the computational optimisation of ICE's is the large quantity of 3D CFD simulated designs required for surrogate modelling and the associated extensive computational cost and time. The feasibility of rapid engine development improves with optimisation studies at low computational cost.

Therefore, there is a growing interest in reducing the computational cost involved in computational ICE optimisation while also achieving accurate optimal solutions. Reducing the required number of 3D CFD simulated designs for surrogate modelling significantly decreases the computational cost involved in the optimisation process. In this regard, recent improvements include the avoidance of using initial sampling designs and automatic model hyperparameter selection for model [145], [146].

This research optimisation study takes a different and unique approach towards the issue of reducing computational cost. A sufficient balance between exploration and exploitation of the design space was achieved through the implementation of a hybrid design dataset that is formulated using a DoE-Optimiser algorithm approach.

The hybrid dataset implementation commenced with the use of the Uniform Latin Hypercube (ULH) DoE algorithm in generating a relatively small number 3D CFD simulated designs compared to similar investigations. This DoE algorithm was found to be effective over the relatively low dimension design space. Subsequently, the MOGA-II optimiser algorithm guided by the multi-objective was used to generate additional 3D CFD simulated designs closer the pareto front of the design space informed by the ULH design solutions. It should be noted that the MOGA-II design sample size was larger than the ULH design sample size.

This method was in essence a mini-optimisation process with the purpose of utilising a good balance between exploration and exploitation in bringing about faster computation with minimal drawbacks in the future surrogate model learning accuracy. The hybrid design dataset approach, which in itself is a new approach towards generating a set of designs used for regression-based optimisation in this field provided the following features which were found to be beneficial to the optimisation process:

- A ULH generated design dataset which was relatively small but effective in sampling the design space.
- A mixture of designs which provided diversity (mainly from the ULH) and an early visibility/indication of the pareto front/region of the design space (mainly from the MOGA-II).
- An improved generational dynamic learning between the MOGA-II designs, as well as relational learning between the ULH and MOGA-II designs mostly between the closely packed designs of the pareto region.

The motivation behind the formation of the hybrid design dataset approach was that both algorithms had different primary functions of sampling and identifying the pareto optimal frontier within the design space, respectively. Since the aim of the regression modelling in this work was for the purpose of optimisation, the features of the hybrid design dataset enabled a regression learning which focussed mainly on the pareto region/front with a minimal compromise on diversity instead of considering a wider region of designs which mostly consisted of non-pareto or non-optimal design solutions, thereby making the optimisation process much faster.

7.1.3 Calculation of Double Injection Strategy Design Attributes

The workflow and process for calculating each design was implemented in modeFRONTIER as previously seen in Figure 7-2. The three design inputs parameters and their respective domain presented in Table 7-1 were used as the governing attributes for the optimisation of the double injection strategy during the calculation of each design.

During the optimisation process at each engine load, a bespoke algorithm scripted using MATLAB programming was implemented such that it utilised the single injection profiles representing each engine load (i.e., approximately 9.7mm^3/cycle and 18.5mm^3/cycle, for low and high engine loads, respectively) along with the three design input parameters to generate the attributes required to fully define injection profiles, fuel quantities, timings, and dwell angle for each design. The algorithm parameterised the single injection profile based on the profile's rise and fall gradients (to represent the needle lift opening and closing response), the maximum flowrate (due to the injection pressure and fuel quantity) and injection duration. Hence, all

considered attributes of the double injection strategy were linked to the design parameters as depicted in Figure 7-3.

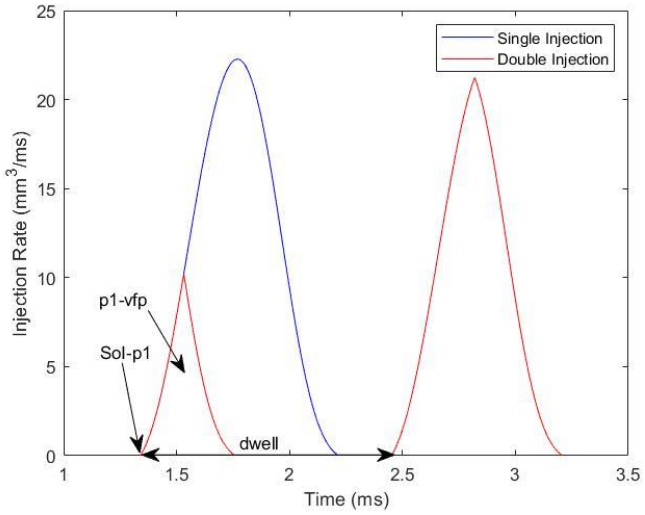

Figure 7-3: Illustration of SoI_p1, p1_vfp and dwell angle design parameters for single and double injection profiles

Subsequently, the AVL Fie solver was populated with the design attributes through a link between the MATLAB and AVL Fire domains within modeFRONTIER shown in Figure 7-2. This process was automated using a set of overwrite transfer ruling protocols which generated a solver file that was specific to each design for its 3D CFD simulation in AVL Fire.

In addition, the process of preparing each design case, tracking its simulation runtime, and extracting its output parameters from the CFD results was complex. Therefore, a DOS Batch script was implemented and embedded within the AVL Fire node in the modeFRONTIER workflow to automate the process. This automated process included the definition of the file directories involved in the optimisation process, inclusion of the solver file for each design in its AVL Fire case folder, starting the AVL Fire simulation for each design case which was performed using an embedded line of python execution code, and extraction of the relevant numerical data for each completed simulation, all of which looped back to the start of the process.

A workstation with 8 logical processors feeding off a 32GB RAM was used for the 3D CFD simulations and entire optimisation study in contrast to the use of super computers similar optimisation studies [132], [144]. Each 3D CFD design simulation took approximately 8 hours for completion. This implied that the generation of 100 3D CFD designs would require approximately 800hours with the assumption that the

processing power was solely used for the simulation process. This highlighted the extensive computational cost of this process and the need for exploring unique methods such as the one implemented in this research work.

A bespoke Crank Angle Reduction Scheme was automatically implemented to further reduce the computational time of the process. In the scheme, the AVL Fire solver file for future designs were modified such that the crank angle for the duration between IVC and EVO was reduced. Since the behaviour of in-cylinder characteristics in the interval between IVC and SoI_p1 remained constant for consecutive designs, a consecutive design simulation could be configured to start from a few crank before the lower bound of the SoI-p1 design parameter range (i.e., 20°bTDC) instead of starting from IVC. In addition, the results for the interval between IVC and its SoI-p1 would be subsequently included to the final result at the end of the design simulation. The implementation of this idea considerably reduced the 3D CFD computational time to about 3hours per design or 37.5% reduction in the computational time for each design simulation. It should be noted that the AVL CPU MPI setup was also initiated to utilise all 8 logical processors.

7.1.4 Regression Modelling: The Hybrid Regression Model

Various regression-based optimisation studies have shown the use single regression methods. However, the investigation by Shi et al., [249] showed that various regression methods often offered different predictive capabilities and performances based on the same dataset due to how they handle complexities such as a varying degree of non-linearity in the relationship between the design and response spaces, as well as non-normality of the design observations and corresponding responses. In more recent studies, [145], [146], the tediousness of manually tuning the hyperparameter within some regression methods to improve model performance towards the same or different response parameters is reduced through automation.

As discussed in section 2.5, the application of advanced optimisation techniques such as the ActivO [146] and Super Learner ML-GA [144], [154] have realised significant reductions to computation cost of 3D ICE CFD optimisation. However, these investigations were limited to fewer design input and output parameters compared to this research work. In this work, a bespoke ensemble optimiser called the Hybrid

Regression-based Technique (HRT) is proposed and implemented for the optimisation of double injection strategy. The processes involved in the implementation of the HRT are discussed next.

Firstly, the k-fold cross validation method was applied to the hybrid design dataset also referred to in the results as the ULH-MOGA-II dataset. Using this method, the dataset was partitioned into k number of subsets from which k-1 subsets were used for model training and the kth subset was used for the model validation iteratively for k number of times. This method was used instead of the more commonly used ratio split method due to its suitability over relatively small datasets similar to those in this work and the reduced tendency of bias and chance through the random selection of k-1 and kth subsets, which improves the confidence in the predictive errors and performances of the realised regression model.

Subsequently, a library consisting of over 20 regression learners using MATLAB programming was trained and validated using the three design input parameters as the predictors and each design output parameter as the response. Furthermore, acceptable regression models were fine-tuned where necessary, for instance the number of hidden layer neurons in the ANN, based on their predictive capabilities for each objective, to explore further predictive performance improvements. Hence, the relationship between the predictors and each response was successfully mapped to a regression model such that a hybrid of the five best regression models (one for each response) was formulated to enable a simultaneous prediction during the optimisation run.

This method of regression modelling provided the following features which were found to be beneficial to the optimisation process:

- A comparative and competitive analysis of an extensive library of regression models over the same set of designs which improves the identification of a reliable model as well reducing the tuning time.
- An identification of a set of regression models which offer the strongest predictive capability for the relationships between the design parameters and the respective objectives.

- A hybrid regression model suitable for the mapping and predictive modelling of complex nonlinear relationships between the design and multi-objective domain for which single regression models may not be suitable.
- The approach avoids the requirement of larger 3D CFD simulated design datasets consequently reducing computational cost significantly with minimal compromise to the predictive capability of regression model.

The set of statistical metrics presented in equation 7.1 to equation 7.4 were used to assess the performance of the regression models obtained.

Coefficient of determination (R^2): representing the percentage of the output objective variation expressed as,

$$1 - \left(\frac{\sum_{i=1}^{n}(a_i - p_i)^2}{\sum_{i=1}^{n}(p_i)^2}\right) \tag{7.1}$$

Log Accuracy Ratio (LAR): representing the logarithm of the ratio of the predicted values to the actual values expressed as,

$$\sum_{i=1}^{n}\left(\frac{p_i}{a_i}\right)^2 \tag{7.2}$$

Mean Absolute Error (MAE): representing the mean of the absolute residual (i.e., error) between the actual and predicted values expressed as,

$$\frac{1}{n}\sum_{i=1}^{n}|a_i - p_i| \tag{7.3}$$

Root Mean Squared Error (RMSE): representing the square root of the average residual (i.e., error) which arises as the difference between the actual and predicted values expressed as,

$$\sqrt{\frac{1}{n}\sum_{i=1}^{n}(a_i - p_i)^2} \tag{7.4}$$

Where a_i is the actual value, p_i is the predicted value, i is the number count of all actual and predicted values and n is the total number of actual/predicted values for

each design. The results obtained from the regression-based optimisation process are presented and discussed in the following sections.

7.2 Optimisation Results at Low Load using the HRT

For the low load optimisation, a hybrid design dataset comprising of 15 ULH designs, and 59 MOGA-II designs was formulated. The crossover, selection and mutation probabilities of MOGA-II were kept at 0.5, 0.05 and 1, respectively, based on the values reported in a similar investigation [254]. During the regression modelling process, the k-fold cross validation, wherein k is equal to 5 folds, was found to be effective towards mapping the relationship between the design parameters and the respective responses through consecutive trials. A relatively high level of complexity was observed during the modelling of the relationship between the design parameters and NOx and soot responses compared to those for IMEP, ISFC and combustion noise due to the visibility of the regression models to the relationship between these responses and the design parameters. Therefore, the log-constant transformation wherein a constant value of 20 was added to the log of the respective responses was performed to improve the visibility.

Table 7-2 presents the performance of the regression models selected for each response. Here, it was clear that the relationship between the design parameters and each objective response was mapped by different kernel functions/models of the Gaussian Processes Regression (GPR) method. This suggested that the GPR could be easily applied towards mapping a relatively wide range of relationships. As listed in Table 7-2, the relationships for IMEP and noise were represented using the GPR method with the Matern5/2 kernel function. The relationship for NOx was represented by the GPR with exponential matern5/2 kernel function while the relationships for ISFC and soot were represented by the GPR with squared exponential kernel function.

Table 7-2: Statistical performance of the regression models under low load

Objectives	Regression Method	R^2	RMSE	MAE	LAR
IMEP	GPR-Matern5/2	0.94	0.0454	0.02263	0.00710
ISFC	GPR-Sqd-Exp	0.96	0.0048	0.00225	0.00421
Noise	GPR-Matern5/2	0.99	0.0438	0.00907	5.82522E-07
NOx	GPR-Exp-Matern5/2	0.95	0.1277	0.06675	0.00213
Soot	GPR-Sqd-Exp	0.97	0.2553	0.13220	0.00152

Figure 7-4 to Figure 7-13 present graphical illustration of the predictive performance of the models presented in Table 7-2. The results suggested that the adopted k-fold validation could result in reliable predictions during the optimisation process. Strong correlations coupled with relatively small residuals as well as relatively low variance was observed in the relationship between the design parameters and the objective responses especially in the directions towards the objective of the respective responses. For instance, lower residuals were observed at higher levels of IMEP compared to the lower levels thus signifying better learning towards its pareto optimal region as seen in Figures 7-4 and 7-5.

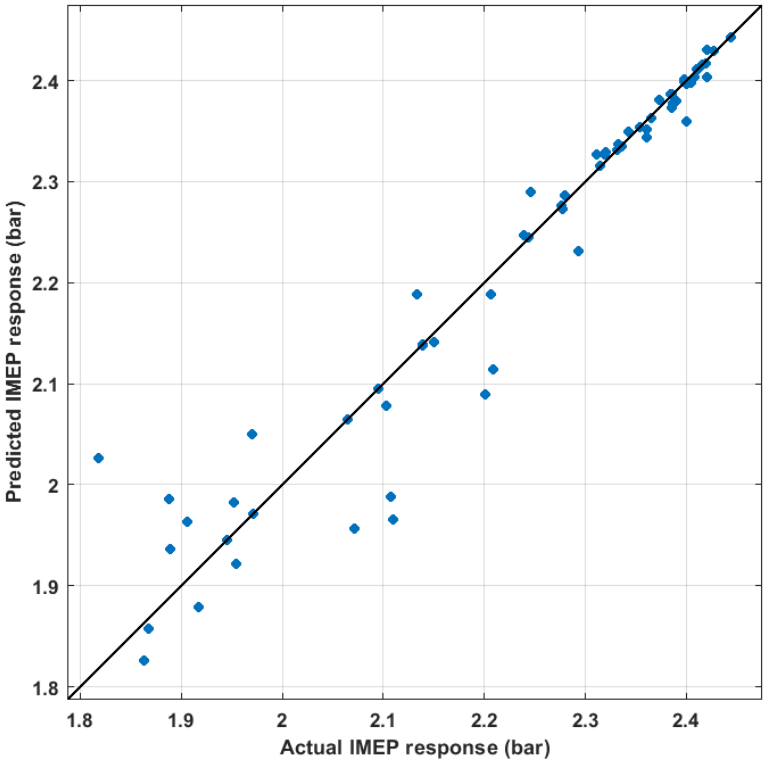

Figure 7-4: Predicted vs actual IMEP response at low load

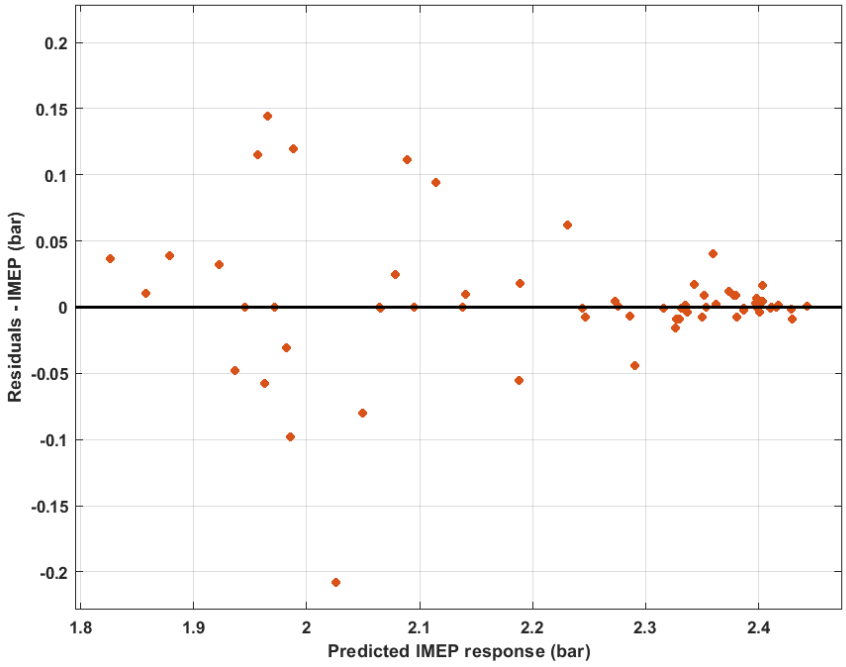

Figure 7-5: Residuals vs actual IMEP response at low load

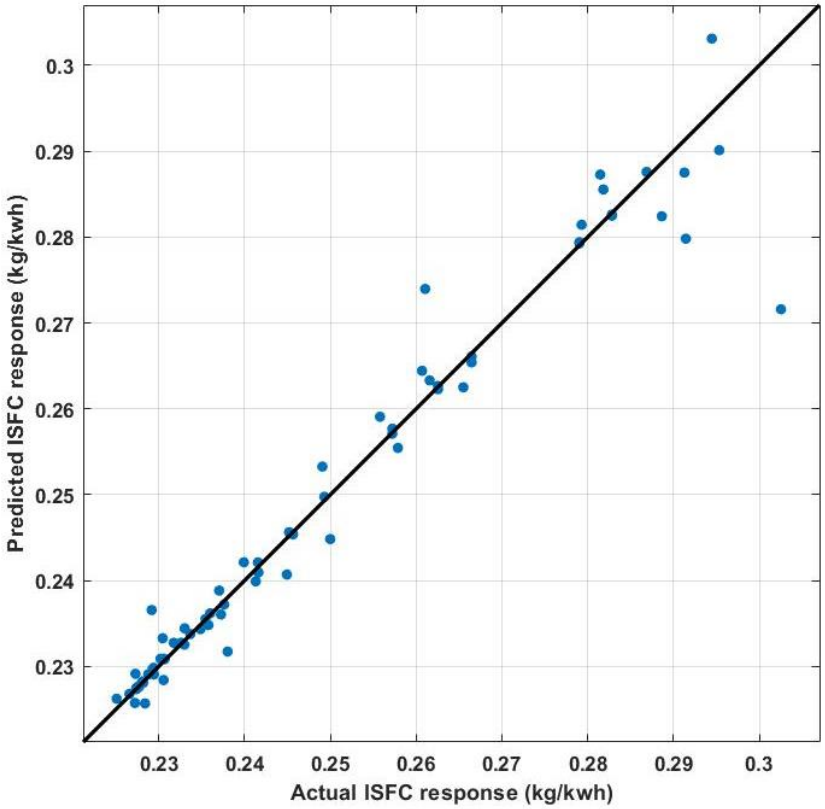

Figure 7-6: Predicted vs actual ISFC response at low load

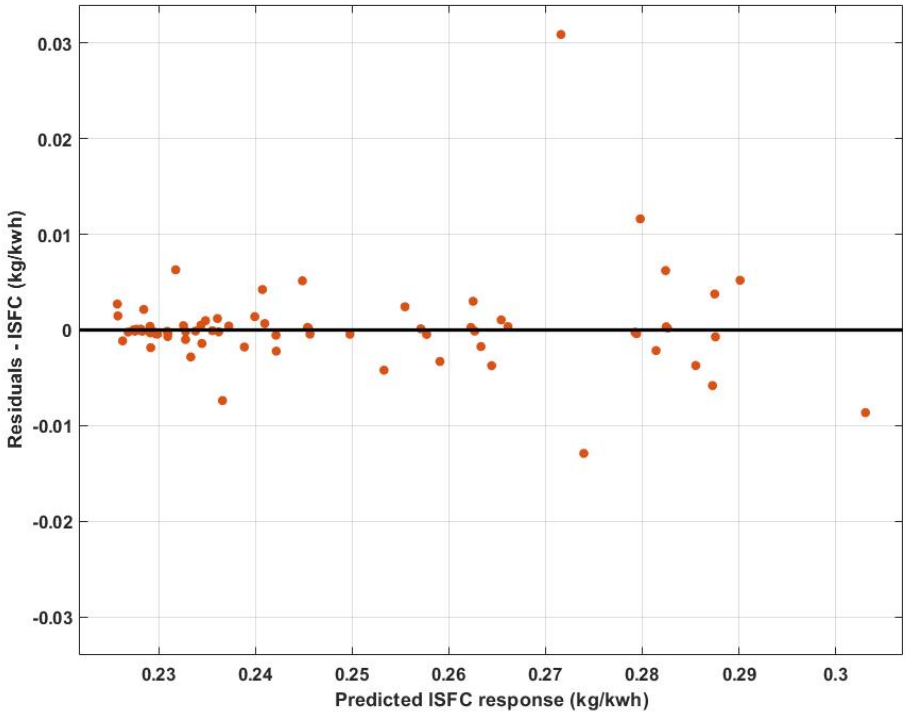

Figure 7-7: Residuals vs actual ISFC response at low load

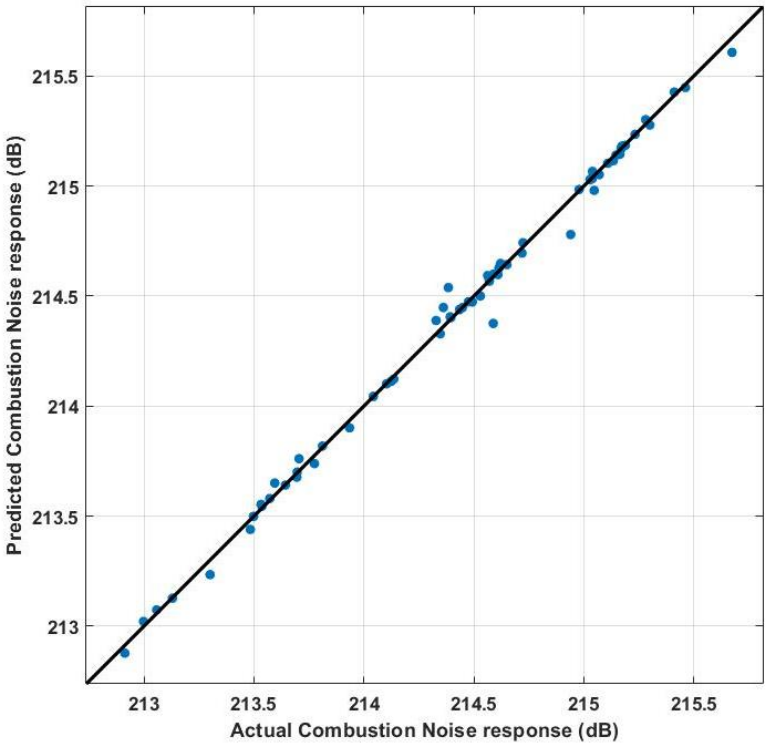

Figure 7-8: Predicted vs actual combustion noise response at low load

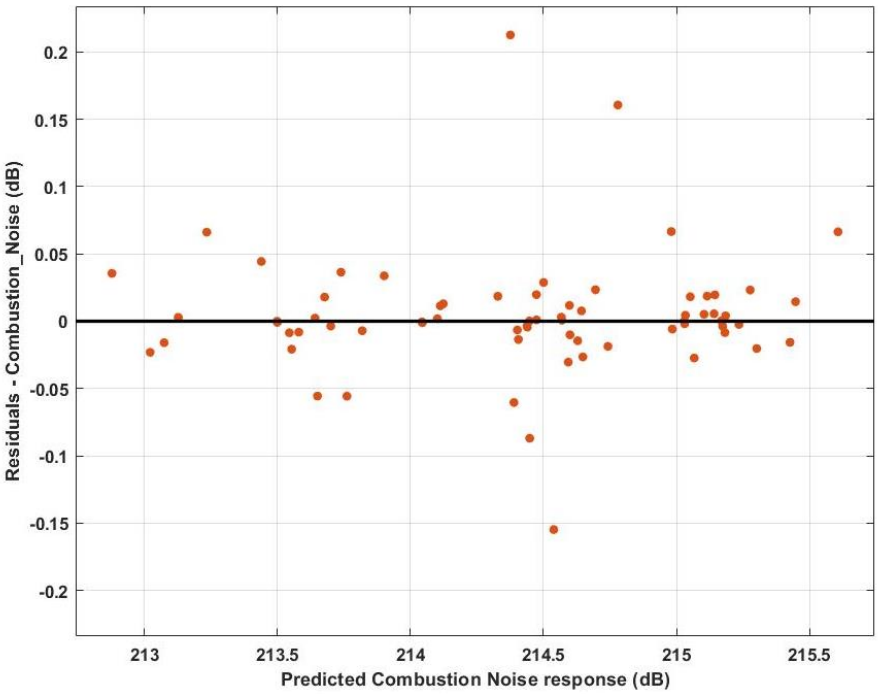

Figure 7-9: Residuals vs actual combustion noise response at low load

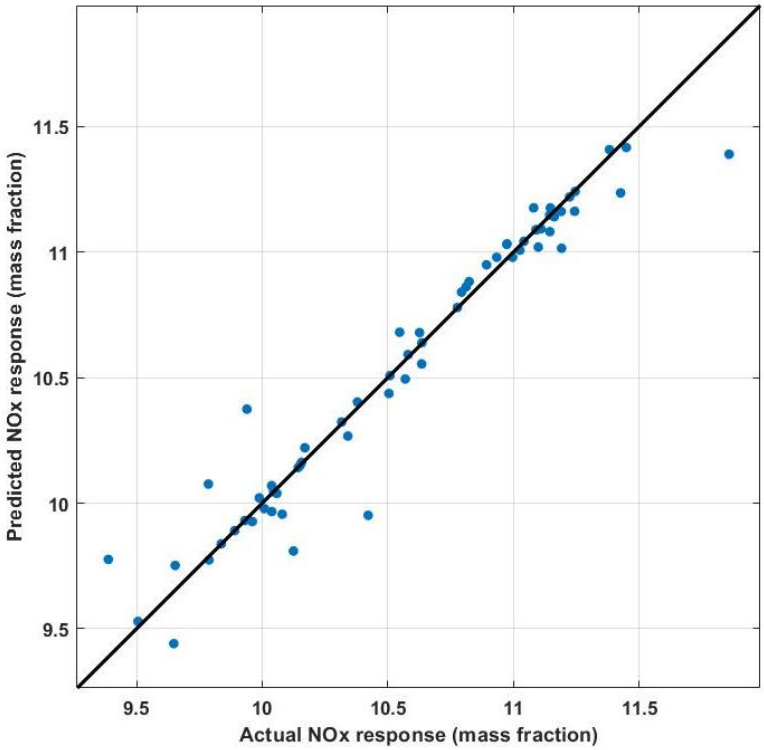

Figure 7-10: Predicted vs actual log-constant transform NOx response at low load

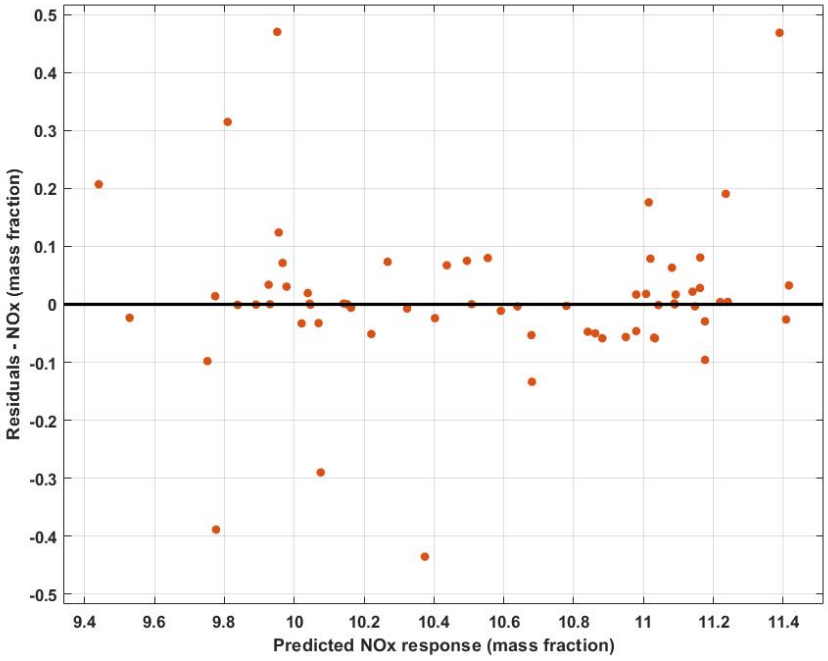

Figure 7-11: Residuals vs actual log-constant transform NOx response at low load

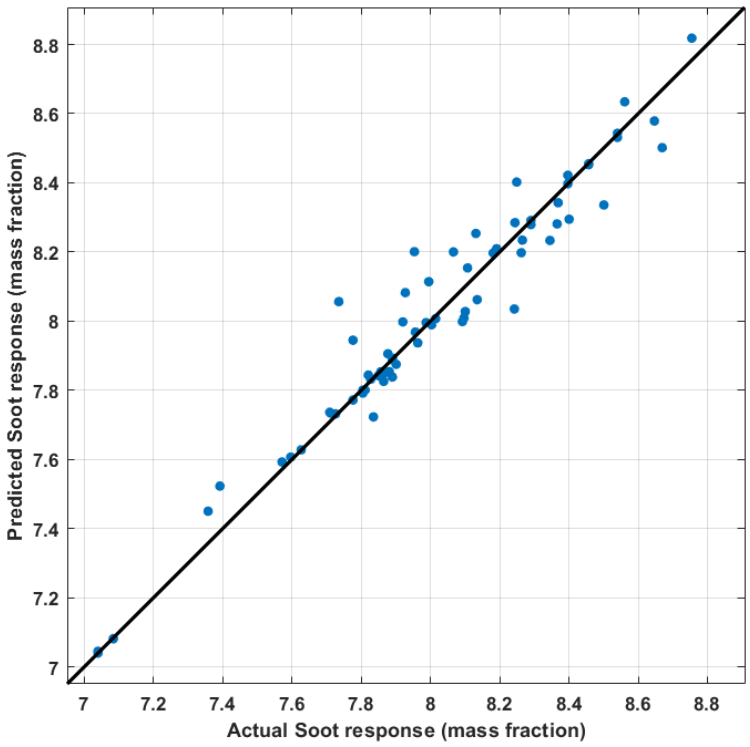

Figure 7-12: Predicted vs actual log-constant transform soot response at low load

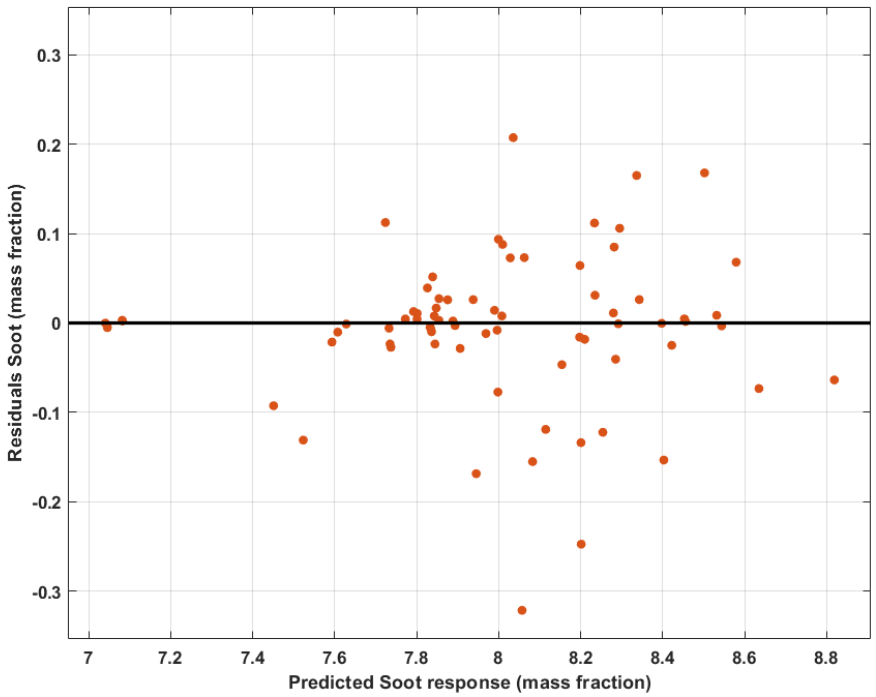

Figure 7-13: Residuals vs actual log-constant transform soot response at low load

Figure 7-14 to Figure 7-20 present the results of the optimisation process at low load in the form of the objective spaces of the multi-objective domain. A total of 750 designs categorised into CFD generated designs, virtual regression-based generated

designs and the pareto optimal designs were formed using the hybrid regression model. In addition, the design and output parameters of ORB2-7030-(20b,10b)TDC at low load were also included as the starting point to be compared to the designs.

An overview of the objective spaces showed that the hybrid regression-based optimisation methodology was effective in approaching the pareto region and frontier of the multi-objective domain to yield optimal design solutions at low load. Several pareto optimal designs were observed to be vastly far from the starting point, suggesting that there were more double injection strategies capable of yielding engine performance and emissions improvements.

The parallel coordinates tool within modeFRONTIER was used to analyse the designs with respect to the parameters of ORB2-LL-7030-(20b,10b)TDC in order to extract the pareto optimal strategies most-nearest to the pareto front. The three pareto optimal design strategies (i.e., ID14, ID38 and ID67) highlighted in green were obtained using this process. Interestingly, ID14 and ID38 were the hybrid design dataset CFD simulated designs whereas ID67 was a hybrid regression model generated design the first two selected pareto optimal designs were part of the hybrid design dataset (i.e., CFD simulated category). Although this did not necessary provide sufficient indication of the hybrid regression model optimisation performance, it strongly suggested that the small hybrid design dataset was effective in indicating and identifying the pareto region of the multi-objective domain as well as obtaining pareto optimal design solutions early on in the optimisation process.

The computational time of the optimisation process at low load was also analysed. Here, the durations for optimisation process using the HRT with and without the crank angle reduction scheme were compared to a similar preliminary optimisation study in which 425 CFD simulated designs were generated using the 3D CFD-MOGA-II. It was found that simulating 74 3D CFD designs based on the hybrid dataset for HRT instead of 425 designs without the reduction scheme resulted in the HRT being 82.6% faster than 3D CFD-MOGA-II. Since the Crank Angle Reduction Scheme reduced each simulation time to 3 hours, its application resulted in the HRT being 93.4% faster than the 3D CFD-MOGA-II.

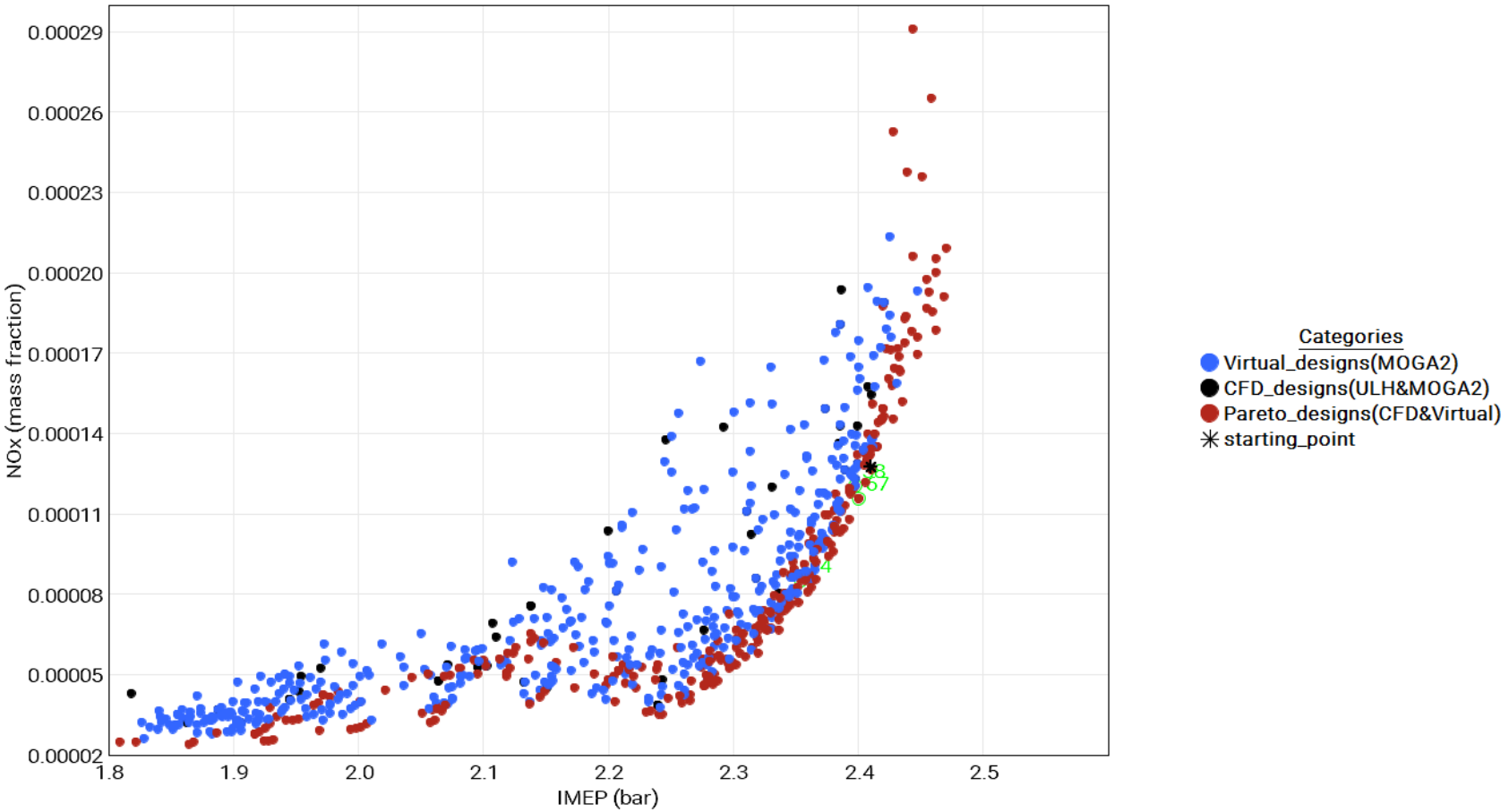

Figure 7-14: IMEP-NOx objective space at low load

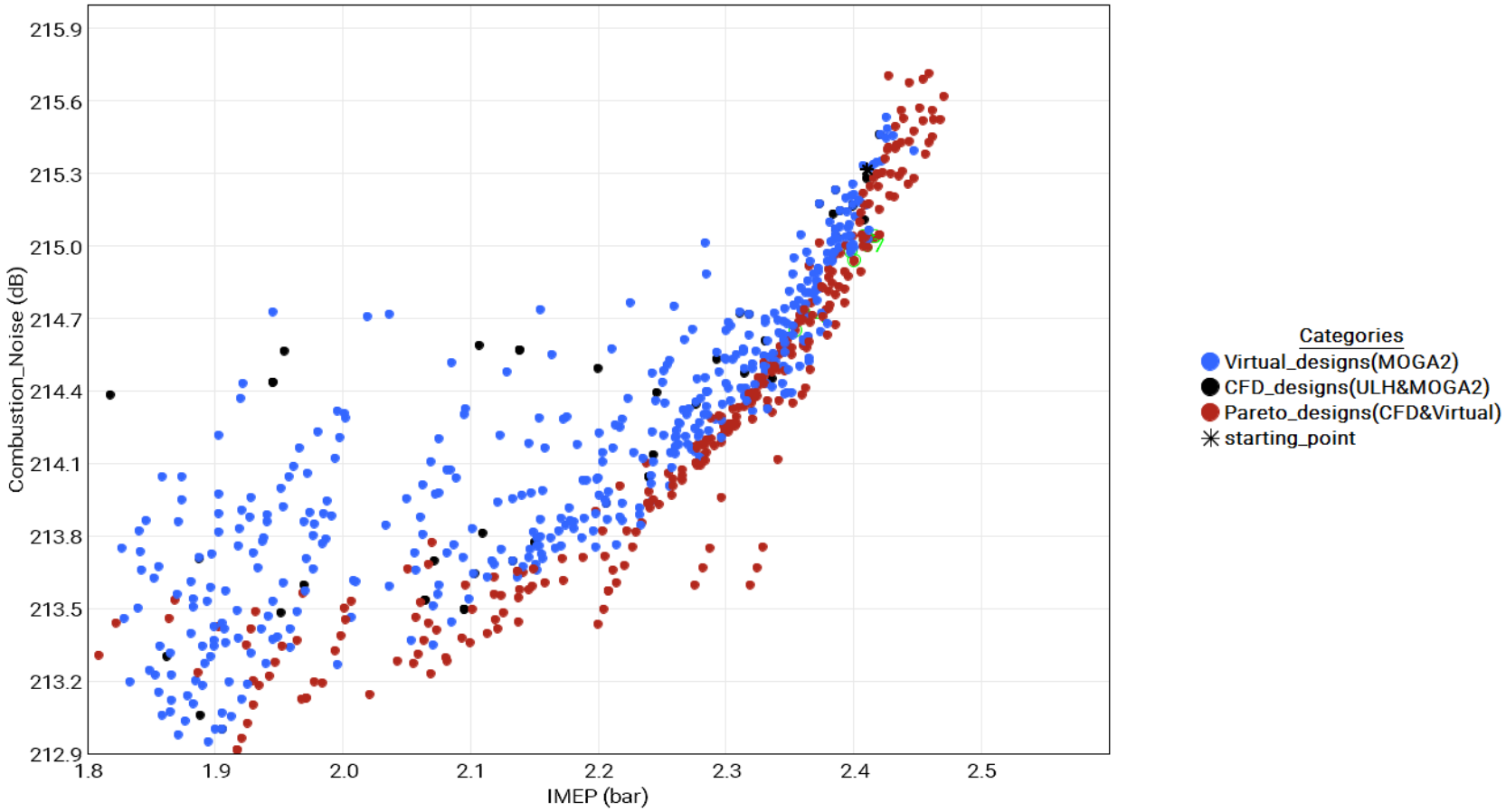

Figure 7-15: IMEP-combustion noise objective space at low load

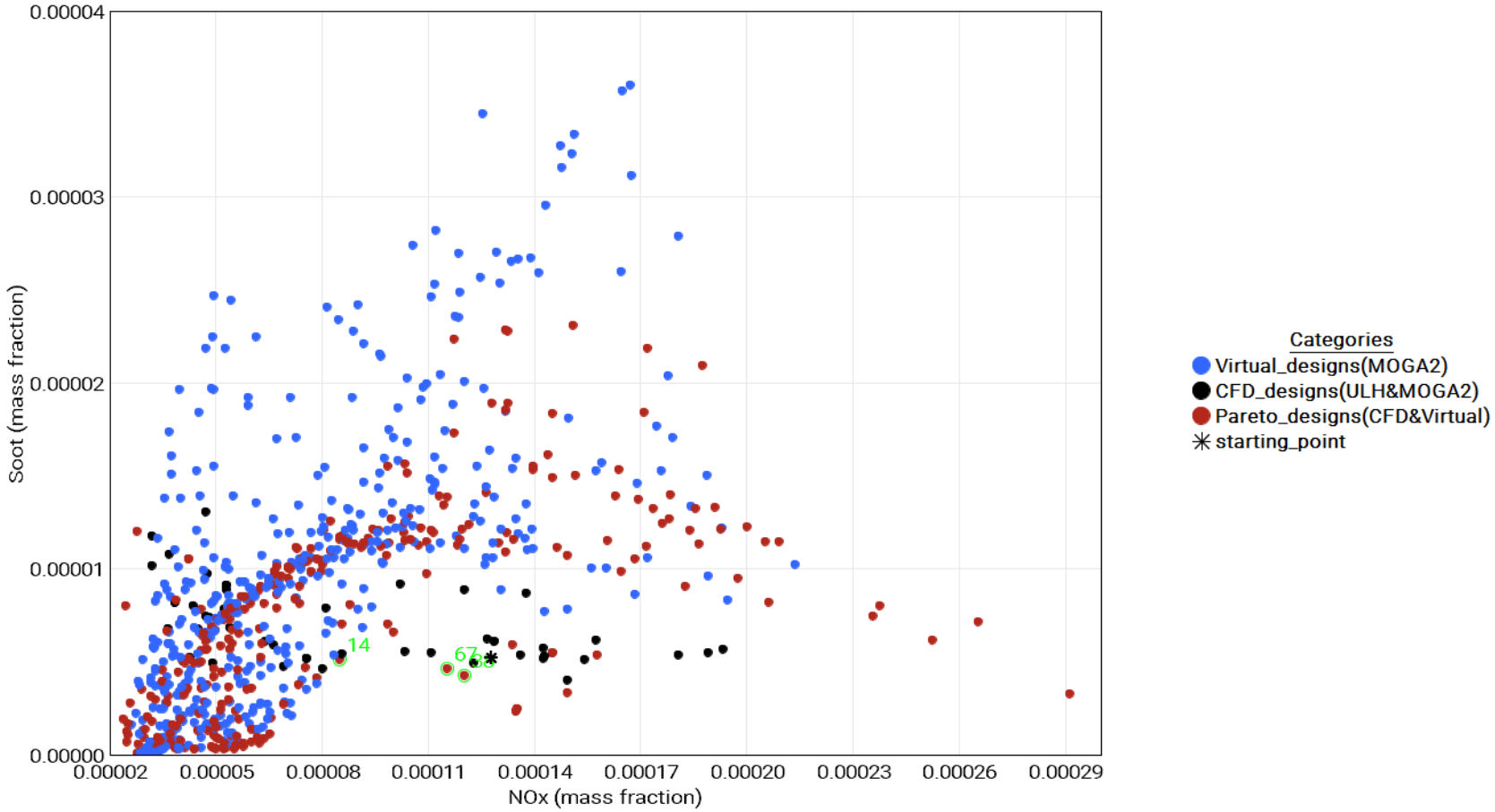

Figure 7-16: NOx-soot objective space at low load

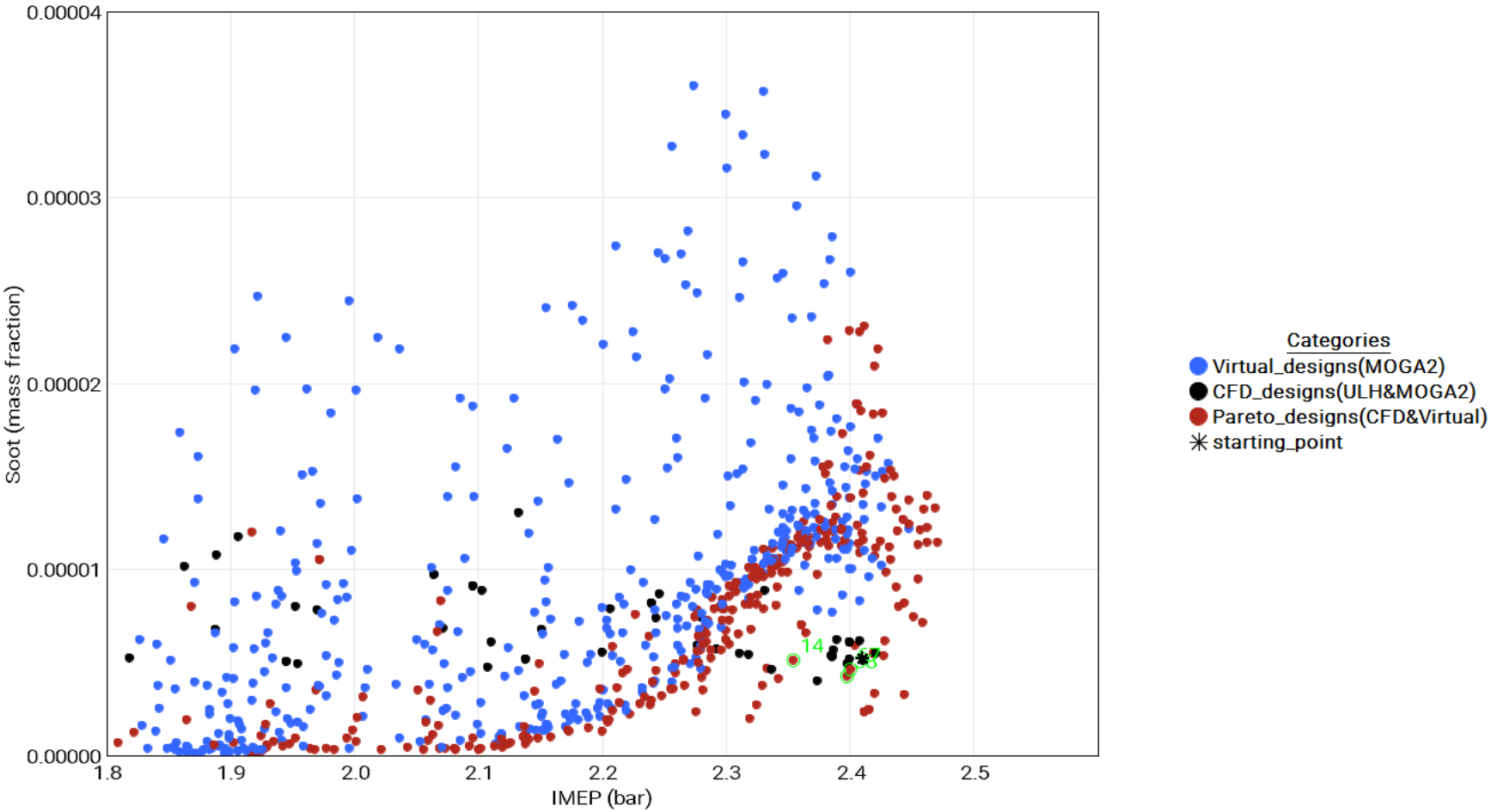

Figure 7-17: IMEP-soot objective space at low load

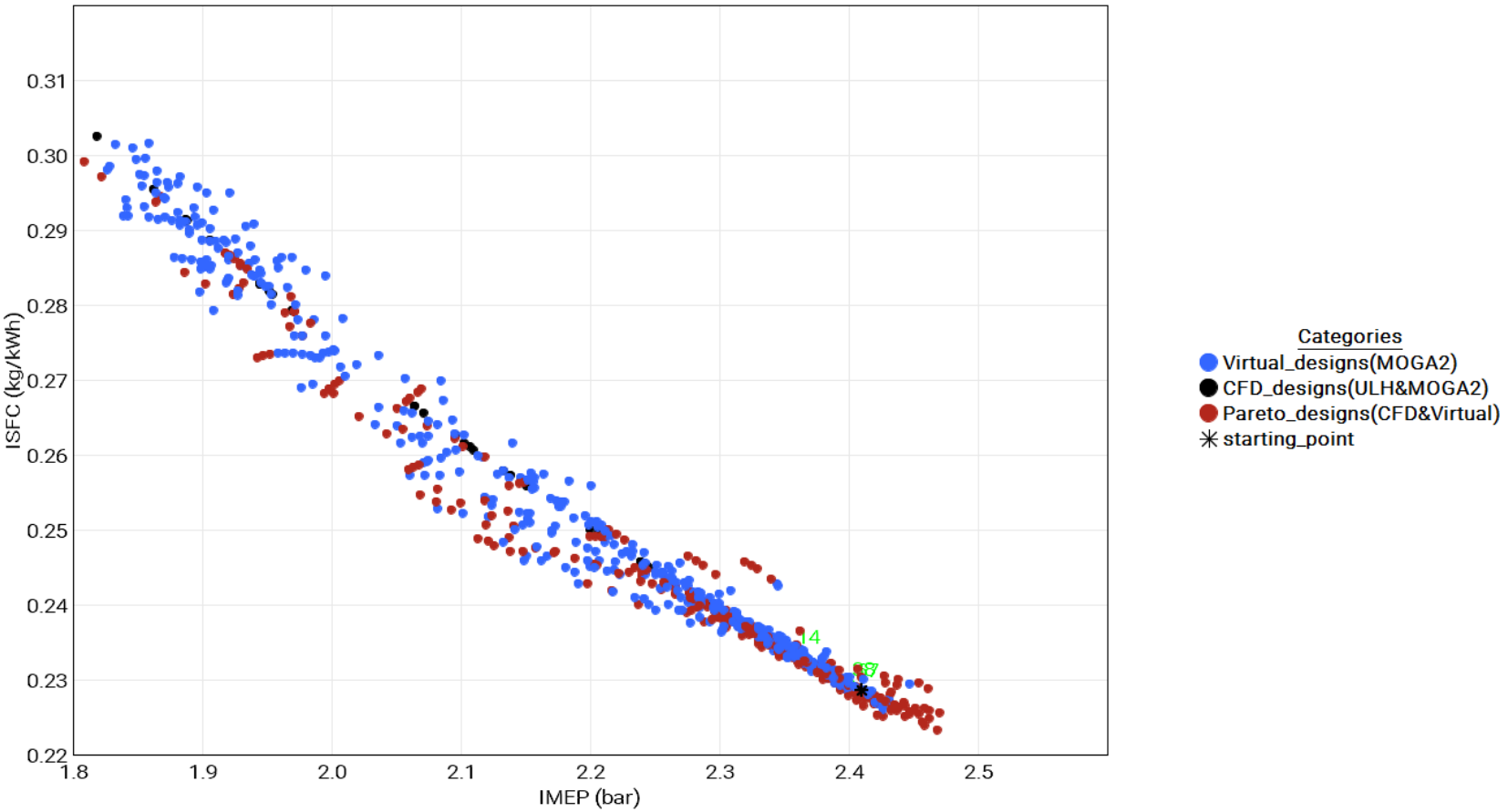

Figure 7-18: IMEP-ISFC objective space at low load

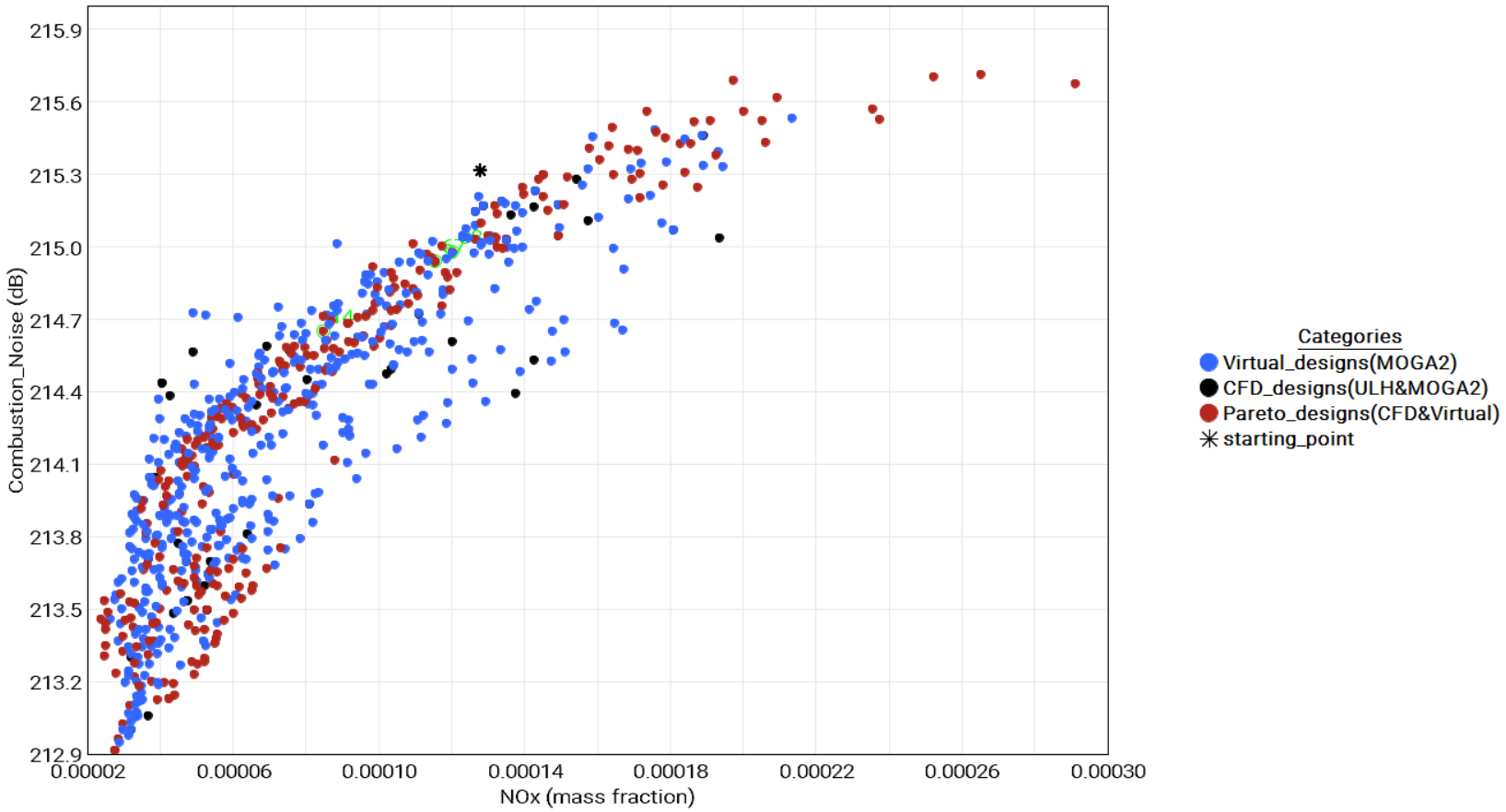

Figure 7-19: NOx-combustion noise objective space at low load

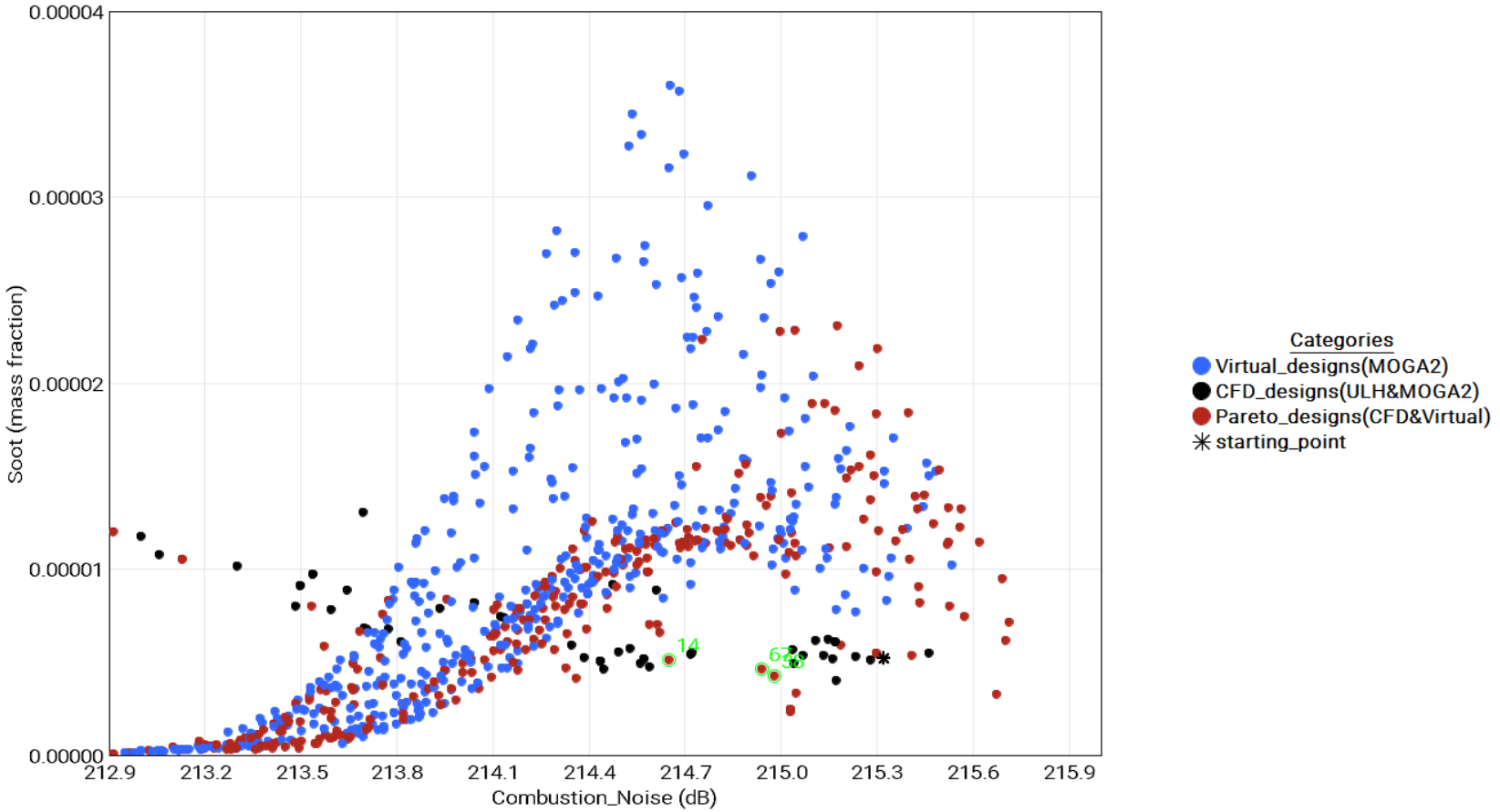

Figure 7-20: Combustion noise-soot objective space at low load

The injection and output parameters of ID67 were verified using 3D CFD engine simulation to provide certainty of the model's reliability, noted as ID67(CFD) in Table 7-3. The comparison of ID67 and ID67(CFD) shows that the model was able to predict the numerical solutions of ID67 with a deviation of less than 1% for IMEP, ISFC, combustion noise and soot and a 6% deviation for NOx emission which is still acceptable.

Table 7-3 also provides a comparison of ID14, ID38 and ID67(CFD) to ORB2-LL-7030-(20b,10b)TDC which shows deviations of less than 3% for IMEP, ISFC and combustion noise levels but moderate to considerable deviations for NOx and soot levels compared to ORB2-LL-7030-(20b,10b)TDC. ID14, ID38 and ID67(CFD) had approximately 33.5%, 5.8%, and 15% lower NOx emissions, respectively, as well as 2.1%, 19.2% and 6.5% lower soot emissions which indicated that considerable to significant reductions in emissions could be obtained at similar performance levels.

Table 7-3: Comparison of starting point and ID14, ID38 and ID67 designs

Design ID	**Injection strategy**	**IMEP (bar)**	**ISFC (kg/kwh)**	**Combustion Noise (dB)**	**NOx (ppm)**	**Soot (ppm)**
Starting Point	ORB2-LL-7030-(20b,10b)TDC	2.41	0.2286	215.32	127.62	5.24
14	ORB2-LL-8020-(13b,3b)TDC	2.35	0.2336	214.65	84.9	5.13
38	ORB2-LL-8515-(15b,5b)TDC	2.39	0.2294	214.98	120.2	4.23
67 (virtual)	ORB2-LL-8020-(15b,7b)TDC	2.4	0.2292	214.94	115.42	4.60
67 (CFD)	ORB2-LL-8020-(15b,7b)TDC	2.39	0.2304	214.91	108.40	4.90

Furthermore, the in-cylinder characteristics of ID67(CFD) were compared to that of ORB2-LL-7030-(20b,10b)TDC which was previously presented in Chapter 5. Figure 7-21 presents the in-cylinder pressure and HRR results for these two strategies. The in-cylinder pressure profiles indicated a slightly later start of pressure rise with approximately 4.6% lower peak pressure for ID67(CFD). The observed trend was

attributed to the retardation of the first injection event for ID67(CFD) which resulted in the injection of fuel at higher in-cylinder residence pressure and temperature closer to TDC. Although, ID67(CFD) is a high load strategy thus expecting higher in-cylinder pressure, shorter ignition delays due to improved air-fuel mixing closer to TDC constrained the extent of premixed formation.

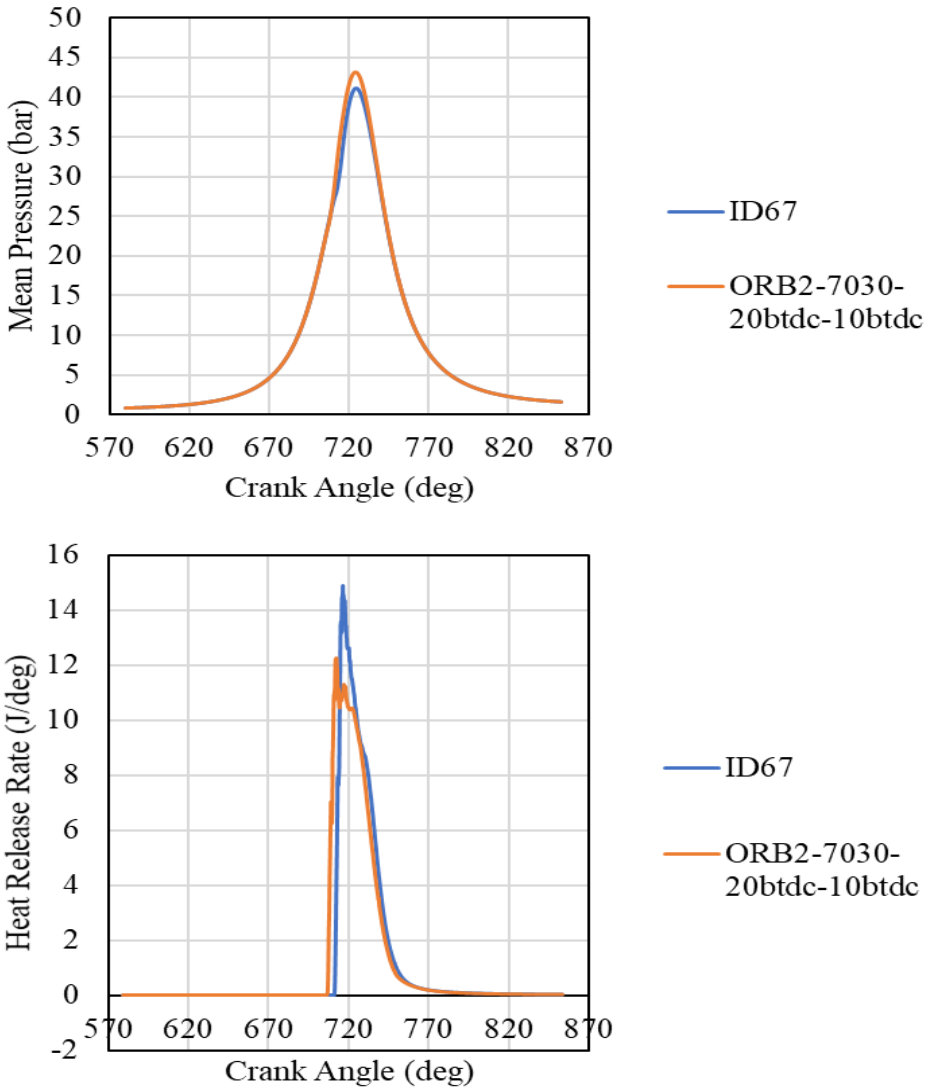

Figure 7-21: In-cylinder pressure (top) and HRR (bottom) results for ID67 and ORB2-LL-7030-(20b,10b)TDC

Moreover, the gradual pressure rise and lower peak pressure of ID67(CFD) contributed to its negligibly lower IMEP seen in Table 6-4. The gradual pressure rise also resulted in lower in-cylinder pressure fluctuations and wave reflections which resulted in relatively lower combustion noise. A comparison of the HRR results showed that ID67(CFD) exhibited about 23.9% higher peak HRR and slightly higher

heat release rate trend in the diffusion and late combustion phases. This characteristic was mainly attributed to the injection of higher fuel quantity during the first injection. However, since higher HRR levels lasted for a shorter period of time compared to ORB2-LL-7030-(20b,10b)TDC, it did not translate to increase in in-cylinder pressure and IMEP. This suggested that high HRRs could be achieved by retarding the injection timing when higher quantities of fuel injection during the first injection without a rapid increase in in-cylinder pressure. The equivalence ratio contours of ID67 are presented in Figure 7-22, illustrating the air-fuel mixing characteristics of this strategy.

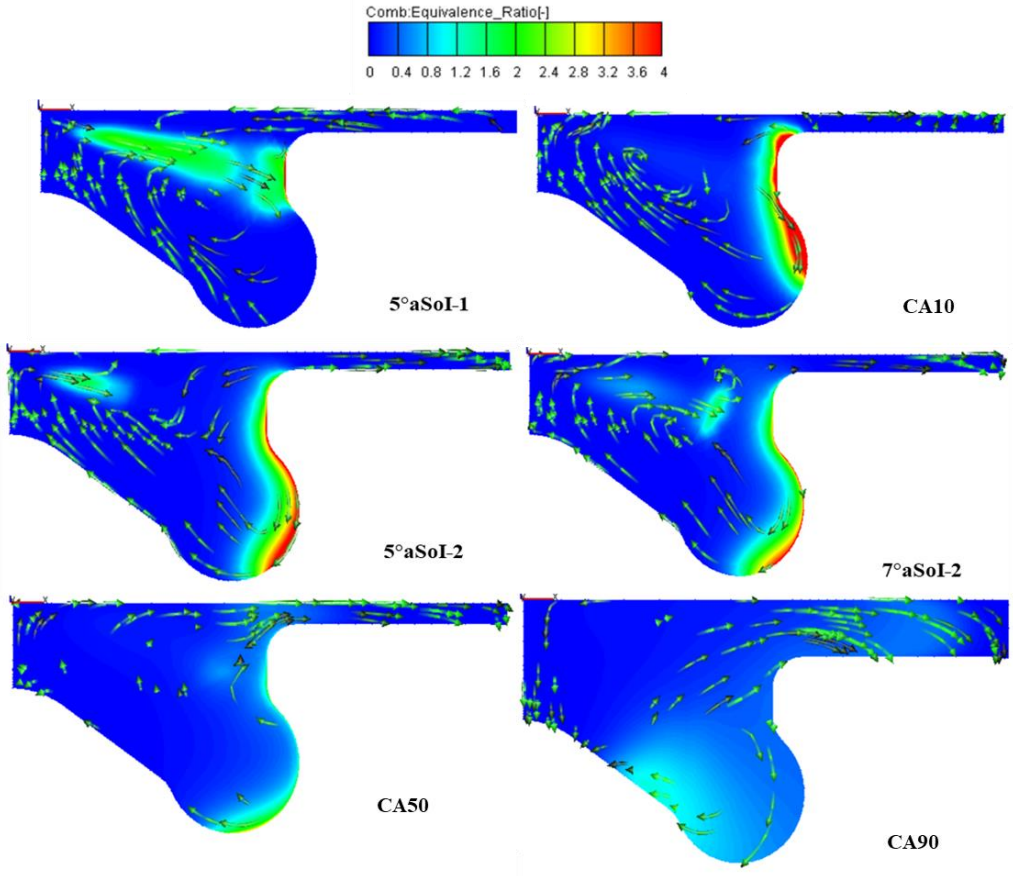

Figure 7-22: Equivalence ratio contours of ID67 including 10%, 50% and 90% heat release timings

It can be seen from Figure 7-22 that the in-cylinder turbulence generated by the bowl geometry influenced the incoming fuel stream during the first injection which promoted bulk fuel dispersion over a higher area upon impact with the bowl side wall. The results also showed that this behaviour gave rise to a large mixing front aided by the bowl geometry's re-entrance curvature. The large mixing front contributed to an improved air-fuel reaction during and after the first injection. Figure 7-22 also

indicated that the bowl geometry and consequential turbulence causes the mixing front to grow, moving more fuel rich mixtures towards air (oxygen) rich regions within the chamber which further improved air-fuel mixing, promoted higher HRR and global temperature distribution thus reducing local temperature hotspots.

The combined effect of bowl geometry's re-entrance curvature and injection strategy by virtue of the mixing front also resulted in reduced NOx and soot emissions formation as shown in Table 7-3. Lower NOx formation occurred due to enhanced air-fuel mixing and improved spatial distribution of premixed mixture which in turn resulted in less localised temperature hotspots. Similarly, reduced soot formation also occurred as a result of enhanced air-fuel mixing and improved spatial distribution of premixed mixture caused by the mixing front which led to pockets of fuel rich mixtures to move towards air rich regions thus improving fuel oxidation. In addition, lower second fuel injection quantity resulted in less diffusion combustion. Figure 7-22 demonstrated that fuel during the second injection was not injected into burning regions due to the combustion of fuel during the first injection but rather in an air rich environment which limited diffusion combustion and consequently soot formation.

7.3 Optimisation Results at High Load using the HRT

For the high load optimisation process, a hybrid design dataset comprising of 20 ULH designs and 42 MOGA-II designs. The crossover, selection and mutation probabilities of MOGA-II were kept at 0.5, 0.05 and 1, respectively, based on the values reported in a similar investigation [254]. During the regression modelling process, the k-fold cross validation, wherein k is equal to 5 folds, was found to be effective towards mapping the relationship between the design parameters and the responses.

The log-constant transformation method which involved addition of a constant value of 20 to the log of soot response data was performed to improve the visibility of its relationship to the design parameters. Table 7-4 presents a set of statistical metrics which indicate the performance of the regression models selected for each response. An overview of the regression models showed that the relationships between the design parameters and the respective objective responses were mapped by different regression methods which supported the initial notion that various regression methods could yield different mapping relationships. Apart from that, it also showed that the

regression modelling analysis also showed that the Gaussian Processes Regression (GPR) could be easily applied towards mapping more relationships than others.

GPR models with exponential kernel functions were used to accurately represent the relationship between the design parameters and IMEP and ISFC responses whereas the squared exponential kernel function was used for the soot response. Furthermore, the relationship between the design parameters and combustion noise was represented by the SVM regression model with a quadratic kernel function while the relationship for NOx was represented by the linear interaction model.

Table 7-4: Statistical performance of the regression models at high load

Objectives	**Regression Model**	**R^2**	**RMSE**	**MAE**	**LAR**
IMEP	GPR-Exp	0.96	0.0666	0.04907	0.00269
ISFC	GPR-Exp	0.95	0.0038	0.00252	0.00296
Noise	SVM-Quad	0.96	0.2084	0.10422	0.000013
NOx	Linear_Interaction	0.98	0.0920	0.07092	0.4232
Soot	GPR-Sqd-Exp	0.90	0.42303	0.29309	0.0276

Figure 7-23 to Figure 7-32 present graphical illustration of the predictive performance of the models presented in Table 7-4. The results along with the performance metrics suggested that the adopted k-fold validation could result in reliable predictions during the optimisation process. Strong correlations coupled with relatively small residuals and a relatively low variance for IMEP, ISFC and combustion noise were observed whereas that of NOx and soot were slightly higher but still acceptable.

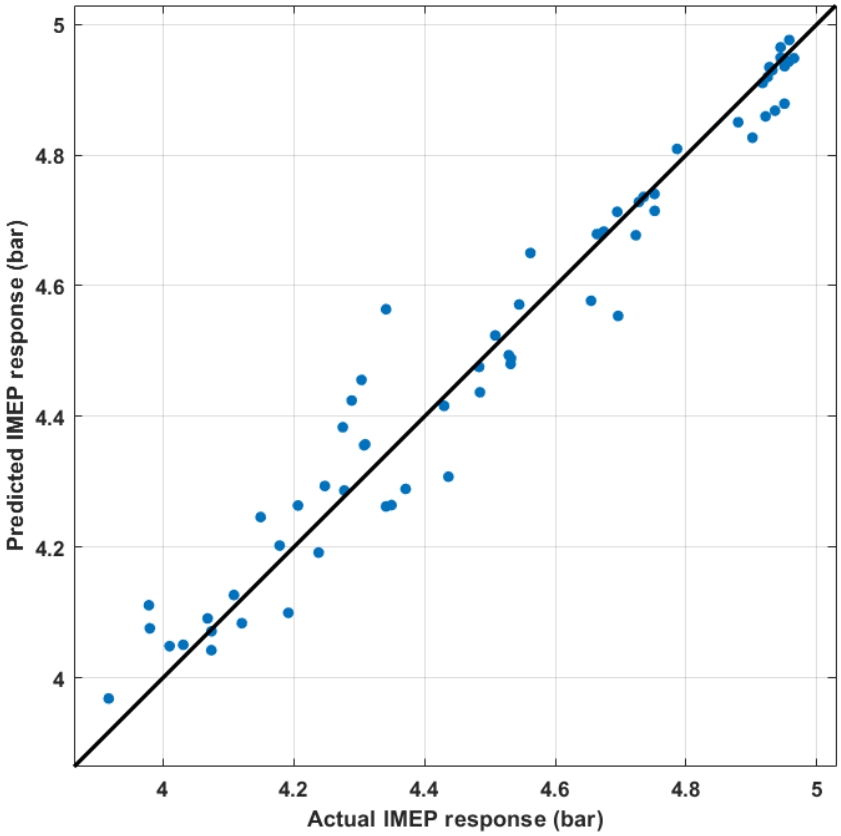

Figure 7-23: Predicted vs actual IMEP response at high load

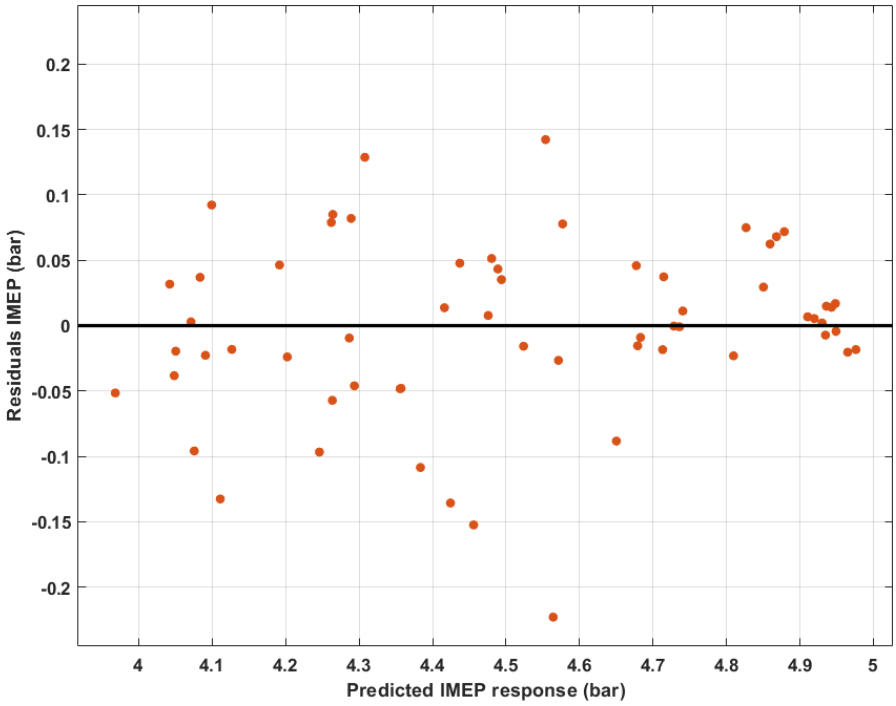

Figure 7-24: Residuals vs actual IMEP response at high load

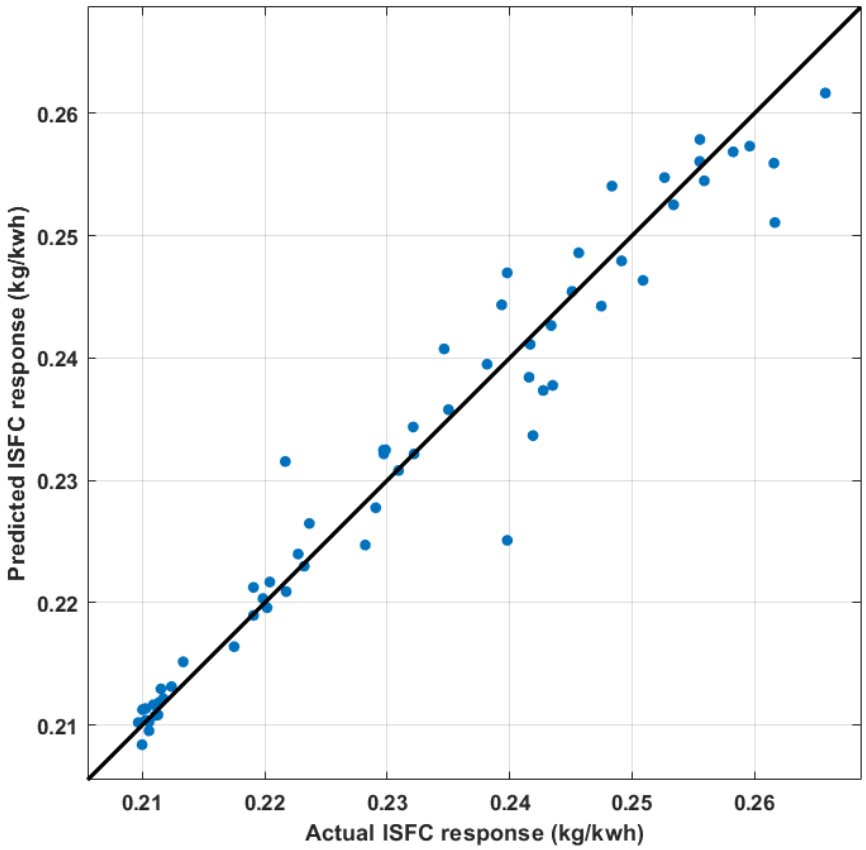

Figure 7-25: Predicted vs actual ISFC response at high load

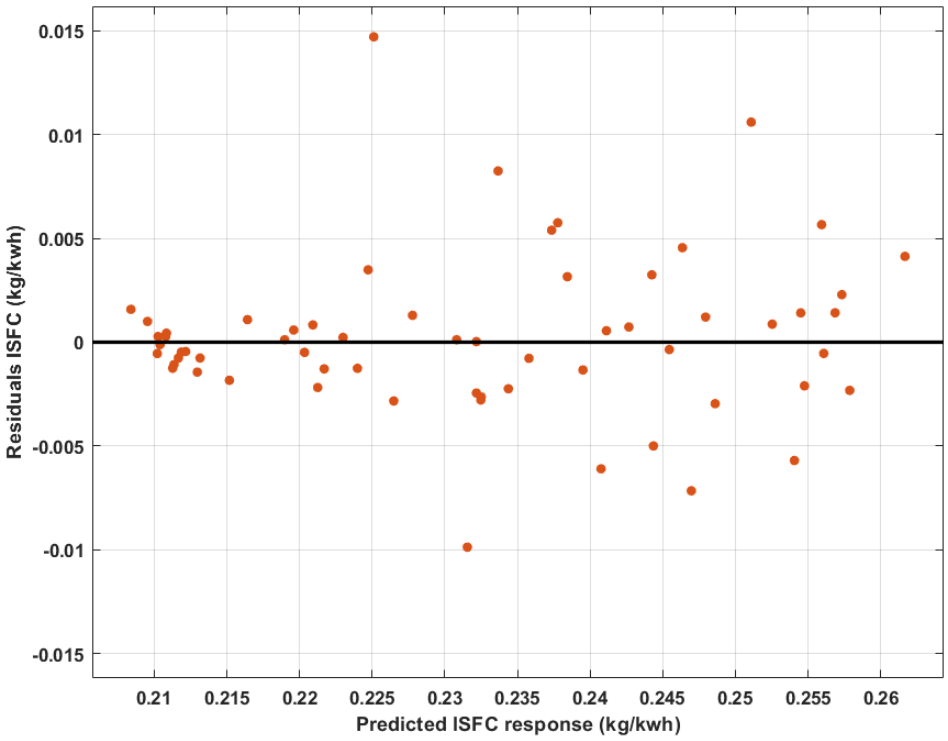

Figure 7-26: Residuals vs actual ISFC response at high load

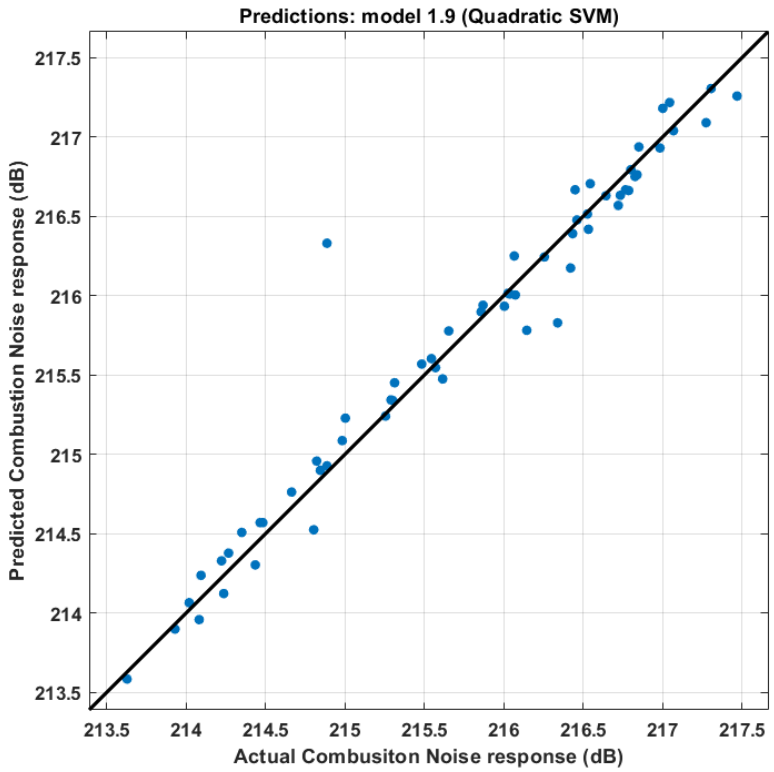

Figure 7-27: Predicted vs actual combustion noise response at high load

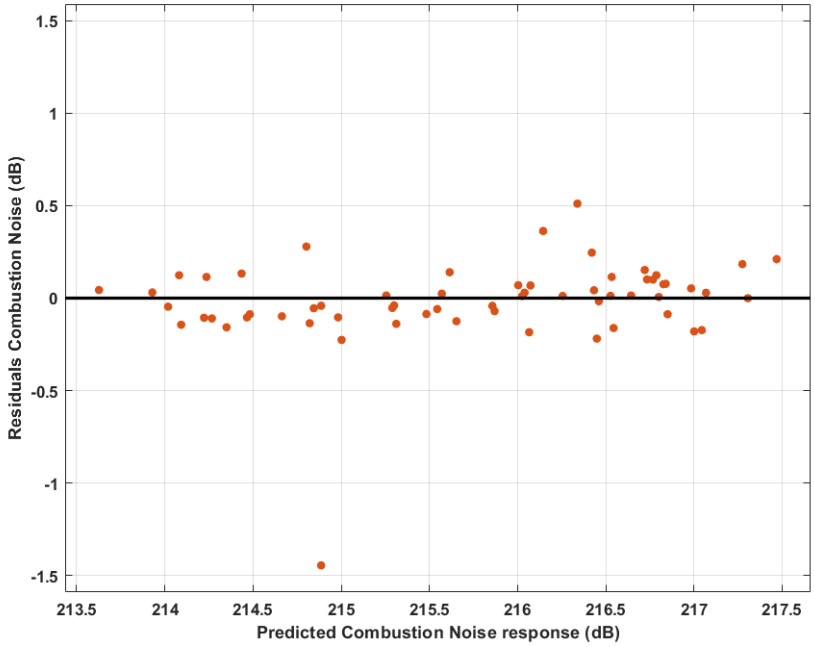

Figure 7-28: Residuals vs actual combustion noise response at high load

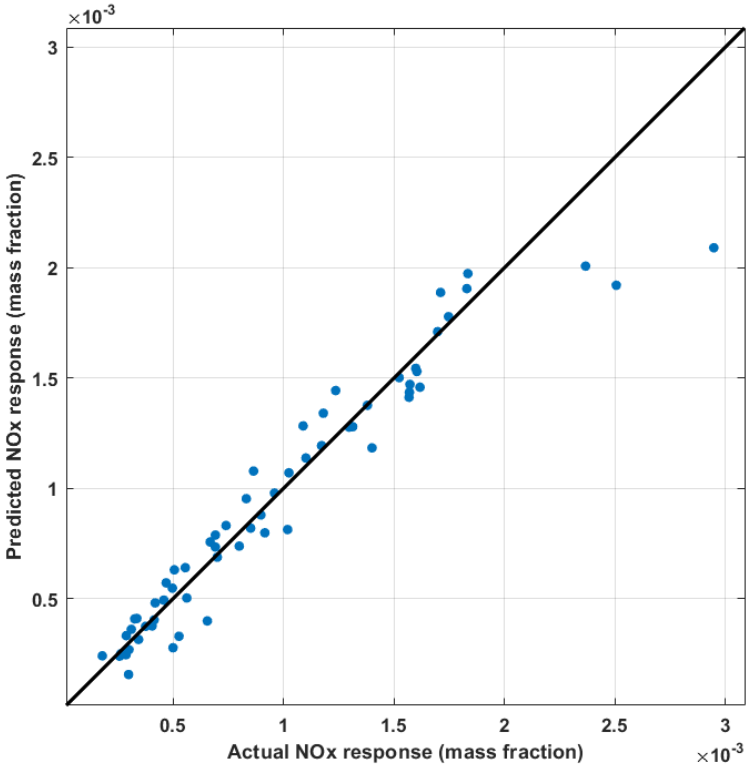

Figure 7-29: Predicted vs actual NOx response at high load

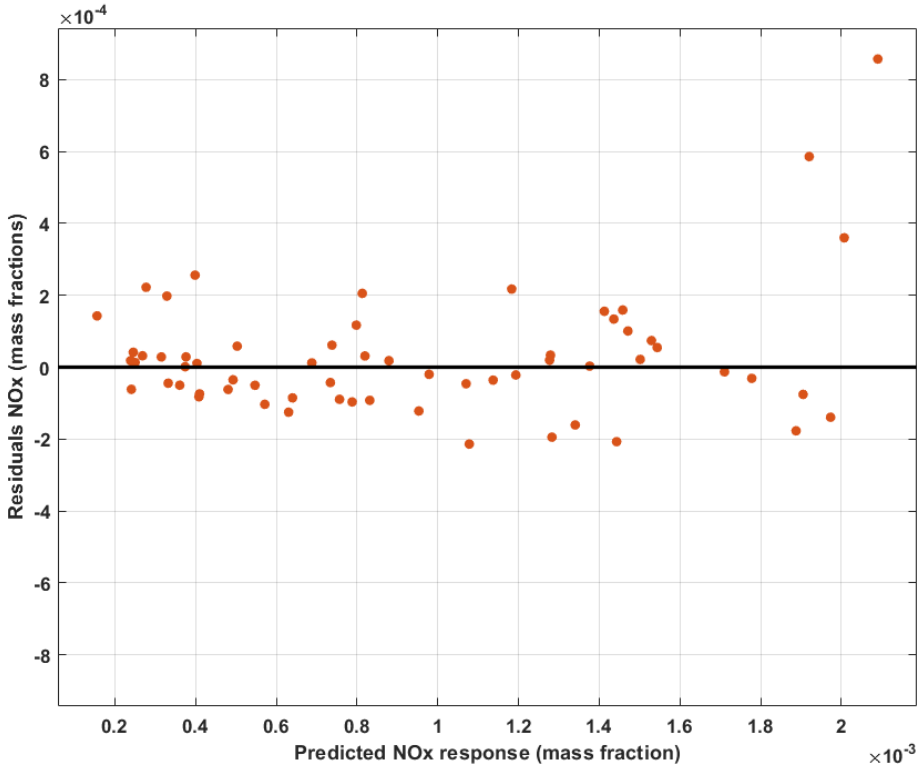

Figure 7-30: Residuals vs actual NOx response at high load

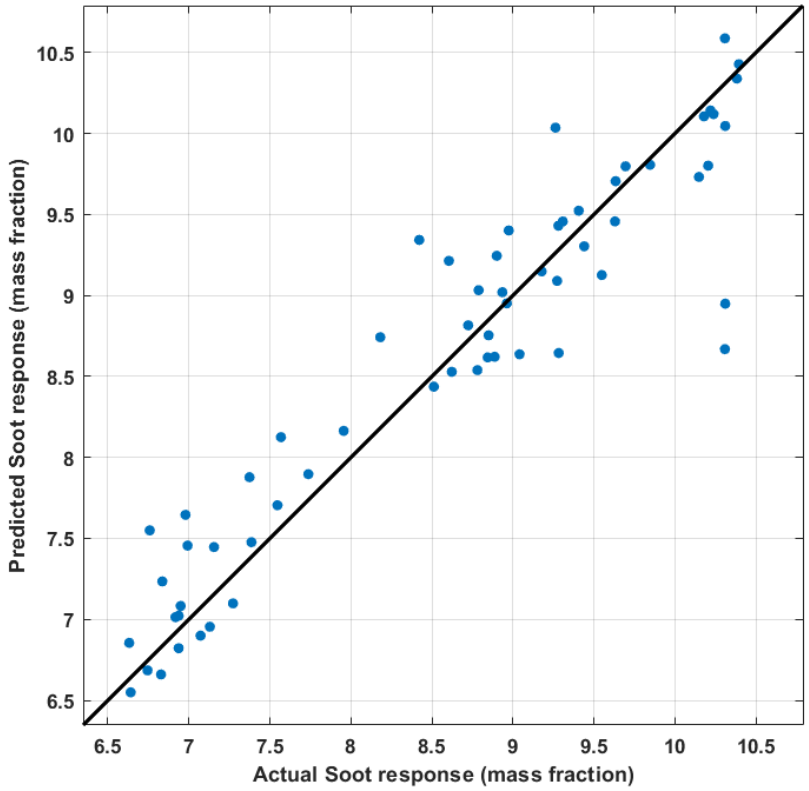

Figure 7-31: Predicted vs actual log-constant transform of soot response at high load

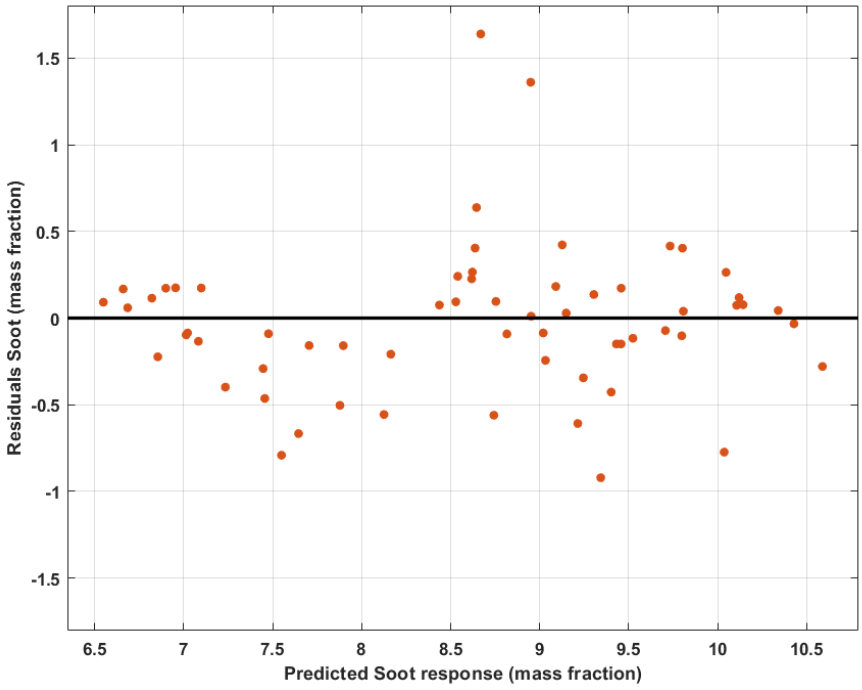

Figure 7-32: Residuals vs actual log-constant transform soot response at high load

Figure 7-33 to Figure 7-39 present the results of the optimisation process at high load in the form of the objective spaces of the multi-objective domain. A total of 655 designs categorised into CFD generated designs, virtual regression-based generated designs and pareto optimal designs were formed. In addition, the design and output parameters of ORB2-7030-(15b,5b)TDC at high load were used as the starting point for comparison against the generated designs since it yielded improved performance and emissions in the earlier investigation.

An overview of the objective spaces showed that the hybrid regression-based optimisation methodology was effective in approaching the pareto region of the multi-objective domain containing predicted optimal design solutions. Several pareto optimal designs were observed to be vastly far from the starting point, suggesting that there were more double injection strategies capable of yielding engine performance and emissions improvements.

The parallel coordinates tool within modeFRONTIER was used to analyse the designs with respect to the parameters of ORB2-HL-7030-(15b,5b)TDC in order to extract the pareto optimal solutions that satisfied the multi-objective criteria or provided negligible losses in performance but significant reductions in emissions in the pareto region. The three pareto optimal designs (i.e., ID192, ID1232 and ID1242) highlighted in green were obtained using this process. ID192, ID1232 and ID1242 were regression generated strategies of the optimisation and were verified using 3D CFD engine simulation to provide certainty of the model's reliability.

The computational time of the optimisation process at high load was also analysed in a similar manner as that of the low load. Here, the durations for optimisation process using the HRT with and without the crank angle reduction scheme were compared to a similar preliminary optimisation study in which 425 CFD simulated designs were generated using the 3D CFD-MOGA-II. It was found that simulating 62 3D CFD designs based on the hybrid dataset for HRT instead of 425 designs without the reduction scheme resulted in the HRT being 85.4% faster than 3D CFD-MOGA-II. Since the Crank Angle Reduction Scheme reduced each simulation time to 3 hours, its application resulted in the HRT being 94.5% faster than the 3D CFD-MOGA-II.

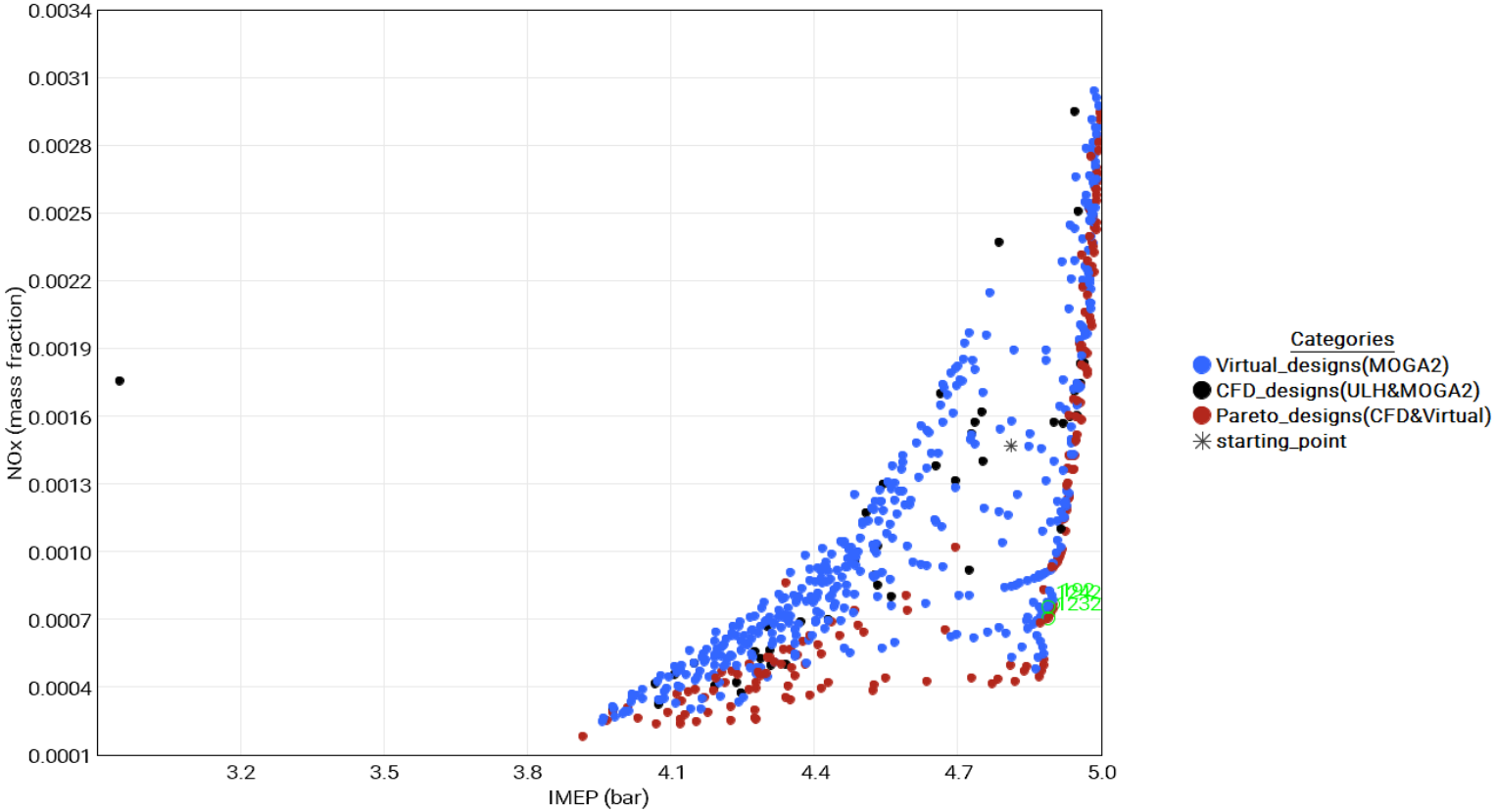

Figure 7-33: IMEP-NOx objective space at high load

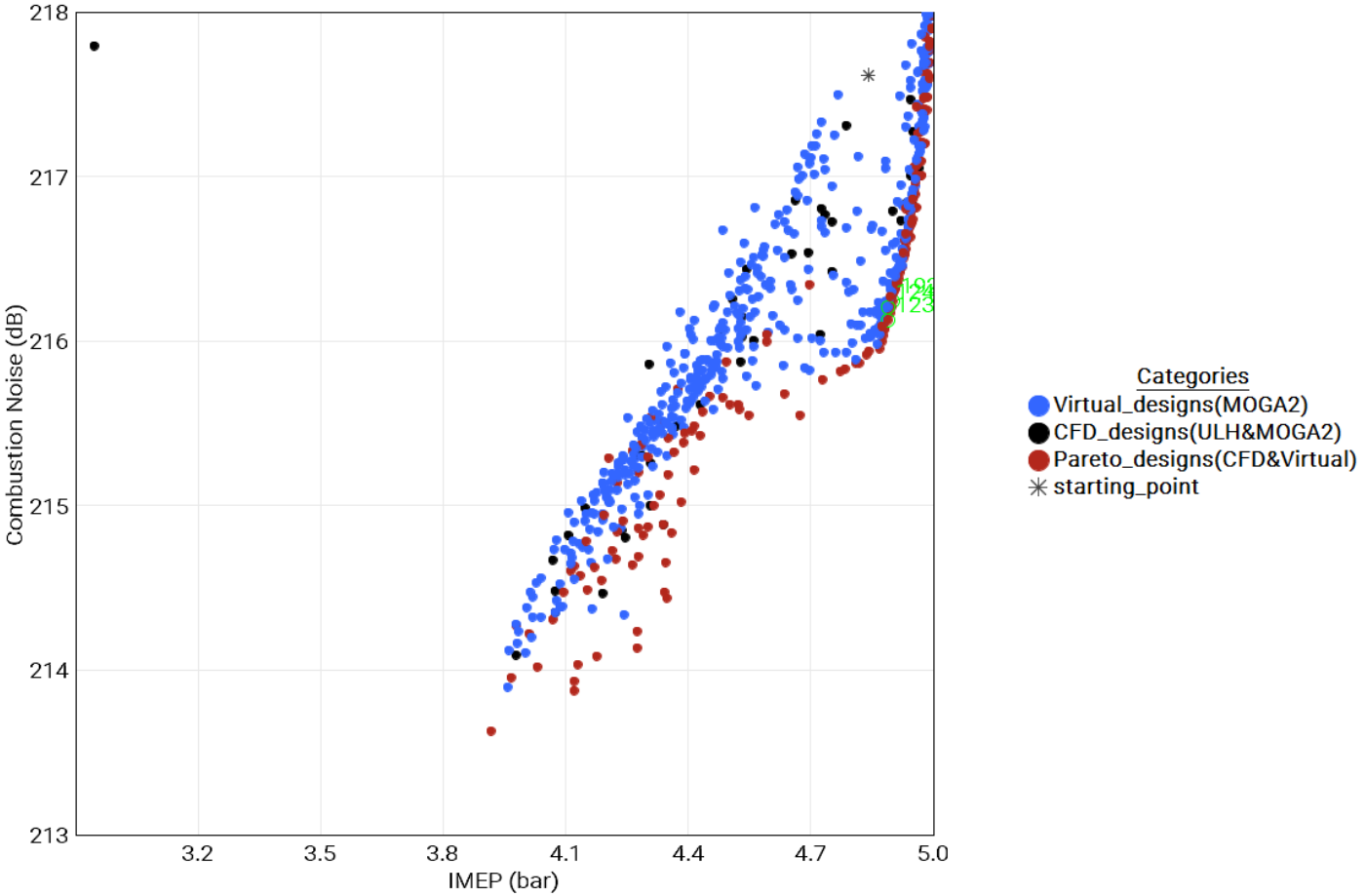

Figure 7-34: IMEP-Noise objective space at high load

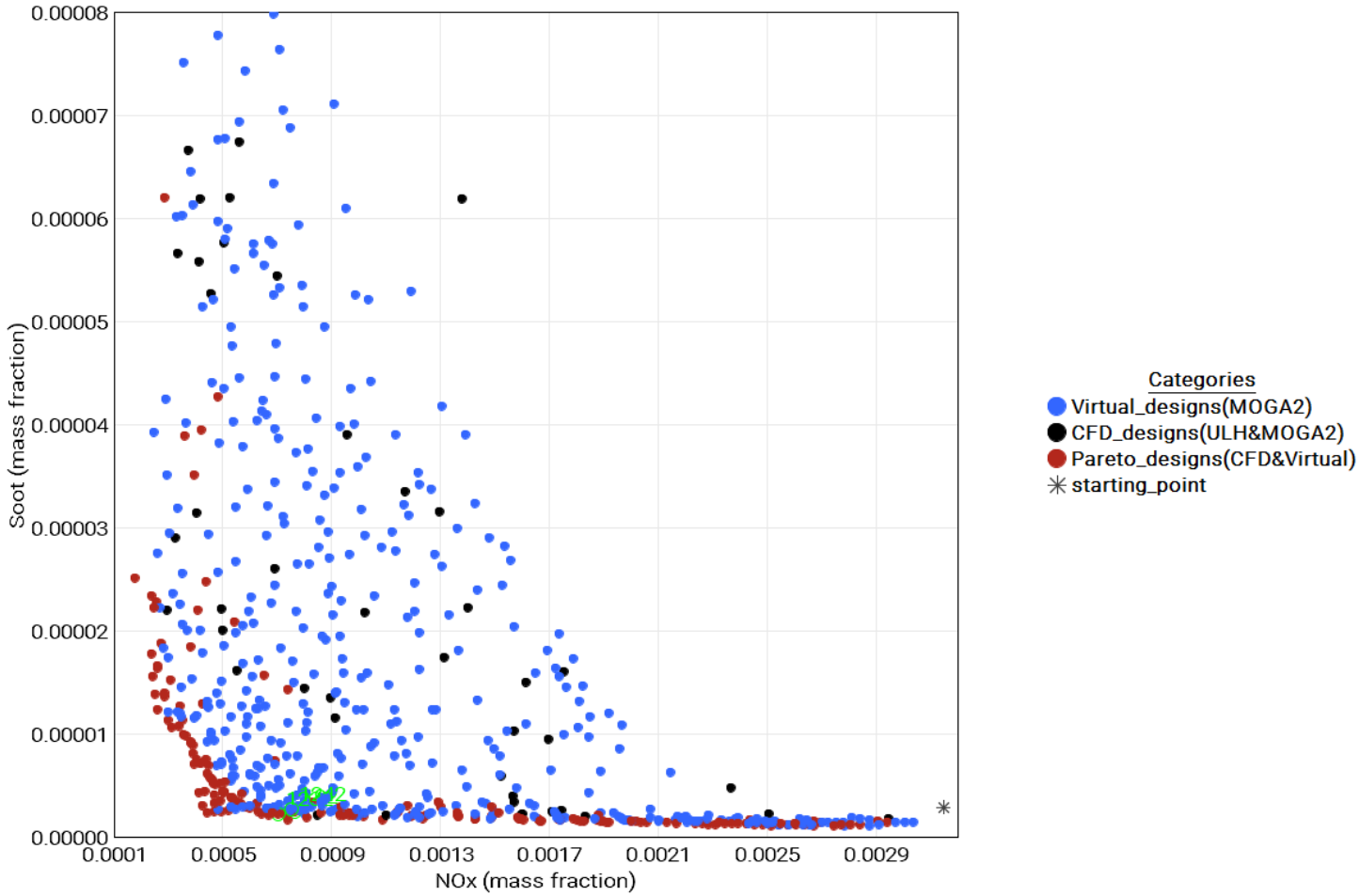

Figure 7-35: NOx-Soot objective space at high load

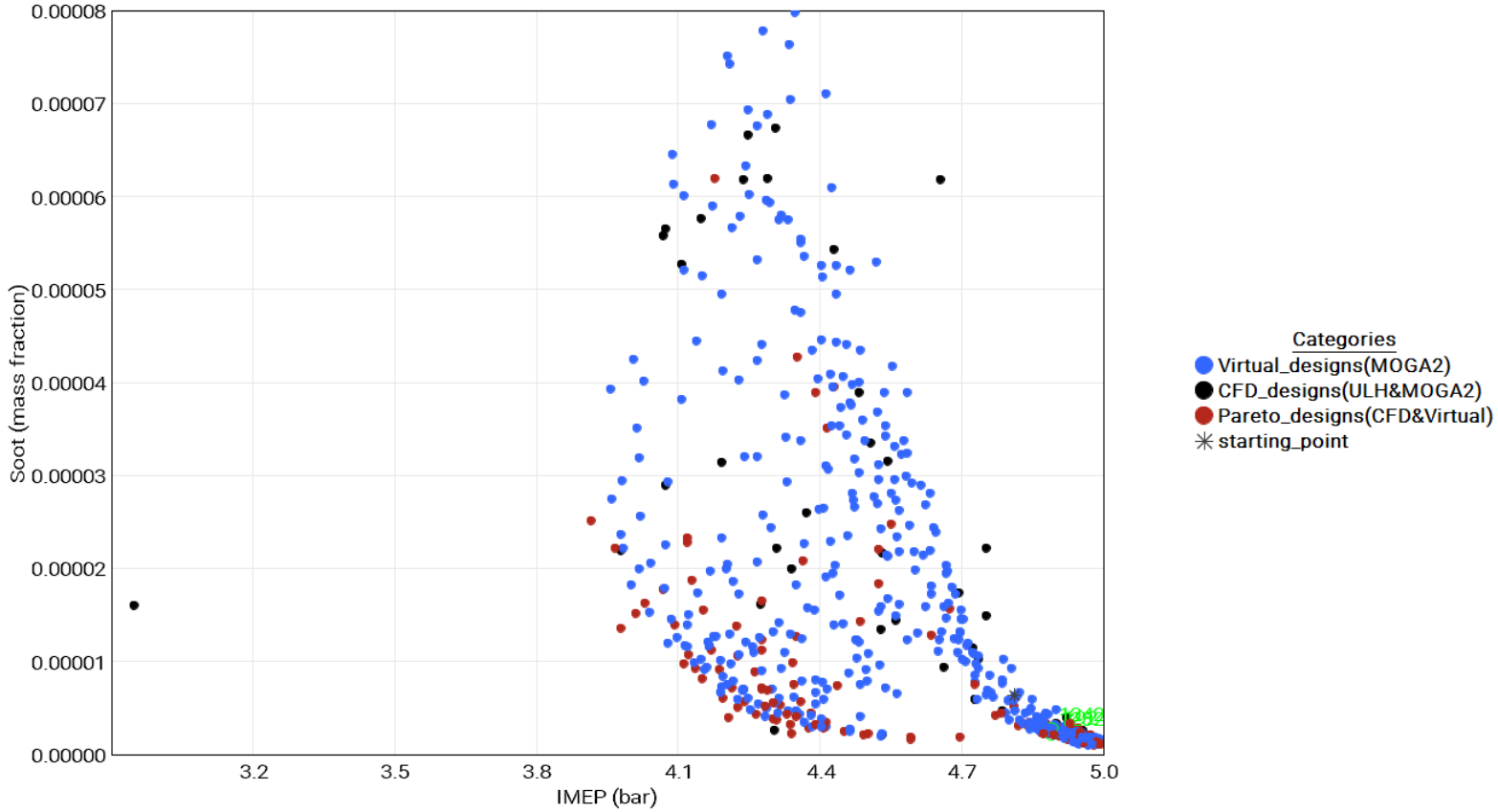

Figure 7-36: IMEP-Soot objective space at high load

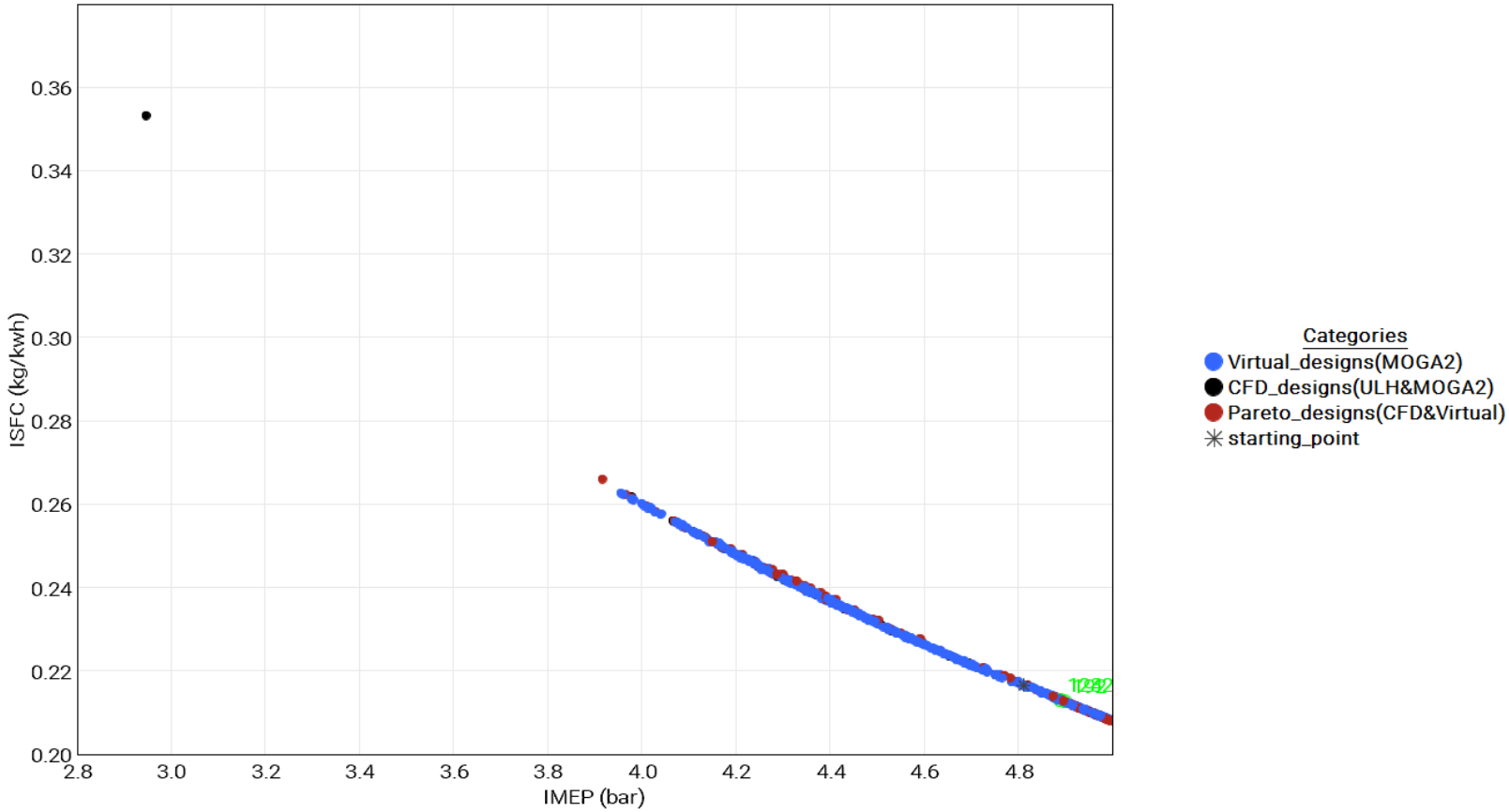

Figure 7-37: IMEP-ISFC objective space at high load

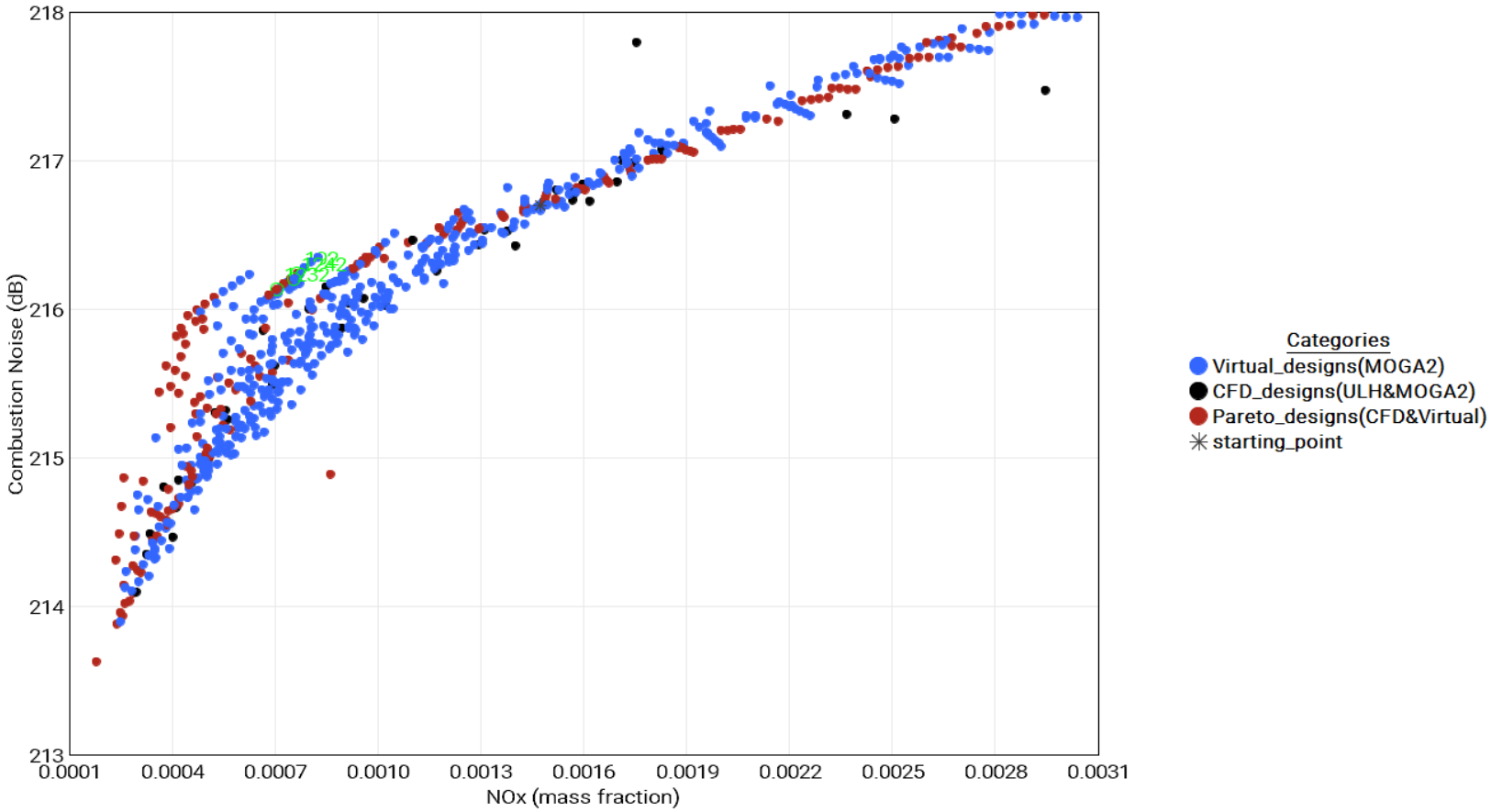

Figure 7-38: NOx-combustion noise objective space at high load

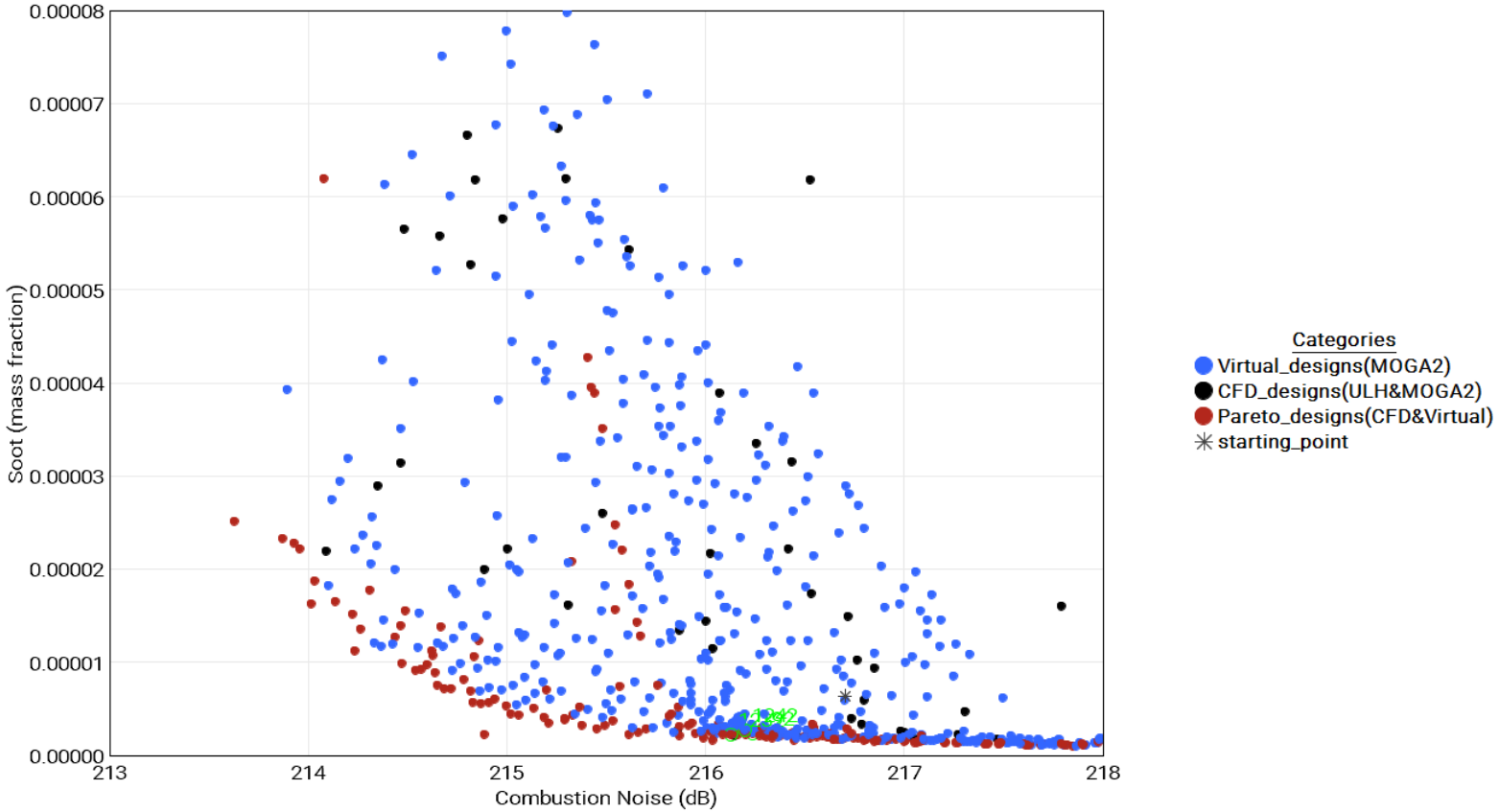

Figure 7-39: Combustion noise-soot objective space at high load

Table 7-5 presents the verified strategies as ID192(CFD), ID1232(CFD) and ID1242(CFD). The verification process showed that CFD results for the strategies were in good agreement with their respective regression estimates by the model. ID192(CFD) had about 1.6% lower IMEP, 1.8% higher ISFC, less than 1% lower combustion noise, 4.8% lower NOx and 8% higher soot. On the other hand, ID 1232(CFD) had about 1.2% lower IMEP, 1.1% lower ISFC, less than 1% lower combustion noise, 10% lower NOx and 1.8% higher soot. Finally, ID1242 had about 1.4% lower IMEP, 1.4% higher ISFC, less 1% lower combustion noise, 9.4% lower NOx and 8.3% higher soot. The deviations in regression for high load was observed to be higher than those seen for the low load especially with regards to the emissions. This was attributed to uncertainties associated with the influence of fuel quantity which was only captured as a ratio rather than chemical reaction in the regression modelling. These uncertainties could impact the visibility of the relationship between the design parameters and the soot response by the models especially for ID1232 and ID1242. Such issues have also been highlighted as a challenge in in previous studies. Nevertheless, the deviations were within the acceptable limits.

Table 7-5: Validation of optimal injection strategies with 3D CFD modelling

Design ID	**Injection strategy**	**IMEP (bar)**	**ISFC (kg/kwh)**	**Combustion Noise (dB)**	**NOx (ppm)**	**Soot (ppm)**
192	ORB2-HL-9505-(11b,0b)TDC	4.89	0.2127	216.24	765.09	2.36
192(CFD)		4.81	0.2165	216	728.65	2.55
1232	ORB2-HL-9505-(11b,3b)TDC	4.88	0.2132	216.13	704.85	2.18
1232(CFD)		4.83	0.2157	216.03	776.5	2.22
1242	ORB2-HL-9010-(11b,1a)TDC	4.89	0.2131	216.2	755.07	2.65
1242(CFD)		4.82	0.2160	215.95	683.85	2.87

Table 7-6 also provides a comparison of ID192(CFD), ID1232(CFD) and ID1242(CFD) to ORB2-HL-7030-(15b,5b)TDC which shows deviations of less than 1% for IMEP, ISFC and combustion noise levels but significant deviations in NOx and soot levels compared to ORB2-HL-7030-(15b,5b)TDC. ID192(CFD),

ID1232(CFD) and ID1242(CFD) had about 50.5%, 47.3% and 53.6% lower NOx emissions, respectively, as well as 60.2%, 65.3% and 55.1% lower soot emissions, respectively, which indicated that significant reductions in emissions could be obtained at similar performance levels.

Table 7-6: Comparison of starting point to ID192, ID1232 and ID1242 designs

Design ID	**Injection strategy**	**IMEP (bar)**	**ISFC (kg/kwh)**	**Combustion Noise (dB)**	**NOx (ppm)**	**Soot (ppm)**
Starting Point	ORB2-HL-7030-(15b,5b)TDC	4.81	0.2165	216.7	1472.47	6.4
192(CFD)	ORB2-HL-9505-(11b,0b)TDC	4.81	0.2165	216.00	728.65	2.55
1232(CFD)	ORB2-HL-9505-(11b,3b)TDC	4.83	0.2157	216.03	776.5	2.22
1242(CFD)	ORB2-HL-9010-(11b,1a)TDC	4.82	0.2160	215.95	683.85	2.87

Furthermore, the in-cylinder characteristics of ID192(CFD), ID1232(CFD) and ID1242(CFD) were compared to that of ORB2-HL-7030-(15b,5b)TDC which was previously presented in Chapter 4. Figure 7-40 shows the in-cylinder pressure and HRR results for these strategies. The in-cylinder pressure profiles for the optimal strategies indicated a slightly later start of pressures rise with approximately 9.6% lower peak pressures. This behaviour for all three strategies was attributed to the retardation of the first injection event which resulted in the injection of fuel at a time of higher in-cylinder residence pressure and temperature closer to TDC, thus leading to shorter ignition delay and reduced air-fuel mixing time. This control over air-fuel mixing also led to a constrained premixed formation.

The HRR results showed that these strategies also exhibited higher peak HRR, higher levels of heat release rate in the diffusion combustion phase as well as towards the end of the combustion compared to ORB2-HL-7030-(15b,5b)TDC despite having smaller fuel injection quantities in their respective second injection events. This HRR

behaviour contributed to the slightly higher-pressure trends after TDC which resulted in negligibly higher IMEP levels for ID1232 and ID1242.

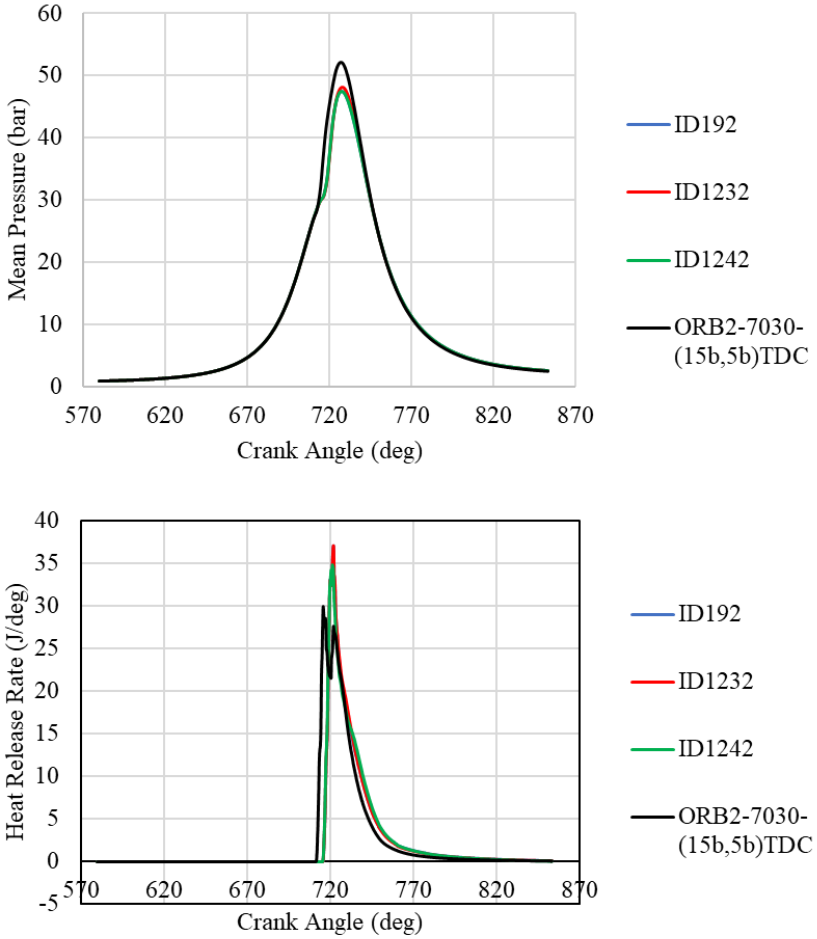

Figure 7-40: In-cylinder pressure (top) and HRR (bottom) results for ID192(CFD), ID1232(CFD), ID1242(CFD) and ORB2-HL-7030-(15b,5b)TDC

Moreover, the gradual pressure rise also resulted in lower in-cylinder pressure fluctuations and wave reflections which resulted in relatively lower combustion noise. A comparison of the HRR results showed that all three strategies exhibited higher peak HRR with ID192(CFD) and ID1242(CFD) having about 16.6% higher peak HRR levels while ID1232(CFD) had about 23.3% higher peak HRR level. In addition, the three strategies had slightly higher heat release rate trends in their respective diffusion and late combustion phases. This commonality between them was mainly attributed to the injection of higher fuel quantities in their respective first injection events which suggested that higher HRR could be achieved by retarding the injection timing when higher quantities of fuel is injected during the first injection without a rapid increase in in-cylinder pressure.

The higher HRRs were also attributed to a global improvement in air-fuel mixing within the chamber promoted by the formation of large mixing front from the interaction between their respective fuel injection characteristics and the re-entrance curvature of the ORB2 bowl. The equivalence ratio contours of ID1242 are presented in Figure 7-41 to provide further insight into air-fuel mixing characteristics. Here, it can be seen that the in-cylinder turbulence generated especially above and below the bowl side region causes the incoming fuel stream during the first injection event to disperse over a large area upon wall impingement. The results also showed that this characteristic gave rise to a large mixing front aided by the bowl geometry's re-entrance curvature. This mixing front which contributed to an improved air-fuel reaction during and after the first injection event was also observed to grow, moving more fuel rich mixtures towards air (oxygen) rich regions within the chamber which further improved air-fuel mixing, promoted higher HRR and global temperature distribution thus reducing local temperature hotspots.

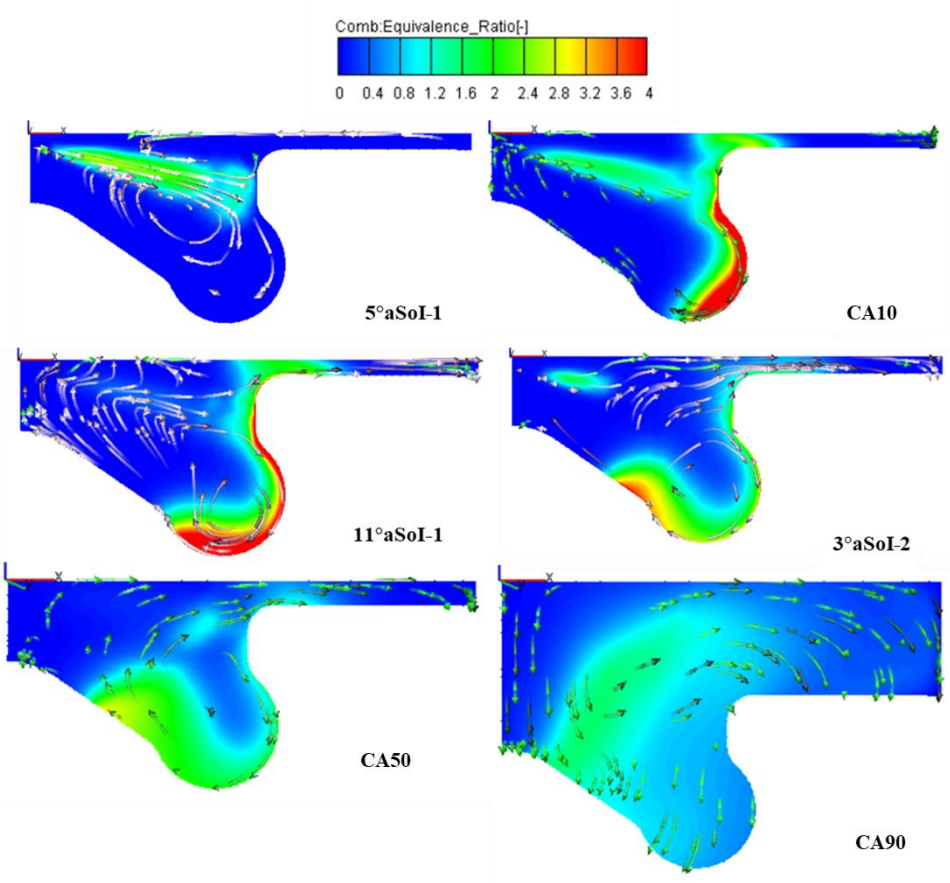

Figure 7-41: Equivalence ratio contours of ID1242 including 10%, 50% and 90% heat release timings

The combined effect of bowl geometry's re-entrance curvature and injection strategy through the mixing front also resulted in reduced NOx and soot emissions formation as shown in Table 7-6. Lower NOx formation occurred due to enhanced air-fuel mixing and improved spatial distribution of premixed mixture which in turn resulted in less localised temperature hotspots. On the other hand, lower soot formation occurred due to smaller fuel quantity injected during the second injection event which is seen to occur in an air rich region which limited diffusion combustion and consequently soot formation. In addition, the migration of fuel rich formations by the mixing front towards air rich regions as well as the influence of the bowl re-entrance curvature on turbulence during the chamber expansion stroke promoted fuel oxidation and thus reduced soot formation.

7.4 Concluding Remarks

In this chapter, a unique "Hybrid Regression-based Technique" was developed and used for the double injection strategy optimisation that consisted of a hybrid design dataset and ensemble hybrid regression model. The hybrid regression model featured a k-fold cross validation process used to split the dataset, and a hybrid regression predictive model which consists of multiple regression models for the respective relationships between each response and the three design predictors. This hybrid regression model was used for the simultaneous prediction of each response towards optimality.

At low load, the effectiveness of the technique especially that of its unique hybrid design dataset was evident whereas that of the hybrid regression model was more evident at the high load based on the selected optimal designs. Small and acceptable deviations between the model predictions and their respective CFD validations showed its effectiveness in replacing CFD simulations to a great extent. The optimisation process resulted in marginal differences in the performance parameters IMEP, ISFC and combustion noise as well as significant reductions in the NOx and soot emissions across both engine loads which were achievable with the injection of 90% to 95% of the total fuel quantity during the first injection event at injection timings closer to 711.4CA and a dwell angle of approximately 8 to 13CA.

In addition, the optimisation process required about 94% less computational time compared to the 3D CFD-MOGAII approach mainly due to the combined effect of the hybrid dataset and crank angle reduction scheme. The optimisation process required about 80% less computational time without the crank angle scheme thus making it time effectiveness comparable to other recent approaches such as the ActivO.

8 Conclusions and Future Recommendations

This research study focused on the interaction and optimisation of piston bowl geometry and double fuel injection strategy under low and high engine load conditions using a bespoke hybrid multi-objective optimisation algorithm and 3D CFD engine modelling which was validated based on the experimental data obtained from a Ricardo Hydra single cylinder optical diesel engine.

In-cylinder pressure and HRR results as well as equivalence ratio, temperature distribution, NOx and soot emissions data under various operating conditions were employed to study air-fuel mixing, combustion process and emissions formation as a function of piston bowl re-entrance curvature and the consequential mixing front as a key factor. In addition, performance and emissions results were also utilised in extracting vital information on the effects of the highlighted interactions. Section 8.1 and 8.2 present the conclusions of the research work.

8.1 Conclusions from the study in Chapter 4 and 5

The effects from the interactions between piston bowl geometry and double injection strategy were investigated at low and high loads and presented in chapter 4 and 5 respectively. Three piston bowl geometries were investigated, namely FRB, ORB1 and ORB2 under 50:50 and 70:30 injection ratios and six double injection timings with the start of the first injection ranging from 20bTDC to 5aTDC at an interval of 5CA and a dwell angle of 10CA.

The following conclusions were drawn from the investigation detailed in Chapter 4 and 5:

1. The influence of piston bowl geometry, injection timing retardation and injection ratio on IMEP was explored at low and high load.
    i. Regarding piston bowl geometry, the FRB and ORB2 exhibited the highest and second highest IMEP levels in the majority of the tested cases for both injection ratios at low load while ORB1 and ORB2 exhibited the highest the second highest IMEP levels in majority of the cases for both injection ratios at high load.
    ii. Regarding injection timing retardation, the FRB and ORB2 exhibited 38.5% and 24.2% reduction in IMEP respectively for the 50:50 ratio

as injection timing was retarded from LL-5050-(20b,10b)TDC to LL-5050-(5a,15a)TDC. Both bowl geometries also exhibited a 34.8% and 31.1% reduction in IMEP respectively for the same range of injection retardation for the 70:30 ratio.

iii. For the 50:50 ratio at high load, ORB1 and ORB2 exhibited a 20% and 26.4% reduction in IMEP respectively as injection timing was retarded from HL-5050-(20b,10b)TDC to HL-5050-(5a,15a)TDC. For the 70:30 ratio, both bowl geometries exhibited a 14.9% and 26.3% reduction in IMEP respectively as injection timing was retarded from HL-7030-(20b,10b)TDC to HL-7030-(5a,15a)TDC.

iv. Regarding injection ratio, the cases for the 70:30 ratio exhibited higher IMEP levels compared to the same cases for 50:50 ratio at low load. For the FRB, LL-7030-(20b,10b)TDC had a 2.5% higher IMEP compared to LL-5050-(20b,10b)TDC while the LL-7030-(5a,15a)TDC had an 8.6% higher IMEP compared to LL-5050-(5a,15a)TDC. For ORB2, LL-7030-(20b,10b)TDC had a 19.3% higher IMEP compared to LL-5050-(20b,10b)TDC while LL-7030-(5a,15a)TDC had an 8.4% higher IMEP compared to LL-5050-(5a,15a)TDC.

v. The cases for the 70:30 ratio also exhibited higher IMEP levels compared to the same cases for 50:50 ratio at high load. For the ORB1, HL-7030-(20b,10b)TDC had a 3.3% higher IMEP compared to HL-5050-(20b,10b)TDC and HL-7030-(5a,15a)TDC had a 9.9% higher IMEP compared to HL-5050-(5a,15a)TDC. For ORB2, HL-7030-(20b,10b)TDC had a 3.6% higher IMEP compared to HL-5050-(20b,10b)TDC while HL-7030-(5a,15a)TDC had a 3.7% higher IMEP compared to HL-5050-(5a,15a)TDC.

2. The influence of the piston bowl geometry, injection timing retardation and injection ratio on combustion noise was explored. The results showed that the changes in piston bowl geometry and injection strategy with regards to injection retardation and ratios had minimal influence on combustion noise.

   i. The FRB, ORB1 and ORB2 geometries resulted in negligible differences to combustion noise of less than 1% in cases with the same injection timings for the 50:50 and 70:30 ratios at low and high load.

ii. Retardation of the injection timing resulted in less than 2% reduction in combustion noise at low and high loads for all three bowl geometries at the 50:50 and 70:30 injection ratios.

iii. The cases for the 70:30 injection ratio had higher combustion noise levels compared to the cases for the 50:50 injection ratio. Nevertheless, the differences were minimal of less than 1% at low and high load.

3. The influence of piston bowl geometry, injection timing and injection ratio on NOx and soot emissions was explored.

   i. At low load 50:50 ratio, the FRB and ORB2 exhibited the highest and second highest NOx emissions in all the cases except for LL-5050-(5a,15a)TDC where ORB2 had the highest NOx emissions. The NOx emissions for ORB2 were 84.3%, 84.7%, 83.7%, 77.9% and 65.4% lower compared to FRB for LL-5050-(20b,10b)TDC, LL-5050-(15b,5b)TDC, LL-5050-(10b,0)TDC, LL-5050-(5b,5a)TDC and LL-5050-(0,10a)TDC compared to FRB. This showed that the presence of re-entrance curvature in the bowl geometry as seen in ORB2 significantly influenced NOx formation. A similar trend also held true for the 70:30 ratio at low load.

   ii. At high load 50:50 ratio, ORB1 and ORB2 exhibited the highest and second highest NOx emissions in all cases. The NOx emissions for ORB2 were 13.4%, 25.2%, 39.5%, 51.9%, 50.3% and 56.1% lower compared to ORB1 for HL-5050-(20b,10b)TDC, HL-5050-(15b,5b)TDC, HL-5050-(10b,0)TDC, HL-5050-(5b,5a)TDC, HL-5050-(0,10a)TDC and HL-5050-(5a,15a)TDC. This showed that the degree of re-entrance curvature and bowl depth in the bowl geometry as seen in ORB2 significantly influenced NOx formation. A similar trend was also observed for the 70:30 ratio at high load.

   iii. Regarding the influence of injection timing and ratio on NOx emission, ORB2-HL-5050-(5a,15a)TDC had a 97.3% lower NOx emission compared to ORB2-HL-5050-(20b,10b)TDC while ORB2-HL-7030-(5a,15a)TDC had a 68.5% lower NOx emission compared to ORB2-HL-7030-(20b,10b)TDC. Similar trends were also observed for ORB1. Also, the 70:30 ratio cases had higher NOx emissions compared to the 50:50 ratio cases in all the cases. ORB2-HL-7030-(20b,10b)TDC had a

40% higher NOx emissions compared to ORB2-HL-5050-(20b,10b)TDC which showed that both injection timing retardation and ratio had a significant influence on NOx emission at low and high load.

iv. At high load, FRB and ORB1 exhibited the highest and lowest soot emissions for both injection ratios in all cases. At low load, the ORB1 and ORB2 exhibited the highest and second highest soot emissions for the 70:30 injection ratio in most of the cases except for LL-7030-(0,10a)TDC and LL-7030-(5a,15a)TDC in which the FRB had the highest soot emissions. Soot levels for the FRB were 41.7% and 16.1% higher compared to ORB1 and ORB2 at LL-7030-(0,10a)TDC respectively. Soot levels for the FRB were 118.9% and 41% higher compared to ORB1 and ORB2 at LL-7030-(5a,15a)TDC. Similar trends were also observed for at high loads for the respective cases. This showed that piston bowl geometry significantly influenced soot emissions.

v. Regarding the influence of injection timing on soot emissions, soot emissions for both injection ratios and both loads were found to increase significantly as injection timing was retarded. For instance, ORB2-HL-5050-(5a,15a)TDC had a 351% higher soot level compared to ORB2-HL-5050-(20b,10b)TDC and ORB2-LL-7030-(5a,15a)TDC had a 141.3% higher soot level compared to ORB2-LL-7030-(20b,10b)TDC. Similar trends were also exhibited and ORB1 for both injection ratios at low and high loads which showed that both injection timing and injection ratio influenced soot emissions significantly.

4. Inadequate air-fuel mixing contributed to rich mixture formations which generated HRR, high combustion temperatures and high peak in-cylinder pressures for the FRB at low load. However, under the high load condition, rich mixture formations led to lower HRR, combustion temperatures and pressures. Improved air-fuel mixing from a large mixing front area caused by the re-entrance curvature radius of ORB2 also led to high HRR and in-cylinder pressures under both load conditions.
5. The effects of the duality caused by improved air-fuel mixing led to a gradual rise in HRR and lower peak HRR in some cases and a steep rise in HRR and higher peak HRR in other cases.

i. The former instance of the duality was observed in cases such as ORB1-LL-5050-(10b,0)TDC, and resulted in lower combustion temperatures and lower NOx emissions.
ii. The later instance of the duality was observed in cases such as ORB2-LL-5050-(10b,0)TDC which resulted in higher combustion temperatures and higher NOx emissions.
iii. The duality caused by improved air-fuel mixing contributed to the lack of correlation between the extent of re-entrance curvature and IMEP levels.

8.2 Conclusions from the study in Chapter 6 and 7

The optimisation method developed as part of this research work involved a two-stage approach such that the first stage was that of the piston bowl geometry performed as an optimisation by analysis to select the most suitable bowl geometry to be used in the second stage which employed the hybrid regression-based methodology for the optimisation of the double injection strategy.

The following conclusions were made from the first stage of the optimisation process.

1. At low load, the FRB was suitable for improvements in only IMEP and ISFC whereas ORB1 was only suitable for the reduction of NOx and soot emissions. On the other hand, at high load, the FRB exhibited high levels of ISFC, combustion noise, NOx, and soot as well as low IMEP levels whilst ORB1 was suitable only if improvements to IMEP, ISFC and soot levels were desired at the expense of very high NOx levels.
2. The optimisation showed that the FRB and ORB1 were the extremes of the bowl designs with regards to the design and multi-objective spaces as well as multi-objective criteria for both engine loads.
3. ORB2 exhibited the most acceptable compromise between the highlighted extremes as it provided considerable improvements to IMEP and ISFC, negligible improvements to combustion noise and significant reductions in NOx and soot emissions over the range of injection strategies considered.
4. ORB2 was identified as the optimal piston geometry and thus, selected for the second stage of the optimisation process.

The following conclusions were drawn from the second stage of the optimisation process under both engine loads.

1. The implementation of hybrid datasets involving a mixture of DoE and MOGA-II generated designs for regression-based optimisation was effective for predictive regression modelling as evident in the results.
2. Application of the k-fold cross validation during the training and validation process of the regression modelling approach provided robust model inferences based on a relatively small dataset compared to the split ratio method during the regression analysis phase, the latter was not presented in this research work.
3. The optimisation results at both load regimes showed that the hybrid regression-based optimisation method can be used as an alternative methodology for effectively optimising complex engine parameters to yield reliable optimal strategies with significantly reduced computational cost and time.

8.3 Future Recommendations

The limitations of fully electric powertrains imply continued application of internal combustion engines for heavy-duty application and also light-duty applications in global regions wherein the ban of ICE's has not been initiated. Therefore, the areas covered in this research work should be extended to the application of renewable and synthetic fuels such as biodiesel and biofuel blends to approach net zero carbon applications of ICEs.

Presently, the application of biofuels such as biodiesel in greater amounts than currently utilised in CI engines has been reported to introduce further challenges. Therefore, investigations with the focus on the application of such fuels within the scope of this research could provide further insights and improvements in CI engine development towards reducing emissions while maintaining or improving hybrid powertrain performance.

The hybrid regression-based optimisation methodology presented in this work demonstrated that it can be used to obtain optimal and reliable strategies with significantly lower computational cost and time. Moving forward, its robustness could be further stress tested by considering the inclusion of parameterised piston bowl geometry be optimised together with the fuel injection strategy, sensitivity to the size and composition of the hybrid design dataset, and/or the range of the design parameters as well as the number of responses or objectives considered to reveal the depths of its capability and consequently improve its architecture.

References

[1] A. G. Olabi, D. Maizak, and T. Wilberforce, “Review of the regulations and techniques to eliminate toxic emissions from diesel engine cars,” *Science of the Total Environment*, vol. 748, p. 141249, 2020, doi: 10.1016/j.scitotenv.2020.141249.

[2] European Parliament, “Comparative Study on teh differences between the EU and US legislations on emissions in the automotive sector,” *Policy Department Economic and Scientific Policy A*, 2016.

[3] Department Business Energy and Industrial Strategy, “Government takes historic step towards net-zero with end of sale of new petrol and diesel cars by 2030,” 2020.

[4] British Petroleum Company, “BP Energy Outlook Energy 2017,” *BP Statistical Review of World Energy*, pp. 1–103, 2017, doi: 10.1017/CBO9781107415324.004.

[5] US Energy Information Administration (EIA), “International Energy Outlook 2017 Overview,” *International Energy Outlook 2017*, vol. IEO2017, no. 2017, p. 143, 2017.

[6] A. Kozina, G. Radica, and S. Nižetić, “Analysis of methods towards reduction of harmful pollutants from diesel engines,” *Journal of Cleaner Production*, vol. 262, 2020, doi: 10.1016/j.jclepro.2020.121105.

[7] S. Lion, I. Vlaskos, and R. Taccani, “A review of emissions reduction technologies for low and medium speed marine Diesel engines and their potential for waste heat recovery,” *Energy Conversion and Management*, vol. 207, no. February, p. 112553, 2020, doi: 10.1016/j.enconman.2020.112553.

[8] E. Shim, H. Park, and C. Bae, “Comparisons of advanced combustion technologies (HCCI , PCCI , and dual- fuel PCCI) on engine performance and emission characteristics in a heavy- duty diesel engine,” *Fuel*, vol. 262, no. October 2019, p. 116436, 2020, doi: 10.1016/j.fuel.2019.116436.

[9] J. Benajes, A. García, J. Monsalve-Serrano, and S. Martínez-Boggio, “Emissions reduction from passenger cars with RCCI plug-in hybrid electric vehicle technology,” *Applied Thermal Engineering*, vol. 164, no. June 2019, p. 114430, 2020, doi: 10.1016/j.applthermaleng.2019.114430.

[10] A. K. Agarwal, A. P. Singh, and R. K. Maurya, “Evolution, challenges and path forward for low temperature combustion engines,” *Progress in Energy and Combustion Science*, vol. 61, pp. 1–56, 2017, doi: 10.1016/j.pecs.2017.02.001.

[11] R. Mobasheri, Z. Peng, and S. Mirsalim, “Analysis the e ect of advanced injection strategies on engine performance and pollutant emissions in a heavy duty DI-diesel engine by CFD modeling,” *International Journal of Heat Fluid Flow*, vol. 33, no. 1, pp. 59–69, 2012.

[12] J. Li, W. M. Yang, H. An, A. Maghbouli, and S. K. Chou, “Effects of piston bowl geometry on combustion and emission characteristics of biodiesel fueled diesel engines,” *Fuel*, vol. 120, pp. 66–73, 2014.

[13] A. Navid, S. Khalilarya, and M. Abbasi, “Diesel engine optimization with multi-objective performance characteristics by non-evolutionary Nelder-Mead algorithm: Sobol sequence and Latin hypercube sampling methods comparison in DoE process,” *Fuel*, vol. 228, no. March, pp. 349–367, 2018, doi: 10.1016/j.fuel.2018.04.142.

[14] A. Navid, S. Khalilarya, and H. Taghavifar, “Comparing multi-objective non-evolutionary NLPQL and evolutionary genetic algorithm optimization of a DI diesel engine: DoE estimation and creating surrogate model,” *Energy Conversion and Management*, vol. 126, pp. 385–399, 2016, doi: 10.1016/j.enconman.2016.08.014.
[15] N. Hu, P. Zhou, and J. Yang, “Comparison and combination of NLPQL and MOGA algorithms for a marine medium-speed diesel engine optimisation,” *Energy Conversion and Management*, vol. 133, pp. 138–152, 2017, doi: 10.1016/j.enconman.2016.11.066.
[16] F. Bozza, M. Costa, D. Siano, L. Allocca, and A. Montantaro, “Light Duty Diesel Engine: Optimization of Performances, Noxious Emission and Radiated Noise,” *SAE International Journal of Engines*, 2009.
[17] S. Lotfan, R. A. Ghiasi, M. Fallah, and M. H. Sadeghi, “ANN-based modeling and reducing dual-fuel engine’s challenging emissions by multi-objective evolutionary algorithm NSGA-II,” *Applied Energy*, vol. 175, pp. 91–99, 2016, doi: 10.1016/j.apenergy.2016.04.099.
[18] J. B. J. B. Heywood, *Internal combustion engines fundamentals*, vol. 21. 1988. doi: 10987654.
[19] G. Lavoie, J. Heywood, and J. Keck, “Experimental and Theoretical Study of Nitric Oxide Formation in INternal Combustion Engines,” *Combustion Science and Technology*, vol. 1, no. 4, pp. 313–326, 2007, doi: 10.1080/00102206908952211.
[20] P. Hellier and N. Ladommatos, “The influence of biodiesel composition on compression ignition combustion and emissions,” *Proceedings of the Institution of Mechanical Engineers, Part A: Journal of Power and Energy*, vol. 229, no. 7, pp. 714–726, 2015, doi: 10.1177/0957650915598424.
[21] EPA, “Acid Rain,” *Environmental Protection Agency*, 2017.
[22] EPA, “Ground-level Ozone Pollution: Health Effects of Ozone Pollution,” *Environmental Protection Agency*, 2017.
[23] H. H. Sheikh *et al.*, “ABU DHABI STATE OF ENVIRONMENT REPORT 2017 ABU DHABI STATE OF ENVIRONMENT REPORT 2017 Contents FOREWORDS 4 H,” 2017.
[24] M. V. Twigg and P. R. Phillips, “Cleaning the air we breathe - controlling diesel particulate emissions from passenger cars,” *Platinum Metals Review*, vol. 53, no. 1, pp. 27–34, 2009, doi: 10.1595/147106709X390977.
[25] J. E. Dec, “A conceptual model of di diesel combustion based on laser-sheet imaging,” *SAE Technical Papers*, 1997, doi: 10.4271/970873.
[26] C. Du, *Studies on Diesel sprays under non-reacting and reacting conditions*. 2017.
[27] H. Bohm, M. Bonig, C. Feldermann, H. Jander, G. Rudolph, and H. G. Wagner, “Pressure Dependence of formation of soot and PAH in premixed flames,” *Soot Formation in Combustion*, 1994.
[28] D. Bohm *et al.*, “The Influence of Pressure and Temperature on Soot Formation in Premixed Flames,” in *21st International Symposium on Combustion*, 1988, p. 403.
[29] H. Bockhorn, F. Fetting, A. Heddrich, and G. Wannemacher, “Investigation of the Surface Growth of Soot in Flat Low Pressure Hydrogen Oxygen Flames,” in *Twentieth International Symposium on Combustion*, 1985, p. 879.

[30] J. Appel, H. Bockhorn, and M. Frenklach, “Kinetic Modelling of Soot Formation with Detailed Chemistry and Physics: Laminar Premixed Flames of C2 Hydrocarbons,” *Combustion Flame*, vol. 121, no. 1–2, pp. 122–136, 2000.
[31] R. Tatschl and P. Priesching, “3D-Cfd Simulation of Di-Diesel Engine,” *Automotive*, vol. 20, no. 20, 2016.
[32] Environmental Protection Agency, “Particulate Matter (PM) Pollution,” 2018.
[33] Environmental Protection Agency, “Health and Environmental Effects of Particulate Matter (PM),” 2018.
[34] W. Wu, Y. Jin, and C. Carlsten, “Inflammatory Health Effects of Indoor and Outdoor Particulate Matter,” *The Journal of Allergy and Clinical Immunology*, vol. 141, no. 3, pp. 833–844, 2018, doi: https://doi.org/10.1016/j.jaci.2017.12.981.
[35] R. Yu and S. Shahed, “Sources of hydrocarbon emissions from direct injection diesel engines,” no. SAE Paper 800048, 1980.
[36] S. Jaichandara and K. Annamalaib, “Combined impact of injection pressure and combustion chamber geometry on the performance of a biodiesel fueled diesel engine,” *Energy*, vol. 55, pp. 330–339, 2013.
[37] D. K. Soni and R. Gupta, “Numerical analysis of flow dynamics for two piston bowl designs at different spray angles,” *Journal of Cleaner Production*, vol. 149, pp. 723–734, 2017, doi: 10.1016/j.jclepro.2017.02.142.
[38] D. K. Soni and R. Gupta, “Emission Control Using Methanol, Ethanol And Butanol In Diesel Engine: A Comparison Through CFD Simulation,” *IOSR Journal of Mechanical and Civil Engineering*, vol. 12, no. 6, pp. 2278–1684, 2015, doi: 10.9790/1684-12661723.
[39] A. C. P. Gaffor and R. Gupta, “Numerical Investigations of piston bowl geometry and swirl ratio on emissions from diesel engines,” *Energy Conversion and Management*, vol. 101, pp. 541–551, 2015.
[40] R. Montajir, H. Tsunemoto, H. Ishitani, and T. Minami, “Fuel Spray Behavior in a Small DI Diesel Engine: Effect of Combustion Chamber Geometry,” *SAE Technical Paper*, 2000, [Online]. Available: https://doi.org/10.4271/2000-01-0946
[41] D. K. Soni and R. Gupta, “Numerical investigation of emission reduction techniques applied on methanol blended diesel engine,” *Alexandria Engineering Journal*, vol. 55, no. 2, pp. 1867–1879, 2016, doi: 10.1016/j.aej.2016.02.019.
[42] S. P. Venkateswaran and G. Nagarajan, “Effects of the Re-Entrant Bowl Geometry on a DI Turbocharged Diesel Engine Performance and Emissions—A CFD Approach,” *Journal of Engineering. Gas Turbines Power*, vol. 132, no. 12, 2010.
[43] S. Khan, R. Panua, and P. K. Bose, “Combined effects of piston bowl geometry and spray pattern on mixing, combustion and emissions of a diesel engine: A numerical approach,” *Fuel*, vol. 225, no. March, pp. 203–217, 2018, doi: 10.1016/j.fuel.2018.03.139.
[44] G. Zexian *et al.*, “Optimization of Piston Bowl Geometry for a Low Emission Heavy-Duty Diesel Engine,",” *SAE Technical Paper*, no. 2020-01–2056, 2020, p. 18, 2020, doi: https://doi.org/10.4271/2020-01-2056.
[45] P. Jose V, G. Antonio, M. Carlos, and L. Felipe, “Soot reduction for cleaner Compression Ignition Engines through innovative bowl templates,” *International Journal of Engine Research*, 2020, doi: https://doi.org/10.1177%2F1468087420951324.

[46] T. Ilker and C. Omer, “Analysis of different combustion chamber geometries using hydrogen / diesel fuel in a diesel engine,” *Energy Sources, Part A: Recovery, Utilization, and Environmental Effects*, 2020, doi: https://doi.org/10.1080/15567036.2020.1811808.
[47] D. K. Soni and R. Gupta, “Numerical analysis of flow dynamics for two piston bowl designs at different spray angles,” *Journal of Cleaner Production*, vol. 149, pp. 723–734, 2017, doi: 10.1016/j.jclepro.2017.02.142.
[48] S. P. Venkateswaran and G. Nagarajan, “Effects of the Re-Entrant Bowl Geometry on a DI Turbocharged Diesel Engine Performance and Emissions—A CFD Approach,” *Journal of Engineering. Gas Turbines Power*, vol. 132, no. 12, 2010.
[49] J. Lim and K. Min, “The Effects of Spray Angle and Piston Bowl Shape on Diesel Engine Soot Emissions Using 3-D CFD Simulation,” *SAE Technical Paper*, 2005, [Online]. Available: https://doi.org/10.4271/2005-01-2117
[50] B. Gainey, J. Gohn, D. Hariharan, M. Rahimi-Boldaji, and B. Lawler, “Assessing the impact of injector included angle and piston geometry on thermally stratified compression ignition with wet ethanol,” *Applied Energy*, vol. 262, no. January, p. 114528, 2020, doi: 10.1016/j.apenergy.2020.114528.
[51] A. T. Hoang, “Applicability of Fuel Injection Techniques for Modern Diesel Engines,” 2020. doi: https://doi.org/10.1063/5.0000133.
[52] M. R. Herfatmanesh, Z. Peng, and A. Ihracska, “Characteristics of pressure wave in common rail fuel injection system of high-speed direct injection diesel engines,” *Advances in Mechanical Engineering*, vol. 8, no. 5, pp. 1–8, 2016, doi: 10.1177/1687814016648246.
[53] H. Breitbach, “Fuel Injection Systems Overview.” Delphi Corporation, 2002.
[54] M. R. Herfatmanesh, H. Zhao, and L. Ganippa, “In-cylinder studies of split injection in a single cylinder optical diesel engine BT - Internal Combustion Engines: Improving Performance, Fuel Economy and Emission,” no. 4, pp. 99–109, 2011, doi: http://dx.doi.org/10.1533/9780857095060.3.99.
[55] d’ A. Stefano, F. Alessandro, M. Alessandro, and A. Mittica, “Effects of Rate-Shaped and Multiple Injection Strategies on Pollutant Emissions, Combustion Noise and Fuel Consumption in a Low Compression Ratio Diesel Engine,” *International Journal of Automotive Technology*, no. 21, pp. 197–214, 2020, doi: https://doi.org/10.1007/s12239-020-0020-0.
[56] A. Asadi, O. Nouri, and M. Hossein, “Numerical study on the application of biodiesel and bioethanol in a multiple injection diesel engine,” *Renewable Energy*, vol. 150, pp. 1019–1029, 2020, doi: 10.1016/j.renene.2019.11.088.
[57] A. Amir, G. Antonio, D. S. Clarisse Pinto, and T. Martin, “Impact of Multiple Injection Strategies on Performance and Emissions of Methanol PPC under Low Load Operation,” *SAE Technical Paper 2020-01-0556*, 2020, doi: https://doi.org/10.4271/2020-01-0556.
[58] P. Kasinath and R. A., “Experimental Investigation of Multiple Injection Strategies on Combustion Stability, Performance and Emissions in a Methanol-Diesel Dual Fuel Non-Road Engine,” *SAE Technical Paper 2020-01-0308*, 2020, doi: https://doi.org/10.4271/2020-01-0308.
[59] D. T. Montgomery and R. D. Reitz, “Effects of Multiple Injections and Flexible Control of Boost and EGR on Emissions and Fuel Consumption of a Heavy-Duty Diesel Engine,” *SAE Technical Paper*, 2001, doi: 10.4271/2001-01-0195.

[60] C. Park, S. Kook, and C. Bae, “Effects of Multiple Injections in a HSDI Diesel Engine Equipped with Common Rail Injection System,” *SAE Paper*, no. 004-01–0127, 2004, doi: 10.4271/2004-01-0127.
[61] P. Shayler, T. D. Brooks, G. Pugh, and R. Gambrill, “The in uence of pilot and split-main injection parameters on diesel emissions and fuel consumption,” *SAE Paper*, vol. 2005-01–03, 2005.
[62] B. Yang and K. Zeng, “Effects of natural gas injection timing and split pilot fuel injection strategy on the combustion performance and emissions in a dual-fuel engine fueled with diesel and natural gas,” *Energy Conversion and Management*, vol. 168, no. February, pp. 162–169, 2018, doi: 10.1016/j.enconman.2018.04.091.
[63] A. Kesharwani and R. Gupta, “Evaluation of performance and emission characteristics of a diesel engine using split injection,” *Journal of the Brazilian Society of Mechanical Sciences and Engineering*, vol. 42, no. 6, pp. 1–14, 2020, doi: 10.1007/s40430-020-02421-3.
[64] J. Zhang, W. Jing, W. L. Roberts, and T. Fang, “Soot measurements for diesel and biodiesel spray combustion under high temperature highly diluted ambient conditions,” *Fuel*, vol. 135, no. x, pp. 340–351, 2014, doi: 10.1016/j.fuel.2014.06.071.
[65] A. K. Azad, M. G. Rasul, M. M. K. Khan, S. C. Sharma, and M. M. K. Bhuiya, “Recent development of biodiesel combustion strategies and modelling for compression ignition engines,” *Renewable and Sustainable Energy Reviews*, vol. 56, no. April, pp. 1068–1086, 2016, doi: 10.1016/j.rser.2015.12.024.
[66] S. Kiplimo, R., Tomita, E., Kawahara, N., and Yokobe, “E ects of spray impingmnent, injection parameters and EGR on the combustion and emission characteristics of a PCCI diesel engine,” *Applied Thermal Engineering*, vol. 37, pp. 165–175, 2012.
[67] R. Hardy, W. and Reitz, “A study of the e ects of high EGR, high equivalence ratio and mixing time on emissions level in a heavy-duty diesel engine for PCCI combustion,” *SAE Paper*, no. 2006-01–0026, 2006.
[68] G. Bhiogade and J. G. Suryawanshi, “Effects of External Mixture Formation and EGR Technique on a Diesel-Fueled PCCI Engine.,” *Journal Institute of Engines*, 2020, doi: https://doi.org/10.1007/s40032-020-00631-1.
[69] K. Poorghasemi, R. K. Saray, E. Ansari, B. K. Irdmousa, M. Shahbakhti, and J. D. Naber, “Effect of diesel injection strategies on natural gas/diesel RCCI combustion characteristics in a light duty diesel engine,” *Applied Energy*, vol. 199, pp. 430–446, 2017, doi: 10.1016/j.apenergy.2017.05.011.
[70] E. Ansari, T. Menucci, and M. Shahbakhti, “Experimental investigation into e ff ects of high reactive fuel on combustion and emission characteristics of the Diesel - Natural gas Reactivity Controlled Compression Ignition engine,” vol. 239, no. November 2018, pp. 948–956, 2019, doi: 10.1016/j.apenergy.2019.01.256.
[71] A. P. Singh, V. Kumar, and A. K. Agarwal, “Evaluation of comparative engine combustion, performance and emission characteristics of low temperature combustion (PCCI and RCCI) modes,” *Applied Energy*, vol. 278, no. May, p. 115644, 2020, doi: 10.1016/j.apenergy.2020.115644.
[72] S. Ghaffarzadeh, A. Nassiri Toosi, and V. Hosseini, “An experimental study on low temperature combustion in a light duty engine fueled with diesel/CNG and biodiesel/CNG,” *Fuel*, vol. 262, no. October 2019, p. 116495, 2020, doi: 10.1016/j.fuel.2019.116495.

[73] O. Motallebi Hasankola, S.S., Shafaghat, R., Jahanian, “Numerical investigation of the effects of inlet valve closing temperature and exhaust gas recirculation on the performance and emissions of an RCCI engine.,” *Journal of Thermal Analysis and Calormetry*, no. 139, pp. 2465–2474, 2020, doi: https://doi.org/10.1007/s10973-019-08513-0.
[74] H. Mabadi Rahimi, S. A. Jazayeri, and M. Ebrahimi, “Hydrogen energy share enhancement in a heavy duty diesel engine under RCCI combustion fueled with natural gas and diesel oil,” *International Journal of Hydrogen Energy*, vol. 45, no. 35, pp. 17975–17991, 2020, doi: 10.1016/j.ijhydene.2020.04.263.
[75] C. Bae and J. Kim, “Alternative fuels for internal combustion enignes,” *Proceedings of the Combustion Institute*, vol. 36, pp. 3389–3413, 2017.
[76] J. Kim, H. Park, and C. Bae, “21st Interantional Symposium on Alcohol Fuels (ISAF),” pp. 10–13, 2015.
[77] S. Xu, Y. Wang, X. Zhang, X. Zhen, and C. Tao, “Development of a novel common-rail type Dimethyl ether (DME) injector h,” *Applied Energy*, vol. 94, pp. 1–12, 2012, doi: 10.1016/j.apenergy.2012.01.030.
[78] S. Sasaki, M. Kato, T. Yokota, M. Konno, and D. Gill, “Injection Nozzle Performance fuelled with DME,” *SAE Technical Paper*, vol. 2015-01–09, 2015.
[79] R. Tatschl, “3D-CFD Simulation of IC-Engine Flow, Mixture Formation and Combustion with AVL FIRE,” 2015.
[80] H. Pitsch, M. Chen, and N. Peters, “Unsteady flamelet modeling of turbulent hydrogen-air diffusion flames,” *Symposium (International) on Combustion*, vol. 27, no. 1, pp. 1057–1064, 1998, doi: 10.1016/S0082-0784(98)80506-7.
[81] M. Baburić, Ž. Bogdan, and N. Duić, “A new approach to CFD research: Combining AVL’s FIRE code with user combustion model,” *Proceedings of the International Conference on Information Technology Interfaces, ITI*, pp. 383–388, 2002, doi: 10.1109/ITI.2002.1024703.
[82] M. Hanjalic, K; Popovac, M; Hadziabdic, “A robust near-wall elliptic relaxation eddy-viscosity turbulence model for CFD,” *International Journal of Heat and Fluid Flow*, vol. 25, pp. 1047–1051, 2004.
[83] H. Laramee, Robert S; Garth, Christoph; Schneider, Jurgen; Hauser, “Texture Advection onStream Surfaces: A Novel Hybrid Visualisation Applied to CFD Simulation Results,” 2006. https://www.researchgate.net/figure/220778346_fig1_Figure-1-left-The-swirling-motion-of-flow-in-the-combustion-chamber-of-a-diesel (accessed Jul. 20, 2017).
[84] A. Horvat, “Fire Modeling in CFD,” pp. 12–65, 2010.
[85] Ł. J. Kapusta and A. Teodorczyk, “Numerical Simulations of a Simultaneous Direct Injection of a Liquid and Gaseous Fuel Into Constant Volume Chamber,” *Journal of Power Technologies*, vol. 92, no. 1, pp. 12–19, 2012, [Online]. Available: http://www.doaj.org/doaj?func=openurl&issn=20834187&date=2012&volume=92&issue=1&spage=12&genre=article
[86] W. K. George, “CFD Online,” 2013. http://www.cfd-online.com/Wiki/Introduction_to_turbulence/Reynolds_averaged_equations (accessed Jan. 22, 2017).
[87] . P. V. M., “Optimization of Time Step and Cfd Study of Combustion in Di Diesel Engine,” *International Journal of Research in Engineering and*

Technology, vol. 03, no. 20, pp. 22–26, 2014, doi: 10.15623/ijret.2014.0320006.
[88] R. Bhoobathi, "Diesel Engine Combustion Simulation using Computational Fluid Dynamics," vol. 01, no. 01, pp. 17–21, 2010.
[89] N. M. S. Hassan, M. G. Rasul, and C. A. Harch, "Modelling and experimental investigation of engine performance and emissions fuelled with biodiesel produced from Australian Beauty Leaf Tree," *Fuel*, vol. 150, pp. 625–635, 2015, doi: 10.1016/j.fuel.2015.02.016.
[90] AVL List GmbH, "Engine Simulation Environment (ESE)," Austria, 2017.
[91] AVL LIST Gmbh, "AVL FIRE," 2018.
[92] N. Hu, "An investigation into the characteristics and optimisation of a high-pressure common rail injection system," no. September, 2017.
[93] N. Hu, P. Zhou, and J. Yang, "Reducing emissions by optimising the fuel injector match with the combustion chamber geometry for a marine medium-speed diesel engine," *Transportation Research Part D: Transport and Environment*, vol. 53, pp. 1–16, 2017, doi: 10.1016/j.trd.2017.03.024.
[94] I. . M. Sobol, "Distribution of points in a cube and approximate evaluation of integrals. (in English).," *U.S.S.R Computer Mathematics adn Physics*, vol. 7, pp. 86–112, 1967.
[95] AVL LIST Gmbh, "DoE and Optimisation," *SOftware Documentation*, 2017.
[96] AVL LIST Gmbh, "DoE and Optimisation," *SOftware Documentation*, 2017.
[97] A. Astolfi, "Optimisation: An introduction," London, 2006.
[98] S. Siedlerstr, "NLPQLP : A Fortran Implementation of a Sequential Quadratic Programming Algorithm with Distributed and Non-Monotone Line Search," 2015.
[99] B. J. A. Nelder and R. Meadf, "A simplex method for function minimization," 1964.
[100] J. H. Holland, *Adaptation in natural and artificial systems: An Introductory analysis to biology, control and artificial intelligence*. Cambridge: MIT Press, 1975.
[101] D. E. Goldberg, *Genetic algorithms in search, optimization and machine learning.* Reading: Addison- Wesley, 1989.
[102] M. Gen and R. Cheng, *Genetic algorithms and engineering designs.* New York: Wiley, 1997.
[103] K. Deb, *Multi-objective optimization using evolutionary algorithms.* New York: John Wiley & Sons, 2001.
[104] A. Astolfi, "Optimisation: An introduction," London, 2006.
[105] C. A. Coello Coello and G. T. Pulido, "A micro-genetic algorithm for multiobjective optimization.," in *First international conference on evolutionary multi-criterion optimization.*, 2001, pp. 126–140. doi: 10.1007/3-540-44719-9_9.
[106] K. Deb, A. Pratap, S. Agarwal, and T. Meyarivan, "A fast and elitist multiobjective genetic algorithm: NSGA-II.," *Evolutionary Computing*, vol. 6, pp. 182–197, 2002, doi: 10.1109/4235.996017.
[107] D. Sasaki and S. Obayashi, "Efficient search for trade-offs by adaptive range multi-objective genetic algorithms.," *Journal of Aerospace Computing Informantion and Communication*, no. 2, pp. 44–64, 2005.
[108] T. Hastie, R. Tibshirani, and J. Friedman, *The Elements of Statistical Learning*, 2nd ed. Stanford,California: Springer, 2008.

[109] A. S. M. S. Ali O.M., Mamat R., Najafi G., Yusaf T., "Optimization of biodiesel-diesel blended fuel properties and engine performance with ether additive using statistical analysis and response surface methods.," *Energies (Basel)*, vol. 8, no. 12, pp. 14136–14150, 2015.
[110] ESTECO, "Response Surface Models (RSMs) - modeFRONTIER User Guide," 2019.
[111] S. Roy, R. Banerjee, and P. K. Bose, "Performance and exhaust emissions prediction of a CRDI assisted single cylinder diesel engine coupled with EGR using artificial neural network," *Applied Energy*, vol. 119, pp. 330–340, 2014, doi: 10.1016/j.apenergy.2014.01.044.
[112] S. Poles and A. Lovison, "Shepard ' s and k – Nearest ' s Methods in the Newly Implemented Response Surfaces," *ESTECO, Technical Report 2006-004*, 2006.
[113] E. Rigoni, "Radial Basis Functions Response Surfaces," *ESTECO, Technical Paper 2007-001*, 2007.
[114] A. Lovison, "Kriging," *ESTECO, Technical Report 2007-003*, 2007.
[115] ESTECO, "Response Surface Models (RSMs) - modeFRONTIER User Guide," 2019.
[116] E. Rigoni, "Stepwise Regression RSM," *ESTECO, Technical Report 2014-003*, 2014.
[117] E. Rigoni and S. Silvetti, "New Gaussian Processes in mF 2017R4," *ESTECO, Technical Report 2017-001*, 2017.
[118] T. E., A. K., and B. M., "Comparison of linear regression and artificial neural network model of a diesel engine fueled with biodiesel-alcohol mixtures.," *Alexandria Engineering Journal*, vol. 55, no. 4, pp. 3081-3089., 2016.
[119] T. H., T. H., M. A., M. A., K. S., and J. S., "On the modeling of convective heat transfer coefficient of hydrogen fueled diesel engine as affected by combustion parameters using a coupled numerical-artificial neural network approach.," *International Journal of Hydrogen Energy*, vol. 40, no. 12, pp. 4370–4381, 2015.
[120] T. H., T. H., M. A., M. A., and K. S., "A numerical investigation on the wall heat flux in a DI diesel engine fueled with n-heptane using a coupled CFD and ANN approach.," *Fuel*, vol. 140, pp. 227–236, 2015.
[121] T. H., T. H., M. A., and M. A., "Modeling the impact of in-cylinder combustion parameters of DI engines on soot and NOx emissions at rated EGR levels using ANN approach.," *Energy Conversion and Management*, vol. 87, pp. 1–9, 2014.
[122] H. Taghavifar, S. Jafarmadar, H. Taghavifar, and A. Navid, "Application of DoE evaluation to introduce the optimum injection strategy-chamber geometry of diesel engine using surrogate epsilon-SVR," *Applied Thermal Engineering*, vol. 106, pp. 56–66, 2016, doi: 10.1016/j.applthermaleng.2016.05.194.
[123] H. Taghavifar, "Towards multiobjective Nelder-Mead optimization of a HSDI diesel engine: Application of Latin hypercube design-explorer with SVM modeling approach," *Energy Conversion and Management*, vol. 143, pp. 150–161, 2017, doi: 10.1016/j.enconman.2017.04.008.
[124] Y. Chen and L. Lv, "The multi-objective optimization of combustion chamber of DI diesel engine by NLPQL algorithm," *Applied Thermal Engineering*, vol. 73, no. 1, pp. 1332–1339, 2014, doi: 10.1016/j.applthermaleng.2014.09.028.
[125] M. Costa, G. Marco, C. Forte, and G. Cazzoli, "A Numerical Methodology For The Multi-Objective Optimization Of The DI Diesel Engine Combustion,"

Energy Procedia, vol. 45, pp. 711–720, 2014, doi: 10.1016/j.egypro.2014.01.076.
[126] Z. Li *et al.*, "Parametric study of a diesel engine fueled with directly injected methanol and pilot diesel," *Fuel*, vol. 256, no. July, p. 115882, 2019, doi: 10.1016/j.fuel.2019.115882.
[127] A. I. Jabbr, H. Gaja, and U. O. Koylu, "Multi-objective optimization of operating parameters for a H2/ Diesel dual-fuel compression- ignition engine," *International Journal of Hydrogen Energy*, vol. 45, no. 38, pp. 19965–19975, 2020, doi: 10.1016/j.ijhydene.2020.05.071.
[128] J. Liu, B. Ma, and H. Zhao, "Combustion parameters optimization of a diesel/natural gas dual fuel engine using genetic algorithm," *Fuel*, vol. 260, no. October 2019, p. 116365, 2020, doi: 10.1016/j.fuel.2019.116365.
[129] H. Taghavifar, S. Jafarmadar, H. Taghavifar, and A. Navid, "Application of DoE evaluation to introduce the optimum injection strategy-chamber geometry of diesel engine using surrogate epsilon-SVR," *Applied Thermal Engineering*, vol. 106, pp. 56–66, Aug. 2016, doi: 10.1016/j.applthermaleng.2016.05.194.
[130] Y. Chen and L. Lv, "The multi-objective optimization of combustion chamber of DI diesel engine by NLPQL algorithm," *Applied Thermal Engineering*, vol. 73, no. 1, pp. 1332–1339, Dec. 2014, doi: 10.1016/j.applthermaleng.2014.09.028.
[131] M. Costa, D. Siano, L. Allocca, A. Montanaro, and F. Bozza, "Light duty diesel engine: Optimization of performances, noxious emission and radiated noise," *SAE International Journal of Engines*, vol. 2, no. 2, pp. 740–748, 2010, doi: 10.4271/2009-32-0105.
[132] Y. Shi, H.-W. Ge, and R. D. Reitz, "Computational Optimization of Internal Combustion Engines," 2011.
[133] H.-W. Ge, Y. Shi, R. D. Reitz, D. D. Wickman, and W. Willems, "Optimization of a HSDI Diesel Engine for Passenger Cars Using a Multi-Objective Genetic Algorithm and Multi-Dimensional Modeling," 2009.
[134] H. Taghavifar, H. Taghavifar, A. Mardani, and A. Mohebbi, "Modeling the impact of in-cylinder combustion parameters of di engines on soot and NOx emissions at rated EGR levels using ANN approach," *Energy Conversion and Management*, vol. 87, pp. 1–9, 2014, doi: 10.1016/j.enconman.2014.07.005.
[135] M. Costa, G. M. Bianchi, C. Forte, and G. Cazzoli, "A numerical methodology for the multi-objective optimization of the DI diesel engine combustion," in *Energy Procedia*, 2014, vol. 45, pp. 711–720. doi: 10.1016/j.egypro.2014.01.076.
[136] T. Y. Motlagh, L. N. Azadani, and K. Yazdani, "Multi-objective optimization of diesel injection parameters in a natural gas/diesel reactivity controlled compression ignition engine," *Applied Energy*, vol. 279, Dec. 2020, doi: 10.1016/j.apenergy.2020.115746.
[137] Y. Shi, H.-W. Ge, and R. D. Reitz, *Computational Optimisation of Internal Combustion Engines*. London: Springer Inc, 2011.
[138] H. W. Ge, Y. Shi, R. D. Reitz, D. D. Wickman, and W. Willems, "Optimization of a HSDI diesel engine for passenger cars using a multi-objective genetic algorithm and multi-dimensional modeling," *SAE Technical Papers*, vol. 2, no. 1, pp. 691–713, 2009, doi: 10.4271/2009-01-0715.
[139] H. Taghavifar, H. Taghavifar, A. Mardani, and A. Mohebbi, "Modeling the impact of in-cylinder combustion parameters of di engines on soot and NOx

emissions at rated EGR levels using ANN approach," *Energy Conversion and Management*, vol. 87, pp. 1–9, 2014, doi: 10.1016/j.enconman.2014.07.005.
[140] M. Costa, G. M. Bianchi, C. Forte, and G. Cazzoli, "A numerical methodology for the multi-objective optimization of the DI diesel engine combustion," in *Energy Procedia*, 2014, vol. 45, pp. 711–720. doi: 10.1016/j.egypro.2014.01.076.
[141] T. Y. Motlagh, L. N. Azadani, and K. Yazdani, "Multi-objective optimization of diesel injection parameters in a natural gas/diesel reactivity controlled compression ignition engine," *Applied Energy*, vol. 279, no. March, 2020, doi: 10.1016/j.apenergy.2020.115746.
[142] M. Costa, G. Marco, C. Forte, and G. Cazzoli, "A Numerical Methodology For The Multi-Objective Optimization Of The DI Diesel Engine Combustion," *Energy Procedia*, vol. 45, pp. 711–720, 2014, doi: 10.1016/j.egypro.2014.01.076.
[143] Y. Shi and R. D. Reitz, "Optimization study of the effects of bowl geometry, spray targeting, and swirl ratio for a heavy-duty diesel engine operated at low and high load," *International Journal of Engine Research*, vol. 9, no. 4, pp. 325–346, 2008, doi: 10.1243/14680874JER00808.
[144] A. A. P. P. P. D. P. Y. Z. Y. S. S. K. J. Moia, "A Machine Learning-Genetic Algorithm (ML-GA) Approach for Rapid Optimization Using High-Performance Computing," *SAE International Journal of Commercial Vehicles* , vol. 11, no. 5, pp. 291–306, 2018, doi: https://doi.org/10.4271/2018-01-0190.
[145] O. Owoyele *et al.*, "Application of an automated machine learning-genetic algorithm (AutoML-GA) coupled with computational fluid dynamics simulations for rapid engine design optimization," 2020.
[146] O. Owoyele and P. Pal, "A novel machine learning-based optimization algorithm (ActivO) for accelerating simulation-driven engine design," *Applied Energy*, vol. 285, no. 116455, Mar. 2021, doi: 10.1016/j.apenergy.2021.116455.
[147] M. R. Herfatmanesh, "INVESTIGATION OF SINGLE AND SPLIT INJECTION STRATEGIES IN AN OPTICAL DIESEL ENGINE," 2010.
[148] M. R. Herfatmanesh and H. Zhao, "Experimental investigation of effects of dwell angle on fuel injection and diesel combustion in a high-speed optical CR diesel engine," *Proceedings of the Institution of Mechanical Engineers, Part D: Journal of Automobile Engineering*, vol. 227, no. 2, pp. 246–260, Feb. 2013, doi: 10.1177/0954407012450656.
[149] M. R. Herfatmanesh, P. Lu, M. A. Attar, and H. Zhao, "Experimental investigation into the effects of two-stage injection on fuel injection quantity , combustion and emissions in a high-speed optical common rail diesel engine," *Fuel*, vol. 109, pp. 137–147, 2013, doi: 10.1016/j.fuel.2013.01.013.
[150] M. R. Herfatmanesh, Z. Peng, and A. Ihracska, "Characteristics of pressure wave in common rail fuel injection system of high-speed direct injection diesel engines," *Advances in Mechanical Engineering*, vol. 8, no. 5, pp. 1–8, 2016, doi: 10.1177/1687814016648246.
[151] J. Kashdan and B. Thirouard, "Optical Engines as Representative Tools in the Development of New Combustion Engine Concepts," 2012. doi: 10.2516/ogst/2011134.
[152] J. V Pastor, P. Olmeda, J. Mart, and F. Lewiski, "Methodology for Optical Engine Characterization by Means of the Combination of Experimental and

Modeling Techniques," *Applied Science*, pp. 1–17, 2018, doi: 10.3390/app8122571.
[153] A. J. Torregrosa, A. Broatch, J. Martín, and L. Monelletta, "Combustion noise level assessment in direct injection Diesel engines by means of in-cylinder pressure components," *Measurement Science and Technology*, vol. 18, no. 7, pp. 2131–2142, Jul. 2007, doi: 10.1088/0957-0233/18/7/045.
[154] D. M. Probst *et al.*, "Evaluating optimization strategies for engine simulations using machine learning emulators," *Journal of Engineering for Gas Turbines and Power*, vol. 2, Sep. 2019, doi: 10.1115/ICEF2018-9726.
[155] F. Bozza, M. Costa, D. Siano, L. Allocca, and A. Montantaro, "Light Duty Diesel Engine: Optimization of Performances, Noxious Emission and Radiated Noise," *SAE International Journal of Engines*, 2009.
[156] J. D. Anderson Jr., "Computational fluid dynamics- The basics with applications," *McGraw-Hill, Inc.*, vol. 27, no. 6. pp. 1661–71, 1995.
[157] C. A. Harch, M. G. Rasul, N. M. S. Hassan, and M. M. K. Bhuiya, "Modelling of engine performance fuelled with second generation biodiesel," *Procedia Engineering*, vol. 90, pp. 459–465, 2014, doi: 10.1016/j.proeng.2014.11.757.
[158] H. A. Khairallah, "Combustion and pollutant characteristics of IC engines fueled with hydrogen and diesel / hydrogen mixtures using 3D computations with detailed chemical kinetics," Missouri University of Science and Technology, 2015.
[159] D. Moldovanu and N. Burnete, "Computational fluid dynamics simulation of a single cylinder research engine working with biodiesel," *Thermal Science*, vol. 17, no. 1, pp. 195–203, 2013, doi: 10.2298/TSCI111004021M.
[160] Ł. J. Kapusta and A. Teodorczyk, "Numerical Simulations of a Simultaneous Direct Injection of a Liquid and Gaseous Fuel Into Constant Volume Chamber," *Journal of Power Technologies*, vol. 92, no. 1, pp. 12–19, 2012.
[161] M. Hanjalic, K; Popovac, M; Hadziabdic, "A robust near-wall elliptic relaxation eddy-viscosity turbulence model for CFD," *International Journal of Heat and Fluid Flow*, vol. 25, pp. 1047–1051, 2004.
[162] P. Durbin, "Near-wall turbulence closure modelling without damping functions," *Theoretical and Combustion Fluid Dynamics*, vol. 3, pp. 1–13, 1991.
[163] AVL LIST GmbH, "Combustion Module," Hans-List-Platz 1, A-8020 Graz, Austria, 2017.
[164] A. Liu, D. A. N. Mather, and R. Reitz, "D T | C," *SAE Technical Paper*, no. 930072, 1993.
[165] K. Dukowicz, John, "A Particle-Fluid Numerical Model for Liquid Sprays," *Journal of Computational Physics*, vol. 35, pp. 229–253, 1980.
[166] J. Naber, Enright B., and P. Farrell, "Fuel impingement in a direct injection diesel engine," *SAE Technical Paper Series*, no. 881316, pp. 1–14, 1988, doi: 10.4271/881316.
[167] AVL List GmbH, "Engine Simulation Environment (ESE)," Austria, 2017.
[168] AVL List GmbH, "Spray Module," 2017.
[169] O. Colin and A. Benkenida, "The 3-zones extended coherent flame model (ECFM3Z) for computing premixed/diffusion combustion," *Oil and Gas Science Technology Review IFP*, vol. 59, no. 6, pp. 593–609, 2004.
[170] R. Tatschl, "3D-CFD Simulation of IC-Engine Flow, Mixture Formation and Combustion with AVL FIRE," 2015.
[171] ANSYS Incorporation, "NOx Thermal formation," 2017.

[172] AVL List GmbH, “Emissions Module,” 2017.

Appendix A

A1 Experimental Facilities

A1.1 General Description of the Ricardo Hydra Diesel Engine

A single cylinder Ricardo Hydra engine modified for optical access was used in generating the experimental data used in this research work. Table A1-1 shows the engine specifications. The engine consists of an optical window, a Ricardo Hydra crankcase with a standard production cylinder head, an extended cylinder block and a high-pressure common rail (HPCR) fuel injection system. The engine is mounted on a single cylinder test bed using a seismic mass engine mounting provided by Cussons Technology and is coupled to a 30 kW DC dynamometer which acts as an engine brake during firing. The control system of the dynamometer allows an engine speed to be set and maintained under engine braking.

Table A1- 1: Ricardo Hydra Engine Specifications

Ricardo Hydra Single Cylinder Engine	
Bore (mm)	86
Stroke (mm)	86
Connecting Rod Length (mm)	154
Swept Volume (cm^3)	499
Compression Ratio	16:1
Engine Speed used for testing (rpm)	1500
Piston Bowl Diameter/Depth (mm/mm)	43.4/ 16.6
Piston Bowl Geometry	Shallow rectangular bowl
Swirl Ratio	1:4

The extended cylinder block consists of an upper part connected to the cylinder head and a lower part connected to the engine crankcase to accommodate the extended piston. As an optical engine, the cylinder block has three holes cut out on the side with quartz glass windows fitted for optical access. The cylinder head of the Ricardo Hydra engine was designed to use the standard production Duratorq four-cylinder head of a Ford 2.0 litre ZSD 420 turbocharged engine consisting of two air induction and two exhaust valves, double overhead camshafts, a glow plug and a centrally

located fuel injector. Since only one cylinder and value train set is used in all experiments, the valve train of the unused cylinders is deactivated by removing the rocker arms while their corresponding oil feeds on the rocker shafts are closed off in order to prevent oil spillage and thus, reduced oil pressure. Figure A1-1 shows the Ricardo Hydra Engine used for the experiment.

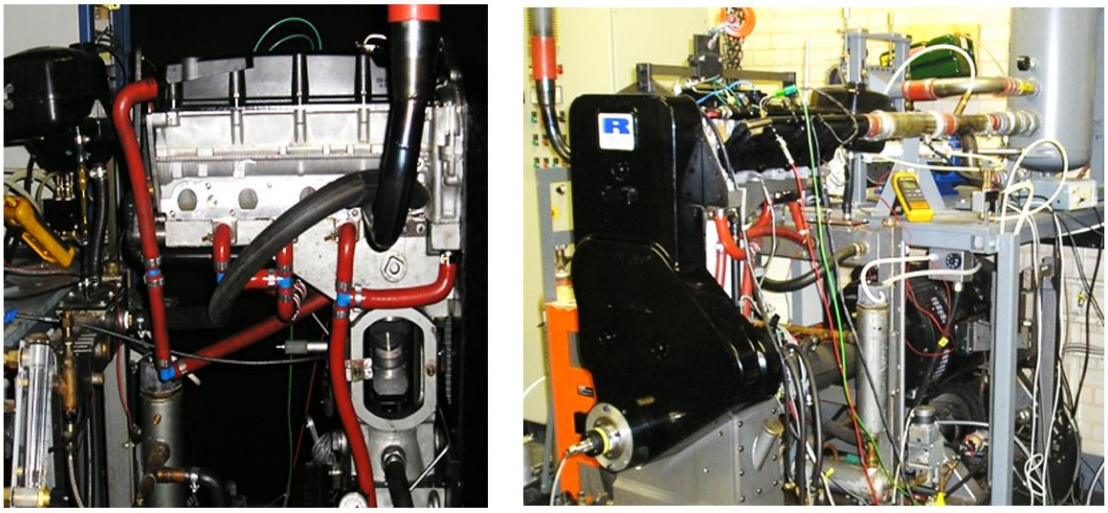

(a) (b)

Figure A1- 1: Front view (a) and Side view (b) of the Ricardo Hydra Engine [149]

A1.2 Cooling and Lubrication Systems

Experimental time was limited considering the mechanical and thermal stresses on the optical components due to their exposure to the engine firing cycles. Regarding this consideration, both the engine coolant and lubricant were heated before their use to ensure reasonable engine operating temperatures are achieved. The engine cooling system consists of an immersion heater controlled by a thermostat and an electric water pump mounted on the engine test bed. The coolant used with the system was heated to 90℃. The engine lubrication system consists of a wet sump, a gravity-fed pressure pump mounted to the test bed, an electric motor which drives the pressure pump and two immersion heaters in the sump. The lubricating oil used with the system was heated to 80℃. An additional advantage of heating up the engine before its use in the experimental work was the elimination of cold start problems. This also enabled the engine to be used with an in-cylinder pressure transducer in place of the glow plug to obtain in-cylinder pressure measurements.

A1.3 Fuel Injection System

The Ricardo Hydra engine uses a HPCR fuel injection system to provide high pressure fuel independent of the engine speed. This promotes improved fuel atomisation aimed at enhancing fuel evaporation and mixture formation with flexible injection rates and times across the engine's operating range. The fuel supply and control system consist of a fuel tank and filter, a 12V low pressure pump, a pneumatic high-pressure pump driven by an electric motor, a Delphi HPCR system, Delphi rail pressure sensor, Delphi Valve Covered Orifice (VCO) injector, fuel injector driver, EC-GEN 500 ECU and the EC-Lab software installed on a computer as seen in Figure A1-2.

The fuel is fed to the Delphi HPCR system from the fuel tank through the low-pressure pump, fuel filter and high-pressure pump. The Delphi common rail has four outlets for the connection of four fuel injectors, but three outlets are closed off as only one is required for the engine.

The EC-GEN 500 ECU receives signals from the hall-effect sensor and the shaft encoder fitted to the engine, the common rail pressure sensor, and the EC-lab software to control the number of injection pulses, injection timing, quantity, and pressure. The ECU sends signals to the high-pressure pump to control injection pressure and to the fuel injection driver to generate and send a current signal to the injector. The Delphi multi-hole VCO injector is used to inject diesel fuel into the combustion chamber of the engine. The injection pressure of the fuel injector is limited by the high-pressure pump to 1350 bar although it has the capability of achieving an injection pressure of 1600 bar. Table A1-2 presents the specifications of the HPCR fuel injection system.

Table A1- 2: Fuel Injection System Specifications

Delphi Standard fuel injector	
Type	VCO
Flow Rate (l/min)	0.6971
Number of Holes	6
Hole Size (mm)	0.154
Cone Angle (°)	154
CRS Injection System	
Maximum Injection pressure (bar)	1350

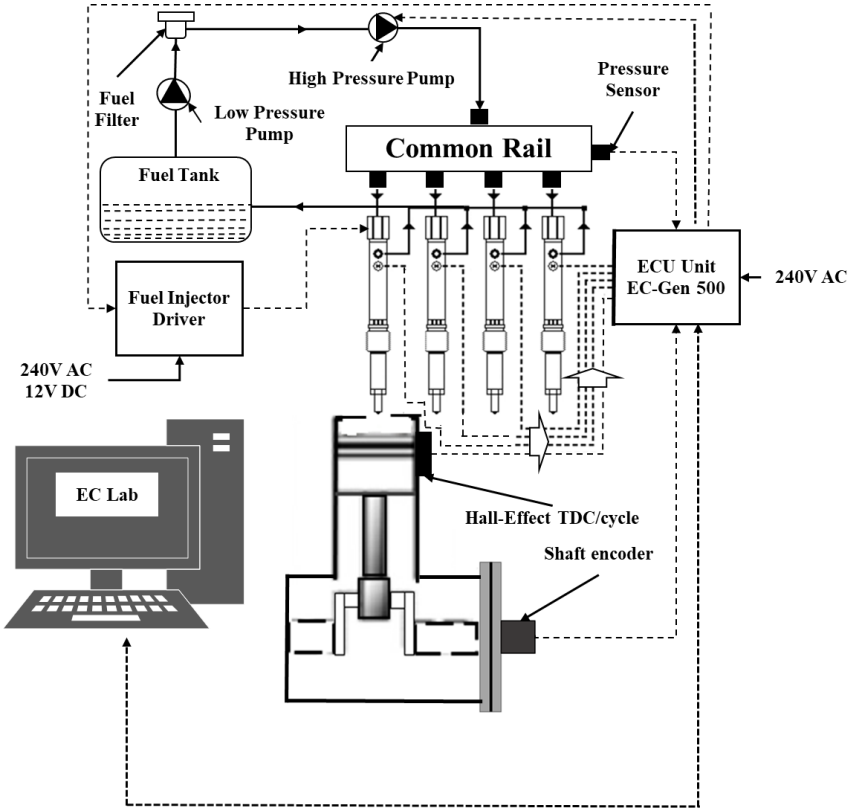

Figure A1- 2: Diagram of the HPCR fuel injection and control systems

A1.4 Air Induction System and Heating

The intake system used for the Ricardo Hydra engine used a naturally aspirated air induction, although it is fitted with a changeover valve to allow for supercharged air induction. Thus, it is possible to set up air boosting and EGR conditions. Apart from this, the intake air was heated to replicate typical operating conditions of a HSDI diesel engines. Here, the air was heated to 100℃ for this study using a 3kW heater which was controlled using a thermocouple fed to the heater control box. The heater and thermocouple setup were installed upstream of the intake manifold.

A2 Experimental Data Collection

A2.1 In-Cylinder Pressure Measurement

A Kistler 6125A un-cooled piezoelectric pressure transducer connected to a Kistler 5011 charge amplifier was used to measure in-cylinder pressure. The pressure transducer was mounted in place of the glow plug as mentioned previously. The electrical charge produced at the transducer was converted to an amplified voltage signal that was fed to the data acquisition system. The transducer has a measuring range of 0 to 250 bar with a sensitivity of -15pC/bar. The pressure transducer and

charge amplifier unit were calibrated using a deadweight tester. The amplifier was calibrated for a range from 0 to 200 bar and set to give the maximum voltage output of 10V at 200 bar in order to prevent an overload.

A2.2 In-Cylinder Pressure Measurement

The data acquisition system used in this investigation comprised of an interface board with a National Instrument (NI) data acquisition card and a data acquisition program within LabVIEW. Signals from the shaft encoder and in-cylinder pressure transducer charge amplifier were connected to the NI BNC-2110 board which was connected to the NI OCI-MIO-16E data acquisition board. The 1 ppr and 1800 ppr signals were used by the software as the reference point and clock for the start of the data recording cycles with 0.2CA intervals. The software records real-time display of the in-cylinder pressure as a function of crank angle. The system was used to record only in-cylinder pressure data while heat release rate, Indicated Mean Effective Pressure (IMEP), pressure-volume (p-V) diagrams and mass fraction burned were calculated using Microsoft Excel.

A2.3 In-Cylinder Data Calculation

The in-cylinder pressure and shaft encoder data were collected to determine the combustion characteristics of the engine. These characteristics are discussed briefly below.

A2.3.1 Cylinder Volume

The cylinder volume of the engine is calculated based on the piston geometry for any crank angle degree. This calculation is done using equation (A2.1).

$$V = \frac{\pi B^2}{4}(l + a - s) + V_c \qquad \text{(A2.1)}$$

Where V is the cylinder volume

B is the cylinder bore

l is the connecting rod length

a is the crank radius

s is the distance between crankshaft and piston pin axis

V_c is the clearance volume

The distance between the crankshaft and the piston axis *s* is given by:

$$s = acos\theta + \sqrt{(l^2 + a^2 sin^2\theta)} \quad \text{(A2.2)}$$

The compression ratio (CR) of the engine can be calculated using equation (A2.3):

$$CR = \frac{V_d + V_c}{V_c} \quad \text{(A2.3)}$$

Where *CR* is the compression ratio

V_d is the displacement volume

The ratio *R*, of the length of the connecting rod to the crank radius is expressed below:

$$R = \frac{l}{a} \quad \text{(A2.4)}$$

Thus, equation (A2.1) can be rearranged to:

$$V = V_c \left\{1 + \frac{1}{2}(r_c - 1)[R + 1 - cos\theta - \sqrt{(R^2 + sin^2\theta)}]\right\} \quad \text{(A2.5)}$$

A2.3.2 Heat Release Rate (HRR)

The heat release rate (HRR) for the optical engine is calculated by applying the first law of thermodynamics seen in equation (A2.6) using the in-cylinder volume and pressure. This also takes into consideration the mass flow across the system boundary at intake and exhaust valve closure, the air mass lost due to crevice flow and the fuel mass injected. This method is used instead of the apparent heat release rate which yields inaccurate HRR measurement due to the leakage of in-cylinder charge caused by the optical components of the engine. Although the leakage due to optical components is to be considered, it is very difficult to compute and thus, the effects of the leakage are neglected due to the fact that the heat release is used as an approximate measure.

$$\frac{dQ}{dt} - p\frac{dV}{dt} + \dot{m}_f h_f = \frac{dU}{dT} \quad \text{(A2.6)}$$

Where $\frac{dQ}{dt}$ is the heat transfer rate into the system across its boundary

$p\frac{dV}{dt}$ is the work transfer rate by the system

$\dot{m}_f$ is the fuel mass flow rate into the system

h_f is the enthalpy of flux

U is the internal energy of the contents inside the combustion chamber

Furthermore, the internal energy *U* is taken as the sensible in-cylinder internal energy, U_s and the enthalpy of flux as the sensible enthalpy of the injected fuel. Thus, equation (A2.6) becomes equation (A2.7) as $h_{f_s} \approx 0$ and the rate of heat transfer into the system, $\frac{dQ}{dt}$ becomes the net heat release rate, while $\frac{dQ_n}{dt}$ represents the difference between heat release rate due to fuel combustion and the system heat transfer.

$$\frac{dQ_n}{dt} = p\frac{dV}{dt} + \frac{dU_s}{dT} \tag{A2.7}$$

By assuming the in-cylinder charge as an ideal gas, equation (A2.7) becomes:

$$\frac{dQ_n}{dt} + p\frac{dV}{dt} + mc_v\frac{dT}{dt} \tag{A2.8}$$

Where c_v is the specific heat at constant volume

T is the absolute temperature

By using the ideal gas law, $PV = mRT$ where *R* is the ideal gas constant:

$$V\frac{dp}{dt} + p\frac{dV}{dt} = mR\frac{dT}{dt} \tag{A2.9}$$

In addition, the combination of equation (A2.8) and (A2.9) eliminates the gas temperature *T* to form equation (A2.10) below:

$$\frac{dQ_n}{dt} = \frac{\gamma}{\gamma-1}p\frac{dV}{dt} + \frac{1}{\gamma-1}V\frac{dp}{dt} \tag{A2.10}$$

Here, γ is the specific heat ratio. Although its value varies through different stages of the engine cycle, it is commonly taken as 1.3 in diesel combustion.

A2.3.3 Combustion Efficiency

The combustion efficiency of the engine was calculated using the heating value of the fuel and the cumulative heat release of the in-cylinder combustion as seen below:

$$CHR_n = HRR_{n-1} + (HRR_n \times \Delta\theta) \tag{A2.11}$$

Where *HRR* is the heat release rate

$\Delta\theta$ is the interval change in crank angle of 0.2 CAD in this study

CHR_n is the cumulative heat release which can also be represented as $\frac{dQ_n}{dt}$

Thus, the combustion efficiency, η_c is calculated using equation (A2.12) shown below:

$$\eta_c = \frac{\sum \frac{dQ_n}{dt}}{\dot{m}_f \times Q_{HV}} \quad \text{(A2.12)}$$

Where $\frac{dQ_n}{dt}$ is the *CHR*

Q_{HV} is the lower heating value of the fuel

A2.3.4 Ignition Delay (ID)

The ID was calculated using the heat release rate data wherein ID refers to the time between the start of fuel injection (SoI) and the start of combustion (SoC) where SoC is recognised as the point where HRR begins to increase . Although the heat transfer rate in the early stages of combustion is more dominant than the first positive heat release before the start of more significant heat release, the SoC is taken as the point when first combustion occurs.

A2.3.5 Indicated Mean Effective Pressure (IMEP)

The IMEP of the engine is the measure of how effective it is in producing work. It is equal to the enclosed areas of the p-V diagram as a function of engine cylinder displacement volume with respect to maximum pressure. Using the p-V diagram of a four-stroke diesel engine, the net IMEP obtained from the subtraction of the pumping loop from the working loop or Gross IMEP is used. However, the IMEP of the engine is easily calculated by using equation (A2.13) below:

$$IMEP = \frac{1}{V_d} \int_{0°}^{720^\circ} p.dV \quad \text{(A2.13)}$$

Where *p* is the in-cylinder pressure

During the sampling of the in-cylinder pressure data, an interval of 0.2 CAD is used in this study. Moreover, the crank angle duration from 0 CAD to 720 CAD represents the full cycle of the engine.

A2.3.6 Indicated Specific Fuel Consumption (ISFC)

The ISFC of the engine is a measure of its fuel efficiency and is calculated using the output work and fuel flow rate which can be expressed as:

$$ISFC = \frac{rpm \times \dot{m}_f}{IMEP \times V_d} \quad \text{(A2.14)}$$

Where rpm is the engine speed

$IMEP$ is the indicated mean effective pressure

V_d cylinder displacement volume

$\dot{m}_f$ is the mass flow rate of the fuel

A2.4 Exhaust Emission Measurement

A Horiba MEXA-7170DEGR exhaust analyser which consists of four modules used for the measurement of NOx, uHC, O_2 and CO-CO_2 while an AVL 415 smoke meter was used for the measurement of soot emissions. These modules are controlled by a PC which acts as the main control unit. In addition, the unit has a touch screen user interface which displays prompt emission values either numerically or graphically.

A2.4.1 Horiba FIA-720 Emission Module for uHC Measurement

The Horiba FIA-720 emission module is a Flame Ionisation Detector (FID) was used for the measurement of uHC emission. The module works based on ion production from burned hydrocarbons wherein the rate of ion production is directly proportional to the hydrocarbon concentration.

A2.4.2 Horiba MPA-720 Module for O_2 Measurement

The Horiba MPA-720 module is a pneumato-magnetic analyser that was used for the measurement of oxygen concentration in the exhaust. Although its operation is based on the effect of magnetism on the exhaust gas components mostly oxygen and the oxides of nitrogen, the influence of nitrogen oxides is negligible compared to oxygen. The exhaust gas sample flows through a magnetic cell whose electromagnetic field is generated by an AC current. The generated magnetic field attracts the oxygen

molecules from the passing exhaust gas towards the poles which causes an increase in pressure around the poles that is proportional to the oxygen concentration. The pressure change is detected and converted into an electrical output signal by a condenser microphone in the analyser.

A2.4.3 Horiba AIA-72X Emission Module for CO and CO_2 Measurement

This emission module was used for the measurement of CO and CO_2 emissions through the use of a Non-Dispersive Infrared (NDIR) method. It works based on the principle of infrared radiation absorption at various wavelengths by the emitted molecules. Here, the level of absorption is proportional to the concentration of each molecule.

A2.4.4 Horiba CLA-720A for NOx Measurement

The Horiba CLA-720A is a chemiluminescence analyser module used for the measurement of NO and NO2 concentrations in the exhaust gas. This module works based on the reaction between NO and ozone (O_3) that results in the NO oxidation to NO_2. Some of the NO_2 produced during the oxidation process are in the excited form which decay to the ground state through a photon emission process known as chemiluminescence. The intensity of the emitted photon light is proportional to the concentration of NO molecules in the sample gas. Moreover, it is filtered by a bandpass filter located before the light detector which outputs a voltage signal.

A2.4.5 AVL 415 Soot Emission Measurement

Soot emission was measured using an AVL 415 smoke meter. The analyser works by sucking exhaust gas into a sample line using a diaphragm pump. The sampled exhaust gas passes through a paper filter and flow meter, respectively, while a reflectometer measures and compares the reflectance of the clean and the blackened filter papers. The measurement process works by obtaining the level of paper blackening wherein a clean white filter paper has a value of 0 and a completely blackened paper has a value of 10 both of which correspond to the soot concentration of 0 and 32000 mg/m3, respectively. For this study, the meter was set to carry out three consecutive automatic measurements wherein the average result of the FSN was displayed on the meter screen.

Appendix B

B1 CFD Governing Equations

AVL Fire code applies the Navier-Stokes equations for the conservation of mass (continuity), momentum and energy equations in predicting in-cylinder species, flows and interaction [156]. These equations are presented as equation B1.1, B1.2 and B1.3 respectively:

- **The Continuity Equation:**

$$\frac{\partial \rho}{\partial t} + \nabla \cdot (\rho V) = 0 \tag{B1.1}$$

Where ρ, t, V and ∇ represent the fluid density, time, velocity, and divergence.

- **The Momentum Equation:**

$$x\ component: \frac{\partial(\rho u)}{\partial t} + \nabla \cdot (\rho u V) = -\frac{\partial p}{\partial x} + \frac{\partial \tau_{xx}}{\partial x} + \frac{\partial \tau_{yx}}{\partial y} + \frac{\partial \tau_{zx}}{\partial z} + \rho f_x \tag{B1.2}$$

$$y\ component: \frac{\partial(\rho v)}{\partial t} + \nabla \cdot (\rho v V) = -\frac{\partial p}{\partial y} + \frac{\partial \tau_{xy}}{\partial x} + \frac{\partial \tau_{yy}}{\partial y} + \frac{\partial \tau_{zy}}{\partial z} + \rho f_y$$

$$z\ component: \frac{\partial(\rho w)}{\partial t} + \nabla \cdot (\rho w V) = -\frac{\partial p}{\partial z} + \frac{\partial \tau_{xz}}{\partial x} + \frac{\partial \tau_{yz}}{\partial y} + \frac{\partial \tau_{zz}}{\partial z} + \rho f_z$$

Where *u*, *v* and *w* represent the three-dimensional *x*, *y* and *z* components of the velocity, respectively. Regarding the *x*, *y* and *z* components, the first and second terms on the left-hand side represent the rate of change of momentum and the net momentum flux through the surfaces of the volume boundary, respectively. On the right-hand side, the first term represents the pressure gradient acting on the control volume while the second, third and fourth terms represent the normal and shear stress acting on the surfaces of the control volume and the fifth term represents the density component.

- **The Energy Equation:**

Equation (B1.3) is the energy equation expressed in terms of the total energy, $e + \frac{V^2}{2}$. The terms on the left-hand side represent the kinetic energy while the terms on the right-hand side represent the conductive terms where *k* and *T* are the coefficient and temperature respectively [156].

$$\frac{\partial}{\partial t}\left[\rho\left(e+\frac{V^2}{2}\right)\right]+\nabla\cdot\left(\rho\left(e+\frac{V^2}{2}\right)V\right) \tag{B1.3}$$

$$=\rho\dot{q}+\frac{\partial}{\partial x}\left(k\frac{\partial T}{\partial x}\right)+\frac{\partial}{\partial y}\left(k\frac{\partial T}{\partial y}\right)+\frac{\partial}{\partial z}\left(k\frac{\partial T}{\partial z}\right)-\frac{\partial(up)}{\partial x}$$

$$-\frac{\partial(vp)}{\partial y}-\frac{\partial(wp)}{\partial z}+\frac{\partial(u\tau_{xx})}{\partial x}+\frac{\partial\left(u\tau_{yx}\right)}{\partial y}+\frac{\partial(u\tau_{zx})}{\partial z}$$

$$+\frac{\partial\left(v\tau_{xy}\right)}{\partial x}+\frac{\partial\left(v\tau_{yy}\right)}{\partial y}+\frac{\partial\left(v\tau_{zy}\right)}{\partial z}+\frac{\partial(w\tau_{xz})}{\partial x}+\frac{\partial\left(w\tau_{yz}\right)}{\partial y}$$

$$+\frac{\partial(w\tau_{zz})}{\partial z}+\rho f\cdot V$$

B2 CFD Sub-Models

The CFD sub-models described below were implemented within AVL Fire ESE Diesel for the predictions of turbulence, spatial and temporal distribution of fuel, combustion characteristics and emission formation of the engine CFD model. They were selected based on the existing information available in the literature for similar CFD models and simulations [38], [89], [157]–[160].

B2.1 Turbulence Model

The k-ζ-f model developed by Hanjalic et al., [161] was adopted for predicting the in-cylinder turbulence. It is widely used due to its robustness and low sensitivity to non-uniformities and clustering of the computational grid with moving boundaries for highly turbulent and compressible flows. It uses the Durbin's elliptic relaxation concept for eddy viscosity to improve the numerical stability of the computational model by solving the velocity scale-kinetic energy ratio transport equation $\zeta=\frac{\overline{v^2}}{k}$ where $\overline{v^2}$ is the velocity scale and k is the kinetic energy [162]. Furthermore, it is highly independent to near-wall computational meshing due to its more convenient approach in the formulation of the equation for the elliptic function f and particularly for the wall boundary condition for this function [161][163].

B2.2 Fuel Spray Models

B2.2.1 Fuel Spray Break-Up Model

The wave model formulated by Reitz et al., [164] was adopted for the prediction of fuel break-up and droplet formation in the CFD model. Atomisation of fuel spray is simulated in two stages, the primary break-up that occurs near the nozzle hole and the secondary break-up that occurs further downstream of the spray. The wave model has been widely used to model fuel spray break-up and atomisation. Furthermore, it assumes that primary agitation on the surface of a liquid is associated to its wavelength using the fuel injection pressure and in-cylinder pressure as the initial conditions. For high fuel velocities, the size of the secondary droplets is equivalent to the wavelength of the fastest growing surface. The wavelength Λ and growth rate of the fastest growing surface Ω are determined from equations B2.1 and B2.2.

$$\Lambda = 9.02 r_d \frac{(1 + 0.45 \cdot Oh^{0.5})(1 + 0.4 \cdot T^{0.7})}{(1 + 0.87 \cdot {We_g}^{1.67})^{0.6}} \tag{B2.1}$$

$$\Omega = -\sqrt{\frac{\rho_d {r_d}^3}{\sigma}} \frac{0.34 + 0.38 \cdot {We_g}^{1,5}}{(1 + Oh)(1 + 1.4 \cdot T^{0.6})} \tag{B2.2}$$

Where r_d, ρ_d , σ, We_g, Oh and T represent the droplet radius, density, surface tension, Weber number, Ohnesorge number and Taylor number, respectively. During its implementation, the wave constant C_1 , C_2, C_3 values were set to 0.61, 15, and 1 while the C_4 and C_5 values were set to 0.1 for stable droplet size and time, respectively, based on benchmark experimental data.

B2.2.2 Evaporation Model

The Dukowitz model [165] was adopted for the prediction of fuel droplet evaporation for diesel fuel. It has additional correction coefficients that consider internal circulation, droplet deformation, non-uniform, and transient heating. It assumes a uniform distribution of temperature along the diameter of the fuel droplet, quasi steady gas properties around the droplet, the presence of a spherical symmetric flow near the droplet as well as a thermal equilibrium between liquid and vapor on the surface of the droplet. During its implementation, its E_1 and E_2 constant values were

set to 1 each. Further details of its implementation for the rate of change of fuel droplet temperature and mass are available in the literature [165].

B2.2.3 Wall Interaction Model

The Walljet model was adopted for predicting the fuel droplet-wall interaction. It is based on Naber and Reitz's spray-wall impingement model [166], it works by forming a vapor bolster between the droplet and the wall surface under that causes the droplet to recoil or slide along the walls without considering wall film physics upon collision. Furthermore, the droplet-wall collision results in either a droplet recoil or reflection depending on the critical Weber number, W_c = 80. Zones in which the droplet Weber number is less than W_c are considered as the recoil zones while zones with droplet Weber number greater than W_c are considered as the liquid jet zones.

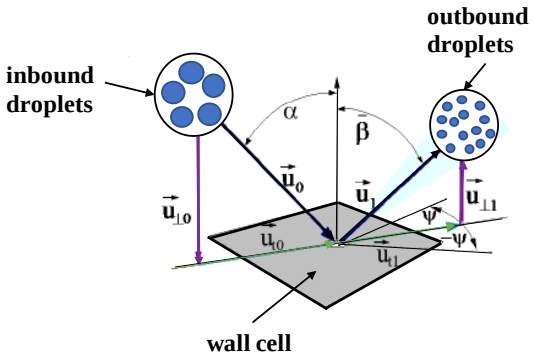

Figure B2- 1: Wall Interaction of Droplets for Walljet model [167], [168]

Figure B2-1 illustrates the working principle of the Walljet model in which the inbound (primary) parcel is characterised by mass, diameter, and velocity, m_p, d_p and u_p, respectively, while the outbound or reflected (secondary) parcel is characterised by mass, diameter, and velocity, m_s, d_s and u_s, respectively. Regarding the Walljet model parameters, the droplet diameter post wall impingement in both zones is calculated as a function of the Weber number using the criteria depicted in equation (B2.3) wherein the angle of reflection can vary within the range, $0 < \beta < 5°$ [167], [168].

$$We < 50 \qquad d_s = d_p \tag{B2.3}$$

$$50 \leq We \leq 300 \quad d_s = d_p \times f(We_{\perp in})$$

$$We > 300 \quad d_s = 0.2 \times d_p$$

B2.3 Combustion Model

The Extended Coherent Flame Model 3 Zones (ECFM-3Z) illustrated in Figure B2-2 was adopted for predicting combustion characteristics. It relies on the ECFM combustion model flame surface density transport equation but with an improved burnt gas chemistry description and a three-zone mixing model capable of predicting inhomogeneous turbulent premixed and diffusion combustion. According to the direction of flame propagation shown in Figure 8-4, the model is divided vertically into the burned and unburned gases and divided horizontally into the air, mixing and fuel regions. The mixing region is divided into auto-ignition, premixed flame and diffusion flame zones distributed within the computational cell. The auto-ignition and diffusion zones occur in the regions of the mixed unburned and mixed burned gases.

During fuel injection, fuel droplets are assumed to be in the unmixed fuel region, F, while evaporated fuel is placed in the mixing region, M. The ignition delay of the unburned air-fuel mixture is predicted using tabulated ignition data for diesel based on the functions of chemical kinetics, pressure, temperature, fuel/air equivalence ratio and residual gas content. The mixing of fuel and air is then computed with a time scale based on the turbulence model [169].

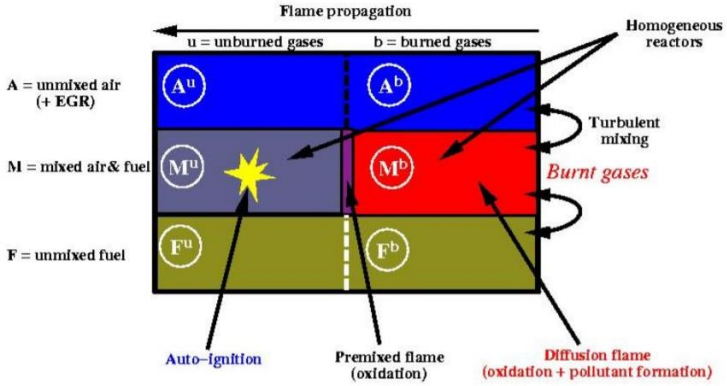

Figure B2- 2: Illustration of the ECFM-3Z Model along with its zones [163]

Furthermore, the auto-ignition intermediate species, CO, H_2, and NO tracers are considered by the model to obtain the mixing quantities through mass fraction in the unburned gases and species that describe the mixing process. Thus, the transport equations for the mean quantities of the CO, CO_2, H, OH, H_2, H_2O, O, O_2, N, NO, N_2 species are solved. The intermediate species integrate the auto-ignition advance process wherein the mixed fuel is oxidised either when the delay time is reached or

when the molar concentration of the intermediate species exceed that of the fuel tracer [163].

B2.4 Soot Emissions Model

The Kinetic model is used in predicting the soot formation which is based on detailed chemical reaction scheme for calculating soot oxidation and formation. It consists of the combination of the following formation mechanisms; hydrocarbon oxidation reactions, polyaromatic hydrocarbons (PAH) reaction mechanism, acetylene pyrolysis and pure carbon cluster formation mechanism, a set of two mechanisms for soot precursor formation from polyene and polyaromatic molecule condensation, and the reaction of HACA mechanism and addition of polyene molecule for soot particle growth[170] [163][171]. Furthermore, it comprises of about 1850 gas-phase reactions, 100 heterogenous reactions and 186 species with contributions from four different groups of micro heterogenous particles. This model can efficiently describe the formation and oxidation of soot during combustion while parameters required for fuel that do not correlate with one of the species is decided automatically by the AVL Fire solver using the local equivalence ratio of the mixture reaction [172].

B2.5 NOx Emissions Model

The "Extended Zeldovich + Prompt + Fuel" model is adopted for the prediction of NO formation and formation rate. This model was adopted instead of the more commonly used Extended Zeldovich model due to its better prediction of NOx emission for the engine configuration used in this investigation for model validation purposes. This was attributed to the significant contribution of prompt NOx formation to the overall NOx emission. The net rate of NO formation, $\frac{\partial c_{NO}}{\partial t}$ for the extended Zeldovich model alone is seen in equation (B2.4) assuming a steady state for nitrogen atoms (N) where (NO), (N_2) and (O) are nitric oxide, molecular nitrogen, and atomic oxygen concentrations, respectively. However, the total rate of NO formation for the extended Zeldovich + Prompt + Fuel model is seen in equation (B2.5).

$$\frac{\partial c_{NO}}{\partial t} = k_1 c[N_2]c[O] - k_{-1}c[N]c[NO] + k_2 c[N]c[O_2] - k_{-2}c[NO]c[O] + k_3 c[NO]c[OH] - k_{-3}c[NO]c[H] \quad \text{(B2.4)}$$

$$\frac{\partial c_{NO}}{\partial t} = 2k_{1f}c_o c_{N_2} \frac{\left(1-\frac{k_{1b}k_{2b}c_{NO}^2}{k_{1f}c_{N_2}k_{2f}c_{O_2}}\right)}{1+\frac{k_{1b}c_{NO}}{k_{2f}c_{O_2}+k_{3f}c_{OH}}} \tag{B2.5}$$

$$k = \beta T^{\propto} exp\left(\frac{-E_a}{R_u T}\right) \tag{B2.6}$$

Here, c is the concentration in gmol/m^3, and k is the kinetic reaction rate coefficient seen in equation (B2.5) where E_a, is the activation energy, R_u ,$\propto \equiv \frac{[NO]}{[NO]_e}$ and $\beta \equiv \frac{[N]}{[N]_e}$, are constants.

The NOx transport equation is seen in equation (B2.7) where Y_{NO} , ρ and S_{NO} represent the local NOx mass fraction in gas phase, density and the source term seen in equation (B2.8). The source term is the product of the molecular weight of NO, $M_{w,NO}$, and the NO formation thermal prediction mechanism, $\frac{d[NO]}{dt}$ [65],[171].

$$\frac{\partial}{\partial x}(\rho Y_{NO}) + \nabla \cdot (\rho \vec{v} Y_{NO}) = \nabla \cdot (\rho D \nabla Y_{NO}) + S_{NO} \tag{B2.7}$$

$$S_{thermal,NO} = M_{w,NO} \frac{d[NO]}{dt} \tag{B2.8}$$